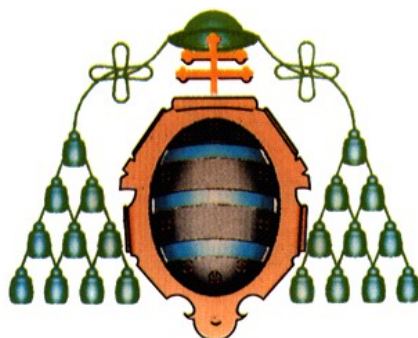# UNIVERSIDAD DE OVIEDO

Programa de Doctorado de Ciencia y Tecnología de Materiales

GRAFENOS PREPARADOS POR MÉTODOS QUÍMICOS: CARACTERÍSTICAS Y APLICACIONES

TESIS DOCTORAL

MARIA JESUS FERNANDEZ MERINO

JULIO 2013

UNIVERSIDAD DE OVIEDO

Programa de Doctorado de Ciencia y Tecnología de Materiales

GRAFENOS PREPARADOS POR MÉTODOS QUÍMICOS: CARACTERÍSTICAS Y APLICACIONES

TESIS DOCTORAL

Juan Ignacio Paredes Nachón
Silvia María Villar Rodil
Amelia Martínez Alonso

AGRADECIMIENTOS

Quisiera expresar mi agradecimiento a todas las personas e instituciones que, directa o indirectamente han contribuido ha hacer realidad este trabajo:

A mis directores de tesis, los doctores Amelia Martínez Alonso, Juan Manuel Diez Tascón, Silvia María Villar Rodil y Juan Ignacio Paredes Nachón, gracias por vuestra orientación, ideas, consejos y por darme la oportunidad de trabajar con ellos.

Al doctor José Rubén García Menéndez por aceptar ser el tutor de esta tesis.

Al Ministerio de Ciencia e Innovación por la concesión de la beca predoctoral FPI, que hizo posible la realización de este trabajo. Al Instituto Nacional del Carbón, centro donde se ha realizado este trabajo.

A los doctores Emilia Morallón Núñez y Diego Cazorla Amorós, que me brindaron la oportunidad de realizar un estancia de investigación bajo su tutela. Gracias por todo vuestro apoyo, tanto profesional como personal, conseguisteis que me sintiese una más de vuestro grupo y no añorase mi casa.

A Ana López, secretaria del departamento de Ciencia y Tecnología de los Materiales. Ana, no se como hubiese hecho todo el papeleo sin ti, gracias por tu paciencia infinita, tu amabilidad y tu gran profesionalidad.

A todos los trabajadores del Incar, por hacer que los días sean más agradables con vuestra simpatía y amabilidad, es especial a Josefina, que con su cariño nos hace sentir como en casa desde el primer dia.

A mis compañeros de laboratorio, tanto a los que están como a los que se han ido para comenzar nuevas aventuras: Marley, Ángela, Rubén, Miguel, Katia, Marina, Pablo, Marlen, gracias por lo buenos momentos pasados. Tomás creo que eres una de las mejores personas que conozco, conserva tu inocencia y bondad, te hacen único y especial. Silvia, Bea, Yoli y Nuria, gracias por hacer que las comidas y cafés sean un espacio de relajación absoluta, por compartir mis risas y confidencias, muchísimas gracias por vuestra amistad.

A mis compañeros de Alicante, en especial a David, Miriam, Alonso y Juan Manuel, por tratarme como si fuese una más de vosotros, conseguisteis disminuir la morriña en todo momento.

Nacho, Silvia y Laura, sabéis que esta tesis es tanto mía como vuestra. Gracias por vuestro esfuerzo, ideas, consejos y trabajo, nunca olvidaré todo lo que habéis echo por mi. De todo corazón, gracias.

Laura, gracias por todo. Estos cuatro años no serían los mismos sin ti. Gracias por aguantarme, ayudarme en todo, preocuparte por mí, compartir mis alegrías y preocupaciones. Gracias por estar en los buenos momentos y en los malos, cuando todo se vuelve negro y solo los buenos se quedan, tú siempre serás una parte fundamental de mi vida y nunca podré agradecerte lo suficiente el cariño y apoyo recibidos.

A mis amigos. Tengo la inmensa fortuna de tener los mejores amigos del mundo, que en cada momento me demuestran que puedo contar con ellos para todo, incluso en los momentos más oscuros. Laura, Nico, David, Laura, Lucas, Ali, gracias por acompañarme durante tantos años con vuestro cariño y buen humor: Gracias por estar siempre a mi lado.

A mis "susiítas", Sara, Ame, Eli y Andrea. Gracias por todo chicas, por estar siempre a mi lado, tantos años y aquí seguimos dando guerra, e igual de unidas que siempre. Gracias por vuestro apoyo incondicional a cada paso que doy en la vida, por celebrar mis logros como vuestros, hacerme reír en los mejores momentos, llorar conmigo en los peores, y morder por mí a quien se ponga por delante. Sois el mejor apoyo que se pueda tener.

A mis padres y mi hermano, todo lo que tengo os lo debo a vosotros. Gracias por todo el esfuerzo y sacrificios que habéis echo por mí y por inculcarme que todo se puede conseguir, aunque sea con mucho esfuerzo y lo más importante, sin perjudicar a nadie. Gracias por vuestro cariño y apoyo, todo lo que tengo es vuestro.

A Juan, la persona más fuerte, valiente, generosa, inteligente y maravillosa que conozco. Gracias por tu apoyo incondicional y tu fortaleza en los momentos más oscuros, por conseguir que me ría de todo y de nada, en definitiva, por hacerme feliz. Gracias por todo, nada sería igual sin ti.

Resumen

El presente trabajo tiene como objetivo principal el desarrollo de técnicas de preparación de grafeno que puedan utilizarse a gran escala de forma eficaz y segura. Actualmente, una de las técnicas más prometedoras es la basada en la exfoliación de óxido de grafito a óxido de grafeno y su posterior reducción. En este trabajo se han investigado agentes reductores eficaces y seguros del óxido de grafeno, como alternativa a la hidracina, que se usa comúnmente, pero es tóxica y dañina para el medio ambiente. En particular, se ensayaron numerosos antioxidantes naturales, entre ellos vitaminas, aminoácidos o ácidos orgánicos como posibles reductores del óxido de grafeno. Fue posible identificar 9 nuevos agentes reductores eficaces, siendo alguno de ellos (por ejemplo, la vitamina C) sustitutos potenciales de la hidracina.

Para que las dispersiones acuosas de láminas de óxido de grafeno reducido químicamente sean coloidalmente estables, es necesario mantener dichas dispersiones bajo condiciones fisicoquímicas (pH, concentración de láminas, concentración de electrolito, etc.) estrictas, y si estas condiciones varían debe utilizarse un agente que estabilice coloidalmente las láminas. En este trabajo, se realizó un estudio comparativo del uso de un amplio conjunto de surfactantes para estabilizar dispersiones de óxido de grafeno en condiciones fisicoquímicas adversas. Se observó que la eficacia de los surfactantes dependía de las características del surfactante utilizado y de su concentración, y que el surfactante más adecuado para estabilizar las láminas varía en función de las condiciones específicas del medio coloidal.

Otro método de preparación de grafeno investigado en el presente trabajo fue la exfoliación directa de grafito prístino en agua inducida por ultrasonidos, que requiere necesariamente el uso de estabilizadores de la dispersión. Se llevó a cabo un estudio comparativo sobre la capacidad y eficacia de distintos surfactantes iónicos y no iónicos para dicho fin. Se concluyó que, en general, los surfactantes no iónicos son más eficaces que los iónicos para exfoliar y estabilizar altas concentraciones de grafeno estructuralmente perfecto.

Finalmente, en el presente trabajo se prepararon y caracterizaron materiales híbridos formados por grafeno y bien nanopartículas metálicas o nanopartículas de sílice mesoporosa, que tienen utilidad potencial en diversas aplicaciones. En particular, se ha

demostrado que determinados híbridos grafeno-nanopartícula de plata poseen una excelente actividad catalítica en la reducción de 4-nitrofenol con borohidruro de sodio.

Abstract

The main goal of the present work is the development of techniques for the preparation of graphene that can be used effectively and safely on a large scale. Currently, one of the most promising techniques is based on the exfoliation of graphite oxide to graphene oxide and its subsequent reduction. In this work, effective and safe alternatives to the commonly used but hazardous hydrazine as a reducing agent of the graphene oxide are investigated. In particular a range of natural antioxidants were tested including vitamins, amino acids and organic acids, as potential reducing agents of graphene oxide. Nine novel reducing agents were identified; some of them, e.g. vitamin C appeared as potential substitutes for hydrazine.

To make sure that aqueous dispersions of chemically reduced graphene oxide sheets are colloidally stable, it is necessary to keep these dispersions within a strict range of physicochemical conditions (pH, sheet concentration, electrolyte concentration, etc.), and under different conditions a dispersing agent should be used to stabilize the sheets. In this work, a comparative study was made towards the use of a wide range of surfactants in the stabilization of reduced graphene oxide under non optimal physicochemical conditions. It was observed that the efficacy of the surfactants depends on the specific characteristics of the surfactant and its concentration, and the specific conditions of the colloidal environment determine the most suitable surfactants in each case.

Another method for the preparation of graphene investigated here was the direct exfoliation of the pristine graphite in water induced by ultrasound, which strictly requires the use of stabilizers. A comparative study regarding the capacity and the efficacy of different ionic and non-ionic surfactants was carried out to this effect. The conclusion was that, in general, non-ionic surfactants were more effective than their ionic counterparts towards exfoliation and stabilisation of high concentrations of structurally perfect graphene.

Finally, several hybrid materials made up of graphene and either metallic nanoparticles or mesoporous silica nanoparticles, with potential use in several applications were prepared and characterized. In particular, it was demonstrated that certain graphene-silver nanoparticle hybrids possess an excellent catalytic activity for the reduction of 4-nitrophenol with sodium borohydride.
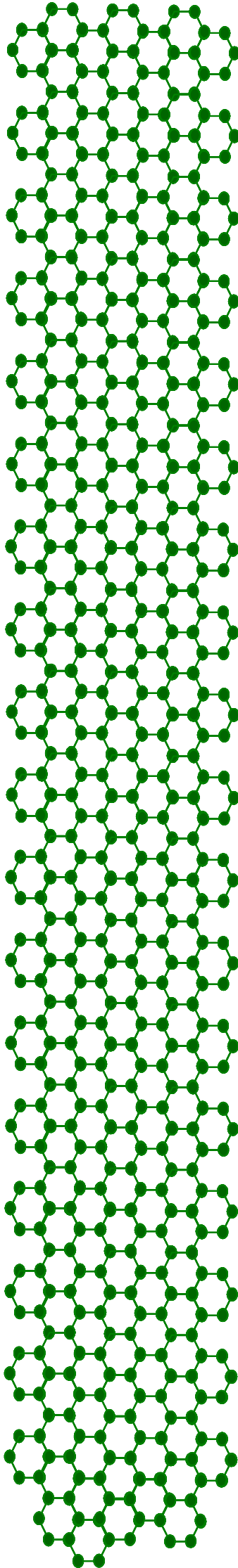
1. INTRODUCCIÓN

1.1. El grafeno.

El grafeno es una forma bidimensional del carbono consistente en átomos unidos entre sí por fuertes enlaces covalentes basados en la hibridación sp^2 que forman una red hexagonal. El grafeno se puede considerar como la unidad básica de distintas estructuras de carbono, como grafito, fulerenos o nanotubos de carbono (Fig. 1). Los primeros estudios teóricos sobre el grafeno se remontan a la década de 1960, cuando se pensaba que su obtención experimental no sería posible debido a la suposición de que los cristales bidimensionales de cualquier material no eran termodinámicamente estables a temperaturas finitas [1, 2].
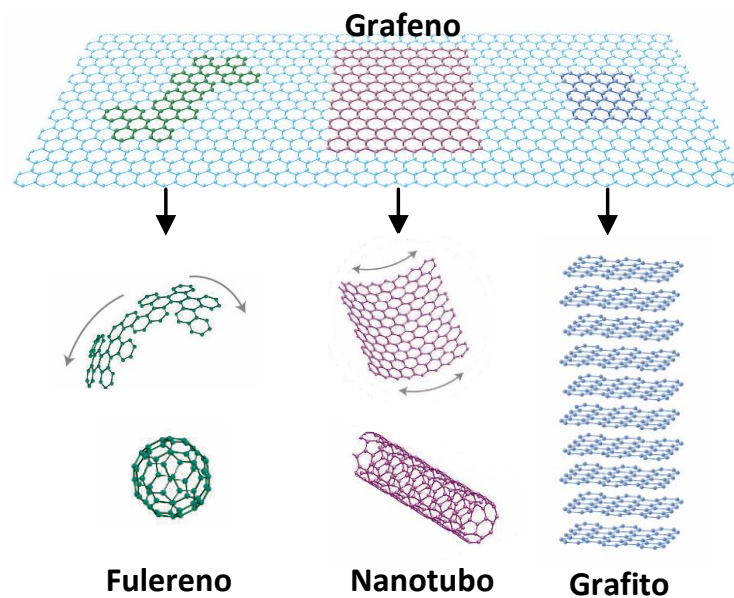
Figura 1. Formación de estructuras de carbono a partir de grafeno bidimensional. Reproducido de [3].

Esta suposición se basaba en la hipótesis de los físicos Peierls y Landau, que argumentaban que las fluctuaciones térmicas en redes cristalinas bidimensionales deben conducir a desplazamientos de los átomos comparables a las distancias interatómicas a cualquier temperatura finita. En efecto, era un hecho conocido que la temperatura de fusión de películas delgadas disminuye rápidamente con la disminución de su espesor, volviéndose inestables y segregándose en islas para espesores típicos de unas pocas docenas de capas atómicas [4, 5]. Por esta razón, antes del descubrimiento del grafeno las monocapas atómicas solo se conocían como parte integral de estructuras

tridimensionales, generalmente en forma de estructuras epitaxiales sobre monocristales [4, 5]. Sin embargo, en 2004 se puso en duda esta teoría con la consecución experimental del grafeno [6] y otros cristales bidimensionales, como por ejemplo nitruro de boro y disulfuro de molibdeno [7]. Con el tiempo, la existencia de estos cristales de espesor atómico ha podido conciliarse con esta teoría. De hecho, se puede argumentar que los cristales bidimensionales obtenidos a partir de sus correspondientes estructuras tridimensionales se "congelan" en un estado metaestable durante su exfoliación, mientras que su pequeña superficie (<< 1 mm) y sus fuertes enlaces interatómicos aseguran que las fluctuaciones térmicas no puedan conducir a la generación de dislocaciones u otros defectos cristalinos, incluso a elevada temperatura [3, 8, 9].

El grafeno fue aislado por primera vez por los físicos Geim y Novoselov [6] mediante exfoliación micromecánica de grafito aprovechando las débiles interacciones cohesivas entre los planos atómicos (002) que forman este material. Desde entonces, el grafeno ha despertado un gran interés en la comunidad científica debido a las extraordinarias propiedades que ha ido revelando.

1.2. Propiedades y aplicaciones del grafeno.

Propiedades electrónicas. El grafeno está formado por átomos de carbono unidos entre sí mediante enlaces covalentes basados en la hibridación sp^2 en una estructura hexagonal donde cada átomo de carbono contribuye con tres electrones a los orbitales sp^2. El electrón de valencia restante está en un orbital atómico p_z perpendicular al plano de los orbitales sp^2. El solapamiento de los orbitales p_z no hibridados da lugar a orbitales π en los que los electrones están deslocalizados al plano del grafeno. Estos electrones determinan en gran medida las excepcionales propiedades electrónicas del grafeno, entre ellas el hecho de ser un semiconductor de gap de banda cero y su relativamente elevada conductividad eléctrica, debido a que la deslocalización electrónica produce una elevada movilidad de carga (20 m^2 V^{-1} s^{-1}) [10]. La calidad estructural del grafeno afectará a la conductividad eléctrica, debido a que, en general, las impurezas y defectos estructurales actúan como centros de dispersión que inhiben la movilidad de los portadores de carga.

Otra característica especial del grafeno es que estos electrones deslocalizados se comportan como fermiones de Dirac carentes de masa, lo que se demuestra al presentar un efecto Hall cuántico anómalo. El efecto Hall es la aparición de una diferencia de potencial eléctrico (voltaje Hall) en un conductor por el que circula una corriente, en presencia de un campo magnético perpendicular al movimiento de las cargas. El campo eléctrico generado en el interior del conductor (campo Hall) es perpendicular al movimiento de las cargas y al campo magnético aplicado. El efecto Hall cuántico se produce en sistemas electrónicos bidimensionales sometidos a campos magnéticos fuertes y bajas temperaturas y consiste en la cuantización del voltaje Hall. En el caso del grafeno, si un campo electromagnético atraviesa perpendicularmente una lámina y se induce una corriente a lo largo del eje X de dicha lámina, en la dirección del eje Y aparecerá una conductividad cuantizada en semienteros, en lugar de en enteros como ocurre en el efecto Hall cuántico. Por ello, estos electrones se comportan como cuasipartículas con carga fraccionada, no entera.

El grafeno ha permitido formular la paradoja de Klein. Según la teoría clásica una partícula no puede propagarse a través de una región donde su energía potencial sea superior a su energía total: la partícula rebota contra la barrera de potencial. Los electrones, al obedecer las leyes de la mecánica cuántica, poseen una probabilidad finita de atravesar la barrera por efecto túnel y aparecer al otro lado [11]. Pues bien, en el caso del grafeno la probabilidad de transmisión del electrón es siempre 1, independientemente de la altura y anchura de la barrera, lo cual se conoce como paradoja de Klein [12].

Propiedades ópticas. El grafeno absorbe un 2.3% de la luz incidente en una amplia gama de longitudes de onda [13]. La absorbancia presenta un máximo a ~ 270 nm en la región ultravioleta, lo que se atribuye a transiciones electrónicas entre estados π y π^* y es esencialmente constante entre 300 y 2500 nm. Además, las transiciones ópticas se pueden modular considerablemente por medio del uso de la compuerta eléctrica. Dicha ajustabilidad puede servir para el desarrollo de dispositivos ópticos y optoelectrónicos basados en grafeno.

Otra propiedad destacable de determinados derivados del grafeno es la fotoluminiscencia. Es posible conseguir derivados fotoluminiscentes de grafeno mediante la inducción de un gap de banda adecuado [14, 15]. En el grafeno el gap de

banda es cero, lo cual por un lado puede ser una propiedad interesante debido a que favorece su conductividad eléctrica en comparación con semiconductores con gap de banda finito, pero por otra parte puede ser considerado un gran inconveniente debido a la imposibilidad de interrumpirla cuando se desea, lo cual es deseable en aplicaciones del grafeno en dispositivos electrónicos. Estudios recientes han demostrado que el gap de banda cero en el grafeno es resultado del entorno idéntico que poseen las dos subredes atómicas en el grafeno. Esto sugiere que rompiendo esta simetría lateral en el plano, bien de forma estructural o por modificaciones químicas [16], podría crearse un gap de banda en el grafeno. Hasta el momento, los métodos más prometedores han sido los siguientes:

- Producción de puntos cuánticos o nanocintas de grafeno, es decir, láminas de grafeno de dimensiones laterales por debajo de ~20 nm, que exhiben un fuerte confinamiento cuántico y por tanto un gap de banda finito [14].
- Funcionalización covalente del grafeno. Un ejemplo extremo es el óxido de grafeno [17], que está formado por una lámina de grafeno decorada por grupos funcionales oxigenados, donde muchos de sus átomos de carbono han pasado de tener una hibridación sp^2 a sp^3. En este caso, se abre un gap de banda tan grande que el material se vuelve eléctricamente aislante.

La combinación de las propiedades ópticas y electrónicas del grafeno abre nuevas oportunidades para distintas aplicaciones en fotónica y optoelectrónica, por ejemplo en pantallas táctiles [13], diodos emisores de luz [18], transistores de alta frecuencia [19], sensores químicos [20], etc.

Propiedades mecánicas. Se ha predicho que las láminas de grafeno monocapa presentan propiedades mecánicas excepcionales, superiores a las de prácticamente cualquier otro material. De hecho, diversos estudios muestran valores de módulo de Young del orden de 1 TPa y resistencias a la tracción de ~ 130 GPa para deformaciones de 0.25% [21]. Estas propiedades son de gran importancia para la fabricación de dispositivos basados en grafeno, ya que la aplicación de tensiones mecánicas no deseadas (golpes, caídas, etc.) puede afectar al rendimiento y durabilidad de estos dispositivos.

Como consecuencia de sus excelentes propiedades mecánicas se ha postulado el uso del grafeno como elemento de refuerzo en materiales compuestos, por ejemplo materiales compuestos grafeno-polímero. Aunque el grafeno prístino presenta mejores propiedades mecánicas que el óxido de grafeno reducido debido a que los defectos y grupos funcionales de este último tiendes a degradar sus propiedades mecánicas, la presencia de dichos grupos puede ser beneficiosa, ya que puede mejorar su interacción interfacial con la matriz, facilitando la transferencia de esfuerzos de la matriz a la lámina y consiguiendo con ello buenas propiedades mecánicas en el material compuesto final.

Propiedades térmicas. Las propiedades térmicas del grafeno son un factor a tener en cuenta con vistas a su uso en dispositivos electrónicos, durante cuyo funcionamiento es necesario disipar una gran cantidad de calor. Es un hecho bien conocido que las formas del carbono basadas en la hibridación sp^2, como el grafito o los nanotubos de carbono, poseen elevadas conductividades térmicas debido a sus fuertes enlaces covalentes y a la dispersión de fonones, alcanzándose para los nanotubos de carbono valores de 3500 W m^{-1} K^{-1} [22]. Recientes estudios han demostrado valores de conductividad térmica a temperatura ambiente superiores a 5000 W m^{-1} K^{-1} en el caso de grafeno prístino y libre de defectos [23]. Sin embargo factores como el sustrato sobre el que se soporta el grafeno, así como la calidad estructural y el contenido de impurezas presentes en el material bidimensional, degradan significativamente estos valores.

Propiedades químicas. El grafeno prístino, al igual que otros materiales carbonosos basados en la hibridación sp^2, es químicamente anisótropo: mientras que sus planos basales son muy inertes, sus bordes son altamente reactivos debido a la presencia de átomos de carbono con enlaces no saturados. Como la superficie del grafeno está fundamentalmente compuesta por planos basales, se considera que, en general, el grafeno prístino posee una baja reactividad química. Sin embargo, como ocurre con los materiales grafíticos en general, es susceptible de sufrir reacciones de oxidación [24]. Esto hace posible la obtención de un derivado importante del grafeno, el óxido de grafeno, habitualmente utilizado como material de partida en la producción de variantes del grafeno procesables en fase líquida. De hecho, la presencia de grupos oxigenados en el óxido de grafeno favorece su dispersabilidad coloidal en medio acuoso y orgánico, su

combinación con materiales como partículas metálicas y polímeros, y su funcionalización con especies químicas adicionales. Dicha posibilidad permite a su vez su uso en materiales híbridos y compuestos para aplicaciones como catalizadores [25], biosensores [26], materiales de refuerzo estructural [27], etc. La reactividad química del grafeno puede variar por la presencia de impurezas o defectos; en algunos casos, las impurezas pueden tener un efecto catalítico, aumentando la reactividad [28].

1.3. Métodos de preparación de grafeno.

Cuando los físicos Geim y Novoselov consiguieron aislar grafeno por primera vez en 2004 mediante exfoliación mecánica de grafito [6], se hizo posible estudiar experimentalmente este material, lo cual permitió vislumbrar su enorme potencial en aplicaciones prácticas. Sin embargo, aunque la exfoliación mecánica de grafito es sencilla y da lugar a láminas de grafeno de muy alta calidad estructural, este método presenta un rendimiento extremadamente bajo, lo que lo hace totalmente inadecuado para la producción de grafeno a gran escala para usos prácticos. Por ello, en los últimos años se han desarrollado métodos de preparación alternativos a la exfoliación mecánica, todos ellos dirigidos en última instancia a obtener grafeno de buena calidad estructural y/o con características controladas mediante procedimientos económicamente viables.
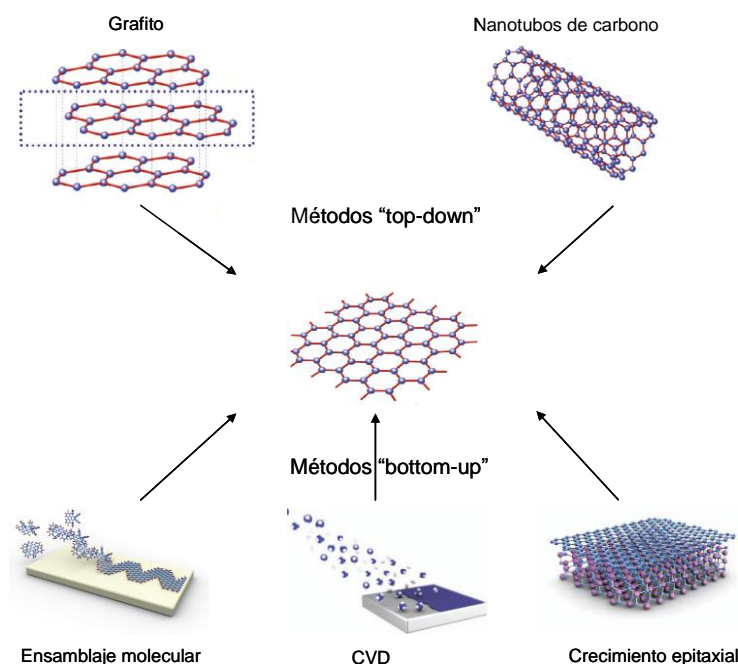
Fig. 2. Clasificación de métodos de preparación de grafeno.

Las alternativas surgidas hasta el momento se pueden clasificar en función de los dos enfoques en los que tradicionalmente se agrupan las metodologías de preparación de materiales nanoestructurados: métodos top-down (o descendentes) y métodos bottom-up (o ascendentes) (Fig. 2). A continuación se describen con mayor detenimiento los principales métodos de obtención de grafeno.

1.3.1. Métodos bottom-up.

Mediante estos métodos, el grafeno se obtiene a partir de átomos de carbono generados mediante la descomposición de precursores moleculares u orgánicos, generalmente a altas temperaturas, como por ejemplo en un horno CVD (Chemical Vapor Deposition) o mediante la descomposición de un sólido (por ejemplo carburo de silicio).

1.3.1.1. Deposito químico en fase vapor (CVD).

En términos generales, el CVD consiste en la deposición de un sólido sobre un sustrato a alta temperatura usando para ello precursores moleculares que se descomponen y/o recombinan para dar lugar al material en cuestión. En el caso del grafeno, el sustrato es un metal de transición, típicamente níquel o cobre, que se calienta a alta temperatura y se expone a una atmósfera de un precursor carbonoso (hidrocarburo) que se descompone, y los átomos de carbono se unen al metal difundiéndose o adsorbiéndose sobre él. A continuación, el sustrato se enfría formándose la lámina de grafeno. Por último, la lámina se separa del sustrato metálico, típicamente mediante la disolución de éste. Estas láminas pueden depositarse sobre otros sustratos sin necesidad de complicados tratamientos químicos o mecánicos que perjudiquen seriamente la calidad estructural del grafeno.

Este método permite la posibilidad de dopar grafeno sustitucionalmente por medio de la introducción de otros gases durante el crecimiento, por ejemplo NH_3 [29], o bien usando compuestos que contengan la especie dopante, por ejemplo acetonitrilo [30]. En estos ejemplos concretos, las láminas de grafeno estarán dopadas con átomos de nitrógeno, obteniéndose un material con interesantes propiedades, que resulta potencialmente útil en baterías de ión litio [30], supercondensadores [31] o determinados procesos catalíticos [32].
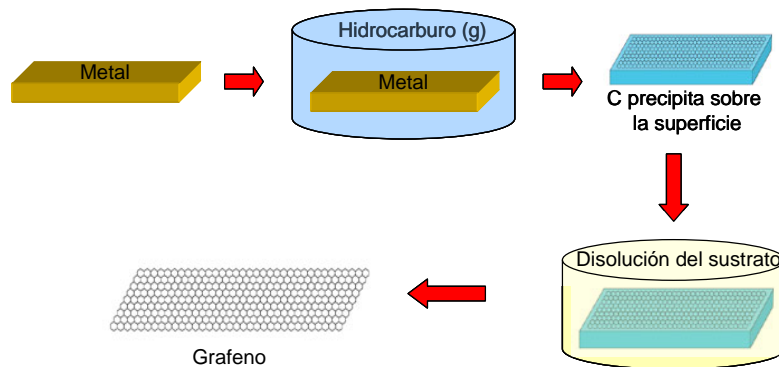
Figura 3. Esquema del proceso CVD para obtener grafeno.

La principal ventaja del método CVD es que permite generar láminas de grafeno de grandes dimensiones y buena calidad estructural, potencialmente muy útiles para aplicaciones electrónicas. No obstante, tiene el inconveniente de requerir temperaturas moderadamente altas (800-1000 ºC).

1.3.1.2.Crecimiento epitaxial sobre sustratos de carburo de silicio a elevada temperatura.

Mediante este método, el grafeno se obtiene por calentamiento, a ultra alto vacío (UHV) o en atmósfera inerte (Ar) a presión atmosférica, de un sustrato de carburo de silicio. Dicho calentamiento (> 1300 ºC) induce la sublimación de los átomos de silicio y la reorganización de los átomos de carbono, que permanecen sobre el sustrato formando láminas de grafeno de calidad estructural razonablemente buena [33] (Fig. 4). En comparación con el CVD es un método poco viable por las condiciones de operación (>1000 ºC) y la calidad estructural relativamente baja del material producido.
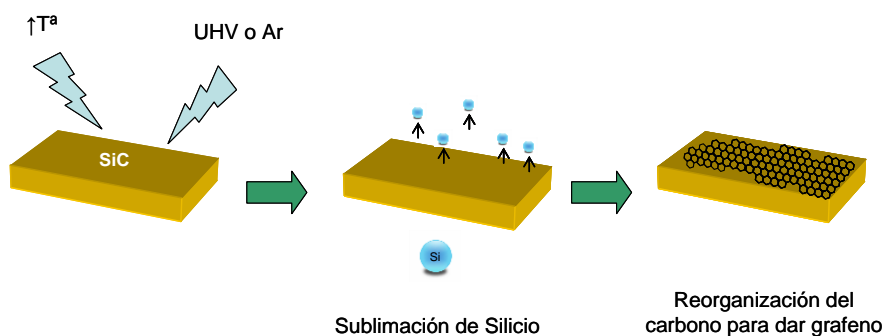
Figura 4. Esquema del crecimiento epitaxial de grafeno sobre sustrato de carburo de silicio

1.3.2. Métodos top-down.

En estos métodos el grafeno se forma mediante el procesado (mecánico, químico, etc.) de materiales carbonosos "bulk" que tienen al grafeno como su unidad estructural básica. Dichos métodos se basan fundamentalmente en el procesado de grafito, aunque también, en menor medida, de otros materiales grafíticos, como nanofibras y nanotubos de carbono. A continuación se describen los principales métodos top-down para la obtención de grafeno.

1.3.2.1. Procesado mecánico de materiales grafíticos.

Consiste fundamentalmente en la exfoliación y dispersión de grafito en polvo u otros materiales grafíticos en medio líquido por medio de ultrasonidos.

Existen estudios sobre la exfoliación inducida por ultrasonidos de grafito [34] en distintos disolventes orgánicos, que han permitido identificar aquellos disolventes más eficaces para la consecución de dispersiones coloidales estables de grafeno. Los resultados obtenidos se han podido interpretar en términos de coste energético, es decir, los disolventes más efectivos para la formación de dispersiones estables de grafeno son aquellos para los cuales se minimiza el coste energético de exfoliar y dispersar (mezclar) el grafito en el disolvente. Este coste energético se estima en base a la energía cohesiva, bien por medio de los parámetros de solubilidad de Hildenbrand y Hansen, o bien por la energía superficial del disolvente y del material a dispersar. Así, se ha predicho y confirmado experimentalmente que los disolventes más efectivos son aquellos que poseen una energía superficial similar a la del material de partida; en el caso del grafito serán los disolventes con energía superficial en torno a 70-80 mJ m^{-2} (tensión superficial entre 40-50 mJ m^{-2}) como el bencilbenzonato o la N-metil-2 pirrolidona (Fig. 5) [34].

El agua no es un disolvente adecuado para la obtención de grafeno por esta vía ya que su energía superficial es muy diferente a la del grafeno. Sin embargo, es posible preparar dispersiones estables de grafeno en medio acuoso por exfoliación de grafito en presencia de estabilizadores adecuados, como surfactantes [35], polímeros [36] o determinadas biomoléculas [37], lo cual puede facilitar el empleo de este tipo de grafeno, por ejemplo, en aplicaciones biomédicas.
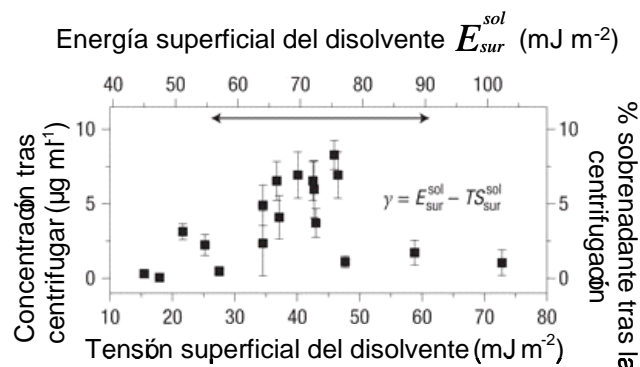
Figura 5. Concentración de grafeno preparado mediante exfoliación y dispersión de grafito en distintos disolventes en función de la energía y tensión superficiales de los disolventes. Reproducido de [34].

Otra técnica de obtención, en este caso de nanocintas de grafeno, se basa en la apertura de nanotubos de carbono mediante oxidación, intercalación en medio ácido y exfoliación térmica [38], o por el paso de una corriente eléctrica a través de los mismos [39].

La principal ventaja de estos métodos es la posibilidad de obtener dispersiones coloidales estables de grafeno de gran calidad estructural mediante técnicas sencillas y fácilmente escalables. El principal inconveniente es que el grafeno obtenido suele ser de varias capas y no monocapa y que presenta unas dimensiones laterales generalmente pequeñas (< 1 μm)

1.3.2.2. Procesado químico de materiales grafíticos.

Este enfoque se basa en la funcionalización covalente del material grafítico con determinados grupos funcionales, dando lugar a un derivado que se puede exfoliar fácilmente y dispersar de manera estable en medio líquido. Ello es posible debido, por un lado, a la afinidad química hacia determinados disolventes que presentan los grupos moleculares injertados sobre la estructura carbonosa y, por otro lado, al debilitamiento de las fuerzas cohesivas entre láminas de grafeno vecinas debido a la presencia de dichos grupos. El ejemplo más importante y representativo de este enfoque lo constituye el óxido de grafito, que es un derivado fuertemente oxigenado del grafito preparado mediante tratamientos agresivos de oxidación en medio ácido [40-42]. Aunque el óxido de grafito se conocía desde mediados del siglo XIX y en los años sesenta del siglo

pasado Boehm realizó los primeros estudios sobre su exfoliación y reducción [43], no fue hasta 2006 cuando este material se propuso como vía para la obtención de grafeno (en forma de óxido de grafeno reducido) en grandes cantidades [44-46].

Al igual que el grafito prístino, el óxido de grafito presenta una estructura laminar. Sin embargo, en el caso del óxido, los planos de átomos de carbono están decorados covalentemente con grupos funcionales oxigenados. Su estructura química no se conoce con exactitud, debido principalmente a su carácter parcialmente amorfo. Aún así diversos investigadores han propuesto modelos estructurales para el óxido de grafito, siendo el de Lerf y Klinowski el más aceptado [47, 48]. Este es un modelo no estequiométrico (Fig. 6), en el que los planos basales de grafeno están decorados aleatoriamente con grupos hidroxilo y epoxi, mientras que en los bordes de los planos se encuentran grupos carbonilo y carboxilo. Debido a que el número de grupos oxigenados introducidos en la estructura carbonosa es muy alto (relación atómica O/C ~ 0.4-0.5), gran parte de los átomos de carbono en el óxido de grafito adquieren hibridación sp^3, la cual es responsable de su carácter eléctricamente aislante.
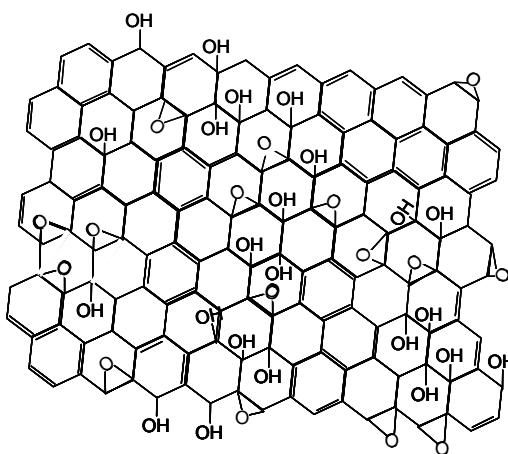
Figura 6. Representación de óxido de grafito según el modelo de Lerf-Klinowsli omitiendo los grupos minoritarios (carboxilos, carbonilos, lactonas, etc.) [44, 45].

Los grupos funcionales oxigenados favorecen la exfoliación del óxido de grafito, ya que no sólo inducen un aumento en su distancia interlaminar, sino que también confieren carácter hidrófilo y polar a las láminas. Ello hace posible la exfoliación de óxido de grafito en agua y algunos disolventes polares mediante ultrasonidos o

agitación prolongada, dando lugar a láminas monocapa de óxido de grafito, es decir, a láminas de óxido de grafeno en dispersión coloidal estable.

Es posible eliminar por distintos métodos gran parte de los grupos funcionales oxigenados de las láminas de óxido de grafeno y así recuperar significativamente la hibridación sp^2 original del material, obteniéndose las denominadas láminas de óxido de grafeno reducido. Sin embargo, generalmente no es posible eliminar todos los grupos oxigenados por medio de los procesos de reducción conocidos. Las láminas reducidas suelen retener una cantidad no despreciable de oxígeno residual y defectos estructurales, por lo que el material obtenido no presenta las mismas propiedades físicas que el grafeno prístino. En cualquier caso, este tipo de grafeno se puede preparar en grandes cantidades de manera relativamente sencilla y ha mostrado su utilidad con vistas a muy diversos usos prácticos. Los primeros trabajos realizados sobre reducción de óxido de grafito/grafeno se llevaron a cabo usando hidracina como agente reductor [43, 44], y desde entonces, este método ha sido ampliamente adoptado en la preparación de dispersiones coloidales de grafeno a partir de óxido de grafito. Desafortunadamente, la hidracina es un reactivo químico muy peligroso, tanto para la salud humana como para el medio ambiente, por lo que se han hecho esfuerzos en la búsqueda de otras alternativas de reducción. Existen diversos estudios sobre la preparación de grafeno a partir de óxido de grafito mediante procesos respetuosos con el medioambiente y a la vez económicamente viables. Dichos estudios se pueden agrupar fundamentalmente en dos líneas cuyas ideas básicas se pueden resumir en: (i) eludir el uso de agentes reductores en la eliminación de los grupos oxigenados del óxido de grafeno, y (ii) sustitución de la hidracina por otros agentes reductores más respetuosos con el medio ambiente. A continuación se exponen brevemente algunos de los métodos específicos.

Uso de agentes reductores.

Existen determinados agentes reductores que permiten la eliminación de la mayoría de los grupos oxigenados presentes en el óxido de grafeno. Por lo general, la reacción óxido de grafeno-reductor se lleva a cabo a temperatura ambiente o a temperaturas moderadas (< 100 ºC). Como ya se ha mencionado, el primer agente utilizado para reducir óxido de grafeno tanto en medio acuoso como orgánico fue la hidracina [44, 49, 50], permitiendo un grado de reducción bastante alto (relación atómica O/C ~ 0.1). Se ha demostrado que es posible reducir óxido de grafeno en medio

acuoso básico en ausencia de agente reductor [51], sin embargo, el grado de reducción alcanzado es mucho menor que el conseguido usando hidracina, con lo que este método posee una utilidad limitada. Por otra parte, tampoco se conoce bien el mecanismo que permite dicha reducción parcial. De todas maneras, resulta conveniente trabajar en medio básico, ya que la estabilidad coloidal de las láminas de óxido de grafeno es posible debido a la repulsión electrostática entre láminas generada por grupos oxigenados desprotonables [52]. Durante la reducción, gran parte de estos grupos se eliminan, por lo que resulta fundamental mantener desprotonados los que quedan (es decir, se necesita un medio básico) para maximizar la repulsión electrostática y con ello la estabilidad coloidal del óxido de grafeno reducido. De lo contrario (es decir, en medio neutro o ácido) las láminas de óxido de grafeno reducido tienden a aglomerarse y precipitar.

Se han identificado otros agentes reductores para la reducción de óxido de grafeno, como por ejemplo borohidruro de sodio [53], hidroquinona [54], fenilendiamina [55] o hidroxilamina [56], pero no todos estos agentes reductores son tan eficaces como la hidracina, y al igual que ella, no son inocuos para la salud y el medio ambiente. Por lo tanto, se hace necesaria la búsqueda de agentes que reduzcan eficazmente el óxido de grafeno y sean claramente inocuos. Recientemente se han identificado algunos biorreductores como alcoholes [57], azúcares [58] o polifenoles [59], pero su número es pequeño, y algunos poseen una eficacia limitada. Claramente, se hacen necesarios estudios más exhaustivos en este ámbito.

Reducción térmica

La reducción térmica del óxido de grafeno consiste en someterlo a temperaturas elevadas, generalmente en atmósfera inerte, con el propósito de eliminar los grupos funcionales oxigenados lábiles o relativamente lábiles introducidos durante la oxidación y restaurar la estructura electrónica sp^2. La eliminación de los grupos funcionales oxigenados tiene lugar principalmente con evolución a CO y CO_2, lo que implica la generación de vacantes atómicas y huecos en la estructura carbonosa. Aunque la eliminación de un grupo funcional aislado sobre grafeno (por ejemplo, un grupo epoxi eliminado en forma de CO) es energéticamente muy costosa, el proceso se ve favorecido, tanto termodinámica como cinéticamente, en presencia de más grupos funcionales oxigenados situados muy cerca de aquel que se va a eliminar. Ello es debido

a que los grupos cercanos estabilizan energéticamente tanto la estructura final como los estados de transición [60, 61]. Esta circunstancia (alta densidad de grupos oxigenados) se da en el óxido de grafeno, lo cual permite eliminar gran parte del oxígeno presente en el mismo a temperaturas inusualmente bajas para un material carbonoso (150-250 ºC). Sin embargo, una vez eliminada gran parte del oxígeno por esta vía, el oxígeno restante en la estructura carbonosa está muy probablemente en forma de grupos más o menos aislados, requiriendo por tanto temperaturas mucho más elevadas para su eliminación. Este mecanismo general permite explicar el hecho de que el óxido de grafeno reducido térmicamente a temperaturas incluso moderadamente altas (p.e., 1100 ºC) retiene una cantidad significativa de oxígeno residual. En la Figura 7 se muestra la evolución de los distintos grupos oxigenados de hibridación sp^2 y la cantidad de oxígeno presente en el óxido de grafeno con la temperatura de tratamiento [62]. Se puede observar que a temperaturas relativamente bajas se elimina la mayor cantidad de oxígeno presente en el óxido de grafeno.
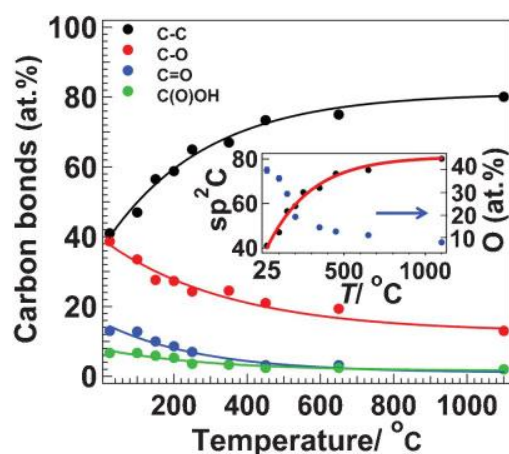
Figura 7. Evolución del grado de reducción del óxido de grafeno. Reproducido de [62]

Estudios muy recientes han mostrado que son necesarias temperaturas de aproximadamente 1500 ºC para eliminar completamente el oxígeno en filmes preparados a partir de láminas de óxido de grafeno, y temperaturas por encima de 2000 ºC para eliminar los defectos estructurales remanentes en dichos filmes [63].

La evolución de gases (CO y CO_2) en los procesos térmicos permite la posibilidad de reducir y exfoliar térmicamente óxido de grafito sin necesidad de exfoliar previamente este material por otros métodos. Cuando el óxido de grafito se calienta muy rápidamente a temperaturas de unos 1000 ºC, se produce una repentina acumulación de gases en los espacios interlaminares. La elevada presión resultante

separa unas láminas de otras, consiguiendo la exfoliación del material a la vez que su reducción térmica [64]. Este proceso es el más extendido en la actualidad para producir comercialmente grafeno en grandes cantidades.

Reducción solvotérmica.

Debido a que gran parte de los grupos funcionales oxigenados presentes en el óxido de grafeno se eliminan térmicamente a temperaturas relativamente bajas (150-250 ºC, Fig. 7), se hace posible la reducción térmica de este material directamente en dispersión coloidal en medio líquido. Esta reducción, llamada solvotérmica, se lleva a cabo en un recipiente herméticamente cerrado (autoclave) a altas presiones de vapor y altas temperaturas, en muchos casos por encima de la temperatura de ebullición del disolvente a presión atmosférica. La reducción solvotérmica del óxido de grafeno se ha llevado a cabo tanto en agua (reducción hidrotérmica) [65], como en distintos disolventes orgánicos [66].

Existen disolventes orgánicos que pueden actuar por sí mismos como agentes reductores del óxido de grafeno, es decir, permiten combinar reducción térmica y química en un solo paso. Entre ellos se encuentra el etilenglicol, el etanol, el 1-butanol [67] o la *N*-metil-2-pirrolidona [68]. Generalmente, la reducción solvotérmica consigue un grado de reducción moderado del óxido de grafeno. Con el fin de aumentar el grado de reducción, se ha combinado la reducción solvotérmica con el uso de agentes reductores como la hidracina [69, 70]. El agua por sí sola no es un buen agente reductor del óxido de grafeno, pero se ha descubierto que un tratamiento hidrotérmico de óxido de grafeno a 180 ºC es equivalente o incluso superior a una reducción térmica del material a 300 ºC [67]. Esto es debido a que a temperaturas altas algunas de las propiedades del agua varían, por ejemplo aumenta su constante de disociación, lo que puede influir en el proceso de reducción al favorecer reacciones que no tendrían lugar a temperaturas menores y que contribuyen a eliminar oxígeno del óxido de grafeno (p.e. reacciones de deshidratación) [65].

Reducción fotoinducida

Este método se basa en los procesos que ocurren como consecuencia de la absorción de radiación electromagnética, generalmente radiación ultravioleta (UV), por parte de determinadas especies químicas o materiales. Sin ir más lejos, el propio óxido

de grafeno absorbe radiación UV de los rangos cercano y medio [52, 71] y se ha demostrado que es posible reducirlo en dispersión acuosa simplemente por medio de exposición a luz UV intensa [72]. Para explicar dicha reducción, se ha interpretado que los electrones fotoexcitados generados en el óxido de grafeno se relajan transfiriendo parte de su energía a la red atómica de las láminas, con lo que éstas se calientan y se reducen por efecto de la alta temperatura local. Dicha reducción fototérmica se lleva a cabo en ausencia de agente reductor y con la dispersión globalmente a temperatura próxima a la ambiental (35 ºC) [72].

El óxido de grafeno también puede ser fotorreducido mediante el uso de fotocatalizadores. Los fotocatalizadores son normalmente partículas de materiales semiconductores, como por ejemplo dióxido de titanio [73], óxido de zinc [74] o vanadato de bismuto [75]. En este caso, la absorción de radiación UV por parte del semiconductor genera huecos electrónicos en su banda de valencia y electrones fotoexcitados en su banda de conducción. En presencia de una especie química aceptora de huecos, por ejemplo etanol, los electrones fotoexcitados pueden ser transferidos con cierta facilidad del semiconductor al óxido de grafeno, donde son utilizados para su reducción (ver Fig. 8) [76].
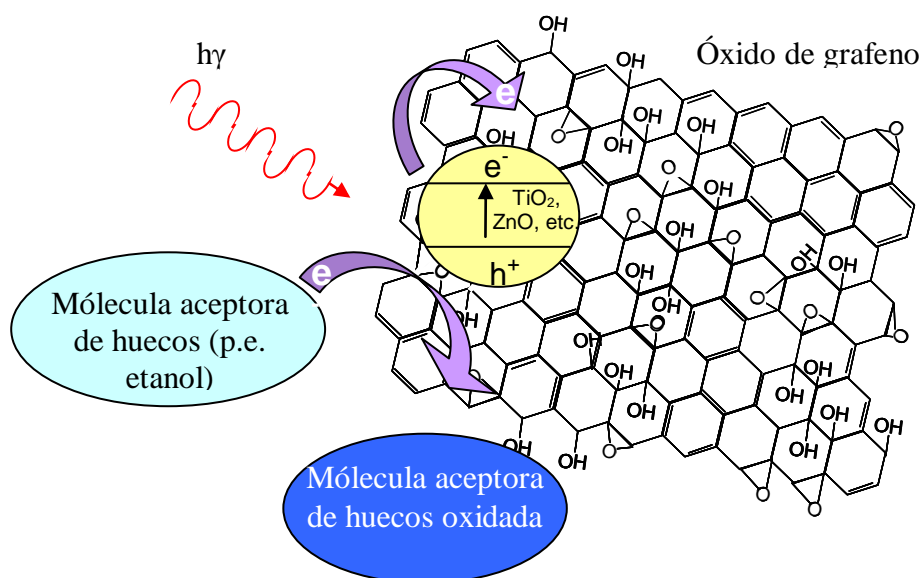
Figura 8. Esquema de reducción fotocatalítica del óxido de grafeno.

Reducción electroquímica

La reducción electroquímica del óxido de grafeno se basa en la transferencia de electrones que se produce al hacer pasar una corriente eléctrica a través de una celda electroquímica formada por un cátodo de óxido de grafeno y un electrodo inerte que actúa como ánodo, ambos sumergidos en un electrolito que puede ser acuoso u orgánico [77]. El cátodo de óxido de grafeno consiste en un filme de dicho material depositado sobre un sustrato como, por ejemplo, óxido de estaño e indio, carbón vítreo u otros. [78, 79]. El potencial de celda necesario para que se produzca la reducción depende del pH del electrolito, de forma que cuanto más bajo sea el pH, más favorable será la reacción, lo que ha llevado a algunos a autores a proponer el siguiente mecanismo de reacción [80]:

$$\text{Óxido de grafeno} + a\ H^+ + b\ e^- \rightarrow \text{Óxido de grafeno reducido} + c\ H_2O \qquad (1)$$

Se ha demostrado que el óxido de grafeno recupera parte de su conjugación electrónica sp^2, aunque para que el grado de recuperación sea apreciable generalmente se eleva la temperatura de reacción o se somete a los productos a un proceso de curado térmico [77]. Como ocurre con otros métodos de reducción, la reducción electroquímica no permite eliminar todos los grupos oxigenados del óxido de grafeno. Por ejemplo, los grupos carboxilo no se reducen electroquímicamente [81].

También se ha demostrado la posibilidad de obtener el grafeno a partir de grafito prístino mediante su exfoliación electroquímica. Para ello se utilizan electrodos de grafito como ánodo y cátodo, y como electrolito se utiliza una mezcla de agua y líquido iónico [77]. Tras aplicarse el potencial necesario, del ánodo se desprenden láminas de grafeno funcionalizadas por el líquido iónico, que tras secarse pueden redispersarse en disolventes polares apróticos, como por ejemplo dimetilformamida.

1.4. Referencias.

[1] Peierls RE. Quelques proprietes typiques des corps solides. Ann. I. H. Poincaré 5 (1935), 177-222.

[2] Landau LD. Zur Theorie der phasenumwandlungen II. Phys. Z. der Sowjetunion 11 (1937), 26-35.

[3] Geim AK, Novoselov KS. The rise of graphene. Nat. Mater. 6 (2007), 183-191.

[4] Venables J, Spiller G, Hanbucken M. Nucleation and growth of thin films. Rep. Prog. Phys. 47 (1999), 399.

[5] Evans J, Thiel P, Bartelt M. Morphological evolution during epitaxial thin film growth: Formation of 2D islands and 3D mounds. Surf. Sci. Rep. 61 (2006), 1-128.

[6] Novoselov KS, Geim AK, Morozov SV, Jiang D, Zhang Y, Dubonos SV, Grigorieva IV, Firsov AA. Electric field effect in atomically thin carbon films. Science 306 (2004), 666-669.

[7] Novoselov KS, Jiang D, Schedin F, Booth TJ, Khotkevich VV, Morozov SV, Geim AK. Two-dimensional atomic crystals. Proc. Natl. Acad. Sci USA 102 (2005), 10451- 10453.

[8] Landau LD, Lifshitz EM. Statical Physics, Part. I. Oxford: Pergamon Press. 1980.

[9] Mermin ND. Crystalline order in two dimensions. Phys. Rev. 176 (1968), 250-254.

[10] Low CTJ, Walsh FC, Chakrabarti MH, Hashim MA, Hussain MA. Electrochemical approaches to the production of graphene flakes and their potential applications. Carbon 54 (2013), 1-21.

[11] Resnick R, Halliday D, Krane KS. Fisica. Mexico: CECSA. 2003.

[12] Katsnelson M, Novoselov K, Geim A. Chiral tunnelling and the Klein paradox in graphene. Nat. Phys. 2 (2006), 620-625.

[13] Bae S, Kim H, Lee Y, Xu X, Park J-S, Zheng Y, Balakrishnan J, Lei T, Kim HR, Song YI, Kim Y-J, Kim KS, Özyilmaz B, Ahn J-H, Hong BH, Iijima S. Roll-to-roll production of 30-inch graphene films for transparent electrodes. Nat. Nanotechnol. 5 (2010), 574-578.

[14] Li Y, Zhao Y, Cheng H, Hu Y, Shi G, Dai L, Qu L. Nitrogen-doped graphene quantum dots with oxygen-rich functional groups. J. Am. Chem. Soc. 134 (2011), 15-18.

[15] Gokus T, Nair RR, Bonetti A, Böhmler M, Lombardo A, Novoselov KS, Geim AK, Ferrari AC, Hartschuh A. Making graphene luminescent by oxygen plasma treatment. ACS Nano 3 (2009), 3963-3968.

[16] Lu G, Yu K, Wen Z, Chen J. Semiconducting graphene: converting graphene from semimetal to semiconductor. Nanoscale 5 (2013), 1353-1368.

[17] Eda G, Mattevi C, Yamaguchi H, Kim H, Chhowalla M. Insulator to semimetal transition in graphene oxide. J. Phys. Chem. C 113 (2009), 15768-15771.

[18] Wu J, Agrawal M, Becerril HA, Bao Z, Liu Z, Chen Y, Peumans P. Organic light-emitting diodes on solution-processed graphene transparent electrodes. ACS Nano 4 (2009), 43-48.

[19] Li X, Wang X, Zhang L, Lee S, Dai H. Chemically derived, ultrasmooth graphene nanoribbon semiconductors. Science 319 (2008), 1229-1232.

[20] Vedala H, Sorescu DC, Kotchey GP, Star A. Chemical sensitivity of graphene edges decorated with metal nanoparticles. Nano Lett. 11 (2011), 2342-2347.

[21] Lee C, Wei X, Kysar J, Hone J. Measurement of the elastic properties and intrinsic strength of monolayer graphene. Science 321 (2008), 385-388.

[22] Pop E, Mann D, Wang Q, Goodson K, Dai H. Thermal conductance of an individual single-wall carbon nanotube above room temperature. Nano Lett. 6 (2005), 96-100.

[23] Balandin AA, Ghosh S, Bao W, Calizo I, Teweldebrhan D, Miao F, Lau CN. Superior thermal conductivity of single-layer graphene. Nano Lett. 8 (2008), 902-907.

[24] Pierson HO. Handbook of carbon, graphite, diamond and fullerenes. Noyes

Publications. Park Ridge. 1993.

[25] Machado BF, Serp P. Graphene-based materials for catalysis. Cat. Sci. Tech. 2 (2012), 54-75.

[26] Shan C, Yang H, Song J, Han D, Ivaska A, Niu L. Direct electrochemistry of glucose oxidase and biosensing for glucose based on graphene. Anal. Chem. 81 (2009), 2378-2382.

[27] Rafiee M, Lu W, Thomas A, Zandiatashbar A, Rafiee J, Tour J, Koratkar NA. Graphene nanoribbon composites. ACS Nano 4 (2010), 7415-7420.

[28] Zhao J-X, Yu Y-Y, Bai Y, Lu B, Wang B-X. Chemical functionalization of BN graphene with the metal-arene group: a theoretical study. J. Mater. Chem. 22 (2012), 9343-9350.

[29] Wei D, Liu Y, Wang Y, Zhang H, Huang L, Yu G. Synthesis of N-doped graphene by chemical vapor deposition and its electrical properties. Nano Lett. 9 (2009), 1752-1758.

[30] Reddy ALM, Srivastava A, Gowda SR, Gullapalli H, Dubey M, Ajayan PM. Synthesis of nitrogen-doped graphene films for lithium battery application. ACS Nano 4 (2010), 6337-6342.

[31] Nakajima T, Koh M, Takashima M. Electrochemical behavior of carbon alloy C_xN prepared by CVD using a nickel catalyst. Electrochim. Acta 43 (1997), 883-891.

[32] Qu L, Liu Y, Baek J-B, Dai L. Nitrogen-doped graphene as efficient metal-free electrocatalyst for oxygen reduction in fuel cells. ACS Nano 4 (2010), 1321-1326.

[33] Penuelas J, Ouerghi A, Lucot D, David C, Gierak J. Surface morphology and characterization of thin graphene films on SiC vicinal substrate. Phys. Rev. B 79 (2009), 033408-033411.

[34] Hernandez Y, Nicolosi V, Lotya M, Blighe FM, Sun Z, De S, De S, McGovern IT, Holland B, Byrne M, Gun'Ko YK, Boland JJ, Niraj P, Duesberg G, Krishnamurthy S, Goodhue R, Hutchison J, Scardaci V, Ferrari AC, Coleman JN. High-yield production of graphene by liquid-phase exfoliation of graphite. Nat. Nanotechnol. 3 (2008), 563-568.

[35] Lotya M, Hernandez Y, King PJ, Smith RJ, Nicolosi V, Karlsson LS, Blighe FM, De S, Wang Z, McGovern IT, Duesberg GS, Coleman JN. Liquid phase production of graphene by exfoliation of graphite in surfactant/water solutions. J. Am. Chem. Soc. 131 (2009), 3611-3620.

[36] Bourlinos AB, Georgakilas V, Zboril R, Steriotis TA, Stubos AK, Trapalis C. Aqueous-phase exfoliation of graphite in the presence of polyvinylpyrrolidone for the production of water-soluble graphenes. Solid State Commun. 149 (2009), 2172-2176.

[37] Laaksonen P, Kainlauri M, Laaksonen T, Shchepetov A, Jiang H, Ahopelto J, Linder MB. Interfacial engineering by proteins: exfoliation and functionalization of graphene by hydrophobins. Angew. Chem.-Ger. Edit. 49 (2010), 4946-4949.

[38] Cano-Márquez AG, Rodríguez-Macías FJ, Campos-Delgado J, Espinosa-González CG, Tristán-López F, Ramírez-González D, Cullen DA, Smith DJ, Terrones M, Vega-Cantú YI. Ex-MWNTs: graphene sheets and ribbons produced by lithium intercalation and exfoliation of carbon nanotubes. Nano Lett. 9 (2009), 1527-1533.

[39] Kim K, Sussman A, Zettl A. Graphene nanoribbons obtained by electrically unwrapping carbon nanotubes. ACS Nano 4 (2010), 1362-1366.

[40] Brodie BC. Sur le poids atomique du graphite. Ann. Chim. Phys. 59 (1860), 466-472.

[41] Staudenmaier L. Verfahren zur darstellung der graphitsäure. Ber. Dtsch. Chem Ges. 31 (1898), 1481-1487.

[42] Hummers WS, Offeman RE. Preparation of graphitic oxide. J. Am. Chem. Soc. 80 (1958), 1339.

[43] Boehm H, Clauss A, Hofmann U, Fischer G. Dünnste kohlenstoff-folien. Z. Naturforsch. 17B (1962), 150-153.

[44] Stankovich S, Piner RD, Chen X, Wu N, Nguyen ST, Ruoff RS. Stable aqueous dispersions of graphitic nanoplatelets via the reduction of exfoliated graphite oxide in the presence of poly(sodium 4-styrenesulfonate). J. Mater. Chem. 16 (2006), 155-158.

[45] Stankovich S, Dikin DA, Dommett GHB, Kohlhaas KM, Zimney EJ, Stach EA, Piner RD, Nguyen ST, Ruoff RS. Graphene-based composite materials. Nature 442 (2006), 282-286.

[46] Stankovich S, Piner RD, Nguyen ST, Ruoff RS. Synthesis and exfoliation of isocyanate-treated graphene oxide nanoplatelets. Carbon 44 (2006), 3342-3347.

[47] Lerf A, He H, Forster M, Klinowski J. Structure of graphite oxide revisited. J. Phys. Chem. B 102 (1998), 4477-4482.

[48] He H, Klinowski J, Forster M, Lerf A. A new structural model for graphite oxide. Chem. Phys. Lett. 287 (1998), 53-56.

[49] Stankovich S, Dikin DA, Piner RD, Kohlhaas KA, Kleinhammes A, Jia Y, Wu Y, Nguyen ST, Ruoff RS. Synthesis of graphene-based nanosheets via chemical reduction of exfoliated graphite oxide. Carbon 45 (2007), 1558-1565.

[50] Park S, An J, Jung I, Piner RD, An SJ, Li X, Velamakanni A, Ruoff RS. Colloidal suspensions of highly reduced graphene oxide in a wide variety of organic solvents. Nano Lett. 9 (2009), 1593-1597.

[51] Fan X, Peng W, Li Y, Li X, Wang S, Zhang G, Zhang F. Deoxygenation of exfoliated graphite oxide under alkaline conditions: a green route to graphene preparation. Adv. Mater. 20 (2008), 4490-4493.

[52] Li D, Mueller M, Gilje S, Kaner R, Wallace G, Müller M. Processable aqueous dispersions of graphene nanosheets. Nat. Nanotech. 3 (2008), 101-105.

[53] Shin H-J, Kim K, Benayad A, Yoon S-M, Park H. Efficient reduction of graphite oxide by sodium borohydrilde and its effect on electrical conductance. Adv. Funct. Mater. 19 (2009), 1987-1992.

[54] Wang G, Shen X, Wang B, Yao J, Park J. Synthesis and characterisation of hydrophilic and organophilic graphene nanosheets. Carbon 47 (2009), 1359-1364.

[55] Hu N, Wang Y, Chai J, Gao R, Yang Z, Kong ES-W, Zhang Y. Gas sensor based on p-phenylenediamine reduced graphene oxide. Sensor. Actuat. B-Chem. 163 (2012), 107-114.

[56] Zhou X, Wu H, Yang H, Zhang J. Reducing graphene oxide via hydroxylamine: a simple and efficient route to graphene. J. Phys. Chem. C 115 (2011), 11957-11961.

[57] Dreyer DR, Murali S, Zhu Y, Ruoff RS, Bielawski CW. Reduction of graphite oxide using alcohols. J. Mater. Chem. 21 (2011), 3443-3447.

[58] Zhu C, Guo S, Fang Y, Dong S. Reducing sugar: new functional molecules for the green synthesis of graphene nanosheets. ACS Nano 4 (2010), 2429-2437.

[59] Wang Y, Shi Z, Yin J. Facile synthesis of soluble graphene via a green reduction

of graphene oxide in tea solution and its biocomposites. ACS Appl. Mater. Interfaces 3 (2011), 1127-1133.

[60] Sun T, Fabris S, Baroni S. Surface precursors and reaction mechanisms for the thermal reduction of graphene basal surfaces oxidized by atomic oxygen. J. Phys. Chem. C 115 (2011), 4730-4737.

[61] Larciprete R, Fabris S, Sun T, Lacovig P, Baraldi A, Lizzit S. Dual path mechanism in the thermal reduction of graphene oxide. J. Am. Chem. Soc. 133 (2011), 17315-17321.

[62] Mattevi C, Eda G, Agnoli S, Miller S, Mkhoyan KA. Evolution of electrical, chemical, and structural properties of transparent and conducting chemically derived graphene thin films. Adv. Funct. Mater. 19 (2009), 2577-2583.

[63] Rozada R, Paredes J, Villar-Rodil S, Martinez-Alonso A, Tascón JMD. Towards full repair of defects in reduced graphene oxide films by two-step graphitization. Nano Res. 6 (2013), 216-233.

[64] McAllister M, Li J-L, Adamson D, Schniepp H, Abdala A. Single sheet functionalized graphene by oxidation and thermal expansion of graphite. Chem. Mater. 19 (2007), 4396-4404.

[65] Zhou Y, Bao Q, Zhong Y, Loh K. Hydrothermal dehydration for the "green" reduction of exfoliated graphene oxide to graphene and demonstration of tunable optical limiting properties. Chem. Mater. 21 (2009), 2950-2956.

[66] Zhou D, Cheng Q-Y, Han B-H. Solvothermal synthesis of homogeneous graphene dispersion with high concentration. Carbon 49 (2011), 3920-3927.

[67] Nethravathi C, Rajamathi M. Chemically modified graphene sheets produced by the solvothermal reduction of colloidal dispersions of graphite oxide. Carbon 46 (2008), 1994-1998.

[68] Dubin S, Gilje S, Wang K, Tung VC, Cha K, Hall AS, Farrar J, Varshneya R, Yang Y, Kaner RB. A one-step, solvothermal reduction method for producing reduced graphene oxide dispersions in organic solvents. ACS Nano 4 (2010), 3845-3852.

[69] Wang H, Robinson JT, Li X, Dai H. Solvothermal reduction of chemically exfoliated graphene sheets. J. Am. Chem. Soc. 131 (2009), 9910-9911.

[70] Wang R, Wang Y, Xu C, Sun J, Gao L. Facile one-step hydrazine-assisted solvothermal synthesis of nitrogen-doped reduced graphene oxide: reduction effect and mechanisms. RSC Adv. 3 (2013), 1194-1200.

[71] Paredes JI, Villar-Rodil S, Martínez-Alonso A, Tascón JMD. Graphene oxide dispersions in organic solvents. Langmuir 24 (2008), 10560-10564.

[72] Guardia L, Villar-Rodil S, Paredes JI, Rozada R, Martínez-Alonso A, Tascón JMD. UV light exposure of aqueous graphene oxide suspensions to promote their direct reduction, formation of graphene–metal nanoparticle hybrids and dye degradation. Carbon 50 (2012), 1014-1024.

[73] Williams G, Seger B, Kamat PV. TiO$_2$-Graphene nanocomposites. UV-Assisted photocatalytic reduction of graphene oxide. ACS Nano 2 (2008), 1487-1491.

[74] Williams G, Kamat PV. Graphene−semiconductor nanocomposites: excited-state interactions between ZnO nanoparticles and graphene oxide. Langmuir 25 (2009), 13869-13873.

[75] Ng YH, Iwase A, Kudo A, Amal R. Reducing graphene oxide on a visible-light BiVO$_4$ photocatalyst for an enhanced photoelectrochemical water splitting. J. Phys. Chem. Lett. 1 (2010), 2607-2612.

[76] Hegyi J, Horváth O. Photocatalytic reduction of mercury (II) and simultaneous

oxidative degradation of surfactants in titanium dioxide suspensions. In: Zrínyi M, Hórvölgyi ZD, eds. From Colloids to Nanotechnology: Springer Berlin Heidelberg 2004 10-16.

[77] Low CTJ, Walsh FC, Chakrabarti MH, Hashim MA, Hussain MA. Electrochemical approaches to the production of graphene flakes and their potential applications. Carbon 54 (2012), 1-21.

[78] Pei S, Cheng H-M. The reduction of graphene oxide. Carbon 50 (2012), 3210-3228.

[79] Shao Y, Wang J, Engelhard M, Wang C, Lin Y. Facile and controllable electrochemical reduction of graphene oxide and its applications. J. Mater. Chem. 20 (2010), 743-748.

[80] Dreyer DR, Park S, Bielawski CW, Ruoff RS. The chemistry of graphene oxide. Chem. Soc. Rev. 39 (2010), 228-240.

[81] Pumera M. Graphene-based nanomaterials and their electrochemistry. Chem. Soc. Rev. 39 (2010), 4146-4157.

[82] Park S, Ruoff RS. Chemical methods for the production of graphenes. Nat. Nanotech. 4 (2009), 217-224.
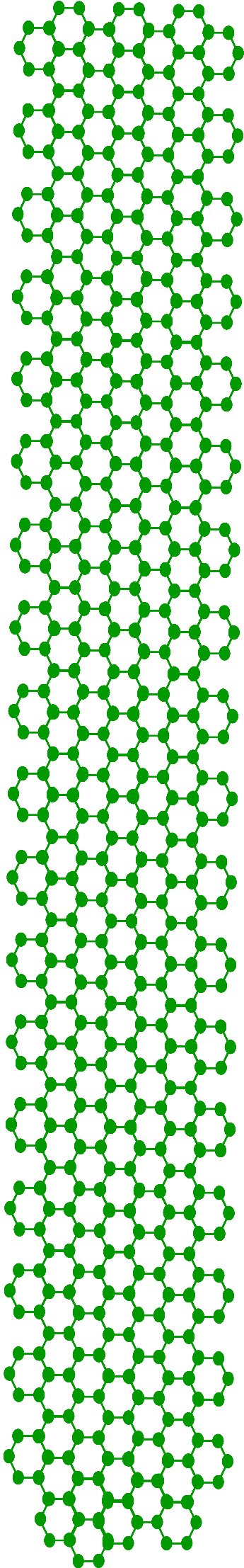
2. OBJETIVOS Y PLANTEAMIENTO DE LA MEMORIA

2.1. Objetivos.

En la actualidad, existe un enorme interés en la investigación y desarrollo de materiales de carbono basados en grafeno debido a sus atractivas propiedades, lo que hace prever su posible uso en múltiples aplicaciones. Este enorme potencial del grafeno sólo podrá aprovecharse si se desarrollan metodologías que permitan su preparación y procesado en grandes cantidades, para dar lugar a estructuras macroscópicas útiles y de características controlables. Basándose en lo ya conocido para otros materiales nanoestructurados (nanopartículas, nanotubos, etc.), la preparación y procesado en medio líquido de grafeno parece el método óptimo para alcanzar dichos objetivos. Hasta la fecha, la técnica en la que se han depositado más esperanzas es la basada en la exfoliación de óxido de grafito a óxido de grafeno y su posterior reducción, aunque también se investigan rutas alternativas, como la exfoliación de grafito prístino en medio líquido por medio de ultrasonidos.

En virtud de lo anteriormente expuesto, en esta memoria se plantea como objetivo general el desarrollo de técnicas de preparación de grafeno tanto prístino como modificado químicamente en forma de dispersiones coloidales. Los objetivos específicos que se plantean son los siguientes:

- Preparación de dispersiones estables de grafeno en medio acuoso mediante la reducción química de láminas de óxido de grafeno. Estudio y comparación del efecto de distintos agentes reductores en las características de las dispersiones resultantes.

- Preparación de dispersiones estables de grafeno mediante exfoliación de grafito prístino en medio acuoso con ayuda de distintos surfactantes, llevando a cabo un estudio comparativo de su eficacia.

- Preparación de filmes nanoestructurados de grafeno a partir de diferentes dispersiones coloidales de grafeno. Investigación de las características morfológicas, estructurales y químicas de los filmes.

- Preparación de materiales híbridos formados por grafeno y un segundo componente, en concreto nanopartículas metálicas y estructuras de sílice mesoporosas, con vistas a aplicaciones prácticas, por ejemplo catalíticas. Caracterización morfológica, estructural y química de estos híbridos.

2.2. Organización de la memoria.

Tras la introducción (capítulo 1) y el presente capítulo, en el capítulo 3 se describen brevemente los materiales utilizados, los diferentes métodos de preparación de grafeno y sus híbridos así como las técnicas de caracterización empleadas.

En el capítulo 4 se exponen los resultados obtenidos, así como una discusión de los mismos. Los resultados se recogen en un compendio de artículos publicados o enviados a revistas englobadas dentro del área de ciencia de los materiales. En la Tabla 1 se incluyen los índices de calidad de las revistas en las que se han publicado los artículos, así como el puesto que ocupa cada una de ellas en relación al número total de revistas del área correspondiente; en la Tabla 2, su fecha de publicación y aceptación.

Tabla 1. Índices de calidad (2012) de las revistas en las que se han publicado los artículos recogidos en la presente memoria.

Revista	Índice de impacto	Puesto/ nº de revistas total	Área
Carbon	5.868	22/239	Materials Science, Multidisciplinary
Journal of Physical Chemistry C	4.814	26/239	Materials Science, Multidisciplinary
Microporous and Mesoporous Materials	3.365	38/239	Materials Science, Multidisciplinary

Fuente: Journal Citation Reports (2012), www.isiwebfknowledge.com

Tabla 2. Artículos recogidos en esta memoria con sus correspondientes datos de publicación.

Artículo	Revista	Fecha aceptación	Fecha publicación
Vitamin C is an ideal substitute for hydrazine in the reduction of graphene oxide suspensions	Journal of Physical Chemistry C	4/3/2010	15/4/2010
High-throughput production of pristine graphene in an aqueous dispersion assisted by non-ionic surfactants	Carbon	15/12/2010	21/12/2010
Investigating the influence of surfactants on the stabilization of aqueous reduced graphene oxide dispersions and the characteristics of their composite films	Carbon	24/10/2011	28/10/2011
Synthesis and characterization of graphene-mesoporous silica nanoparticle hybrids	Microporous and Mesoporous Materials	24/4/2012	2/5/2012
Identifying efficient natural bioreductants for the preparation of graphene and graphene-metal nanoparticle hybrids with enhanced catalytic activity from graphite oxide	Carbon	13/6/2013	20/06/2013
Developing green photochemical approaches towards the synthesis of carbon nanofiber- and graphene-supported silver nanoparticles and their use in the catalytic reduction of 4-nitrophenol	Enviado para publicación		

El capítulo 4 se divide en tres bloques, cada uno de ellos precedido de un resumen en el que se recogen los objetivos, los resultados más relevantes y las conclusiones de los artículos correspondientes a cada una de las partes. Cada parte esta compuesta por dos artículos correspondientes a las siguientes temáticas:

- Estudio comparativo de distintos agentes reductores en la preparación de grafeno por la vía de la reducción química de óxido de grafeno.

- Estudio comparativo de distintos surfactantes para la estabilización de dispersiones coloidales de grafeno, obtenidas a partir de óxido de grafeno reducido químicamente o de grafito prístino exfoliado mediante ultrasonidos.
- Preparación de materiales híbridos basados en grafeno.

La memoria concluye con un breve capítulo de conclusiones generales (capítulo 5) y un anexo en el que se incluye una lista de publicaciones complementarias y de contribuciones a congresos.
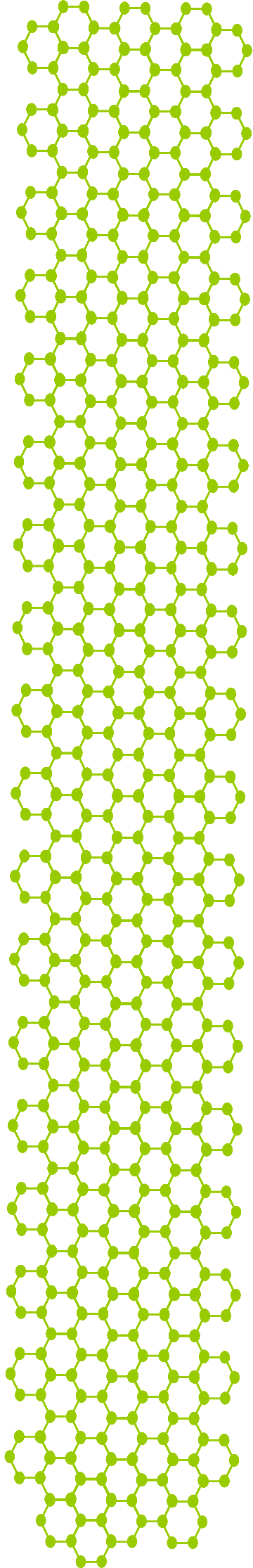
3. MATERIALES Y MÉTODOS

3.1. Materiales.

3.1.1. *Materiales carbonosos de partida.*

- Grafito natural (Fluka 50870) en polvo, con 99.9% de pureza y con tamaño de partícula menor de 1 mm.
- Óxido de grafito, obtenido a partir de grafito natural en polvo oxidado mediante el método de Hummers [1].
- Nanofibras de carbono tipo "platelet" (Sigma Aldrich 698830) con 99% de pureza, longitud entre 0.5 y 5 µm (~2.5 µm de media) y grosor de 50-250 nm (~100 nm de media).

3.1.2. *Reactivos químicos.*

A continuación se detallan los principales reactivos utilizados en esta memoria. Se pueden clasificar en agentes reductores, surfactantes y otros materiales.
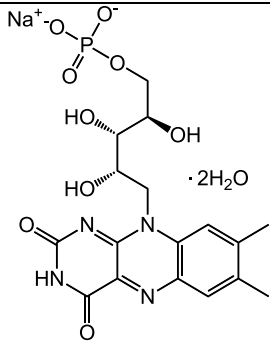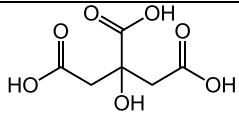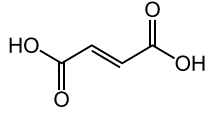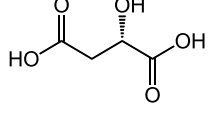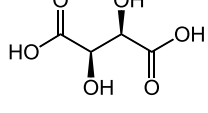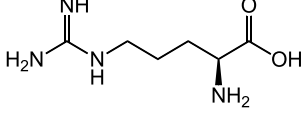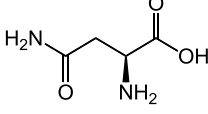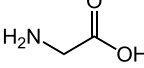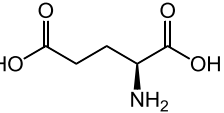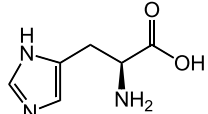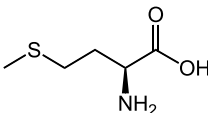
- Agentes reductores. Parte de esta memoria se centra en la búsqueda de agentes reductores eficaces del óxido de grafeno que no sean tóxicos o perjudiciales para el medio ambiente. Se ensayaron distintos productos naturales como, por ejemplo, aminoácidos, péptidos y vitaminas, los cuales se recogen en la Tabla 3.

Tabla 3. Agentes reductores utilizados en esta memoria.
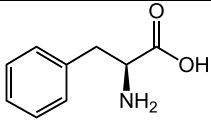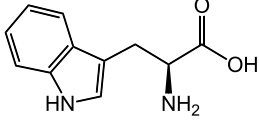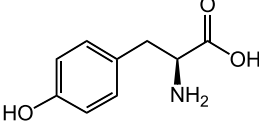
Clasificación	Reductor químico	Referencia	Estructura química
	Amoníaco, disolución al 25%	Merck 1054321000	NH_3
	Hidróxido de potasio	Fluka 60380	KOH
	Monohidrato de hidracina	Merck 8046081000	N_2H_4
	Borohidruro de sodio	Prolabo 27885.134	$NaBH_4$

Clasificación	Reductor químico	Referencia	Estructura química
	Pirogalol	Sigma Aldrich 254002	
Dipéptido	**Carnosina**	Sigma Aldrich C9625	
Tripéptido	**Glutatión**	Sigma Aldrich G4251	
Azúcar	**Glucosa**	Sigma Aldrich 158968	
Vitaminas	**Vitamina C o ácido ascórbico**	Sigma Aldrich 255564	
	Piridoxina o vitamina B$_6$	Sigma Aldrich P5669	
	Piridoxamina diclorohidrato	Sigma Aldrich P9380	
	Riboflavina o vitamina B$_2$	Sigma Aldrich R4500	
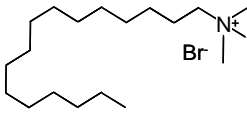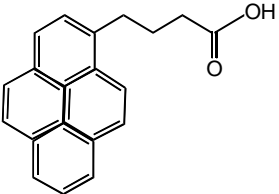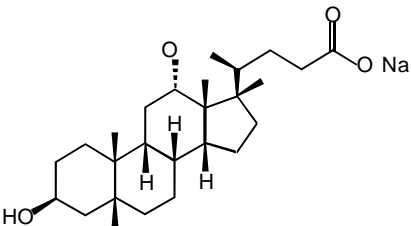
Clasificación	Reductor químico	Referencia	Estructura química
Vitaminas	**Sal sódica riboflavina-5'-monofosfato**	Sigma Aldrich R6750	
Ácidos orgánicos naturales	**Ácido cítrico**	Sigma Aldrich C1909	
	Ácido fumárico	Sigma Aldrich 240745	
	Ácido L-málico	Sigma Aldrich 02288	
	Ácido L-tartárico	Sigma Aldrich 251380	
Aminoácidos	**L-Arginina**	Sigma Aldrich A5006	
	Asparagina	Sigma Aldrich 11149	
	Glicina	Sigma Aldrich 50046	
	Ácido L-glutámico	Sigma Aldrich 49449	
	Histidina	Sigma Aldrich 53319	
	Metionina	Sigma Aldrich 64319	

Clasificación	Reductor químico	Referencia	Estructura química
	Fenilalanina	Sigma Aldrich 78019	
Aminoácidos	**Triptofano**	Sigma Aldrich T0254	
	Tirosina	Sigma Aldrich T3754	

- *Surfactantes.* En esta memoria se estudia la preparación de dispersiones acuosas estables de grafeno con distintos surfactantes, que se detallan en la Tabla 4:
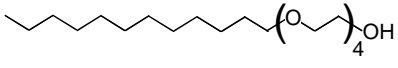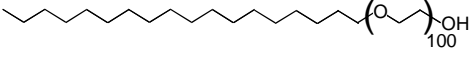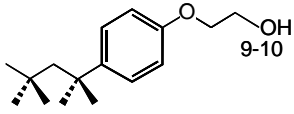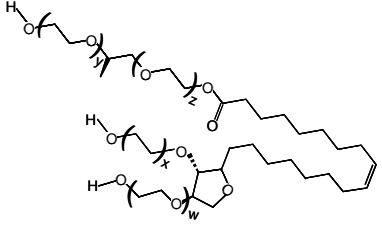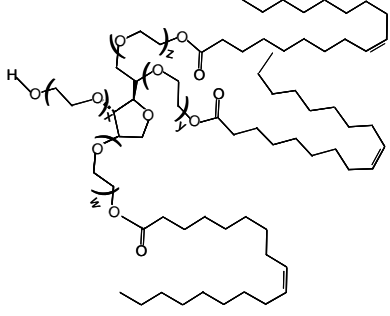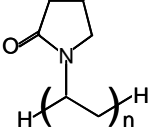
Tabla 4. Surfactantes utilizados en esta memoria.

Tipo	Surfactante	Referencia	Estructura química
Surfactante catiónico	**Bromuro de hexadeciltrime-tilamonio (CTAB)**	Sigma Aldrich H9151	
Surfactantes aniónicos	**Ácido pirenobutírico, PBA**	Merck S36159 218	
	Deoxicolato de sodio, DOC	Sigma Aldrich D6750	

Tipo	*Surfactante*	*Referencia*	*Estructura química*
	Taurodeoxico-lato de sodio, TDOC	Sigma Aldrich T0875	
Surfactantes aniónicos	**Poli (4-estirensulfonato de sodio), PSS**	Sigma Aldrich 243051	
	Dodecilbenceno sulfonato de sodio, SDBS	Sigma Aldrich D2525	
	Dodecilsulfato de sodio, SDS	Sigma Aldrich L5750	
Surfactante anfotérico	**CHAPS**	Sigma Aldrich C3023	
	N-Dodecil β-D-maltosa, DBDM	Sigma Aldrich D4641	
Surfactantes no iónicos	**Goma arábiga del árbol de la acacia**	Sigma Aldrich G9752	
	Pluronic® P-123, P-123	Sigma 9003-11-6	

Tipo	Surfactante	Referencia	Estructura química
Surfactantes no iónicos	**Polioxietilen (4) dodecil eter, Brij 30**	Sigma Aldrich P4391	
	Polioxietilen (100) octadecil eter, Brij700	Sigma Aldrich 466387	
	Polioxietilen octil (9-10) fenileter, Triton X-100	Sigma Aldrich T8787	
	Polioxietilen sorbitan monooleato, Tween80	Sigma Aldrich P1754	
	Polioxietilen sorbitan trioleato, Tween85	Sigma Aldrich P4634	
	Polivinilpirrolido-na, PVP	Sigma Aldrich PVP10	

- Otros materiales.

- **Nitrato de plata, AgNO$_3$** (Sigma Aldrich 209139).
- **Ácido cloro aúrico, HAuCl$_4$** (Sigma Aldrich 520918).

- **4-Nitrofenol** (Sigma Aldrich 241326).
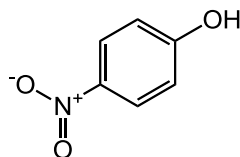
- **Tetraetilortosilicato, TEOS** (Sigma Aldrich 131903).
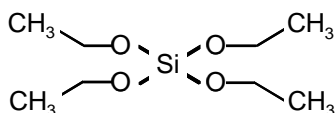
- **Argón** (Air liquide, pureza 99.999%).

3.2. Métodos de preparación de materiales.

3.2.1. *Preparación de óxido de grafeno.*

La Figura 9 ofrece una visión esquemática del proceso seguido en la preparación de óxido de grafeno. El óxido de grafeno se preparó a partir de óxido de grafito obtenido mediante el método de Hummers [1]. Dicho método consiste en oxidar grafito con permanganato potásico empleando nitrato sódico y ácido sulfúrico como agentes intercaladores. El medio fuertemente ácido facilita la oxidación. Tras un proceso de purificación, el óxido de grafito obtenido se dispersó en agua mediante ultrasonidos, obteniéndose así una suspensión coloidal de óxido de grafeno. La introducción de grupos funcionales oxigenados durante la oxidación tanto en el plano basal como en los bordes de las láminas grafíticas [2] confiere carácter hidrófilo al grafito a la vez que aumenta su distancia interplanar, facilitando su exfoliación en láminas monocapa de óxido de grafeno. La estabilidad coloidal de las dispersiones acuosas de óxido de grafeno viene dada por la repulsión electrostática entre sus grupos oxigenados ionizables (desprotonables) [3]. La dispersión obtenida se centrifugó para separar el óxido de grafeno, que permanece en el sobrenadante, del óxido de grafito sin exfoliar, que sedimenta.
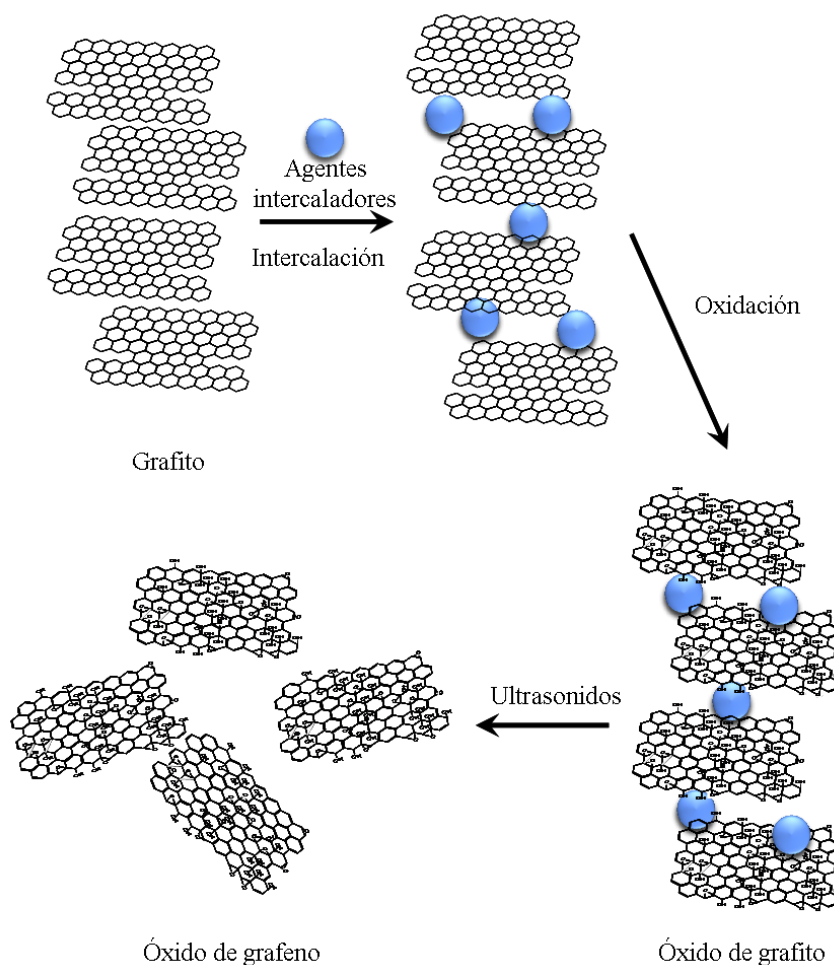
Figura 9. Esquema de preparación de óxido de grafeno.

3.2.2. *Reducción química de óxido de grafeno.*

La presencia de grupos funcionales oxigenados y defectos en el óxido de grafeno hacen que este no posea las mismas propiedades que el grafeno prístino, por lo que se hace importante eliminar dichos grupos. Para ello, el óxido de grafeno se redujo químicamente con distintos agentes reductores. La reducción se llevó a cabo en medio acuoso básico calentando las dispersiones de óxido de grafeno a 95ºC en presencia de un agente reductor. Como en el caso de las dispersiones acuosas de óxido de grafeno sin reducir, la estabilidad coloidal de las dispersiones de óxido de grafeno reducido proviene de la repulsión electrostática entre los grupos oxigenados ionizables, que no desaparecen en su totalidad durante el proceso de reducción [3] y el medio básico es necesario para que dichos grupos ionizables estén desprotonados.

En esta memoria se llevó a cabo un estudio comparativo entre distintos agentes reductores, principalmente de origen natural, respecto a su capacidad para reducir el

óxido de grafeno. Las dispersiones usadas contenían óxido de grafeno en concentraciones relativamente bajas (~ 0.1 mg mL^{-1}), a las que se añadía amoníaco hasta pH~10 y el agente reductor estudiado en cada caso. Para todos los agentes reductores se realizó un estudio de la concentración óptima, siendo la concentración mínima necesaria para la cual se conseguía el máximo grado de reducción posible manteniendo constantes otras variables. Otro factor estudiado fue el tiempo óptimo de reacción, definido como el tiempo mínimo necesario para el cual se consigue el máximo grado de reducción posible manteniendo constantes otras variables. Asimismo, para dispersiones con concentraciones altas de óxido de grafeno (>1 mg mL^{-1}) o para dispersiones en medio ácido, es necesario introducir un agente estabilizador (surfactante) en el medio acuoso para estabilizar coloidalmente las láminas de óxido de grafeno una vez reducidas. En esta memoria se ensayaron surfactantes de varios tipos y estructuras.

3.2.3. Preparación de grafeno prístino estabilizado por surfactantes mediante exfoliación de grafito en medio acuoso.

Al ser el grafeno la unidad estructural básica del grafito, la manera más obvia de obtener grafeno en grandes cantidades sería la exfoliación directa de grafito prístino en fase líquida. El principal problema de este enfoque en lo que respecta al uso del agua como medio de dispersión reside en su incompatibilidad con el grafito/grafeno (hidrófobo), por lo que se requiere la presencia en el medio acuoso de algún estabilizador. En este trabajo se realizó un estudio sobre la capacidad de distintos surfactantes para exfoliar y estabilizar coloidalmente grafito prístino en agua, dando lugar a dispersiones de grafeno de alta calidad estructural. Se trato en baño de ultrasonidos grafito prístino en agua a muy alta concentración inicial durante varias horas (típicamente dos) en presencia de distintos surfactantes a distintas concentraciones (0.5 y 1% p/vol.). La concentración de cada surfactante no fue optimizada, pero en todos los casos fue superior a la concentración micelar crítica. Las dispersiones de grafeno se obtenían tras sedimentar el material no exfoliado mediante centrifugación.

3.2.4. Preparación de materiales híbridos de grafeno.

3.2.4.1. Preparación de materiales híbridos formados por un material de carbono y nanopartículas metálicas.

Se prepararon materiales híbridos de óxido de grafeno y nanopartículas metálicas mediante el calentamiento de dispersiones acuosas de óxido de grafeno en presencia de un precursor de las nanopartículas (nitrato de plata) y un agente reductor.

Otra forma de obtener estos híbridos de óxido de grafeno y nanopartículas metálicas consiste en someter las dispersiones de óxido de grafeno a radiación UV a temperatura ambiente en presencia de un precursor metálico y un agente reductor, en lugar de calentarlas a 95 ºC, como mencionamos anteriormente. Mediante un procedimiento análogo se obtuvieron híbridos de nanopartículas de plata con nanofibras de carbono tipo "platelet"en lugar de óxido de grafeno como soporte de las nanopartículas. En este caso el medio líquido fue etanol en lugar de agua, ya que este tipo de nanofibras de carbono no se dispersa en agua, pero sí en etanol, y además se necesitó la presencia de un surfactante para controlar el tamaño de las nanopartículas metálicas.

3.2.4.2. Preparación de materiales híbridos grafeno-nanopartícula de sílice mesoporosa.

En esta memoria, se sintetizaron materiales híbridos de grafeno y nanopartículas de sílice mesoporosa. El material de partida usado fue una dispersión de óxido de grafeno que cumplía la doble función de inducir la nucleación de las nanopartículas y de servir de precursor del grafeno. El óxido de grafeno se mezcló con un surfactante catiónico [bromuro de hexadeciltrimetilamonio (CTAB)], que en forma de micelas previene la agregación de las láminas de óxido de grafeno y actúa como agente director de la mesoestructura de las nanopartículas de sílice. Tras ajustarse el pH de la dispersión con NaOH y homogeneizar mediante ultrasonidos, se añadió el precursor de la estructura de sílice, tetraetilortosilicato (TEOS). Se usaron distintas cantidades de TEOS para estudiar su efecto en las estructuras formadas. La mezcla se calentó durante 20 horas a 40 ºC con agitación y a continuación el producto obtenido se lavó mediante centrifugación en etanol. Este producto se secó y se sometió a un tratamiento térmico con flujo de argón para eliminar el CTAB y reducir térmicamente el óxido de grafeno.

3.2.5. Preparación de filmes.

Se obtuvieron filmes tipo papel a partir de distintas suspensiones coloidales de grafeno filtrando dichas suspensiones a través de membranas de alúmina de 47 mm de diámetro y 0.2 µm de tamaño de poro (Whatman). Estos filmes fueron analizados mediante una variedad de técnicas de caracterización, principalmente microscópicas y espectroscópicas.

3.3. Técnicas de caracterización.

3.3.1. Espectroscopía absorción ultravioleta-visible (UV-vis).

Como las moléculas poseen un conjunto discreto de estados, para que se produzca la absorción de radiación, la energía de los fotones incidentes debe coincidir con la diferencia de energía entre dos de estos estados. Dado que dichas diferencias son singulares para cada especie, el estudio de la energía (o frecuencia o longitud de onda) de la radiación absorbida permite en principio caracterizar a los constituyentes de la muestra. En el caso de la espectroscopía de absorción UV-vis, la energía de los fotones está en el rango de la separación energética entre niveles electrónicos correspondientes a pares electrónicos no enlazados y enlaces insaturados. Los diferentes tipos de transiciones electrónicas moleculares que se observan típicamente en los espectros UV-vis se muestran en la Fig. 10. Generalmente, la separación entre orbitales electrónicos tipo σ es demasiado grande y se requieren fotones de mayor energía (ultravioleta de vacío).
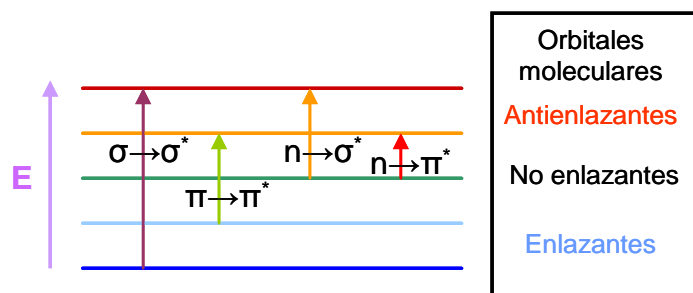
Figura 10. Niveles electrónicos de energía en una molécula y posibles transiciones entre ellos

Para cada estado electrónico, la molécula puede encontrase en diferentes estados vibracionales y rotacionales próximos en energía. La energía asociada a las bandas de absorción UV-vis de una molécula tiene por tanto tres componentes: uno de energía de excitación electrónica, otro de energía vibracional, y un tercero de excitaciones

rotacionales. En muestras líquidas o en disolución (como las tratadas en este trabajo) se pierde la estructura fina asociada a vibraciones y rotaciones debido a la solvatación y a la interacción con moléculas vecinas [4, 5]. Se obtienen bandas anchas centradas en torno a la longitud de onda correspondiente a la transición electrónica.

En este trabajo se utiliza la espectroscopía de absorción UV-vis para realizar análisis cualitativos y cuantitativos de las muestras estudiadas. Cuantitativamente se utiliza para estimar la concentración de grafeno y óxido de grafeno en dispersión. Esto es posible porque tanto el grafeno prístino como el óxido de grafeno (reducido o no) son sistemas eminentemente aromáticos y, por tanto, susceptibles de ser detectados y cuantificados mediante espectroscopía UV-vis. Se aplica la ley de Lambert-Beer:

$$Abs = \alpha \, l \, Conc \tag{1}$$

donde Abs es la absorbancia, α es el coeficiente de extinción molar, l es la longitud del medio que es atravesada por la luz y Conc es la concentración de la dispersión de grafeno u óxido de grafeno.
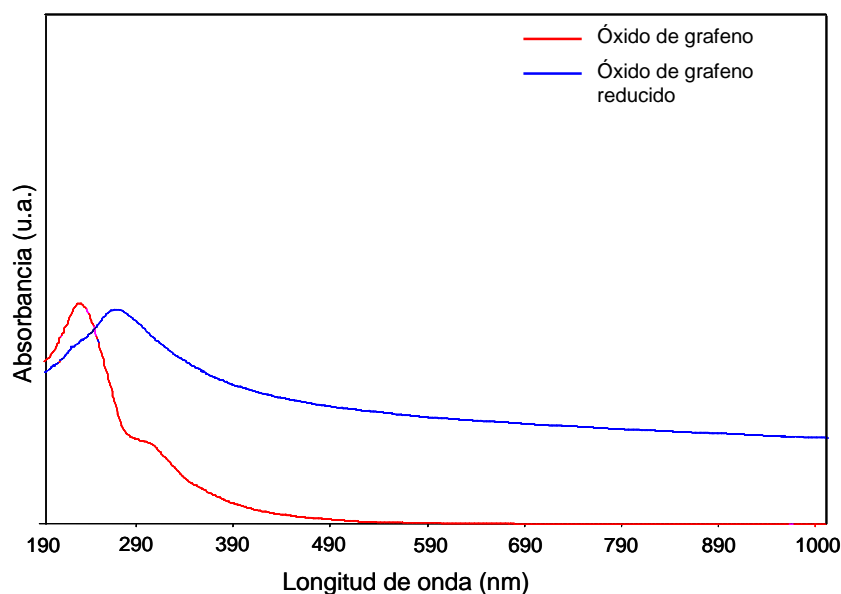
Figura 11. Espectro de absorción UV-vis de óxido de grafeno (rojo) y óxido de grafeno reducido (azul).

El análisis cualitativo permite evaluar de forma aproximada el grado de reducción del óxido de grafeno que se consigue mediante un tratamiento determinado. El estudio del grado de reducción del óxido de grafeno es posible debido a que su espectro de absorción presenta un máximo a 231 nm que se desplaza progresivamente

hacia longitudes de onda mayores a medida que avanza el grado de reducción del material [3]. Esto es debido a que la diferencia de energía entre niveles electrónicos es sensible al grado de conjugación de los sistemas aromáticos. El máximo de absorbancia del óxido de grafeno corresponde a transiciones electrónicas $\pi\rightarrow\pi^*$, y su desplazamiento hacia el rojo con la reducción se debe a la recuperación de la conjugación electrónica en las láminas. Otra característica de las muestras reducidas es la desaparición del hombro presente a 300 nm en el espectro del óxido de grafeno no reducido. Este hombro está asociado a transiciones electrónicas $n\rightarrow\pi^*$, correspondientes a grupos C=O [4], que van desapareciendo a medida que avanza la reducción química (Fig. 11).

Esta técnica también permite detectar nanopartículas metálicas presentes en las dispersiones, ya que estas exhiben el fenómeno de resonancia plasmónica superficial. La resonancia plasmónica se basa en las oscilaciones creadas en los electrones de conducción de la superficie de las nanopartículas al incidir radiación electromagnética de determinada longitud de onda sobre ellas. Ello da lugar a bandas características en el espectro de absorción UV-vis cuya posición viene determinada por la naturaleza del metal así como por el tamaño de las nanopartículas que lo componen.

El equipo utilizado en este trabajo fue un espectrofotómetro Heλios α de doble haz de Thermo Spectronic.

3.3.2. *Análisis térmico.*

El análisis termogravimétrico o termogravimetría (Thermogravimetric Analisys, TGA) permite determinar cambios en la masa de una sustancia en función de la temperatura o del tiempo, ya sean motivados por transformaciones físicas o químicas. La termogravimetría derivada (Derivative Thermogravimetry, DTG) es una forma de representar los resultados de la termogravimetría por medio de la primera derivada de la curva termogravimétrica, en función de la temperatura o el tiempo. La curva DTG representa, por tanto, la velocidad de variación de la masa frente a la temperatura o el tiempo [4, 5].

El TGA y la DTG se utilizaron en esta memoria para análisis cualitativos y cuantitativos. El análisis cualitativo permite determinar el grado de reducción del óxido de grafeno. El óxido de grafeno posee un comportamiento térmico en atmósfera inerte muy característico, presentando una gran pérdida de masa (~ 30%) alrededor de los 200

°C, que corresponde a la pérdida de grupos funcionales oxigenados lábiles presentes en el material en forma de CO, CO_2 y vapor de agua. A partir de 300 °C hay una lenta y constante pérdida de masa (~ 20%), asociada a la desorción de grupos funcionales oxigenados más estables. La eliminación del agua adsorbida se refleja en una pérdida de masa (~ 15%) por debajo de 100 °C [6-8] (Figura 12). Evidentemente, cuanto más reducido se encuentre el óxido de grafeno menores serán las pérdidas de masa debidas a los grupos funcionales oxigenados.
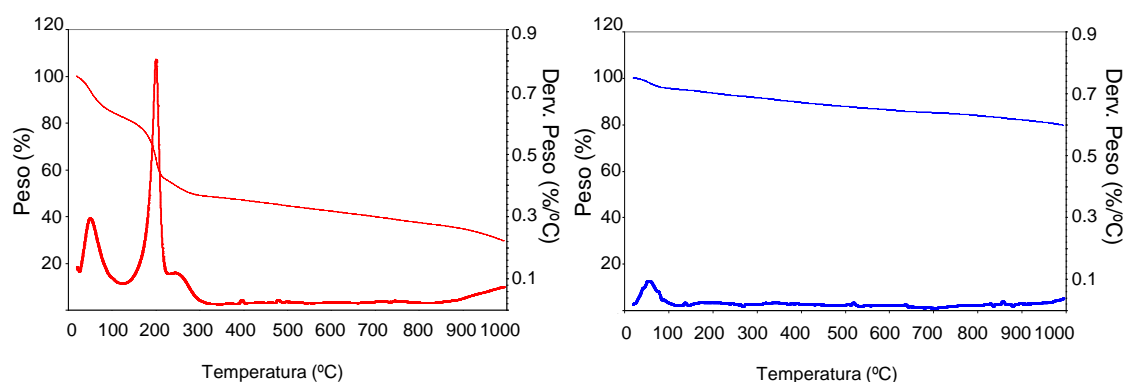
Figura 12. Termograma (línea continua) y termograma derivado (línea punteada) del óxido de grafeno (rojo) y del óxido de grafeno reducido (azul) (Flujo de Argón: 100 mL min^{-1}, velocidad de calentamiento de 10 °C min^{-1}).

Esta técnica también permite realizar análisis cuantitativos a partir de los cambios de peso observados con las variaciones de tiempo o temperatura, [5]. En el caso de las muestras de óxido de grafeno con surfactantes se pudo determinar la cantidad de surfactante presente en cada muestra por los cambios de peso que se producen en los escalones correspondientes en función de la temperatura a la degradación del surfactante y del grafeno en atmósfera oxidante (velocidad de calentamiento de 3 °C min^{-1}).

El equipo utilizado en este trabajo fue una termobalanza SDT Q600 (TA Instruments). Se usó bajo flujo de argón o aire (100 mL min^{-1}) y con unas velocidades de calentamiento de 10 y 3 °C min^{-1}, típicamente desde temperatura ambiente hasta 1000 °C.

3.3.3. Espectroscopía infrarroja.

La espectroscopía infrarroja permite la identificación de grupos funcionales presentes en un compuesto en base a la excitación de modos normales de vibración

característicos de dichos grupos y que se produce como consecuencia de la absorción de radiación electromagnética de frecuencias definidas dentro del rango infrarrojo. En particular, los modos vibracionales detectables mediante espectroscopía infrarroja son aquellos asociados a cambios en el momento dipolar de la molécula o compuesto. El número de bandas obtenidas en el espectro infrarrojo depende del número de átomos y de la simetría del sólido o molécula, mientras que su posición e intensidad son función de la naturaleza química del mismo. El espectrómetro infrarrojo con transformada de Fourier permite la obtención de espectros de forma rápida y con relación señal/ruido elevada. La espectroscopía infrarroja de reflexión total atenuada (Attenuated Total Reflectance, ATR) es una técnica de muestreo basada en el uso de un cristal transmisor a la radiación infrarroja y de alto índice de refracción. El cristal está diseñado para permitir una reflexión interna total que crea una onda evanescente sobre la superficie del cristal. Esta onda se extiende a la muestra en contacto íntimo con el cristal, registrándose su espectro infrarrojo. En este trabajo se utilizó la técnica de ATR ya que es el método particularmente indicado para el análisis de filmes [4, 9, 10].

La espectroscopía infrarroja permite evaluar el grado de reducción de óxido de grafeno, ya que este material presenta una serie de bandas características (Tabla 5) [11-16] cuya intensidad disminuye a medida que avanza el grado de reducción (Fig. 13):
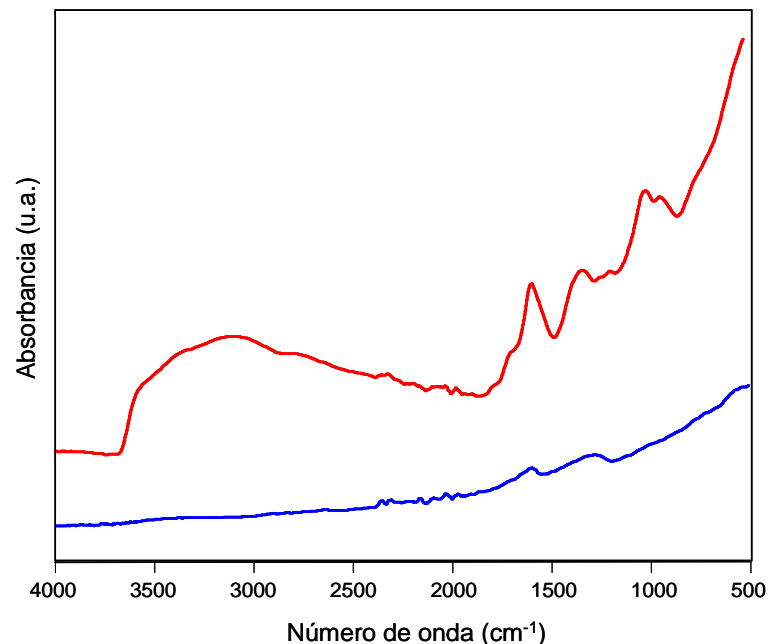
Figura 13. Espectro infrarrojo de óxido de grafeno (rojo) y del óxido de grafeno reducido (azul).

Tabla 5. Asignación de las bandas encontradas en el espectro infrarrojo de óxido de grafeno a vibraciones de grupos funcionales.

Banda	Vibración asociada
Intensa y amplia a 3000 – 3500 cm^{-1}	Vibración de tensión del enlace O-H
Banda estrecha alrededor de 1720 cm^{-1}	Vibración de tensión del enlace C=O en grupos carbonilos y carboxilos
1620 cm^{-1}	Vibración de flexión del enlace C=C debido a vibraciones del esqueleto de los dominios grafiticos sin oxidar
1400 cm^{-1}	Vibración de flexión del enlace O-H en los grupos hidroxilo
1300–1350 cm^{-1}	Vibración de tensión del enlace C-OH
1220 cm^{-1}	Vibración de tensión de grupos epoxi
980 cm^{-1}	Vibraciones de grupos epoxi, éter o peróxido

3.3.4. *Espectroscopía fotoelectrónica de rayos X (X-ray Photoelectron Spectroscopy, XPS).*

Cuando se hace incidir un haz de rayos X de energía apropiada sobre la superficie de un sólido sometido a vacío se extraen electrones de sus átomos debido al efecto fotoeléctrico. La energía cinética medida para uno de estos electrones es igual a la diferencia entre la energía del fotón incidente, que es conocida, y la energía de ligadura del electrón al átomo, que entonces puede determinarse por diferencia. Como la magnitud de la energía de ligadura de los electrones es característica de la capa electrónica y del elemento a que pertenecen, los espectros XPS permiten identificar los elementos presentes el sólido, concretamente en su superficie. La XPS es una técnica de análisis eminentemente superficial ya que, aunque los fotones de rayos X penetran en el sólido varias micras, sólo aquellos electrones arrancados de átomos de las capas más externas del sólido logran escapar del mismo sin sufrir dispersiones inelásticas. En el caso del óxido de grafeno, reducido o no, dado que la muestra es "todo superficie"

(procedente de dispersiones de material exfoliado hasta monocapa), no cabe la distinción entre superficie y "bulk" de la muestra.

En el espectro XPS se representa el número de fotoelectrones detectados en función de su energía de ligadura (o, alternativamente, de su energía cinética). Como la intensidad de las bandas XPS es proporcional al número de átomos del elemento presentes en la muestra, la XPS permite cuantificar los elementos presentes en la superficie de un sólido (salvo el hidrógeno, elemento no detectado por XPS). La composición atómica de la muestra puede ser determinada a partir de espectros XPS generales. Asimismo, la energía de ligadura de los electrones esta modulada por el entorno químico de los átomos a los que pertenecen, con lo que la técnica también proporciona información, por ejemplo, sobre el estado de oxidación del elemento, los grupos funcionales de los que forma parte o fases cristalinas presentes en las muestras objeto de estudio [17, 18].

La técnica XPS ha sido de gran utilidad en este trabajo, ya que ha permitido evaluar, por ejemplo, el grado de reducción de óxido de grafeno o el estado de oxidación de partículas metálicas presentes en algunos de los materiales híbridos que se han preparado. Así, el grado de reducción del óxido de grafeno se pudo determinar en base al análisis de su banda C1s. en la Figura 14 se muestra la banda C1s de óxido de grafeno no reducido. Confirmando estudios previos [6], en el espectro se pueden distinguir tres componentes, localizadas a 284.6 eV, 286.6 eV y 287.9 eV. La componente a 284.6 eV se atribuye a átomos de carbono sin oxidar en estructuras aromáticas sp^2. La componente a 286.6 eV se asigna a carbono enlazado a grupos hidroxilo y epóxido (enlaces C-O) y a C-C en estructuras con defectos. Aunque los defectos en enlaces C-C suelen aparecer a ~285.5 eV, para el óxido de grafeno no es posible distinguir claramente esta señal de la componente a 286.6 eV. La componente a 287.9 eV corresponde a estructuras con enlaces C=O, por ejemplo grupos carbonilo.
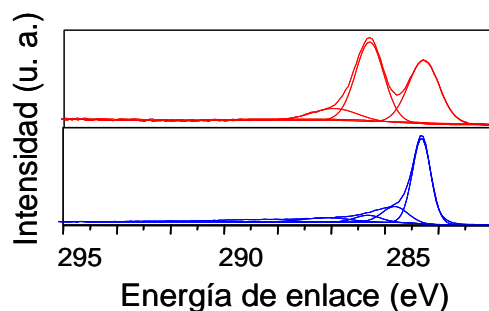
Figura 14. Espectro XPS de la banda C1s del óxido de grafeno (rojo) y del óxido de grafeno reducido (azul).

En el espectro XPS C1s del óxido de grafeno reducido el cambio más significativo que se observa respecto a su equivalente no reducido es la disminución de la contribución relativa de las componentes de mayor energía de enlace (particularmente de la componente a 286.6 eV), lo cual sugiere que en las muestras existe una menor proporción de átomos de carbono oxidados consistente con la consecución del proceso de reducción. La presencia de oxígeno residual en los materiales que poseen un mayor grado de reducción sigue siendo patente en la relación atómica O/C, variando de 0.43 en el caso del óxido de grafeno sin reducir, hasta aproximadamente 0.08 en muestras muy reducidas.

La XPS también permitió confirmar la generación de plata metálica en materiales híbridos de grafeno reducido. Por ejemplo, se observaron dos picos bien definidos y simétricos centrados en 368.4 y 374.4 eV [19], que corresponden a fotoelectrones expulsados, respectivamente, de los niveles $3d_{5/2}$ y $3d_{3/2}$ de Ag^0. Sin embargo, no se observaron componentes a ~ 367 y 373 eV [20], lo que indica que no hay plata oxidada [Ag (I)] en las muestras.

En este trabajo se utilizó un espectrómetro SPECS a una presión residual de 10^{-7} Pa y con una fuente monocromática de rayos X Al Kα (100 W). Para corregir el efecto de acumulación de carga en óxido de grafeno no conductor se utilizó un cañón de electrones a 0.4 eV y 0.10 mA. Las muestras se prepararon bien en forma de filmes, bien depositando las dispersiones correspondientes sobre soportes de acero.

3.3.5. *Espectroscopía Raman.*

La espectroscopía Raman se basa en la dispersión inelástica de luz por parte de los sólidos. Cuando un haz de luz monocromática incide sobre una muestra, la mayoría

de los fotones se dispersan elásticamente y por lo tanto con la misma frecuencia que la de los fotones incidentes (dispersión Rayleigh). Sin embargo, una pequeña fracción de los mismos es dispersada con frecuencias diferentes. Estos cambios de frecuencia son característicos de cada material e independientes de la frecuencia de la luz incidente. Entre los fotones dispersados a distinta frecuencia pueden darse dos situaciones:

(1) los fotones se dispersan a una frecuencia inferior a la de los incidentes, lo que implica que hubo una transferencia de energía de los fotones a la muestra (dispersión de Raman Stokes).

- los fotones se dipersan a una frecuencia superior a los incidentes, por lo que hay una transferencia de energía de la muestra a los fotones (dispersión de Raman anti-Stokes).

La diferencia entre la frecuencia de los fotones incidentes y la de los fotones dispersados inelásticamente no puede ser cualquiera, si no que ha de coincidir con la frecuencia de alguno de los modos vibracionales o rotacionales del material en cuestión. Por ello, la espectroscopía Raman es muy utilizada en la caracterización estructural de sólidos [4, 5, 21].
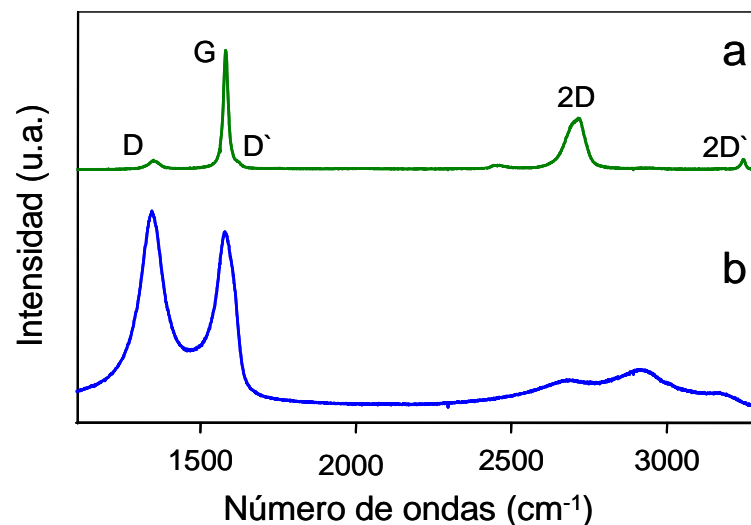
Figura 15. Espectros Raman de (a) grafito y (b) óxido de grafeno reducido.

En el presente trabajo se utilizó esta técnica para identificar distintos tipos de grafeno y estudiar su calidad estructural. Ello es posible debido a que los materiales grafíticos presentan una serie de bandas Raman características en el rango de ~800 a 3200 cm^{-1} [22]. El grafito prístino (Fig. 15) presenta una banda estrecha y bien definida

en su espectro de primer orden (800-1800 cm^{-1}) a ~ 1580 cm^{-1}, denominada banda G, debida al movimiento relativo de pares de átomos de carbono con hibridación sp^2 [23]. A ~ 2700 cm^{-1} aparece otra banda intensa, llamada banda 2D o G´ [24]. En presencia de defectos estructurales aparecen nuevas bandas en el espectro, concretamente una banda localizada a 1360 cm^{-1} (banda D) atribuida a los movimientos radiales de los átomos de carbono en los anillos aromáticos, y un pequeño hombro a ~ 1620 cm^{-1} (banda D´) [25]. En el espectro de segundo orden (2200-3200 cm^{-1}) de grafito/grafeno la banda más característica es la 2D, que corresponde al sobretono de la banda D, pero también aparece una banda a ~ 3250 cm^{-1} (banda 2D´ sobretono de la banda D´) [26]. Estas bandas características del grafito/grafeno nos ayudan a obtener información sobre la calidad estructural del material. Concretamente, la magnitud de la intensidad de la banda D con respecto a la G es un indicador de la cantidad de desorden estructural que presenta una muestra grafítica [27]. Otro indicador es la mejor definición de la banda 2D en grafitos muy ordenados, mientras que dicha banda se ensancha y pierde intensidad con el aumento del desorden. En muestras con buena calidad estructural y apilamiento ordenado (Bernal AB), las características de la banda 2D permiten estimar el número de capas de que consta una lámina de grafeno, es decir, si es grafeno monocapa, bicapa, multicapa o grafito (más de 10 capas) [24, 28].

En esta memoria los espectros Raman se obtuvieron con un equipo Horiba Jobin-Yvon LabRam utilizando un láser con longitud de onda de excitación de 532 nm. Las muestras para esta técnica se prepararon típicamente en forma de filmes a partir de las correspondientes dispersiones.

3.3.6. *Difracción de rayos X.*

Esta técnica permite evaluar el grado de orden estructural de los materiales de carbono. Cuando un haz de rayos X incide sobre una muestra, interacciona con ella dando lugar a una dispersión de la radiación que depende de las distancias entre los distintos planos atómicos de la muestra. En la radiación electromagnética dispersada se producen interferencias constructivas en direcciones espaciales muy definidas que cumplen la ley de Bragg:

$$n\lambda = 2d_{hkl}\mathrm{sen}\theta \tag{2}$$

donde n es un número entero, λ es la longitud de onda de la radiación incidente, d_{hkl} es la distancia interplanar de la familia de planos cristalográficos definida por los índices

de Miller (hkl) y θ es el ángulo de dispersión de la radiación electromagnética. En condiciones ideales, la ley de Bragg predice que la difracción se produce a valores discretos del ángulo θ, pero en la práctica se produce un ensanchamiento alrededor de este ángulo debido a factores instrumentales y al tamaño finito de los cristales [29].

En este trabajo se obtuvieron difractogramas de distintas muestras. Las muestras se prepararon en forma de filme o de polvo. El equipo utilizado fue un difractómetro Bruker D8 Advance con radiación K_α del Cu ($\lambda = 0.154$ nm), con un paso de 0.02° y un segundo de adquisición por paso.

3.3.7. Adsorción física de gases.

En este trabajo se utilizó la técnica de adsorción física de gases para caracterizar la textura porosa de materiales híbridos grafeno-sílice mesoporosa [30-33].

Esta técnica consiste en exponer una muestra sólida (el adsorbente) a un gas (el adsorbato) químicamente inerte, y a una serie de presiones definidas a temperatura constante en un espacio cerrado con el fin de que el gas se adsorba sobre la superficie del sólido. La adsorción provoca una disminución en la presión del gas y un aumento del peso del adsorbente hasta alcanzar el equilibrio. A bajas presiones, la adsorción se produce por la formación de una monocapa de moléculas de gas sobre la superficie del adsorbente (por ejemplo, las paredes de los poros que posea). Al aumentar la presión relativa, el espesor de la capa de gas aumenta hasta que se produce la condensación capilar y el poro se llena de gas adsorbido [34], permitiendo el cambio de su volumen. La etapa de desorción comienza con el poro lleno por un menisco líquido que gobierna el proceso de evaporación, de tal manera que este proceso puede seguir un camino distinto al de la adsorción dando lugar a la histéresis. La representación de la cantidad adsorbida frente a la presión a temperatura constante se denomina isoterma.

Generalmente, se utiliza nitrógeno como adsorbato porque el espesor de las multicapas a la que da lugar es poco sensible a los diferentes tipos de adsorbentes, y también porque la misma isoterma de adsorción/desorción puede ser usada tanto para el análisis del tamaño de poro como para el cálculo de la superficie específica de las muestras.

En este trabajo se estudió la adsorción física de nitrógeno a -196 ºC en un equipo volumétrico automático (Micromeritics, modelo ASAP 2010). Como paso previo a las medidas, las muestras se desgasificaron durante toda una noche a 80 ºC.

3.3.8. *Microscopia electrónica de barrido (Scanning Electron Microscopy, SEM).*

En la microscopia electrónica de barrido un haz de electrones incide sobre la muestra e interacciona con ella, surgiendo electrones de distintos orígenes que pueden ser captados por diversos detectores, proporcionando variedad de información. Este tipo de microscopia proporciona mayor resolución que la microscopia óptica, ya que esta última está limitada por la longitud de onda de la luz visible [5].

En este trabajo se utilizó un microscopio electrónico de barrido con emisión electrónica de campo Quanta FEG 650 (FEI Company) que dispone de distintos detectores:

- detector de electrones secundarios (Secondary Electrons, SE). Estos electrones son arrancados de los átomos de la superficie de la muestra por interacción con los electrones de alta energía del haz incidente. Este modo de detección proporciona imágenes topográficas de alta resolución.

- detector de electrones retrodispersados (Back-Scattered Electrons, BSE). Estos electrones son electrones del haz incidente que han interaccionado (colisionado) con los átomos de la muestra y han sido reflejados. La intensidad de emisión de los electrones retrodispersados depende del número atómico de la muestra, así los átomos más pesados producen mayor cantidad de electrones retrodispersados.

- detector STEM (Scanning Transmission Electron Microscopy). Cuando la muestra es lo suficientemente delgada, el haz de electrones incidente puede ser transmitido a través de la muestra. Este detector puede proporcionar imágenes de mayor resolución que las obtenidas en el detector de electrones secundarios.

- detector de energía dispersiva (Energy-Dispersive Spectroscopy, EDS). Detecta los rayos X generados por la muestra tras irradiarla con el haz de electrones. Permite llevar a cabo análisis cualitativos y cuantitativos de la composición elemental de la superficie de la muestra.

3.3.9. *Microscopia electrónica de transmisión (Transmission Electron Microscopy, TEM).*

El microscopio electrónico de transmisión es un instrumento que aprovecha la interacción entre un fino haz de electrones acelerados que incide sobre una muestra lo suficientemente delgada para que los electrones puedan atravesarla. Cuando los electrones colisionan con la muestra, parte son dispersados, otra parte son transmitidos

y el resto da lugar a interacciones que producen distintos fenómenos, como por ejemplo la emisión de luz. Todos estos fenómenos pueden utilizarse para obtener información sobre la naturaleza de la muestra, pero son los transmitidos los utilizados por unas lentes para formar una imagen final de gran aumento del espécimen [5].

En este trabajo se utilizó un microscopio JEOL 2000 EX-II que trabaja a 160 kV, con el que se obtuvieron imágenes de láminas de grafeno. Para ello, las dispersiones se depositaron sobre rejillas de cobre cubiertas por una capa muy delgada de carbono.

3.3.10. Microscopia de fuerza atómica (Atomic Force Microscopy, AFM).

El AFM se basa en la detección de las fuerzas entre átomos y moléculas. El microscopio registra la topografía superficial de un material mediante una sonda o punta afilada que realiza un barrido lateral sobre su superficie. Entre la punta y la muestra se establecen fuerzas atractivas y repulsivas como consecuencia de su interacción, que producen una deflexión medible en un resorte acoplado a la punta.

Existen distintos modos de operación del AFM. Para eliminar problemas de alteración de las superficies como consecuencia de la aplicación de fuerzas elevadas se han desarrollado modos de no-contacto y de contacto intermitente (modo tapping). En este último, se sustituye el contacto continuo punta-muestra por aproximaciones breves de la punta, que oscila próxima a su frecuencia de resonancia. La amplitud de la oscilación de la punta varía de forma significativa en las proximidades de la superficie de la muestra por la existencia de interacciones con esta. Dicha amplitud se utiliza para obtener imágenes de la topografía superficial de la muestra [35].

En este trabajo se utilizó un microscopio Nanoscope IIIa Multimode (Veeco Instruments) en modo tapping. Se utilizaron cantilevers rectangulares de Si con una constante de fuerza de ~ 40 N m^{-1} y una frecuencia de resonancia entre 250 y 300 kHz. Las muestras fueron preparadas depositando gotas de las suspensiones sobre un sustrato de grafito pirolítico altamente orientado, dejándolas secar y finalmente lavando el sustrato con agua desinonizada.

3.3.11. Microscopia de efecto túnel (Scanning Tunneling Microscopy, STM).

MEl efecto túnel es un fenómeno mecanocuántico que permite a una partícula atravesar una barrera de energía mayor que la de la propia partícula, algo prohibido en la mecánica clásica. En la STM se hace uso de este efecto, ya que la señal que se mide

es precisamente una corriente eléctrica generada por efecto túnel. La sonda consiste en una punta metálica extremadamente afilada, que se sitúa a una distancia de ~ 1 nm de la superficie de la muestra. Al establecer una diferencia de potencial entre punta y muestra, se establece una corriente túnel entre ambas [35].

La corriente túnel decae de manera exponencial con la distancia entre punta y muestra, lo que garantiza que la mayor parte de la corriente fluya a través de un único átomo de la punta (el más cercano a la muestra). Ello proporciona una elevada resolución espacial, tanto lateral como vertical, permitiendo la visualización rutinaria de estructuras a nivel atómico.

Sin embargo, no solo la separación entre punta y muestra determina la magnitud de la corriente túnel, sino también la estructura electrónica de ambas. De este modo, las imágenes obtenidas por STM son en general una combinación de efectos tanto topográficos como electrónicos, lo que dificulta la interpretación de las imágenes.

En este trabajo se utilizó un microscopio Nanoscope IIIa Multimode (Veeco Instruments). Se usaron puntas de aleación de Pt/Ir (80/20) preparadas mecánicamente. Las imágenes fueron obtenidas de filmes de grafeno preparados mediante filtración en vacío de sus correspondientes dispersiones.

3.4. Estudio de las propiedades de los materiales.

3.4.1. Propiedades electroquímicas.

En este trabajo se estudió el efecto de distintos surfactantes intercalados entre láminas de óxido grafeno reducido mediante voltametría cíclica, técnica que permite calcular la capacidad específica de cada material.

La voltametría cíclica (CV) es una técnica electroquímica de tipo potenciostático que se basa en la medida de la intensidad de corriente en un sistema en función del potencial aplicado al electrodo de trabajo, tanto en el sentido directo como en el inverso. La información proporcionada por esta técnica se recoge en las curvas voltamperométricas (I frente a V), que proporcionan información relativa a la presencia de reacciones químicas o la resistividad del material. En este trabajo, se midieron curvas voltmaperométricas para obtener los valores de las capacidads de cada muestra, es decir, la cantidad de energía eléctrica almacenada para una diferencia de potencial eléctrico

dado. Dicha cantidad se puede calcular a partir del área encerrada por la curva voltamperométrica (Fig. 16) [36,37].
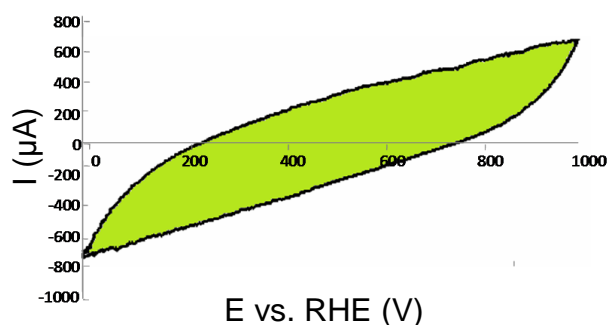
Figura 16. Curva voltamétrica de óxido de grafeno.

Las muestras se prepararon partiendo de dispersiones acuosas mixtas de óxido de grafeno/surfactante (0.1/0.5 mg mL^{-1}). Estas suspensiones se redujeron con hidracina en medio básico en baño de agua a 95 ºC durante 1 hora, obteniéndose suspensiones mixtas de óxido de grafeno reducido/surfactante. También se prepararon dispersiones de óxido de grafeno no reducido y reducido sin surfactante. Todas las dispersiones se filtraron a través de membranas de policarbonato de 47 mm de diámetro y 0.2 μm de diámetro de poro, obteniéndose filmes de cada material. Dichos filmes, soportados sobre una malla de acero, fueron utilizados en una celda electroquímica de tres electrodos. Las medidas electroquímicas se realizaron con un potencióstato (Modelo 263A de EG&G). Como contraelectrodo se utilizó un hilo de platino y como referencia un electrodo reversible de hidrógeno introducido en la misma disolución de trabajo. Todas las medidas se realizaron en una disolución de H$_2$SO$_4$ 0.5 M en un intervalo de potencial de 0 a 1 V y con una velocidad de barrido de 2 mV s^{-1}.

3.4.2. *Actividad catalítica.*

En esta memoria se prepararon distintos materiales híbridos de grafeno y nanopartículas metálicas. Dichos híbridos pueden ser usados potencialmente como catalizadores de distintas reacciones químicas. Se exploró la actividad catalítica de los híbridos en la reacción de conversión de *p*-nitrofenol a *p*-aminofenol usando borohidruro de sodio como agente reductor.
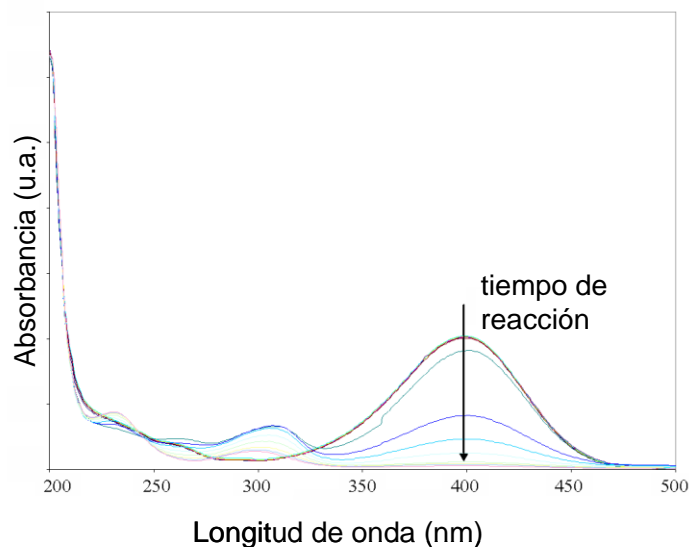
Figura 17. Evolución del espectro UV-vis de *p*-nitrofenol durante su reducción con borohidruro de sodio en presencia de catalizador metálico.

Sin catalizador, esta reacción tarda en completarse varios días. Sin embargo, se ha demostrado que el uso de nanopartículas de metales nobles aumenta enormemente la velocidad de reacción [38, 39]. La cinética de esta reacción se puede seguir fácilmente mediante espectroscopía UV-vis (Fig. 17). El *p*-nitrofenol en agua desionizada presenta una banda de absorción en su espectro UV-vis a 317 nm asociado a la presencia del grupo nitro. Al añadir borohidruro de sodio, el *p*-nitrofenol se desprotona, desplazando la banda de absorción a 400 nm. Tras la conversión de *p*-nitrofenol a *p*-aminofenol, la banda situada a 400 nm desaparece como consecuencia de la conversión de los grupo nitro a grupos amino. De esta manera es posible seguir el avance de la reacción monitorizando la disminución de la banda a 400 nm. La reacción se lleva a cabo en presencia de un exceso de borohidruro que permite considerar su concentración constante a lo largo de la reacción [38], de tal manera que fue posible ajustar la cinética de la reacción a un proceso de pseudo-primer orden:

$$\frac{d[p-NP]}{dt} = -k_{app}[p-NP]$$ (3)
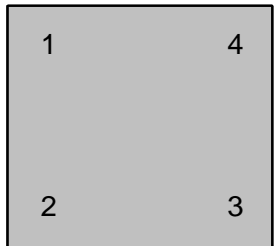
donde $[p-NP]$ es la concentración de p-nitrofenóxido y k_{app} es la constante aparente de reacción.

El avance de la reacción se siguió mediante espectroscopía UV-vis, pudiendo relacionar la absorbancia a 400 nm con la concentración de *p*-nitrofenol a través la ley de Lambert-Beer (Ec. 1) y así poder calcular la constante aparente de reacción, k_{app}.

3.4.3. *Conductividad eléctrica.*

La conductividad eléctrica es la capacidad que tienen las sustancias para permitir el paso de corriente eléctrica a través de ellas, refleja la facilidad que tienen los portadores de carga (electrones, huecos) para moverse a través de la sustancia así como el número de portadores de carga que poseen. La conductividad eléctrica se considera un indicador muy sensible del grado de restauración de la conjugación electrónica que se produce tras la reducción del óxido de grafeno, ya que pasa de ser un material aislante eléctrico (óxido de grafeno) a un material conductor.

Para determinar la conductividad eléctrica se empleo el método de Van der Pauw [40], que consiste en aplicar una corriente en un lado de la muestra de geometría cuadrada (por ejemplo en el lado 1-2) y medir el voltaje en el lado opuesto (lado 3-4), para así calcular su resistencia por la ley de Ohm:

$$R_{12,34} = \frac{V_{34}}{I_{12}} \tag{4}$$

Figura 18. Ley de Ohm y esquema de muestra con la numeración de sus laterales.

En su trabajo, van der Pauw demostró que la resistencia de muestras con formas arbitrarias se puede determinar a partir de dos de estas resistencias (una medida a lo largo de un borde vertical y otra a lo largo de un borde horizontal), pudiendo calcular la resistencia real, R_s, como:

$$e^{-\pi R_{12,34}/R_s} + e^{-\pi R_{23,41}/R_s} = 1 \tag{5}$$

La conductividad eléctrica, σ viene dada por la ecuación 6 :

$$\sigma = \frac{L}{R_s A} \tag{6}$$

siendo L la longitud del filme y A su área transversal.

Las medidas se realizaron utilizaron una fuente de alimentación Agilent 6614C de corriente continua y un multímetro digital Fluke 45. Las muestras se prepararon en forma de filmes de dimensiones 12×12 mm^2 cuyo grosor se estimó mediante SEM.

3.5. Referencias.

[1]   Hummers WS, Offeman RE. Preparation of graphitic oxide. J. Am. Chem. Soc. 80 (1958), 1339.

[2]   Dreyer DR, Park S, Bielawski CW, Ruoff RS. The chemistry of graphene oxide. Chem. Soc. Rev. 39 (2010), 228-240.

[3]   Li D, Muller MB, Gilje S, Kaner RB, Wallace GG. Processable aqueous dispersions of graphene nanosheets. Nat Nanotech. 3 (2008), 101-105.

[4]   Skoog DA, Holler FJ, Nieman TA. Principles of instrumental analysis. Belmont (USA): Thomson Brooks/cole. 2007.

[5]   Faraldos M, Goberna C. Técnicas de análisis y caracterización de materiales. Madrid: Consejo Superior de Investigaciones Científicas 2011.

[6]   Paredes JI, Villar-Rodil S, Martínez-Alonso A, Tascón JMD. Graphene oxide dispersions in organic solvents. Langmuir 24 (2008), 10560-10564.

[7]   Stankovich S, Dikin DA, Piner RD, Kohlhaas KA, Kleinhammes A, Jia Y, Wu Y, Nguyen ST, Ruoff RS. Synthesis of graphene-based nanosheets via chemical reduction of exfoliated graphite oxide. Carbon 45 (2007), 1558-1565.

[8]   Becerril HA, Mao J, Liu Z, Stoltenberg RM, Bao Z, Chen Y. Evaluation of solution-processed reduced graphene oxide films as transparent conductors. ACS Nano 2 (2008), 463-470.

[9]   Smith B. Infrared spectral interpretation. New York (USA). 1999.

[10]   Socrates G. Infrared and Raman characteristics group frecuencies. New York (USA). 2001.

[11]   Park S, An J, Jung I, Piner RD, An SJ, Li X, Velamakanni A, Ruoff RS. Colloidal suspensions of highly reduced graphene oxide in a wide variety of organic solvents. Nano Lett. 9 (2009), 1593-1597.

[12]   Mermoux M, Chabre Y, Rousseau A. FTIR and 13C NMR study of graphite oxide. Carbon 29 (1991), 469-474.

[13]   Stankovich S, Piner RD, Nguyen ST, Ruoff RS. Synthesis and exfoliation of isocyanate-treated graphene oxide nanoplatelets. Carbon 44 (2006), 3342-3347.

[14]   Xu Y, Bai H, Lu G, Li C, Shi G. Flexible graphene films via the filtration of water-soluble noncovalent functionalized graphene sheets. J. Am. Chem. Soc. 130 (2008), 5856-5857.

[15]   Chattopadhyay J, Mukherjee A, Hamilton CE, Kang J, Chakraborty S, Guo W,

Kelly KF, Barron AR, Billups WE. Graphite epoxide. J. Am. Chem. Soc. 130 (2008), 5414-5415.

[16] Shimanouchi T. Tables of molecular vibrational frequencies: consolidated volume II: American chemical society and the American institute of physics, for the National bureau of standards. 1977.

[17] Watts JF, Wolstenholme J. An introduction to surface analysis by XPS and AES. West Sussex (England). 2003.

[18] Briggs D, Seah M. Practical surface analysis. Volume I: Auger and X-ray photoelectron spectroscopy. West Sussex (England). 1983.

[19] Crist BV. Handbook of Monochromatic XPS Spectra. Vol. 1. The elements & Native Oxides. California, USA: XPS International LLC. 2004.

[20] Crist BV. Handbook of Monochromatic XPS Spectra. Vol. 2. Commercially Pure Binary Oxides. California, USA: XPS International LLC. 2004.

[21] Amer S. Raman spectroscopy, fullerenes and nanotechnology. Dayton (USA). 2010.

[22] Tuinstra F, Koenig JL. Raman spectrum of graphite. J. Chem. Phys. 53 (1970), 1126-1130.

[23] Ferrari AC, Robertson J. Interpretation of Raman spectra of disordered and amorphous carbon. Phys. Rev. B 61 (2000), 14095-14107.

[24] Ferrari AC, Meyer JC, Scardaci V, Casiraghi C, Lazzeri M, Mauri F, Piscanec S, Jiang D, Novoselov KS, Roth S, Geim AK. Raman spectrum of graphene and graphene layers. Phys. Rev. Lett. 97 (2006), 187401.

[25] Nemanich RJ, Solin SA. First- and second-order Raman scattering from finite-size crystals of graphite. Phys. Rev. B 20 (1979), 392-401.

[26] Ferrari AC. Raman spectroscopy of graphene and graphite: Disorder, electron–phonon coupling, doping and nonadiabatic effects. Solid State Commun. 143 (2007), 47-57.

[27] Cuesta A, Dhamelincourt P, Laureyns J, Martínez-Alonso A, Tascón JMD. Raman microprobe studies on carbon materials. Carbon 32 (1994), 1523-1532.

[28] Gupta A, Chen G, Joshi P, Tadigadapa S, Eklund. Raman scattering from high-frequency phonons in supported n-graphene layer films. Nano Lett. 6 (2006), 2667-2673.

[29] Ergun S. X-ray studies of coals ans carbonaceous materials. Washington (USA). 1968.

[30] Brunauer S, Emmett PH, Teller E. Adsorption of gases in multimolecular layers. J. Am. Chem. Soc. 60 (1938), 309-319.

[31] Pierotti R, Rouquerol J. Reporting physisorption data for gas/solid systems with special reference to the determination of surface area and porosity. Pure Appl. Chem. 57 (1985), 603-619.

[32] Dubinin MM. Physical adsorption of gases and vapors in micropores. London, Academic Press. 1975.

[33] Béguin F, Frackowiak E. Carbons for Electrochemical energy storage and conversion systems. USA: Taylor & Francis Group, LLC. 2010.

[34] Cohan LH. Sorption hysteresis and the vapor pressure of concave surfaces. J. Am. Chem. Soc. 60 (1938), 433-435.

[35] Magonov SN, Whangbo M-H. Surface Analysis with STM and AFM. VCH: Weinheim, Chapter 8. 1996.

[36] Conway BE. Electrochemical Supercapacitors. Scientific Fundamentals and Technological Applications. Kluwer Academic/ Plenum Publisher. New York

(USA). 1999.

[37] Béguin F, Frackowiak E. Supercapacitors. Materials, Sustems, and Applications. Wiley-VCH Verlag GmbH & Co. Boschdtr (Germany). 2013.

[38] Jana S, Ghosh SK, Nath S, Pande S, Praharaj S, Panigrahi S, Basu S, Endo T, Pal T. Synthesis of silver nanoshell-coated cationic polystyrene beads: A solid phase catalyst for the reduction of 4-nitrophenol. Appl. Catal. A Gen. 313 (2006), 41-48.

[39] Wang P, Han L, Zhu C, Zhai Y, Dong S. Aqueous-phase synthesis of Ag-TiO2-reduced graphene oxide and Pt-TiO2-reduced graphene oxide hybrid nanostructures and their catalytic properties. Nano Res. 4 (2011), 1153-1162.

[40] Van del Pauw LJ. A method of measuring the resistivity and Hall coefficient on lamellae of arbitrary shape: Philips Technical Review 1958.
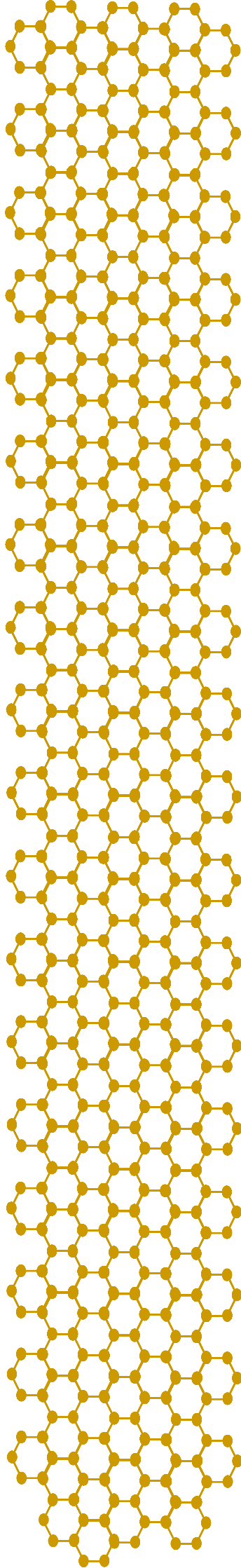
4. RESÚMENES Y ARTÍCULOS

4.1. Reducción química de óxido de grafeno mediante biomoléculas.

Artículo I

Publicado en la revista The Journal of Physical Chemistry C: "Vitamin C is an ideal substitute for hydrazine in the reduction of graphene oxide suspensions".

Artículo II

Publicado en la revista Carbon: "Identifying efficient natural bioreductants for the preparation of graphene and graphene-metal nanoparticle hybrids with enhanced catalytic activity from graphite oxide".

La reducción química de óxido de grafeno es uno de los métodos más prometedores para la obtención de grafeno a escala industrial. Habitualmente esta reducción se lleva a cabo en medio acuoso básico utilizando hidracina como agente reductor debido a su reconocida eficacia. No obstante, su elevada toxicidad y peligrosidad hacen poco recomendable su uso. Por ello, en este trabajo se ha estudiado la forma de sustituirla por reductores inocuos y eficaces para la reacción estudiada.

En el *Artículo I* se realiza un estudio comparativo sobre la eficacia de distintos agentes reductores, entre ellos la hidracina, respecto a la reducción del óxido de grafeno en medio acuoso. Aparte de la hidracina, los agentes reductores estudiados fueron vitamina C, pirogalol y borohidruro de sodio. Todos ellos se ensayaron en medio acuoso básico. También se estudió la reducción simplemente calentando las dispersiones en medio básico, en ausencia de agente reductor. Para poder comparar la eficacia de los distintos agentes reductores, se ensayaron distintas concentraciones y se optimizó el tiempo de reacción.

El grado de avance de las reacciones se siguió mediante espectroscopía de absorción UV-vis. El óxido de grafeno presenta un máximo en su espectro de absorción localizado a 231 nm, el cual se desplaza hacia longitudes de onda mayores a medida que aumenta el grado de reducción química debido al incremento de la conjugación electrónica en la red. Se tomó como referencia de reducción máxima alcanzable la conseguida al utilizar hidracina, que desplaza el máximo de absorbancia hasta 269 nm. Mediante esta técnica se pueden optimizar las condiciones de concentración y tiempo de

cada agente reductor que permiten una reducción más eficaz, y esbozar una primera clasificación de la eficiencia de los distintos agentes reductores.

Con las dispersiones de óxido de grafeno reducidas en las condiciones óptimas para cada agente reductor, se prepararon filmes que permitieron caracterizar los materiales mediante TGA, espectroscopía ATR-FTIR, XPS y medidas de conductividad eléctrica, técnicas que ayudan a realizar un estudio más detallado del grado de reducción alcanzado en cada caso. En función del agente reductor utilizado, se observaron diferencias en la disminución de las bandas asociadas a grupos funcionales oxigenados observadas mediante espectroscopía ATR-FTIR y XPS, técnica con la cual también fue posible observar la recuperación de los dominios grafíticos. Mediante análisis térmico se observaron distintos porcentajes de pérdida de masa asociada a la descomposición de grupos funcionales oxigenados y cada muestra presenta distintos valores de conductividad eléctrica, todo ello indicativo de los distintos grados de reducción logrados.

La vitamina C es inocua y no dañina para el medio ambiente y los resultados obtenidos en este trabajo indican que posee aproximadamente la misma eficacia que la hidracina como agente reductor del óxido de grafeno. Además, la vitamina C presenta frente a la hidracina el valor añadido de no introducir heteroátomos no deseados (nitrógeno, en este caso) en el óxido de grafeno. Por todo ello, se concluye que es un sustituto ideal de la hidracina para la reducción de óxido de grafeno.

La identificación de la vitamina C como agente reductor inocuo del óxido de grafeno sugiere la posibilidad de que otras biomoléculas puedan ser eficaces reductores de este material. La disponibilidad de una variedad de biomoléculas reductoras sería interesante desde un punto de vista práctico, ya que dichas biomoléculas podrían dotar al óxido de grafeno reducido de funcionalidades nuevas y/o mejoradas como por ejemplo biocompatibilidad, mayor estabilidad coloidal, etc. Por ello, en el *Artículo II* se investigaron 20 biomoléculas como potenciales reductores de óxido de grafeno. Estas biomoléculas se eligieron principalmente por su actividad antioxidante y/o reductora demostrada en el contexto bioquímico, aunque su poder reductor respecto al óxido de grafeno no había sido previamente estudiado en la mayoría de los casos. De hecho, solo dos de ellas, la glucosa y el glutatión, habían sido identificadas anteriormente como reductores del óxido de grafeno.

Se estudiaron 20 biomoléculas: piridoxina (PN), piridoxamina dihidrocloruro (PM), riboflavina (B_2), sal sódica de riboflavina-5'-monofosfato (sal de B_2), ácido cítrico, ácido fumárico, ácido málico, ácido tartárico, arginina (Arg), asparagina, carnosina, glicina, ácido glutámico, glutatión (GSH), histidina (His), metionina, fenilalanina, triptofano (Tryp), tirosina y glucosa (Glu). Los ensayos se realizaron en las dispersiones de óxido de grafeno en medio básico, para mantener la estabilidad coloidal, una temperatura de 95ºC, optimizando las concentraciones de las biomoléculas y los tiempos de reducción.

Al igual que en el artículo anterior, se utilizó la espectroscopía de absorción UV-vis como una primera herramienta de diagnóstico rápido para estimar el grado de reducción alcanzado. Como es conocido que simplemente la presencia de un medio básico es suficiente para conseguir una reducción parcial del óxido de grafeno, se consideró que solo aquellas biomoléculas que permitían una reducción del óxido de grafeno claramente mayor que la lograda solo en presencia de un medio básico eran reductores eficientes del óxido de grafeno. En la práctica, esto significa que el máximo de absorbancia del óxido de grafeno se ha de desplazar a valores por encima de 259-261 nm para que su reducción se considere eficaz. Basándonos en este criterio, 9 de las 20 biomoléculas ensayadas resultaron ser eficaces reductores del óxido de grafeno: PN, PM, B_2 y su sal de B_2, Arg, GSH, His, Tryp y Glu. Los bioreductores identificados poseen eficacias diferentes entre sí, ya que dieron lugar a distintos desplazamientos hacia el rojo del máximo de absorbancia, siendo el GSH el agente reductor más débil y la B_2 y su sal correspondiente los más eficaces. Estos resultados se confirmaron mediante TGA, espectroscopías ATR-FTIR, XPS y Raman, difracción de rayos X y conductividad eléctrica.

Los bioreductores identificados permitieron la preparación de híbridos de óxido de grafeno reducido y nanopartículas de plata, ya que actúan como reductores tanto del óxido de grafeno como de una sal de plata ($AgNO_3$), sin necesidad de utilizar otros agentes reductores o estabilizantes. Se optimizó la cantidad de sal metálica y de bioreductor con el fin de generar nanopartículas individuales exclusivamente sobre la superficie de las láminas, con densidades numéricas aceptables y tamaño restringido a unas pocas decenas de nm.

Se determinó que alguno de estos híbridos exhibía tanto estabilidad coloidal a largo plazo en medio acuoso como actividad catalítica excepcionalmente alta para la

reducción de 4-nitrofenol a 4-aminofenol con $NaBH_4$ a temperatura ambiente. En particular, los híbridos obtenidos con piridoxamina demostraron una actividad catalítica muy superior a la de otros catalizadores basados en nanopartículas de plata investigados anteriormente para la reducción mencionada.

Vitamin C Is an Ideal Substitute for Hydrazine in the Reduction of Graphene Oxide Suspensions
(The Journal of Physical Chemistry C 114 (2010), 6426-6432)

M. J. Fernández-Merino, L. Guardia, J. I. Paredes, S. Villar-Rodil, P. Solıís-Fernández, A. Martínez-Alonso, and J. M. D. Tascón

Instituto Nacional del Carbón, CSIC, Apartado 73, 33080 Oviedo, Spain

Abstract

The preparation of solution-processable graphene from graphite oxide typically involves a hydrazine reduction step, but the use of such a reagent in the large-scale implementation of this approach is not desirable due to its high toxicity. Here, we compare the deoxygenation efficiency of graphene oxide suspensions by different reductants (sodium borohydride, pyrogallol, and vitamin C, in addition to hydrazine), as well as by heating the suspensions under alkaline conditions. In almost all cases, the degree of reduction attainable and the subsequent restoration of relevant properties (e.g., electrical conductivity) lag significantly behind those achieved with hydrazine. Only vitamin C is found to yield highly reduced suspensions in a way comparable to those provided by hydrazine. Stable suspensions of vitamin C-reduced graphene oxide can be prepared not only in water but also in common organic solvents, such as N,N-dimethylformamide (DMF) or N-methyl-2-pyrrolidone (NMP). These results open the perspective of replacing hydrazine in the reduction of graphene oxide suspensions by an innocuous and safe reductant of similar efficacy, thus facilitating the use of graphene-based materials for large-scale applications.

1. Introduction

Owing to its remarkable physical properties and to the perspective of important applications, graphene has emerged in recent years as the subject of intense research efforts [1-3]. Although such efforts were originally driven and are still largely motivated by the prospect of graphene as a key component in future nanoelectronic devices [1, 2, 4], other potential applications of this two-dimensional material are also being actively pursued, including its use in composite materials [5, 6], gas sensors [7, 8], solar cells [9], supercapacitors [10], or drug delivery [11].

Central to the success of graphene in practical uses is the availability of production methods that can deliver large quantities of the material at low cost. In this regard, the approach that first led to the isolation of graphene (i.e., micromechanical cleavage of graphite) [4] is a low-yield, low-throughput process and therefore not likely to be industrially scalable, which has made the search for alternative preparation techniques a priority. At present, there are three main routes toward graphene with potential for mass production: (1) processing of graphite and graphite derivatives (mostly graphite oxide) in the liquid phase by chemical methods to afford colloidal suspensions [12, 13], (2) epitaxial growth via high temperature treatment of silicon carbide [14, 15], and (3) chemical vapor deposition (CVD) of hydrocarbons on transition metal substrates such as nickel or copper [16, 17]. Even though the epitaxial growth and CVD techniques are particularly promising in terms of providing the large area, high quality graphene wafers required for applications in electronics [18], the colloidal route, and especially the one based on graphite oxide, is currently considered the most attractive option for many other prospective uses of graphene. The main advantages of this route are its cost-effectiveness, massive scalability, versatility for chemical functionalization, and easy processability into paper-like materials, coatings, composites, etc [12, 13].

The production of colloidal suspensions of graphene from graphite oxide typically involves exfoliation of the latter in a suitable solvent (usually water, but also some polar organic solvents) [19], followed by chemical reduction of the dispersed single-layer sheets (graphene oxide sheets) with hydrazine [12, 13, 20, 21]. When the reduction is carried out under controlled conditions, the resulting deoxygenated graphene oxide sheets form stable suspensions without the need of surfactants or any other stabilizers, which is an added advantage [12, 20, 21]. Unfortunately, hydrazine is a highly toxic and potentially explosive chemical [22], and therefore its use should be avoided in the large-scale implementation of this approach. In the search for alternatives to hydrazine, two relevant factors should be taken into account in addition to environmental and safety issues. First, the process should be at least as effective as hydrazine in the deoxygenation of graphene oxide. Second, for the sake of further processability, the reduced material should remain dispersed as single-layer sheets in aqueous and organic media; that is, it should not precipitate after reduction.

We have carried out an exhaustive comparison of the performance of several different reducing agents toward deoxygenation of graphene oxide suspensions, which has not been previously reported in the literature. Most significantly, we find that the efficiency of hydrazine in the reduction of graphene oxide is only matched by vitamin C (ascorbic acid), a natural antioxidant essential for many metabolic functions in living organisms and widely employed as a food additive [23]. Reduction with vitamin C can be made not only in water, but also in some common organic solvents, such as N,N-dimethylformamide (DMF) and N-methyl-2-pyrrolidone (NMP). These findings, together with the nontoxicity of this natural product, suggest that vitamin C represents an ideal substitute for hydrazine in the large-scale production of solution-processable graphene.

2. Experimental Section

Graphite oxide was prepared in the form of both a thick slurry and a fine dry powder as previously reported [19, 24], starting from natural graphite powder (Fluka 50870) and using the Hummers method [25]. To prepare suspensions of graphene oxide sheets in a given solvent (usually water, but also DMF and NMP), the graphite oxide slurry or dry powder was bath-sonicated (JP Selecta Ultrasons system, 40 kHz) in the solvent for 1 h and then centrifuged (Eppendorf 5424 microcentrifuge) at 10000g for 10 min to remove unexfoliated material, the supernatant being the final graphene oxide dispersion. The concentration of the dispersions was determined through UV-vis absorption spectroscopy using a double-beam Heλios R spectrophotometer, from Thermo Spectronic, and following a procedure described elsewhere [24].

To study the performance of different reducing agents toward the deoxygenation of graphene oxide, dispersions of the latter at a concentration of 0.1 mg mL-1 were reacted at 95 °C with the following reductants: hydrazine monohydrate, sodium borohydride, pyrogallol and vitamin C. When the solvent used was water, the pH of the dispersions was adjusted to ~9-10 with 25% ammonia solution (~2 μL per mL of dispersion) to promote the colloidal stability of the graphene oxide sheets through electrostatic repulsion. For comparison purposes, deoxygenation of the sheets was also carried out in the absence of any reducing agent simply by heating the dispersions at 95 °C under basic conditions [26], which were attained via the addition of either ammonia (25% solution) or potassium hydroxide. In all cases, the reactions were accomplished at

different molar concentrations of reducing agent or base in the dispersions, so as to assess its effect on the reduction level of graphene oxide and to establish the optimal amounts required. The progress of reaction as a function of time was monitored through UV-vis absorption spectroscopy. To this end, 0.5 mL aliquots of dispersion were taken from the reaction vial every 15 min and their UV-vis spectra recorded. It is well-known that the position of the absorption peak of graphene oxide dispersions gradually redshifts from a value of 231 nm as reduction proceeds [12], so such position was routinely used as a quick, convenient probe of the reduction degree achieved with the reductants or bases. Further characterization of the reduced products with different techniques confirmed a generally good correlation between the extent of deoxygenation of the graphene oxide sheets and the absorption peak position.

The reduced dispersions were processed into free-standing, paper-like films via filtration through Anodisc membranes (47 mm in diameter and 0.2 μm pore size, from Whatman) and characterized by thermogravimetric analysis (TGA), attenuated total reflection Fourier transform infrared (ATR-FTIR) spectroscopy, X-ray photoelectron spectroscopy (XPS) and also by measurement of their electrical conductivity. TGA was accomplished by means of an SDT Q600 thermobalance (TA Instruments) under Ar gas flow (100 mL min-1) at a heating rate of 10 °C min-1, using Pt crucibles. ATR-FTIR spectra were recorded in a Nicolet 8700 spectrometer (Thermo Scientific) using diamond as ATR crystal. For XPS measurements, a SPECS apparatus working under 10-7 Pa with a monochromatic Al KR X-ray source (100 W) was employed. The surface charging effect observed for the nonconductive, unreduced graphene oxide sample was corrected by the use of an electron flood gun operating at 0.4 eV and 0.10 mA [19]. Surface composition (atomic %) of the samples was determined from their survey spectra by considering the integrated intensities of the main XPS peaks of the elements that were found. The electrical conductivity of the graphene films was determined through measurement of their resistance with a Fluke 45 digital multimeter [27]. To this end, the films were cut into rectangular strips about 6×25 mm2 large and their thickness was estimated via scanning electron microscopy. To evaluate the dispersion state of the sheets in the suspensions after reaction with the different reductants or bases, atomic force microscopy (AFM) was carried out. Samples for AFM were prepared by drop-casting the suspensions onto preheated (~50-60 °C) freshly cleaved highly oriented pyrolytic graphite (HOPG) substrates, which were subsequently

rinsed with Milli-Q water. Imaging was accomplished under ambient conditions (~22-24 °C, RH ~40%) with a Nanoscope IIIa Multimode apparatus (Veeco Instruments) in the tapping mode of operation and using rectangular Si cantilevers with spring constant of ~40 N m-1 and resonance frequency between 250 and 300 kHz.

3. Results and Discussion

Table 1 summarizes the results of the reaction of 0.1 mg mL-1 aqueous graphene oxide dispersions with different molar concentrations of bases (ammonia and potassium hydroxide) and reductants (sodium borohydride, pyrogallol, vitamin C, and hydrazine monohydrate). The progress of reaction was monitored as a function of time by measuring the position of the UV-vis absorption peak of the dispersions. Such a peak is located at 231 nm for the unreduced dispersion but gradually red-shifts as deoxygenation takes place and electronic conjugation is restored [12]. For a given reductant or base at a given molar concentration, the reaction was considered to be completed when the observed red-shifting became arrested. The final position of the absorption peak upon reaction completion and the time required to reach that position are listed in Table 1, together with the acronyms that will be used to refer to the corresponding samples. The performance of hydrazine monohydrate was used as a reference to establish the suitability of the other reducing agents and bases toward deoxygenation of the graphene oxide dispersions. Indeed, the reported optimal ratio for reduction with such reagent (2.0 mM for 0.1 mg mL-1 dispersions) [12] was taken as a starting point in the case of the other three reductants. Reduction with the two bases was observed to be much less effective, so higher molar concentrations were typically employed for ammonia and potassium hydroxide.

To a first approximation, the overall efficiency of a given reductant or base was estimated from the maximum red-shift that can be attained when its molar concentration is increased (Table 1). For example, in the case of pyrogallol the absorption peak can be red-shifted up to a value of 266 nm regardless of the amount of reagent used above a certain level (samples P2-P4). By contrast, a value of 268 nm is reached with hydrazine monohydrate, suggesting that this reductant is somewhat more efficient than pyrogallol. Based on such assessment, the performance of the reductants and bases can be classified into three groups. The first includes the two bases (ammonia and potassium hydroxide),

which would provide a relatively limited reduction degree (absorption peaks located slightly below 260 nm).

Table 1. UV-vis absorption peak Position of 0.1 mg mL^{-1} aqueous graphene oxide suspensions after completion of deoxygenation with different concentrations of reductants (sodium borohydride, pyrogallol, vitamin C, and hydrazine) and bases (ammonia and potassium hydroxide), with indication of the sample acronyms used throughout the text.

reductant or base	sample acronym	concentration of reductant or base (mM)	absorption peak position (nm)	time to reaction completion (min)
none (*unreduced graphene oxide*)	GO	-	231 ± 2	-
Ammonia	N1	26	257 ± 2	240
	N2	51	260 ± 2	240
	N3	103	256 ± 2	240
	N4	206	257 ± 2	240
Potassium hidroxyde	K1	0.8	252 ± 2	240
	K2	4	258 ± 2	180
	K3	20	258 ± 2	120
	K4	100	251 ± 2	60
Sodium borohydride	B1	0.5	251 ± 2	180
	B2	2	246 ± 2	45
	B3	8	253 ± 2	45
	B4	10	263 ± 2	15
	B5	31	266 ± 2	15
Pyrogallol	P1	0.3	262 ± 2	120
	P2	0.5	266 ± 2	60
	P3	1	266 ± 2	60
	P4	2	266 ± 2	60
Vitamin C	V1	0.3	263 ± 2	240
	V2	0.5	268 ± 2	180

reductant or base	sample acronym	concentration of reductant or base (mM)	absorption peak position (nm)	time to reaction completion (min)
Vitamin C	V3	1	268 ± 2	30
	V4	2	268 ± 2	15
Hidrazine monohydrate	H1	1	268 ± 2	15
	H2	2	268 ± 2	15
	H3	10	268 ± 2	15
	H4	21	268 ± 2	15

The second group is formed by sodium borohydride and pyrogallol, with absorption peaks at 263-266 nm. The third group is constituted by the most efficient reductants (hydrazine monohydrate and vitamin C), with absorbance peaking at 268 nm upon reaction completion. We note that all the reduced suspensions described in Table 1 displayed long-term stability, i.e. they were stable for at least several weeks, except sample K4, which precipitated during reduction, and samples B4 and B5, which precipitated within a few days (B4) and several minutes (B5) after reduction.

TGA, ATR-FTIR spectroscopy and XPS analysis of the reduced suspensions processed into paper-like films provided further evidence of the basic differences in the extent of reduction that can be achieved with the reductants and bases. Figure 1 shows the thermogravimetric (TG) and differential thermogravimetric (DTG) plots of unreduced graphene oxide (a), as well as those of several characteristic reduced samples: N1 (b), B3 (c), P3 (d), V4 (e), and H4 (f). Consistent with previous reports [19, 28, 29], the main mass loss for unreduced graphene oxide (~30%, Figure 1a) takes place around 200 °C, which is attributed to the decomposition of the most labile oxygen functionalities present in the material. The slow, steady mass loss (~20%) observed in the whole temperature range above 300 °C can be ascribed to desorption of more stable oxygen functional groups. Removal of adsorbed water accounts for the mass loss (~15%) measured below 100 °C. Hydrazine appears to be rather efficient in removing the labile functionalities, as the abrupt mass loss at about 200 °C characteristic of unreduced graphene oxide is no longer present after reaction with this reductant (e.g., sample H4, Figure 1f). By contrast, such functionalities can only be partially eliminated when reduction is carried out just by heating the dispersions under alkaline conditions.

This is exemplified in Figure 1b for sample N1, which exhibits a mass loss of ~15% around 200 °C. Reduction with sodium borohydride and pyrogallol lowers the mass loss at this temperature (e.g., ~5-10% for samples B3 and P3 in Figure 1, panels c and d, respectively), but the rate of mass loss is still significantly larger than that measured at higher temperatures (see DTG plots in Figure 1, panels c and d). As noticed in Figure 1e, only vitamin C matches the efficiency of hydrazine monohydrate in the elimination of the labile functional groups. However, in agreement with previous reports [28], there is still a significant mass loss for all the reduced samples in the temperature range above 300 °C (~10-15%), suggesting that even the apparently strongest reductants (hydrazine and vitamin C) cannot remove the most stable functionalities [28].
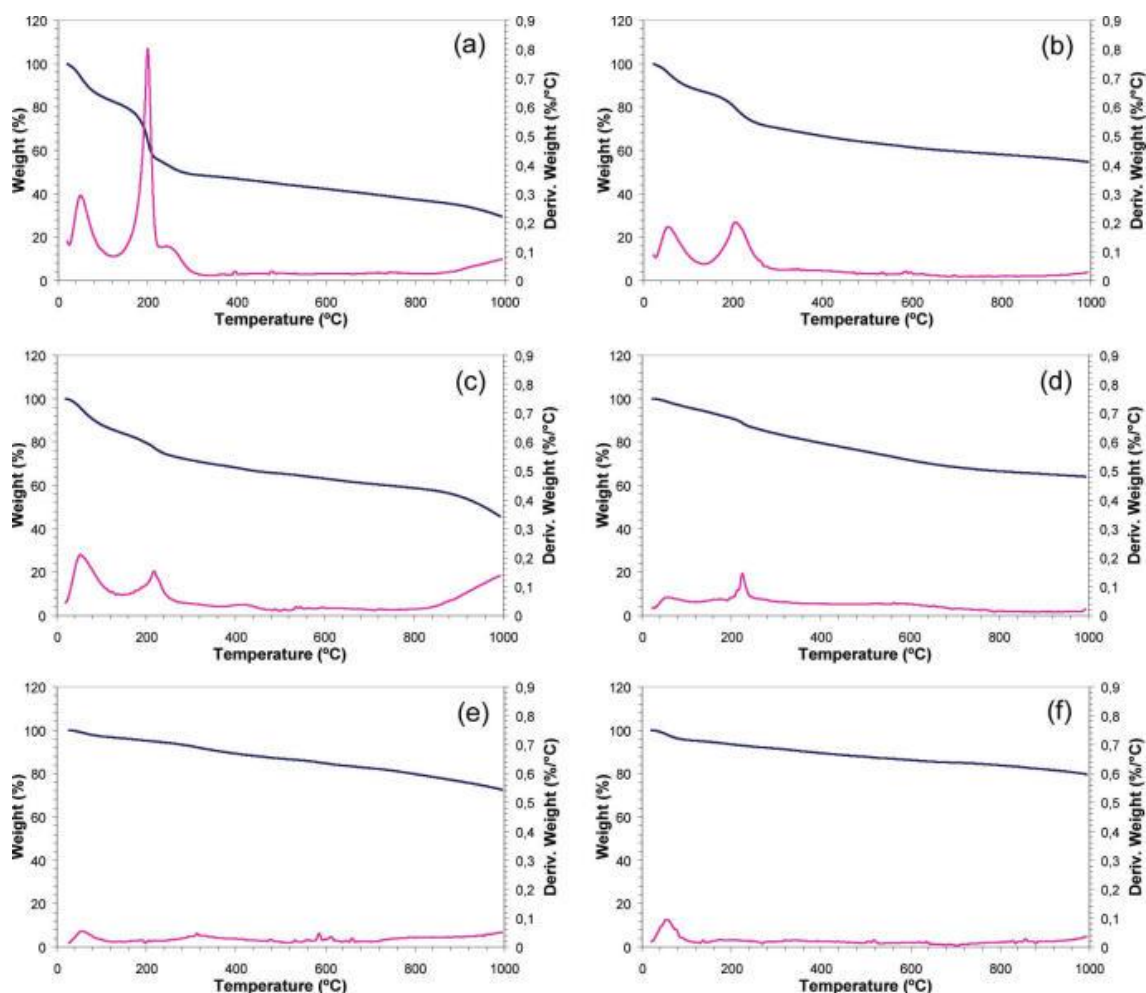
Figure 1. TG (blue) and DTG (red) plots of unreduced graphene oxide (a) and deoxygenated samples N1 (b), B3 (c), P3 (d), V4 (e), and H4 (f). The acronyms of the deoxygenated samples are defined in Table 1.

Representative ATR-FTIR spectra of the different reduced samples are shown in Figure 2. For unreduced graphene oxide (Figure 2a), the following features are observed: a broad, intense band at 3000-3500 cm^{-1} (O-H stretching vibrations) and narrower bands at about 1720 cm^{-1} (C=O stretching vibrations from carbonyl and carboxyl groups), 1620 cm^{-1} (C=C stretching, skeletal vibrations from unoxidized graphitic domains), 1400 cm^{-1} (O-H bending vibrations from hydroxyl groups), 1300-1350 cm^{-1} (C-OH stretching vibrations), 1220 cm^{-1} (breathing vibrations from epoxy groups), and 980 cm^{-1} (attributed to vibrations from epoxy, ether or peroxide groups) [20, 30-34]. For all the reduced materials (Figure 2b-f), the intensities of the bands associated to oxygen functional groups strongly decrease in relation to those of unreduced graphene oxide. However, the decrease is most significant when reduction is carried out with hydrazine and vitamin C (Figure 2, lines e and f) and relatively limited when performed only under alkaline conditions without any reducing agent (e.g., Figure 2b), reduction with sodium borohydride and pyrogallol lying somewhere in between. In particular, for sample N1 (Figure 2b) the intensity of the bands assigned to epoxy groups (~1220 and 980 cm^{-1}) is not very different to that observed for unreduced graphene oxide (Figure 2a). By contrast, the decrease appears to be much more significant for bands related to hydroxyl groups (3000-3500 and ~1350 cm^{-1}), which suggests that reduction under alkaline conditions without reductant removes preferentially hydroxyl groups over epoxides. In the case of reduction with hydrazine and vitamin C, we observe a much more exhaustive decrease of both the hydroxyl and epoxy regions of the spectra. Nevertheless, the elimination of these bands is not complete, as becomes evident when comparing the spectra of samples V4 and H4 (Figure 2e and f, respectively) with that of pristine graphite (Figure 2g). In particular, the persistence of the band at about 1300-1350 cm^{-1} would seem to imply that a certain fraction of hydroxyl functionalities remain even in the most reduced dispersions.
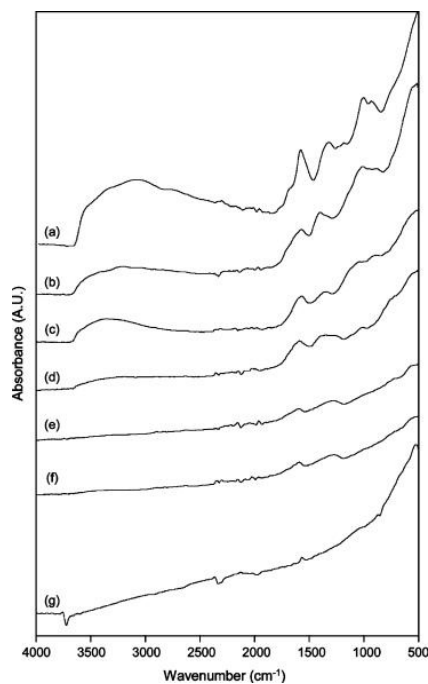
Figure 2. ATR-FTIR spectra of unreduced graphene oxide (a), deoxygenated samples N1 (b), B4 (c), P3 (d), V4 (e), and H4 (f), and pristine graphite (g). The acronyms for the deoxygenated samples are defined in Table 1.

Figure 3 shows the high resolution C1s X-ray photoelectron spectra of unreduced graphene oxide (a), several representative reduced samples (b-f) and the starting pristine graphite (g). As previously reported [19], the C1s band of the unreduced material is characterized by the presence of two maxima separated by ~2 eV. Peak fitting of this band yields three components, located at 284.6 (fwhm = 1.4 eV), 286.6 (fwhm = 1.2 eV), and 287.9 eV (fwhm = 2.0 eV), as illustrated in Figure 3a. The component at 284.6 eV is assigned to carbons in unoxidized, aromatic sp^2 structures, whereas the one at 286.6 eV can be attributed to carbons in hydroxyl and epoxy groups (C-O bonds) and also possibly to C-C bonds in defected structures. The defect C-C component would be located at ~285.5 eV, but for unreduced graphene oxide (Figure 3a) it was not possible to clearly discriminate it from the C-O component at 286.6 eV. The 287.9 eV component can be ascribed to carbons in C=O structures, i.e., carbonyl groups.
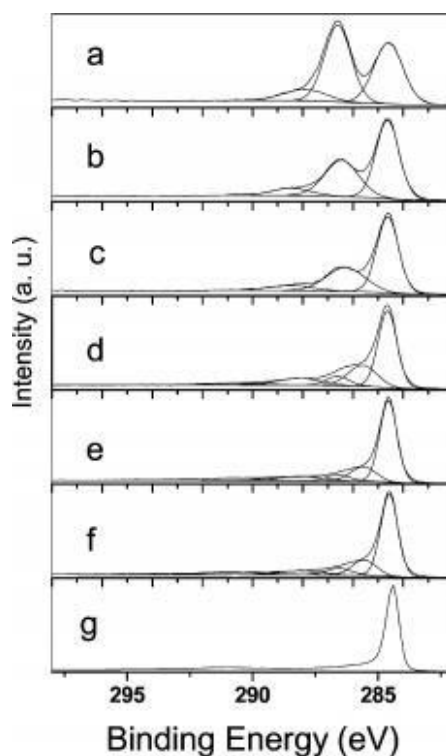
Figure 3. High resolution C1s X-ray photoelectron spectra for unreduced graphene oxide (a), deoxygenated samples N1 (b), B4 (c), P3 (d), V4 (e), and H4 (f), and pristine graphite (g). The acronyms for the deoxygenated samples are defined in Table 1

Following all reductions, a narrowing of the graphitic component at 284.6 eV can be noticed (fwhm values of 0.8-1.1 eV, compared to 1.4 eV for unreduced graphene oxide), which is indicative of the development of a more homogeneous chemical environment and/or ordered structure. However, the most significant change upon reduction is the decrease in the relative contribution of the higher binding energy components of the C1s envelope, reflecting a smaller proportion of oxidized carbons in the samples. In agreement with the TGA and UV-vis and ATR-FTIR spectroscopy results, the relative decline of the higher binding energy components is much larger for dispersions reduced with vitamin C and hydrazine (Figure 3, lines e and f, respectively), intermediate for dispersions reduced with sodium borohydride and pyrogallol (Figure 3, lines c and d, respectively) and less apparent when deoxygenation is carried out just by heating under alkaline conditions without reductant, i.e. in the case of ammonia (Figure 3b) and potassium hydroxide (spectra not shown, but very similar to that of Figure 3b). For those samples that could be sufficiently reduced, i.e. for samples reacted with pyrogallol, vitamin C and hydrazine (Figure 3d, e and f, respectively), peak fitting of

the C1s band allowed discrimination of the defect C-C component (285.5 eV) from the C-O component (286.6 eV). By contrast, such discrimination was not possible with the comparatively limited reduction provided by ammonia, potassium hydroxide and sodium borohydride (e.g., Figure 3, lines b and c), yielding the three same components as those obtained for unreduced graphene oxide (Figure 3a). For the highly reduced samples (vitamin C and hydrazine), the shape of the C1s envelope does not change appreciably with the amount of reductant used once the position of the UV-vis absorption peak reaches the value of 268 nm (Table 1), confirming that reduction was completed. However, as can be noticed by comparing the spectra of these samples (Figure 3, lines e and f) with that of the starting pristine graphite (Figure 3g), the highly reduced materials still contain a certain amount of oxygen functionalities (higher binding energy components) that apparently cannot be removed under the used reaction conditions. Such result is consistent with that obtained by TGA and ATR-FTIR spectroscopy, and also with previous reports on the reduction of graphene oxide with hydrazine [12], supporting the idea that chemical reduction under the present conditions has an intrinsic limit, which is not well understood at present. The presence of residual oxygen even on the most reduced materials is also apparent from the O/C atomic ratios derived from the XPS data: 0.43 for unreduced graphene oxide, ~0.08 for samples reduced with vitamin C and hydrazine, ~0.18 for reduction with pyrogallol, and ~0.20-0.30 for reduction with ammonia, potassium hydroxide and sodium borohydride.

The electrical conductivity is considered a highly sensitive indicator of the extent to which electronic conjugation is restored after deoxygenation of graphene oxide. Electrical conductivity was measured on free-standing paper-like films prepared by vacuum filtration and air-drying of the different reduced suspensions. The data obtained for several representative samples are presented in Table 2. Consistent with the results discussed above, restoration of the π-conjugated structure is most effective using hydrazine and vitamin C (conductivity values between 2690 and 9960 S m^{-1}), intermediate for reduction with pyrogallol (488 S m^{-1}), and relatively inefficient with ammonia, potassium hydroxide and sodium borohydride (0.02-1.55 S m^{-1}). Up to now, only hydrazine reduction could provide conductivity values as large as 5000-10 000 S m^{-1} for as-prepared films of reduced graphene oxide (the conductivity can still be improved to some degree, but only after an additional thermal annealing step of the

films) [35]. The present results show that, as opposed to other reductants, vitamin C can rival hydrazine in this regard.

Table 2. Electrical Conductivities of Free-Standing Paper-Like Films Prepared from Different Deoxygenated Samples*

sample acronym	electrical conductivity (S/m)
N1	0.05
N4	0.32
K1	0.02
K3	0.19
B3	1.55
B4	0.26
P3	488
A2	2690
A4	7700
H1	4160
H4	9960

* The sample acronyms are defined in Table 1.

In addition to constituting a highly efficient reductant for graphene oxide, vitamin C has the advantage of its nontoxicity. In marked contrast to hydrazine, there are virtually no risks to the human health or to the environment associated with the use of this chemical, which is indeed an essential component of a healthy diet in humans [23]. Besides, vitamin C-reduced graphene oxide suspensions can be prepared not only in water but also in some common organic solvents, such as DMF and NMP, which should facilitate the further manipulation and processing of this material for practical applications. The aqueous and organic suspensions display long-term stability, showing no signs of precipitation at least for several weeks (Figure 4), and are constituted by individual, single-layer sheets, just as in the case of unreduced and hydrazine-reduced graphene oxide suspensions. As evidenced by the AFM images of Figure 5 for unreduced and chemically reduced aqueous suspensions, the large majority of the dispersed objects have an apparent thickness of ~1 nm, which are attributed to single-layer sheets [5, 12, 19, 24, 28]. Only less than 5% of the dispersed objects were ascribed

to thicker sheets (mainly two and three layers). Similar conclusions were obtained for the organic suspensions. The combination of all the above-mentioned qualities makes vitamin C reduction a strong candidate to replace hydrazine in the largescale preparation of solution-processable graphene from graphite oxide. Other reductants, such as pyrogallol or the relatively common sodium borohydride, lag behind vitamin C in reduction efficiency, and also present some toxicity. Heating the graphene oxide suspensions under alkaline conditions would in principle be a very attractive route toward solution-processable graphene [26], but the results of this work suggest that deoxygenation in this case is rather poor, which seriously affects the properties of the reduced products (e.g., electrical conductivity).
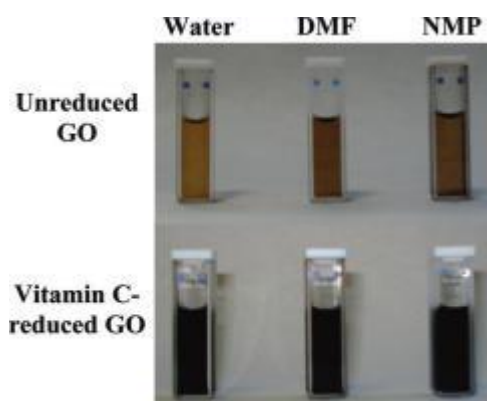
Figure 4. Digital pictures of unreduced graphene oxide suspensions in water, DMF, and NMP (top), together with their deoxygenated counterparts 4 weeks after reduction with vitamin C (bottom).
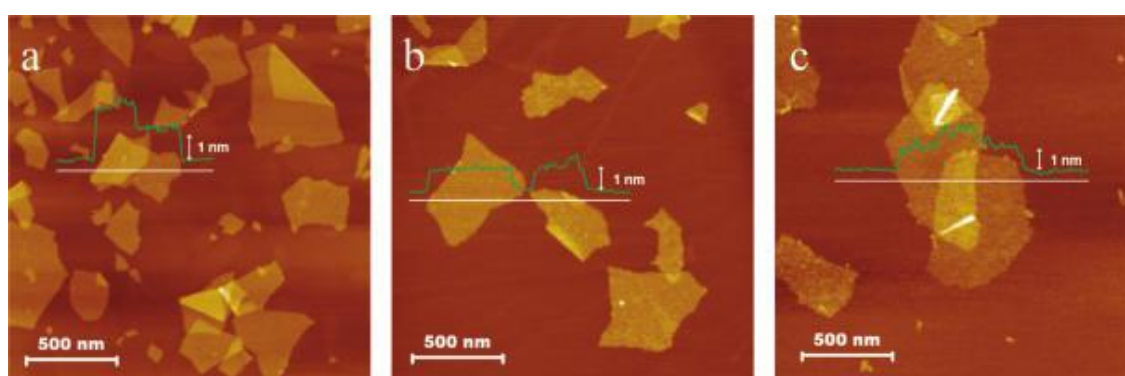
Figure 5. Representative AFM images of unreduced (a), hydrazine-reduced (b), and vitamin C-reduced (c) graphene oxide sheets deposited onto HOPG substrates from their corresponding suspensions. Lines profiles are superimposed onto each image, showing that single-layer sheets are obtained in all cases.

During the last year, several green approaches to the deoxygenation of graphene oxide suspensions that circumvent the use of hydrazine have been documented in the literature. These include electrochemical, hydrothermal and microwave assisted solvothermal reduction methods [36-38]. The performance of such methods in relation to hydrazine reduction has not been thoroughly investigated, but a general comparison of some relevant features of the resulting graphenes can be made based on the published data. Table S1 in the Supporting Information compares such parameters as UV-vis absorption peak position, O/C atomic ratio, stability in solvents and electrical conductivity of graphenes prepared through different green approaches. Weighing up the available data, vitamin C reduction appears as one of the most attractive routes toward deoxygenation of graphene oxide suspensions.

Finally, as is the case with most of the deoxygenation approaches of graphene oxide documented so far, the reduction mechanism of this material by vitamin C and the reason why complete reduction does not appear to be possible under the employed conditions are currently unclear. Reduction probably involves hydride transfer from the 5-membered ring of the vitamin C molecule to either the epoxy or hydroxyl groups of graphene oxide, yielding water molecules [23]. This point is currently the focus of additional experimental and theoretical modeling work in our group.

4. Conclusions

A comparison of the deoxygenation efficiency of graphene oxide suspensions by different reductants, as well as by simply heating the suspensions under alkaline conditions, has been made, revealing that only vitamin C can compete with the widely employed, but highly toxic hydrazine in terms of reducing ability. Using vitamin C, stable suspensions of highly reduced graphene oxide can be prepared not only in water but also in some common organic solvents, such as DMF and NMP. These findings are significant, because an innocuous and effective reagent that can replace hydrazine in the large-scale preparation of solution-processable graphene from graphite oxide has now been identified. Another potential advantage of using vitamin C is that such reductant is only composed of carbon, oxygen, and hydrogen, thus minimizing the risk of introducing heteroatoms in the reduced products that were not present beforehand.

References and Notes

[1] Geim AK, Novoselov KS. The rise of graphene. Nat. Mater. 6 (2007), 183-191.

[2] Allen MJ, Tung VC, Kaner RB. Honeycomb carbon: a review of graphene. Chem. Rev. 110 (2009), 132-145.

[3] Rao CNR, Sood AK, Subrahmanyam KS, Govindaraj A. Graphene: the new two-dimensional nanomaterial. Angew. Chem. Int. Edit. 48 (2009), 7752-7777.

[4] Novoselov KS, Geim AK, Morozov SV, Jiang D, Zhang Y, Dubonos SV, Grigorieva IV, Firsov AA. Electric field effect in atomically thin carbon films. Science 306 (2004), 666-669.

[5] Stankovich S, Dikin DA, Dommett GHB, Kohlhaas KM, Zimney EJ, Stach EA, Piner RD, Nguyen ST, Ruoff RS. Graphene-based composite materials. Nature 442 (2006), 282-286.

[6] Ramanathan T, Abdala AA, Stankovich S, Dikin DA, Herrera Alonso M, Piner RD, Adamson DH, Schniepp HC, Chen X, Ruoff RS, Nguyen ST, Aksay IA, Prud'Homme RK, Brinson LC. Functionalized graphene sheets for polymer nanocomposites. Nat. Nanotechnol. 3 (2008), 327-331.

[7] Schedin F, Geim AK, Morozov SV, Hill EW, Blake P, Katsnelson MI, Novoselov KS. Detection of individual gas molecules adsorbed on graphene. Nat. Mater. 6 (2007), 652-655.

[8] Robinson JT, Perkins FK, Snow ES, Wei Z, Sheehan PE. Reduced graphene oxide molecular sensors. Nano Lett. 8 (2008), 3137-3140.

[9] Wang X, Zhi L, Mullen K. Transparent, conductive graphene electrodes for dye-sensitized solar cells. Nano Lett. 8 (2007), 323-327.

[10] Stoller MD, Park S, Zhu Y, An J, Ruoff RS. Graphene-based ultracapacitors. Nano Lett. 8 (2008), 3498-3502.

[11] Liu Z, Robinson JT, Sun X, Dai H. PEGylated nanographene oxide for delivery of water-insoluble cancer drugs. J. Am. Chem. Soc. 130 (2008), 10876-10877.

[12] Li D, Muller MB, Gilje S, Kaner RB, Wallace GG. Processable aqueous dispersions of graphene nanosheets. Nat. Nano. 3 (2008), 101-105.

[13] Park S, Ruoff RS. Chemical methods for the production of graphenes. Nat. Nano. 4 (2009), 217-224.

[14] Berger C, Song Z, Li X, Wu X, Brown N, Naud C, Mayou D, Li T, Hass J, Marchenkov AN, Conrad EH, First PN, de Heer WA. Electronic confinement and coherence in patterned epitaxial graphene. Science 312 (2006), 1191-1196.

[15] Emtsev KV, Bostwick A, Horn K, Jobst J, Kellogg GL, Ley L, McChesney JL, Ohta T, Reshanov SA, Röhrl J, Rotenberg E, Schmid AK, Waldmann D, Weber HB, Seyller T. Towards wafer-size graphene layers by atmospheric pressure graphitization of silicon carbide. Nat Mater. 8 (2009), 203-207.

[16] Kim KS, Zhao Y, Jang H, Lee SY, Kim JM, Kim KS, Ahn J-H, Kim P, Choi J-Y,

Hong BH. Large-scale pattern growth of graphene films for stretchable transparent electrodes. Nature 457 (2009), 706-710.

[17] Li X, Cai W, An J, Kim S, Nah J, Yang D, Piner R, Velamakanni A, Jung I, Tutuc E, Banerjee SK, Colombo L, Ruoff RS. Large-area synthesis of high-quality and uniform graphene films on copper foils. Science 324 (2009), 1312-1314.

[18] Geim AK. Graphene: status and prospects. Science 324 (2009), 1530-1534.

[19] Paredes JI, Villar-Rodil S, Martínez-Alonso A, Tascón JMD. Graphene oxide dispersions in organic solvents. Langmuir 24 (2008), 10560-10564.

[20] Park S, An J, Jung I, Piner RD, An SJ, Li X, Velamakanni A, Ruoff RS. Colloidal suspensions of highly reduced graphene oxide in a wide variety of organic solvents. Nano Lett. 92(2009), 1593-1597.

[21] Villar-Rodil S, Paredes JI, Martinez-Alonso A, Tascon JMD. Preparation of graphene dispersions and graphene-polymer composites in organic media. J. Mater. Chem. 19 (2009), 3591-3593.

[22] Schmidt EW. Hydrazine and its derivatives. New York. 2001.

[23] Davies MB, Austin J, Partridge DA. Vitamin C: chemistry and biochemistry. Cambridge, U.K. 1991.

[24] Paredes JI, Villar-Rodil S, Solís-Fernández P, Martínez-Alonso A, Tascón JMD. Atomic force and scanning tunneling microscopy imaging of graphene nanosheets derived from graphite oxide. Langmuir 25 (2009), 5957-5968.

[25] Hummers WS, Offeman RE. Preparation of graphitic oxide. J. Am. Chem. Soc. 80 (1958), 1339.

[26] Fan X, Peng W, Li Y, Li X, Wang S, Zhang G, Zhang F. Deoxygenation of exfoliated graphite oxide under alkaline conditions: a green route to graphene preparation. Adv. Mater. 20 (2008), 4490-4493.

[27] Choucair M, Thordarson P, Stride JA. Gram-scale production of graphene based on solvothermal synthesis and sonication. Nat. Nanotech. 4 (2009), 30-33.

[28] Stankovich S, Dikin DA, Piner RD, Kohlhaas KA, Kleinhammes A, Jia Y, Wu Y, Nguyen ST, Ruoff RS. Synthesis of graphene-based nanosheets via chemical reduction of exfoliated graphite oxide. Carbon 45 (2007), 1558-1565.

[29] Becerril HA, Mao J, Liu Z, Stoltenberg RM, Bao Z, Chen Y. Evaluation of solution-processed reduced graphene oxide films as transparent conductors. ACS Nano 2 (2008), 463-470.

[30] Mermoux M, Chabre Y, Rousseau A. FTIR and 13C NMR study of graphite oxide. Carbon 29 (1991), 469-474.

[31] Stankovich S, Piner RD, Nguyen ST, Ruoff RS. Synthesis and exfoliation of isocyanate-treated graphene oxide nanoplatelets. Carbon 44 (2006), 3342-3347.

[32] Xu Y, Bai H, Lu G, Li C, Shi G. Flexible graphene films via the filtration of water-soluble noncovalent functionalized graphene sheets. J. Am. Chem. Soc. 130 (2008), 5856-5857.

[33] Chattopadhyay J, Mukherjee A, Hamilton CE, Kang J, Chakraborty S, Guo W, Kelly KF, Barron AR, Billups W E. Graphite epoxide. J. Am. Chem. Soc. 130 (2008), 5414-5415.

[34] Shimanouchi T. Tables of molecular vibrational frequencies: consolidated volume II: american chemical society and the american institute of physics, for the national bureau of standards. 1977.

[35] Chen H, Müller MB, Gilmore KJ, Wallace GG, Li D. Mechanically strong,

electrically conductive, and biocompatible graphene paper. Adv. Mater. 20 (2008), 3557-3561.

[36] Guo H-L, Wang X-F, Qian Q-Y, Wang F-B, Xia X-H. A green approach to the synthesis of graphene nanosheets. ACS Nano 3 (2009), 2653-2659.

[37] Zhou Y, Bao Q, Zhong Y, Loh K. Hydrothermal dehydration for the "green" reduction of exfoliated graphene oxide to graphene and demonstration of tunable optical limiting properties. Chem. Mater. 21 (2009), 2950-2956.

[38] Murugan AV, Muraliganth T, Manthiram A. Rapid, facile microwave-solvothermal synthesis of graphene nanosheets and their polyaniline nanocomposites for energy strorage. Chem. Mater. 21 (2009), 5004-5006.

Supporting Information for

Vitamin C is an ideal substitute for hydrazine in the reduction of graphene oxide suspensions

(The Journal of Physical Chemistry C 114 (2010), 6426-6432)

M. J. Fernández-Merino, L. Guardia, J. I. Paredes, S. Villar-Rodil, P. Solís-Fernández, A. Martínez-Alonso, and J. M. D. Tascón

Instituto Nacional del Carbón, CSIC, Apartado 73, 33080 Oviedo, Spain

Table S1. Comparison of several characteristics of graphene sheets produced by deoxygenation of graphene oxide suspensions through different green approaches and hydrazine.

Method	UV-vis peak	O/C ratio	Stability in solvents	Electrical conductivity	Ref.
Electrochemical reduction	Unknown	Unknown	Reduced material obtained as a precipitate in water	3500 S/m	[1]
Hydrothermal dehydration	254 nm	0.15 (0.36)	Stable in water	Unkonwn	[2]
MW-assisted solvothermal reduction	Unknown	0.09 (0.43)	Stable in tetraethylene glycol and water. Precipitates in DMF, ethanol, 1-butanol	Unknown	[3]
Ascorbic acid reduction	268 nm	0.08 (0.43)	Stable in water, DMF, NMP	Up to 7700 S/m	Present work
Hydrazine reduction	268 nm	0.08 (0.43)	Stable in water, DMF, NMP	Up to 9960 S/m	Present work

[1] Guo H-L, Wang X-F, Qian Q-Y, Wang F-B, Xia X-H. A green approach to the synthesis of graphene nanosheets. ACS Nano 3 (2009), 2653-2659.

[2] Zhou Y, Bao Q, Zhong Y, Loh K. Hydrothermal dehydration for the "green" reduction of exfoliated graphene oxide to graphene and demonstration of tunable optical limiting properties. Chem. Mater. 21 (2009), 2950-2956.

[3] Murugan AV, Muraliganth T, Manthiram A. Rapid, facile microwave-solvothermal synthesis of graphene nanosheets and their polyaniline nanocomposites for energy strorage. Chem. Mater. 21 (2009), 5004-5006.

Identifying efficient natural bioreductants for the preparation of graphene and graphene-metal nanoparticle hybrids with enhanced catalytic activity from graphite oxide

M. J. Fernández-Merino, S. Villar-Rodil, J. I. Paredes, P. Solís-Fernández, L Guardia, R. García, A. Martínez-Alonso, J. M. D. Tascón

Instituto Nacional del Carbón, CSIC, Apartado 73, 33080 Oviedo, Spain

Abstract

The implementation of green approaches towards the preparation of graphene and graphene-based materials with enhanced functionality from graphite oxide has been relatively little explored. Particularly, the use of bioreductants and the testing of their relative efficacies is an incipient area of research. Here, a pool of 20 environmentally friendly, natural antioxidants has been tested for their ability to reduce graphene oxide. These antioxidants were mostly vitamins, amino acids and organic acids. By establishing a protocol to systematically compare and optimize their performance, several new efficient bioreductants of graphene oxide have been identified, namely, pyridoxine and pyridoxamine (vitamin B_6), riboflavin (vitamin B_2), as well as the amino acids arginine, histidine and tryptophan. These biomolecules were used to prepare reduced graphene oxide-silver nanoparticle hybrids that displayed colloidal stability in water in the absence of additional dispersants. Particularly, hybrids prepared with pyridoxamine exhibited a combination of long-term colloidal stability and exceptionally high catalytic activity among silver nanoparticle-based catalysts in the reduction of p-nitrophenol with NaBH4. Thus, in addition to expanding substantially the number of green reductants available for graphene oxide reduction, the present results underline the idea that proper selection of bioreductant can be relevant to achieve graphene-based materials with improved performance.

1. Introduction

Since its first isolation in 2004, graphene has aroused a great deal of interest in the scientific community, and particularly in the materials research realm, given that its exceptional physical properties promise outstanding performance in a large number of

potential applications [1-3]. However, an obvious prerequisite for the practical use of graphene is the availability of suitable methods that allow its mass production and processing. In this regard, one of the most promising and hitherto widely investigated approaches relies on the use of graphite oxide, which typically comprises the exfoliation of this strongly oxygenated derivative of graphite in aqueous or organic medium followed by chemical reduction of the resulting single-layer sheets (graphene oxide sheets) [4-6]. Hydrazine and some of its derivatives, and later on other reagents commonly used in organic chemistry for the reduction of oxygen-containing groups (e.g., LiAlH4), were found to be highly effective reductants for graphene oxide, and are still broadly employed today for this purpose [4-10]. Nevertheless, the high toxicity and environmental hazard of these reagents have recently driven a move towards the exploration of safer alternatives, to better comply with the principles of green chemistry and sustainability. Thus, solvothermal, electrochemical, catalytic [11] and photocatalytic [12-17] methods as well as the use of environmentally friendly reductants have been proposed during the last two years for the reduction of graphene oxide [18].

Vitamin C was the first green reducing agent that was reported to be effective in the deoxygenation of graphene oxide, affording dispersions of reduced graphene oxide (RGO) sheets in water and some organic solvents whose extent of reduction and colloidal stability matched those of dispersions obtained with hydrazine [19-22]. Such discovery suggested that other innocuous and abundant biomolecules could also act as efficient reductants in the preparation of RGO. Studies carried out subsequently confirmed indeed that certain saccharides (glucose, fructose and sucrose) and polysaccharides (dextran) [23-25], polyphenols (e.g., epigallocatechin gallate and related compounds present in tea solutions, or tannic acid) [26-28] and natural phenolic acids [29, 30], plant extracts [31], a catecholamine polymer (poly(norepinephrine)) [32], the hormone melatonin [33, 34], a tripeptide (L-gluthatione) [35], a protein (bovine serum albumin (BSA)) [36], and bacteria [37, 38] could reduce graphene oxide.

However, the number of biomolecules available at present for the reduction of graphene oxide is still relatively limited, and having a wider range of effective bioreductants to call upon for specific purposes would be highly desirable. There is a large number of natural antioxidants, including amino acids, vitamins and organic acids whose reducing ability towards graphene oxide and potential role in enhancing the functionality of the resulting material is unknown and unexplored. It has been shown in

some cases that the use of selected biomolecules lends added value to RGO other than just acting as reductants of the starting graphene oxide sheets. For example, dextran and tea polyphenols have been reported to increase the colloidal stability in water and/or biocompatibility of RGO [24, 26]. However, other potential benefits of using reducing biomolecules in the preparation of graphene-based materials that could be relevant for applications have been, to the best of our knowledge, far less explored [32].

In the present work, (i) we identify a number of small biomolecules (amino acids and vitamins) as efficient bioreductants of grapheme oxide dispersions, and (ii) significantly, we demonstrate that proper selection of specific bioreductants affords graphene-based materials with enhanced performance towards relevant uses. First of all, a set of 20 biomolecules was investigated for their potential use in the reduction of aqueous graphene oxide dispersions. These biomolecules were mainly chosen on the basis of their known reducing and/or antioxidant activity in the biochemical context, although their reducing power towards graphene oxide was unknown. Several of the tested biomolecules were shown to be efficient reductants of graphene oxide. Then, the previously identified bioreductants were used for the preparation of RGO-silver nanoparticle (Ag NP) hybrids. Furthermore, the use of selected biomolecules was shown to afford hybrids that exhibited an attractive combination of long-term colloidal stability in water and exceptionally high catalytic activity, as gauged from the study of a model reaction (reduction of *p*-nitrophenol to *p*-aminophenol), making them ideal candidates for practical uses.

2. Experimental section

Unless otherwise specified, all the chemicals used were supplied by Sigma-Aldrich® Chemistry.

2.1. Preparation of graphene oxide

Graphite oxide was obtained as thick slurry from natural graphite powder (Fluka 50870) by the Hummers method as described elsewhere [39]. Aqueous graphene oxide dispersions were prepared from the slurry through bath sonication (JP Selecta Ultrasons System, 40 KHz) for 4 h followed by centrifugation (Eppendorf 5424 microcentrifuge) at 10,000 *g* for 10 min to sediment the non-exfoliated graphite oxide particles. The supernatant, a stable dispersion mostly made up of individual, single-layer graphene oxide sheets, was collected and kept for further use. The concentration of such

dispersion was determined by UV-vis absorption spectroscopy as described elsewhere [39].

2.2. Reduction of aqueous graphene oxide dispersions with biomolecules

To investigate and compare the performance of different biomolecules in the reduction of graphene oxide, aqueous dispersions of the latter at a concentration of 0.1 mg mL^{-1} and pH of ~10 (adjusted by the addition of 25% ammonia solution) were mixed with varying amounts of the biomolecules and heated to 95 ºC for different periods of time. The following biomolecules were tested (see Table 1 for their chemical structures): pyridoxine and pyridoxamine dihydrochloride (different forms of vitamin B$_6$), (-)-riboflavin (vitamin B$_2$) and riboflavin 5'-monophosphate salt hydrate (a more soluble form of the latter), citric acid, fumaric acid, L-malic acid, and L-tartaric acid, L-arginine, L-aspargine, L-carnosine, glycine, L-glutamic acid, L-gluthatione, L-histidine, L-methionine, L-phenylalanine, L-tryptophan, L-tyrosine, and α-D-glucose. The extent of reduction achieved with a given biomolecule, concentration of biomolecule and heating time was initially assessed through UV-vis absorption spectroscopy, and more specifically by measuring the position of the absorption peak corresponding to $\pi \rightarrow \pi^*$ transitions of C=C bonds (λ_{max}) in graphene oxide [22]. Some of the tested biomolecules (and/or their oxidized counterparts) exhibited absorption features in the UV-vis spectrum that prevented an accurate determination of λ_{max} for the reduced graphene oxide sheets (typically located between ~231 and 268 nm). In these cases, the reduced dispersions were dialyzed (Spectra/Por$^®$ Float-A-Lyzer$^®$ G2 dialysis membrane made of cellulose ester with 10^6 Da molecular weight cut-off, from Spectrum Laboratories) for the time required to remove the interfering species.

Table 1. Chemical structure of the biomolecules used in the study together with their names.

Reagent			
name	**structure**	**name**	**structure**
pyridoxine		pyridoxamine dihydrochloride	
(-)-riboflavin		riboflavin 5'-monophosphate sodium salt hydrate	
citric acid		fumaric acid	
L-malic acid		L-tartaric acid	
L-arginine		L-aspargine	
L-carnosine		glycine	
L-glutamic acid		L-glutathione	
L-histidine		L-methionine	
L-phenylalanine		L-tryptophan	
L-tyrosine		α-D-glucose	

2.3. Preparation of RGO-Ag NP hybrids

The biomolecules that were found to be successful in the reduction of graphene oxide were also tested for simultaneous reduction of graphene oxide and a silver salt ($AgNO_3$) with the aim of preparing RGO-Ag NP hybrids. Aqueous solutions containing 0.1 mg mL^{-1} graphene oxide, 0.34 mM $AgNO_3$ and varying concentrations of bioreductant (from 0.125 to 8 mM, depending on the particular biomolecule) were heated at 95 ºC for 8 hours. To eliminate possible residual unreacted silver salt and bioreductant (and/or its reacted, oxidized form), the obtained hybrids were subjected to

several cycles of sedimentation by centrifugation (20000 g, 30 min) and re-suspension in Milli-Q water.

2.4. Catalytic activity of RGO-Ag NP hybrids

The catalytic activity of selected RGO-Ag NP hybrids was evaluated towards reduction of p-nitrophenol to p-aminophenol with $NaBH_4$ at RT in aqueous medium. The reaction progress was monitored by UV-vis absorption spectroscopy. To this end, equal volumes of freshly prepared aqueous solutions of p-nitrophenol (10 mM) and $NaBH_4$ (3 M) were mixed and stirred vigorously. The high molar ratio of $NaBH_4$ to p-nitrophenol (300:1) ensured an excess amount of the former and hence that its concentration remained essentially constant during the reduction reaction. This molar ratio was determined by gradually increasing the relative amount of $NaBH_4$ up to the point where further increments did not have any effect on the reaction kinetics. Then, 25 μL of such mixture were added to 2.1 mL of an aqueous RGO-Ag NP dispersion whose concentration of Ag NPs had been adjusted to ~3-4×10^9 mL^{-1}. After vigorous shaking for a few seconds, the absorbance of the mixture at 400 nm was monitored at 0.25 s time intervals. Several consecutive reaction rounds were measured to determine the stability of the catalyst.

2.5. Characterization techniques

UV-vis absorption spectroscopy measurements were carried out with a double-beam Heλios α spectrophotometer (Thermo Spectronic). Thermogravimetric analysis (TGA) was performed by means of an SDT Q600 thermobalance (TA Instruments), using Pt crucibles, under 100 mL min^{-1} Ar flow at a heating rate of 10 ºC min^{-1}. Attenuated total reflection Fourier transform infrared (ATR-FTIR) spectra were recorded on a Nicolet 3700 spectrometer (Thermo Scientific) using diamond as ATR crystal. X-ray photoelectron spectroscopy (XPS) measurements were carried out on a SPECS system under a pressure of 10^{-7} Pa with a monochromatic Al K_α X-ray source operated at 100 W. The surface elemental composition of the samples was determined from the integrated intensities of the main XPS peaks that were detected in survey spectra. To investigate the samples by TGA, ATR-FTIR spectroscopy and XPS, the dispersions were processed into free-standing paper-like films by vacuum filtration through alumina membrane filters 47 mm in diameter and 0.2 μm of pore size

(Whatman). The sheet resistance of the different paper-like films, cut into 10×10 mm^2 squares, was determined by the van der Pauw method with a home-made setup (Agilent 6614C DC power supply and Fluke 45 digital multimeter). Proper characterization of the RGO material itself by these techniques required thorough removal of the bioreductants and/or their oxidized products prior to the filtration step. Otherwise, contributions from these species to the spectra and thermograms of the paper-like films tended to obscure the features associated to the RGO sheets, and thus meaningful conclusions could not be reached. To remove the biomolecules, the reduced dispersions were first destabilized by the addition of 37% HCl solution until flocculation. The solid aggregate was subsequently transferred to filter paper and extensively washed with Milli-Q water for several days. Finally, the solid was re-suspended in a water:ethanol mixture (1:4 by volume) by bath sonication (5 h) and the resulting suspension was vacuum-filtered to yield the free-standing RGO film.

Atomic force microscopy (AFM) measurements were performed under ambient conditions (~22-24 ºC, RH ~40%) with a Nanoscope IIIa Multimode apparatus (Veeco Intruments) in the tapping mode of operation. Rectangular Si cantilevers with spring constant of ~40 N m^{-1} and resonance frequency ~250-300 kHz were used. Samples for AFM were prepared by drop-casting a small volume of diluted suspension (~0.01-0.02 mg mL^{-1} of RGO) onto a pre-heated (~50-60 ºC) highly oriented pyrolitic graphite (HOPG) substrate, which was subsequently rinsed with Milli-Q water and allowed to dry. Scanning transmission electron microscopy (STEM) was performed on a Quanta FEG 650 system (FEI Company) operated at 30 kV. Transmission electron microscopy (TEM) images were recorded with a JEOL 2000 EX-II instrument operated at 160 kV. Specimens for both STEM and TEM were prepared by mixing equal volumes of aqueous sample suspension and ethanol. Then, 40 μL of the resulting mixture were drop-cast onto a copper grid (200 square mesh) covered with a carbon film (Electron Microscopy Science) and allowed to dry.

3. Results and Discussion

3.1. *Reduction of graphene oxide with biomolecules*

The biomolecules that were tested here for their ability to reduce graphene oxide were mostly hydrosoluble vitamins, organic acids and amino acids, and were principally chosen on the basis of their known antioxidant or reducing activity in certain

biochemical reactions. Therefore, it was expected that at least some of them could also act as effective reductants for graphene oxide. Indeed, vitamin C has been previously shown to efficiently deoxygenate graphene oxide in aqueous and organic dispersion [22]. In the present work, other hydrosoluble vitamins, namely vitamin B_6 (in two forms: pyridoxine and pyridoxamine dihydrochloride) [40, 41] and vitamin B_2 ((-)-riboflavin [42] and riboflavin 5'-monophosphate salt hydrate, the latter being a more soluble version of the former) were assayed. Also, the organic acids citric acid, fumaric acid, L-malic acid, and L-tartaric acid, all of which possess known antioxidant activity [43], were tested. Likewise, certain amino acids have been shown to reduce metallic ions [44] and have even been suggested to reduce graphene oxide (specifically, tyrosine) [36], but direct confirmation of the latter point has so far not been provided. Here, we selected a representative set of the 22 naturally occurring amino acids, as well as two peptides: L-arginine, L-asparagine, L-carnosine (dipeptide) [45], glycine, L-glutamic acid, L-gluthatione (tripeptide) [35, 46], L-histidine, L-methionine [46], L-phenylalanine, L-tryptophan [46], and L-tyrosine [36, 46]. In addition, α-D-glucose [23], which together with L-gluthatione [35] has already been reported as a reductant for graphene oxide, was studied in an attempt to optimize its reducing efficiency.

To investigate and optimize the possible reducing effect of the biomolecules on the graphene oxide dispersions, two experimental variables were mainly taken into account: the biomolecule concentration in the dispersion and the reaction time (at 95 °C). In general terms, for a given graphene oxide concentration and a given reductant, we can expect to have a concentration of reductant that is optimum for reducing the graphene oxide sheets. Above such concentration, further reactions between graphene oxide and reductant will not take place, whereas with lower concentrations removal of oxygen functional groups from graphene oxide will be limited to a fraction of those that can be actually eliminated with the optimum amount of that reductant [22]. Similarly, a certain time will be required for reaction completion, which can be expected to depend on the specific reductant used, as different reaction pathways with different kinetic barriers will probably come into play. With these considerations in mind, we set out to optimize the reducing effect of the selected biomolecules by probing different concentrations and reaction times.

Optimization of the reduction conditions was carried out for aqueous dispersions with a graphene oxide concentration of 0.1 mg mL^{-1}. The extent of reduction achieved

was initially followed with UV-vis absorption spectroscopy, by monitoring the position of the absorption maximum for the $\pi \rightarrow \pi^*$ transition of C=C bonds (λ_{max}). λ_{max} is located at ~231 nm for unreduced graphene oxide, but gradually red-shifts as deoxygenation proceeds and electronic conjugation (sp^2 character) is restored in the carbon lattice [5]. Furthermore, a good correlation between the extent of reduction and λ_{max}, which reaches ~268 nm for highly reduced samples, has been previously established in conjunction with other characterization techniques [22]. In the present work, reduction was considered to be successful when the value of λ_{max} for the graphene oxide dispersion after reaction with a given biomolecule was larger than 259-261 nm. A value of 259-261 nm for λ_{max}, which amounts to a relatively limited degree of reduction of the graphene oxide sheets, can be accomplished by simply heating the suspension at 95 ºC under basic conditions (pH 10, achieved with, e.g., ammonia) in the absence of any reducing agent [22]. Because the experiments are carried out in basic medium (pH 10) to promote the colloidal stability of the dispersions [5], a potential reducing agent can only be considered to be successful in that role if it affords values of λ_{max} clearly above 259-261 nm.

Table 2 shows the values of λ_{max} attained with each of the 20 biomolecules under optimized conditions, together with the biomolecule concentration and reaction time required. On the basis of the above criterion, 9 out of the 20 tested reagents were found to be effective in reducing graphene oxide: pyridoxine (PN), pyridoxamine dihydrochloride (PM), riboflavin (B$_2$) and its phosphate salt (B$_2$ salt), arginine (Arg), gluthatione (GSH), histidine (His), tryptophan (Tryp), and glucose (Glu). Quite unexpectedly, some of the biomolecules (e.g., fumaric acid and L-malic acid) yielded λ_{max} values even lower than 259-261 nm, suggesting not only that they are inefficacious as reducing agents for graphene oxide, but also that they hinder the partial reduction of the sheets that otherwise takes place under basic conditions [22]. As noticed from Table 2, the effective biomolecules were seen to display somewhat different values of λ_{max} under optimized conditions, which indicates that they possess different reducing powers towards graphene oxide. According to such criterion, the weakest reducing agent would be GSH (λ_{max} ~264 nm), the strongest being B$_2$ and B$_2$ salt (λ_{max} ~268 nm). Under optimized conditions, Glu appeared to be also quite effective, exhibiting a λ_{max} value of 267 nm, which has to be compared with a value of 261 nm reported beforehand for the

Table 2. Position of the absorption peak corresponding to $\pi \rightarrow \pi^*$ transitions of C=C bonds (λ_{max}) for aqueous graphene oxide dispersions treated with different biomolecules. The biomolecule concentration and reaction time have been optimized to yield λ_{max} values as red-shifted as possible, indicating optimization of the reduction degree of graphene oxide. A given biomolecule is considered to be effective as a reductant when the value of λ_{max} it affords is well above that obtained just by heating the graphene oxide dispersion in basic medium (259-261 nm, ref.[22]). The acronyms used throughout the text for the successful reductants are included.

reagent	λ_{max} (nm)	Reduces graphene oxide?	Concentration (mM)	Time (h)
Pyridoxine (PN)	267	Yes	0.25	10
piridoxamine dihidrochloride (PM)	267	Yes	0.25	8
(-)- riboflavin (B$_2$)	268	Yes	2	8
riboflavin 5`- monophosphate sodium salt hydrate (B$_2$ salt)	268	Yes	2	8
citric acid	256	No	0.25	7
fumaric acid	255	No	0.025	6
L-malic acid	253	No	2.5	10
L-tartaric acid	257	No	2	7
L-arginine (Arg)	266	Yes	1	8
L-asparagine	258	No	0.25	6
L-carnosine	254	No	4	7
glycine	259	No	10	6
L-glutamic acid	257	No	0.5	6
L-glutathione (GSH)	264	Yes	1	3
L-histidine (His)	265	Yes	4	8
L-methionine	261	No	2	4
L-phenylalanine	257	No	1	6
L-tryptophan (Tryp)	267	Yes	2	8
L-tyrosine	261	No	2	8
α-D- glucose (Glu)	267	Yes	0.25	3

same molecule under different conditions [23]. We note that, as explained above, a λ_{max} value of 259-261 nm is obtained in the absence of Glu just by heating the graphene oxide suspension at the same temperature and pH [22]. Likewise, a previous report ascribed the ability of the protein BSA to efficiently reduce graphene oxide to its tyrosine (Tyr) residues [36]. However, in the present work free Tyr molecules did not succeed in reducing the graphene oxide dispersions. As pH has been reported to be crucial in the performance of Tyr as a reducing agent in other cases, here the reaction was conducted both at the usual pH (~10) (see Experimental Section) and at the pH reported to be optimum (pH ~12) [47], but the same (negative) result was obtained in these two cases (λ_{max} ~261 nm). To explain such results, it can be argued that the reducing ability of Tyr residues in BSA towards graphene oxide could be greater than that of free Tyr molecules due to, e.g., synergistic effects with other residues. Alternatively, other residues present in BSA could be responsible for the reduction of graphene oxide instead of its Tyr residues. In this regard, a good candidate would be the Arg residues, given that such amino acid in free form was shown here to successfully reduce graphene oxide (see Table 2). We note that Arg residues outnumber their Tyr counterparts in the BSA molecule (42 vs. 21, respectively).

Digital pictures of aqueous RGO dispersions prepared using the aforementioned nine successful reductants under optimized conditions are shown in Fig. 1, together with that of the starting, unreduced graphene oxide dispersion. The black and strongly opaque tone of the dispersions reacted with these biomolecules, as compared with the yellow-brown color characteristic of the starting dispersion, can be considered as a clear indication of efficient reduction. These reduced dispersions were seen to be stable for at least several months, except for samples reduced with Arg, which tended to aggregate within several days.
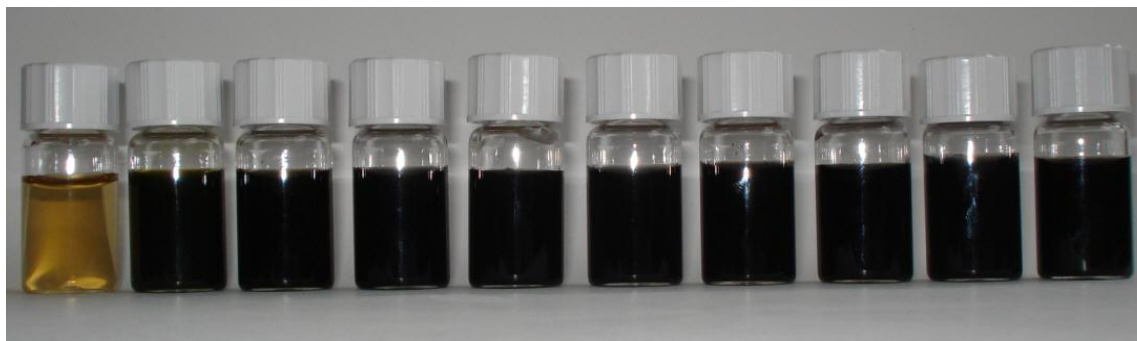
Figure 1. Digital picture of unreduced and biomolecule-reduced graphene oxide dispersions in water. From left to right: unreduced dispersion and dispersions reduced with B_2 salt, B_2, Glu, His, PN, PM, Arg, GSH and Tryp.

To confirm the successful reduction of the graphene oxide sheets, the dispersions were processed into free-standing paper-like films, as detailed in the Experimental Section, and characterized by TGA, ATR-FTIR spectroscopy, XPS and measurement of their sheet resistance. Fig. 2 shows thermogravimetric (TG, panel a) and differential thermogravimetric (DTG, panel b) plots of unreduced graphene oxide and graphene oxide reacted with the different effective bioreductants under the optimized conditions indicated in Table 2. The plots corresponding to the riboflavin salt (B_2 salt) are very similar to those of B_2 and are not shown to avoid repetition. It can be noticed that unreduced graphene oxide exhibits a significant weight loss (~30%) in a narrow temperature range (~180-240 ºC), which has been previously attributed to the decomposition of its labile oxygen functional groups [48]. Such a sharp weight loss step was no longer observed for graphene oxide reacted with the biomolecules (weight losses typically ~5%), indicating that most of these oxygen functional groups were eliminated. When using B_2 as a reductant, a small weight loss step (~5%) appeared around 265 ºC (see Fig. 2a). This feature was never observed for unreduced graphene oxide or graphene oxide reduced with the other biomolecules, and can be tentatively attributed to remnants of riboflavin and/or its oxidized product that interact strongly with the RGO sheets and thus could not be fully washed away.
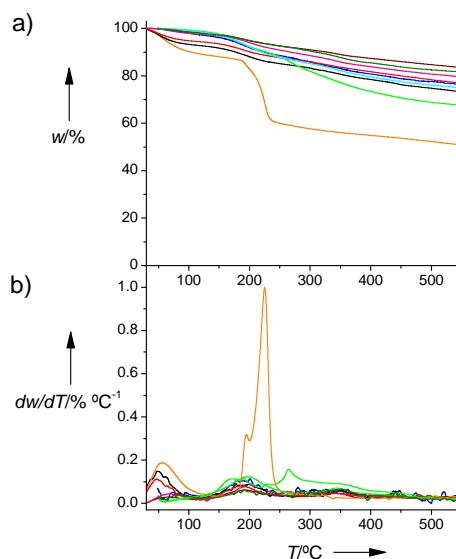
Figure 2. (a) Thermogravimetric (TG) and (b) differential thermogravimetric (DTG) plots recorded under Ar flow for paper-like films of unreduced graphene oxide (orange) and of graphene oxide reduced with PN (cyan), PM (red), B_2 (fluorescent green), Arg (blue), GSH (pink), His (black), Tryp (olive green) and Glu (wine).

The significant decrease in the amount of oxygen functional groups in graphene oxide upon reaction with the bioreductants was further confirmed by the drop in the intensity of all the absorption bands associated to vibrations of such groups in the corresponding ATR-FTIR spectra (Fig. 3). For unreduced graphene oxide (Fig. 3, orange plot), bands at 3000-3500 cm^{-1} (OH stretching), ~1720 cm^{-1} (C=O stretching), 1400 cm^{-1} (O-H bending vibrations), 1300-1350 cm^{-1} (C-OH stretching), 1220 cm^{-1} (breathing vibrations of epoxy groups) and 980 cm^{-1} (vibrations of epoxy, ether or peroxide groups) were clearly observed. By contrast, the intensity of all these bands diminished considerably for the samples treated with any the aforementioned successful bioreductants. The ATR-FTIR spectra of samples reduced with B_2 and B_2 salt (Fig. 3, bright green and yellow plots, respectively) support the idea that, despite the extensive washing step, some residual reducing agent was retained on the RGO sheets, as already suggested by the TGA data. Indeed, the intensity of the absorption bands related to hydroxyl groups, which are present in these two molecules in a significant proportion (see Table 1), is high in relation to that of graphene oxide reacted with any of the other 7 successful bioreductants.
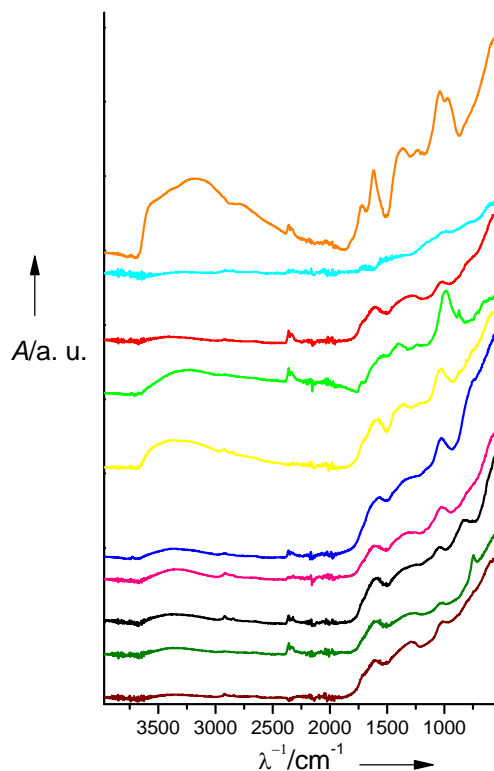
Figure 3. ATR-FTIR spectra of paper-like films of unreduced graphene oxide (orange) and graphene oxide reduced with PN (cyan), PM (red), B_2 (fluorescent green), B_2 salt (yellow), Arg (blue), GSH (pink), His (black), Tryp (olive green) and Glu (wine).

XPS survey spectra confirmed the effective deoxygenation of graphene oxide by the identified bioreductants: the O/C atomic ratio measured on the different paper-like samples dropped from 0.43 in unreduced graphene oxide to 0.13-0.19 after reaction with these biomolecules. Such O/C ratios are similar to those obtained from similar reduction processes [39] although somewhat higher than that obtained when hydrazine is used under optimized conditions (O/C ratio ~0.10) [22]. It must be noted that deoxygenation and reduction, although sometimes used as synonyms, are not equivalent. Deoxygenation can occur without reduction, e. g., two vicinal hydroxyls to yield one epoxy group (and one water molecule). Reduction can occur without deoxygenation as well, e. g., one epoxy group transforming into one hydroxyl group. However, the oxidation state of the C atoms in RGO can be clearly ascertained from the high resolution C1s core level XPS spectra shown in Fig. 4, so that the actual reduction of graphene oxide by reaction with the efficient bioreductants can be confirmed. Unreduced graphene oxide (Fig 4, orange plot) exhibits two main components at 284.6 and 286.6 eV, which can be ascribed, respectively, to carbon atoms in an unoxidized,

graphitic environment and to carbon atoms single-bonded to oxygen (e.g., from hydroxyl or epoxy groups) [39]. A third, minor component is located at about 287.9 eV and can be attributed to carbon atoms double-bonded to oxygen (e.g., carbonyl groups). As clearly noticed from Fig 4, treatment of graphene oxide with any of the bioreductants prompted a significant decrease in the relative contribution of oxygen-bonded carbon to the XPS C1s signal (especially carbon single-bonded to oxygen). Concomitantly, a wide and weak (but nonetheless detectable) component was seen to develop at ~291 eV for the biomolecule-treated samples, which can be assigned to the $\pi \rightarrow \pi^*$ shake-up satellite peak typical of graphitic materials [49]. It is known that deoxygenation occurs to a certain extent just treating graphene oxide under mild basic medium and that a limited degree of reduction is attained in strong basic medium [50]. This last result is what we find if we just heat in NH_3 at 95 ºC in the absence of any reductant, as can be seen in Fig 4 (navy plot). This matches with the already mentioned red-shift of λ_{max} to 259-261 nm in the UV-vis absorption spectrum for such dispersion. Such results clearly indicate that an effective reduction of graphene oxide by these biomolecules was achieved, and also that the electronically conjugated, graphitic character of the original carbon lattice could be restored to a substantial extent.
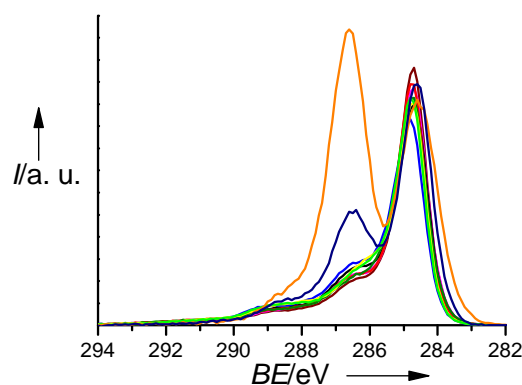
Figure 4. High resolution XPS C1s core level spectra recorded for unreduced graphene oxide (orange) and graphene oxide reduced with PM (red), B_2 (fluorescent green), B_2 salt (yellow), Arg (blue), GSH (pink), His (black), Tryp (olive green) and Glu (wine). Also the spectrum of a graphene oxide dispersion with 26 mM NH_3 heated at 95 ºC during 4 h has been added as a reference (navy blue). BE stands for binding energy.

Another evidence of the restoration of the electronic conjugation is provided by measurement of the sheet resistance (R_s) of the RGO films. The R_s of graphene oxide

before and after reduction with hydrazine has been reported to be in the order of 10^{10}-10^{11} Ω/sq [33, 38] and 10^5-10 Ω/sq [22, 33], respectively. The RGO films obtained in this work through reduction in optimized conditions with different bioreductants yielded R_s values of 8.99×10^2 Ω/sq (PN), 7.57×10^2 Ω/sq (PM), 1.70×10^6 Ω/sq (B$_2$), 4.50×10^6 Ω/sq (B$_2$ salt), 4.52×10^4 Ω/sq (Arg), 1.39×10^3 Ω/sq (GSH), 6.24×10^3 Ω/sq (His), 3.39×10^3 Ω/sq (Tryp), and 2.77×10^2 Ω/sq (Glu), respectively. The relatively low R_s values, in the order of 10^2-10^3 Ω/sq, shown by some of the RGO films prepared in this study are lower than most of the R_s values previously reported in the literature for RGO obtained with green reductants under mild conditions, indicating a high degree of chemical reduction (for a detailed comparison with previously reported values of sheet resistance and/or conductivity of RGO obtained by reduction with environmentally-friendly reductants, see Table S1 in the Supplementary Material). In fact, amongst the previously reported green reductants, only vitamin C yields lower R_s values [22]. B$_2$ and B$_2$ salt show the highest R_s values in this series of RGO films. This can be explained by the retention of some amount of reductant and/or its oxidized on the RGO samples despite extensive washing [24], as the TGA and ATR-FTIR spectroscopy data suggest (see also the X-ray diffraction data in the Supplementary Material). The fact that RGO dispersions obtained with B$_2$ salt show a exceedingly good dispersion stability, better than that of any of the other dispersion, as will be explained below in detail, also points to strong adsorption of B$_2$ salt and/or its oxidized form on the graphene sheets. The adsorption of B$_2$ salt explains in turn that the corresponding paper-like films display the highest R_s in the series.

Although aqueous dispersions of unreduced graphene oxide are made up of individual, single-layer sheets that are highly stable against aggregation and re-stacking, the same does not always hold true following removal of most of their oxygen functional groups in a reduction treatment [5]. This is mainly a consequence of the relatively low concentration of hydrophilic and/or ionizable oxygen-containing groups that remain in well-reduced graphene oxide samples. To investigate the dispersion state of the RGO sheets prepared with the present bioreductants, their aqueous suspensions were drop-cast onto atomically flat HOPG substrates and imaged by AFM (Fig. 5). The results indicated that the reduced sheets did not agglomerate and were kept as individual single-layer objects in their corresponding dispersions, even several months after the reduction treatment was carried out. Fig. 5 illustrates this point with some representative

AFM images obtained from dispersions reduced with Arg (a), GSH (b) and PM (c). Similar to the case of the unreduced dispersions (images not shown), the reduced ones were seen to be constituted by irregular (polygonal) objects a few to several hundred nm in lateral size and ~1 nm of apparent thickness (measured as their height relative to the HOPG substrate), which indicates that they indeed correspond to single-layer sheets [51]. The only notable exception to the long-term colloidal stability observed for the single-layer RGO sheets was, as commented above, that of dispersions reduced with Arg, which were only stable for a few days and tended to agglomerate afterwards. On the other hand, dispersions reduced with B_2 salt were seen to be exceedingly stable compared to those prepared with the other bioreductants, even under conditions that are usually considered extremely unfavorable to their stability (e.g., at low pH) [5]. For example, addition of small amounts of concentrated HCl solution readily destabilized all the biomolecule-reduced dispersions, except those prepared with B_2 salt, which required much larger volumes of the acid to achieve destabilization. The origin of this behavior can be mainly traced to the following two facts: (i) as mentioned before, B_2 salt molecules (or their oxidized product) are strongly adsorbed onto the RGO sheets, possibly by way of π-π interactions between their aromatic domains, and (ii) adsorbed B_2 salt molecules provide colloidal stability to the RGO sheets through electrostatic repulsion afforded by the negatively charged organophosphate group of the salt (see Table 1), even under significantly acidic conditions (the first pK_a of phosphoric acid is ~2) [52]. Thus, in addition to being an effective reductant of graphene oxide, B_2 salt (or its oxidized product) can also be used as a powerful stabilizer of the reduced dispersions, wich can be advantageous with a view to their further processing.
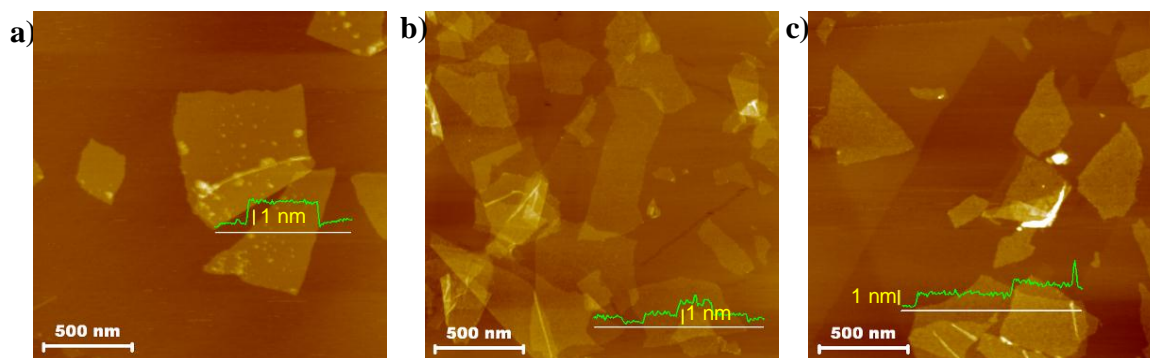
Figure 5. AFM images of graphene oxide sheets reduced with Arg (a), GSH (b) and PM (c) deposited onto HOPG substrates from their corresponding aqueous dispersions. In each case, a representative line profile (green line) taken along the marked white line is shown overlaid on the image.

The mechanism for the removal of oxygen functional groups from graphene oxide by reaction with reducing agents is still an open question even in the case of those most widely employed to this end (e.g., hydrazine). Although some reduction mechanisms involving –OH and/or –NH$_2$ groups from the reductant have been put forward [21, 23, 27, 33, 35], they are generally speculative and mainly based on previous knowledge of the reactions between a given reductant and small organic molecules, but not graphene oxide. A first step in the experimental determination of reduction pathways is the identification of the oxidation products of the reducing agent after reaction with graphene oxide, but in most cases such work has not been carried out [21, 23, 33, 35]. The identification of oxidation products for the newly reported bioreductants (PN, PM, B$_2$, etc) by high performance liquid chromatography/mass spectrometry is currently being undertaken by us, and the results will be documented elsewhere. Preliminary results indicate that, for example, reaction of both PN and PM with graphene oxide yields pyridoxal, which in turn suggests that oxidation of these two bioreductants proceeds through transformation of their hydroxyl and amine groups, respectively, into an aldehyde (see the Supplementary Material for additional data and suggested reaction mechanisms for the rest of the bioreductants). We also note from Table 2 that none of the tested organic acids succeeded in deoxygenating graphene oxide under the basic conditions that were employed here with all the potential reducing agents, implying that these molecules possess a poor reducing ability. However, it should be stressed that some strong inorganic acids, such as HI, have proved to be particularly effective reductants of graphene oxide [53, 54]. Liao *et al* have suggested

that a highly acidic aqueous environment is able to catalyze dehydration reactions of hydroxyl and epoxy groups in graphene oxide, hence leading to its reduction [55]. To test whether the present organic acids are also able to induce the reduction of graphene oxide by the generation of a sufficiently acidic environment, we heated as-prepared, non-basified graphene oxide dispersions in the presence of the organic acids at 95 ºC. In these cases, the pH of the medium was around 3, but no signs of reduction were observed with any of the acids even after long heating times. In the light of this, we hypothesize that the organic acids investigated here are too weak compared with, e.g., HI (pK_a values of ~3 (organic acids) vs. ~-10 (HI)) [52] to induce significant dehydration reactions, and therefore reduction, in graphene oxide.

3.2. Liquid-phase synthesis and catalytic activity of RGO-supported silver nanoparticles

The synthesis of metal nanoparticles is an active area of research due to their potential utility in, e.g., catalysis, photonics, biological labelling or sensing [56]. A simple, easily scalable method towards the preparation of metal nanoparticles in colloidal dispersion is based on the reduction of a metal salt precursor, usually in the presence of a stabilizer [44]. The use of carefully selected reductants and/or stabilizers is the cornerstone of this synthetic approach, given that their specific nature generally impacts the characteristics and performance of the resulting nanoparticles [44, 57] and also that there is a growing need to develop more sustainable preparation processes [58]. In this context, the identification of effective bioreductants for graphene oxide, as reported in the previous section, can be exploited for the preparation of RGO-metal nanoparticle hybrids by simultaneous reduction of graphene oxide and a metal salt. The prospective application of these hybrids in different technologically relevant areas has made them the focus of significant current interest [59, 60]. More specifically, Ag NPs are good candidates for use in catalysis, as silver is relatively cheap and a very active catalyst in several reactions [57, 61]. Many of the effective bioreductants investigated in the previous section, including Glu, Arg, B_2, Tryp and His have already been employed for the preparation of unsupported Ag NPs in aqueous medium [62-66]. However, to the best of our knowledge, there are no previous reports on the use of either PN or PM for the synthesis of metal nanoparticles (either supported or unsupported).

In the present work, RGO-Ag NP hybrids were prepared by the simultaneous reduction of graphene oxide and Ag(I) (in the form of $AgNO_3$) with the nine effective bioreductants of Table 2, without the need to use any additional reducing or stabilizing agents. Control experiments indicated that there was an optimum $AgNO_3$ concentration (0.34 mM for 0.1 mg mL^{-1} graphene oxide dispersions) for the generation of Ag NPs selectively onto the RGO sheets, as opposed to their generation in the bulk of the solution in the form of stand-alone, unsupported nanoparticles. Concentrations significantly below the optimum value did not bring about substantial numbers of Ag NPs, whereas higher concentrations tended to favor the growth of unsupported nanoparticles. Thus, subsequent experiments were accomplished by varying the concentration of bioreductant at the optimum $AgNO_3$ concentration.

Some representative results of the spectroscopic (UV-vis absorption and XPS) and microscopic (AFM, STEM and TEM) characterization of the obtained hybrids are shown, respectively, in Figs. 6 and 7, and Table 3 summarizes their main features (particle size and density). The grayish tinge typical of diluted aqueous dispersions containing only RGO sheets (inset to Fig. 6a, right cuvette) was replaced by a yellowish tone when graphene oxide and $AgNO_3$ were co-reduced with 4 mM His (inset to Fig. 6a, left cuvette). Furthermore, UV-vis absorption spectra revealed the appearance of a feature at ~420 nm for the latter (Fig. 6a), which can be ascribed to the well-known surface plasmon resonance (SPR) band characteristic of metallic silver nanostructures [67]. The generation of metallic silver in the dispersions was further confirmed by XPS measurements (Fig. 6b). Two well-defined and symmetrical peaks centered at 368.4 and 374.4 eV were observed and assigned to photoelectrons ejected, respectively, from $3d_{5/2}$ and $3d_{3/2}$ levels of Ag^0 [68]. No components at ~367 and 373 eV were detected, indicating that oxidized silver (Ag(I)) was not present in the prepared materials in significant amounts.
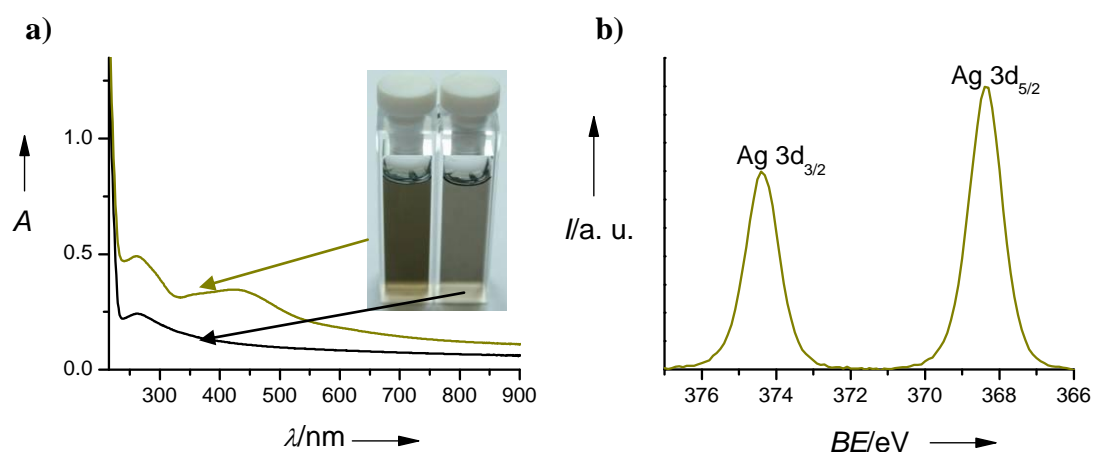
Figure 6. Spectroscopic characterization of RGO-Ag NP hybrids: (a) UV-vis absorption spectra and digital picture (inset) of a graphene oxide dispersion reduced with His in the absence (black curve and inset right) and presence (green curve and inset left) of AgNO$_3$. (b) High resolution Ag3d core level spectrum recorded by XPS of a typical RGO-Ag NP hybrid. BE stands for binding energy.

Fig. 7 shows AFM (a,b), STEM (c,d) and TEM (e,f) images of RGO-Ag NP hybrids prepared with 2 mM His (a), 1 mM PM (b), 1 mM Arg (c), 2 mM Tryp (d), 2 mM B$_2$ salt (e) and 4 mM His (f) as reductants. In all cases, the RGO sheets were found to be decorated with either white (AFM images) or black (bright-field STEM and TEM images) dots, which were never observed for graphene oxide sheets reduced in the absence of AgNO$_3$ (see, e.g., Fig. 5 for the case of AFM), and were therefore attributed to the Ag NPs. As mentioned above, the preparation was performed under conditions (mainly determined by AgNO$_3$ concentration) that led to Ag NPs exclusively associated to the sheets, without stand-alone nanoparticles being generated, and this is reflected in the images of Fig. 7 for the different hybrids. From the AFM images, the density of nanoparticles on the RGO sheets was estimated to be typically between 1-10 μm^{-2}, and higher resolution images by TEM (e.g., Fig. 7e and f) showed that they exhibit a faceted morphology. Estimation of nanoparticle size in the hybrids by TEM revealed it to be highly dependent on the bioreductant used and/or its concentration. This is apparent from the data collected in Table 3 for several selected hybrids. With a proper choice of bioreductant, nanoparticle sizes could be tuned in a range from 5-10 nm (0.1 mM GSH) to 100-150 nm (3 mM Tryp). Only individual nanoparticles (with some occasional agglomerate) were observed in every hybrid except for that prepared with 4mM B$_2$,

which consisted solely of agglomerates. The results of this local, TEM-based characterization of the nanoparticles were generally consistent with those obtained for the bulk of the hybrid in aqueous suspension by UV-vis absorption spectroscopy. It has been demonstrated that the SPR band of Ag NPs becomes progressively broader, more asymmetrical and red-shifted upon increasing their size from several nanometers to many tens of nanometers [67]. As a matter of fact, we observed such correlation between the UV-vis spectral features and the nanoparticle sizes estimated by TEM. We also note that the present bioreductants could be similarly used to prepare RGO hybrids with nanoparticles of other noble metals, for example gold using $HAuCl_4$ as a precursor. A brief characterization of these hybrids is presented in the Electronic Supplementary Information.
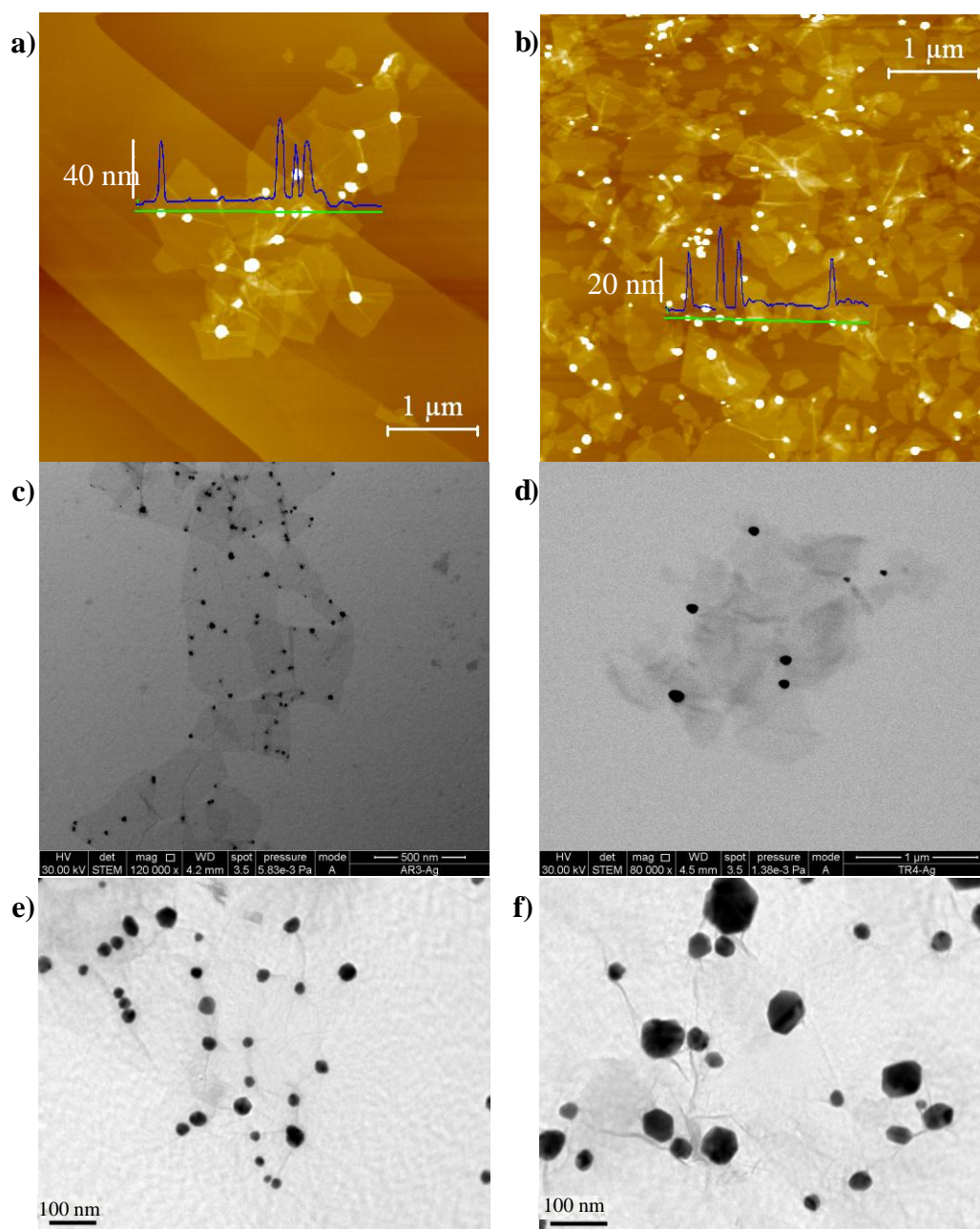
Figure 7. Microscopic characterization of RGO-Ag NP hybrids: (a,b) AFM images of hybrids prepared with 2 mM His (a) and 1 mM PM (b) deposited onto HOPG substrates. A representative line profile (blue line) taken along the marked green line is shown superimposed on each AFM image. (c,d) STEM images of hybrids prepared with 1 mM Arg (c) and 2 mM Tryp (d). (e,f) Detailed TEM images of Ag NPs on RGO sheets obtained with 2 mM B_2 salt (e) and 4 mM His (f).

Table 3. Preparation conditions and microscopic features of RGO-Ag NP hybrids prepared with different bioreductants.

Reductant	Concentration (mM)	Particle size (nm)
pyrydoxine	0.5	~50-90
	1	~70-100
prydoxamine dihydrochloride	1	~20-25
	1.5	~40
(-)-riboflavin	2	~20
	4	~(Only aggregates)
riboflavin salt	2	~25-50
	4	~25-50
L-arginine	1	~20-30
	2	~20-40
L-glutathione	0.1	~5-10
	0.5	>100
	1	Only extended Ag structures formed
L-histidine	2	~20-30 & 50-80 (Bimodal distribution of NP diameter. The smaller NP are more abundant)
	6	~50-80
L-tryptophan	2	~50-150
	3	~100-150
α- D- glucose	0.125	~60-90
	0.5	~80

To evaluate the catalytic activity of the RGO-Ag NP hybrids, the reduction of *p*-nitrophenol to *p*-aminophenol with $NaBH_4$ in aqueous medium at RT was investigated. Such a reaction constitutes a convenient model system to study the catalytic performance of metal nanoparticles and is also relevant from a practical perspective, because it is one of the main steps in the synthesis of widely employed pharmaceutical compounds (e.g., paracetamol) [69]. A selection of the hybrids prepared here was

chosen for the catalytic experiments, namely, hybrids prepared with 2 mM His, 1 mM Arg and 1mM PM; the latter was chosen mainly because it had never been previously used in the synthesis of Ag NPs. The transformation of *p*-nitrophenol to *p*-aminophenol was followed by UV-vis absorption spectroscopy. Fig. 8a shows UV-vis spectra of aqueous solutions of (i) *p*-nitrophenol at the very slightly acidic pH of deionized water (black plot), (ii) deprotonated *p*-nitrophenol (*p*-nitrophenoxide ion) that forms in the basic medium generated by the presence of $NaBH_4$ (dark yellow plot), and (iii) the product of its reduction, *p*-aminophenoxide (violet plot). The strong absorption peak at 400 nm characteristic of *p*-nitrophenoxide is not present in its reduced counterpart, and thus such a peak can be used to monitor the reaction progress, i.e. the evolution of *p*-nitrophenoxide concentration with time. This is exemplified in Fig. 8b for reaction of *p*-nitrophenoxide with $NaBH_4$ in the presence of either the RGO-Ag NP hybrid prepared with PM (black squares) or stand-alone Ag NPs obtained by the standard and widely employed method of $NaBH_4$ reduction of $AgNO_3$ and stabilization with citrate anion (green squares) [67]. In these two cases, the experiments were performed with nanoparticles of similar size (~20-25 nm) and same concentration (~3-4×10^9 mL^{-1}). An initial delay time (~270-280 s) was observed, which can be ascribed to dissolved oxygen in the solution being consumed by $NaBH_4$ [70]. Afterwards, reduction of *p*-nitrophenoxide proper came about and its absorbance at 400 nm was seen to decay in an exponential fashion. Considering also that an excess of $NaBH_4$ was used in the experiments, the reduction can be regarded to proceed at a constant concentration of this reagent, and therefore should follow a pseudo-first-order kinetic behavior, so that,

$$\frac{d[p\text{-}NP]}{dt} = -k_{app}[p\text{-}NP] \tag{1}$$

where (*p*-NP) is the concentration of *p*-nitrophenoxide and k_{app} is the apparent rate constant of the reaction. Indeed, fitting of the experimental data of Fig. 8b to an exponential function yielded residuals in the range of ±0.03, confirming that Eq. (1) applies in the present case.
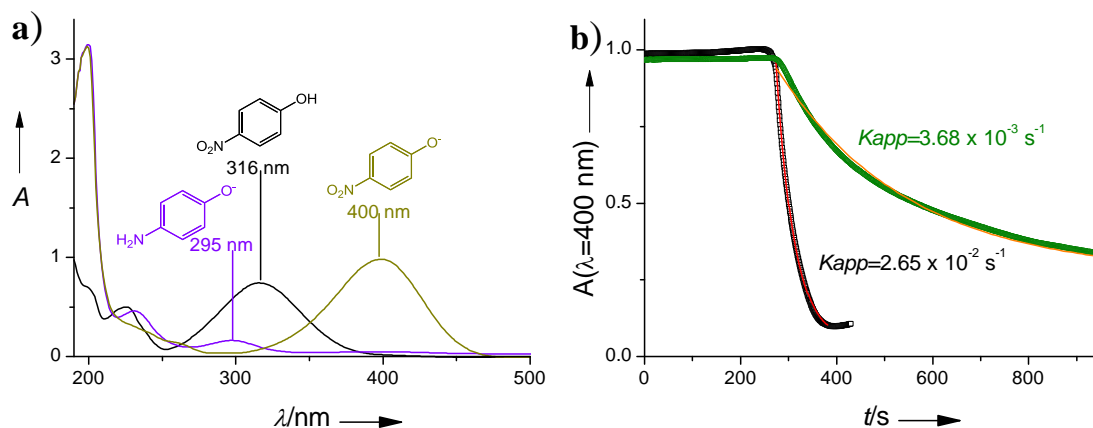
Figure 8. (a) UV-vis absorption spectra of *p*-nitrophenol (black curve), *p*-nitrophenoxide ion (dark yellow), and *p*-aminophenoxide ion (violet). The absorption peak at 400 nm of *p*-nitrophenoxide is used to monitor its conversion to *p*-aminophenoxide by reduction with $NaBH_4$. (b) Plot of absorbance at 400 nm for the reduction of *p*-nitrophenoxide with $NaBH_4$ catalysed with RGO-Ag NP hybrid prepared with PM (black squares) and with stand-alone, citrate-capped Ag NPs prepared by $NaBH_4$ reduction of $AgNO_3$ following standard procedures (green squares). The experimental kinetic profiles could be well fitted to exponential decay functions, which are shown as overlaid red and orange lines, respectively. Experimental conditions: (*p*-nitrophenol) = 0.06 mM; ($NaBH_4$) = 0.018 M; (Ag NP) ~0.2 µg mL^{-1}.

The catalytic experiments yielded k_{app} values of 5.37×10^{-2}, 2.65×10^{-2} and 2.64×10^{-2} s^{-1} for RGO-Ag NP hybrids prepared with Arg, PM and His, respectively, whereas a value of 3.68×10^{-3} s^{-1} was obtained with stand-alone, citrate-capped Ag NP synthesized by standard procedures. In general, the catalysts were seen to be quite stable in the short-term, as k_{app} did not change significantly over 10 consecutive reaction cycles. Furthermore, to allow comparison of these catalytic activities on an equal footing, and also to compare them with data from the literature, the apparent rate constants were normalized to the surface area of silver employed per unit volume of dispersion (areal rate constant), and the results are 7.61, 4.63, 0.56 L m^{-2} s^{-1} for RGO-Ag NP hybrids prepared with Arg, PM and His, respectively, whereas a value of 3.68×10^{-3} s^{-1} was obtained with stand-alone, citrate-capped Ag NPs (for a comparison with previously reported values measured for the same reaction using other Ag NP-based catalysts, see Table S2). To the best of our knowledge, the present Arg- and PM-derived RGO-Ag NP hybrids exhibit the highest catalytic activities that have ever been

documented for Ag NPs in this reaction (areal rate constants ~3-5 times higher than the previous largest values [70-78]. By contrast, the performance of the His-derived hybrids is comparable (slightly lower) to that of the standard, citrate-capped Ag NPs. So far, the largest value of areal rate constant (1.41 L m^{-2} s^{-1}) had been very recently achieved for a system made up of stand-alone nanoparticles synthesized by NaBH$_4$ reduction of AgNO$_3$ and stabilized by dextran [71].

We also note that the areal rate constants of the hybrids were obtained with just-prepared hybrids. Nevertheless, another relevant issue that should be taken into account when assessing the performance of these catalysts concerns their colloidal stability in the medium where the catalytic reaction is carried out (water in the present case). Agglomeration of the metal nanoparticles in the reaction medium inevitably leads to the degradation of their catalytic performance, however active they are as individual entities, thus ruining their actual utility in the long-term. For this reason, the nanoparticles are frequently stabilized by, e.g., anchoring them onto suitable substrates or by coating them with different types of polymers or stabilizers. Although the latter option may limit the catalytic activity of the metal nanoparticles as a result of diffusional barriers between the reactants in the aqueous medium and the metal surface, such a disadvantage is usually far surpassed by the benefit of having a colloidally very stable catalyst that can be used for a very long time. In our case, even though the Arg-derived hybrid displayed a very high catalytic activity, the hybrid was not colloidally stable and precipitated in a matter of just a few days, similar to the stand-alone RGO sheets prepared with the same bioreductant, as noted beforehand. By contrast, the RGO-Ag NP hybrid prepared with PM boasted a combination of very high catalytic activity (4.63 L m^{-2} s^{-1}) and long-term colloidal stability. For example, aqueous dispersions of the PM-derived hybrids did not show any visible sign of agglomeration or precipitation and their catalytic activity was not significantly degraded nine months after their preparation. Therefore, the PM-derived hybrids constitute an exceptional catalyst for the studied reaction.

Finally, we briefly discuss the possible origins of the high catalytic activity of these hybrids. In principle, such activity could be either an intrinsic feature of the Ag NPs or a substrate (RGO)-promoted effect, or a combination of both. For example, relatively strong π-π interactions between *p*-nitrophenol molecules and the RGO sheets could contribute to an increased concentration of this reactant in the neighborhood of

the Ag NPs, thus increasing the reaction rate. To investigate this point, we synthesized Ag NPs using PM as a reductant and following the same procedure as described above, but in the absence of graphene oxide sheets. This resulted in stand-alone nanoparticles with somewhat larger diameters than those of their RGO-supported counterpart but similar areal rate constants, implying that their remarkably high catalytic activity is mainly an intrinsic feature of the Ag NPs and is not caused by the RGO substrate or by substrate-nanoparticle interaction effects. Still, using the RGO sheets as a support for the Ag NPs is advantageous in that the resulting hybrid displayed long-term colloidal stability in water, whereas the stand-alone PM-derived Ag NPs were less stable and tended to agglomerate. Although the origin of the high activity of these nanoparticles remains unknown, one plausible hypothesis could be that these bioreductants, or their oxidation products, tend to favor the growth and stabilization of Ag NPs exhibiting larger fractions of reactive sites and/or crystal planes on their surface, to the detriment of less reactive ones, thus leading to a higher catalytic activity [79].

4. Conclusions

A comprehensive survey using 20 biomolecules, selected on the basis of their known antioxidant and/or reducing ability in the biochemical context, has afforded the identification of several new efficient reductants for graphene oxide. The successful bioreductants are vitamins and amino acids, and include pyridoxine and pyridoxamine (vitamin B_6), riboflavin (vitamin B_2), arginine, histidine and tryptophan. These findings significantly increase the pool of innocuous and safe biomolecules available at present for reduction of graphene oxide and could thus facilitate the implementation of green approaches towards the production of graphene-based materials with improved performance for certain applications, where the selection of appropriate bioreductants could be relevant. As an example of this possibility, reduced graphene oxide-silver nanoparticle hybrids were prepared in aqueous medium using the newly identified bioreductants. In particular, hybrids made with pyridoxamine were shown to exhibit a combination of long-term colloidal stability and an unprecedented level of catalytic activity among silver nanoparticle-based catalysts in the reduction of *p*-nitrophenol with NaBH$_4$, making them an excellent candidate for such application. The exploration of further benefits of using selected bioreductants to the performance of graphene-based materials is currently under way.

Acknowledgements

Supporting Information. Additional characterization of the RGO films by UV-vis spectroscopy, Raman spectroscopy and X-ray diffraction; comparison with previously reported RGO obtained with green reductants; proposed mechanisms for the bioreductants; comparison of areal rate constants obtained for the reduction of p-nitrophenol with NaBH$_4$ using a different Ag NP-based catalysts; general characterization of RGO-Au NP hybrids by UV-vis absorption spectroscopy and STEM.

Reference

[1]   Luo B, Liu S, Zhi L. Chemical Approaches toward Graphene-Based Nanomaterials and their Applications in Energy-Related Areas. Small 8 (2012), 630-646.

[2]   Liu Y, Dong X, Chen P. Biological and chemical sensors based on graphene materials. Chem. Soc. Rev. 41 (2012), 2283-2307.

[3]   Machado BF, Serp P. Graphene-based materials for catalysis. Catal. Sci. Technol. 2 (2012), 54-75.

[4]   Stankovich S, Dikin DA, Piner RD, Kohlhaas KA, Kleinhammes A, Jia Y, Wu Y, Nguyen ST, Ruoff RS. Synthesis of graphene-based nanosheets via chemical reduction of exfoliated graphite oxide. Carbon 45 (2007), 1558-1565.

[5]   Li D, Mueller M, Gilje S, Kaner R, Wallace G, Müller M. Processable aqueous dispersions of graphene nanosheets. Nat. Nanotech. 3 (2008), 101-105.

[6]   Park S, Ruoff RS. Chemical methods for the production of graphenes. Nat. Nanotech. 4 (2009), 217-224.

[7]   Shin H-J, Kim K, Benayad A, Yoon S-M, Park H. Efficient reduction of graphite oxide by sodium borohydrilde and its effect on electrical conductance. Adv. Funct. Mat. 19 (2009), 1987-1992.

[8]   Pei S, Cheng H-M. The reduction of graphene oxide. Carbon 50 (2012), 3210-3228.

[9]   Mao S, Pu H, Chen J. Graphene oxide and its reduction: modeling and experimental progress. RSC Advances 2 (2012), 2643-2662.

[10]   Ambrosi A, Chua CK, Bonanni A, Pumera M. Lithium aluminum hydride as reducing agent for chemically reduced graphene oxides. Chem. Mater. 24 (2012), 2292-2298.

[11]   Xu C, Wang X, Zhu J. Graphene-metal particle nanocomposites. J. Phys. Chem. C 112 (2008), 19841-19845.

[12]   Williams G, Seger B, Kamat PV. TiO2-Graphene nanocomposites. UV-assisted photocatalytic reduction of graphene oxide. ACS Nano 2 (2008), 1487-1491.

[13]   Akhavan O, Ghaderi E. Photocatalytic reduction of graphene oxide nanosheets on TiO2 thin film for photoinactivation of bacteria in solar light irradiation. J. Phys.

Chem. C 113 (2009), 20214-20220.

[14] Akhavan O. Graphene nanomesh by ZnO nanorod photocatalysts. Acs Nano 4 (2010), 4174-4180.

[15] Yun Hau Ng YH, Iwase A, Bell N, Kudo A, Amal R, Amal, Ng A, Iwase N, Bell A, Kudo R. Semiconductor/reduced graphene oxide nanocomposites derived from photocatalytic reactions. Catal. Today 164 (2011), 353-357.

[16] Akhavan O. Photocatalytic reduction of graphene oxides hybridized by ZnO nanoparticles in ethanol. Carbon 49 (2011), 11-18.

[17] Akhavan O, Choobtashani M, Ghaderi E. Protein degradation and RNA efflux of viruses photocatalyzed by graphene–tungsten oxide composite under visible light irradiation. J. Phys. Chem. C 116 (2012), 9653-9659.

[18] Paredes JI, Villar-Rodil S, Fernandez-Merino MJ, Guardia L, Martinez-Alonso A, Tascon JMD. Environmentally friendly approaches toward the mass production of processable graphene from graphite oxide. J. Mater. Chem. 21 (2011), 298-306.

[19] Zhang J, Yang H, Shen G, Cheng P, Zhang J, Guo S. Reduction of graphene oxide vial-ascorbic acid. Chem. Commun. 46 (2010), 1112-1114.

[20] Dua V, Surwade SP, Ammu S, Agnihotra SR, Jain S, Roberts KE, Park S, Ruoff RS, Manohar SK. All-organic vapor sensor using inkjet-printed reduced graphene oxide. Angew. Chem. Int. Edit. 49 (2010), 2154-2157.

[21] Gao J, Liu F, Liu Y, Ma N, Wang Z, Zhang X. Environment-friendly method to produce graphene that employs Vitamin C and amino acid. Chem. Mater. 22 (2010), 2213-2218.

[22] Fernández-Merino MJ, Guardia L, Paredes JI, Villar-Rodil S, Solís-Fernández P, Martínez-Alonso A, Tascón JMD. Vitamin C is an ideal substitute for hydrazine in the reduction of graphene oxide suspensions. J. Phys. Chem. C 114 (2010), 6426-6432.

[23] Zhu C, Guo S, Fang Y, Dong S. Reducing sugar: new functional molecules for the green synthesis of graphene nanosheets. ACS Nano 4 (2010), 2429-2437.

[24] Kim Y-K, Kim M-H, Min D-H. Biocompatible reduced graphene oxide prepared by using dextran as a multifunctional reducing agent. Chem. Commun. 47 (2011), 3195-3197.

[25] Akhavan O, Ghaderi E, Aghayee S, Fereydooni Y, Talebi A. The use of a glucose-reduced graphene oxide suspension for photothermal cancer therapy. J. Mater. Chem. 22 (2012), 13773-13781.

[26] Wang Y, Shi Z, Yin J. Facile synthesis of soluble graphene via a green reduction of graphene oxide in tea solution and its biocomposites. ACS Appl. Mater. Interfaces 3 (2011), 1127-1133.

[27] Lei Y, Tang Z, Liao R, Guo B. Hydrolysable tannin as environmentally friendly reducer and stabilizer for graphene oxide. Green Chem. 13 (2011), 1655-1658.

[28] Akhavan O, Kalaee M, Alavi ZS, Alavi ZS, Esfandiar A. Increasing the antioxidant activity of green tea polyphenols in the presence of iron for the reduction of graphene oxide. Carbon 50 (2012), 3015-3025.

[29] Wang J, Shi Z, Fan J, Ge Y, Yin J, Hu G. Self-assembly of graphene into three-dimensional structures promoted by natural phenolic acids. J. Mater. Chem. 22 (2012), 22459-22466.

[30] Li J, Xiao G, Chen C, Li R, Yan D. Superior dispersions of reduced graphene oxide synthesized by using gallic acid as a reductant and stabilizer. J. Mater. Chem. A 1 (2013), 1481-1487.

[31] Mhamane D, Ramadan W, Fawzy M, Rana A, Dubey M, Rode C, Lefez B, Hannoyer B, Ogale S. From graphite oxide to highly water dispersible functionalized graphene by single step plant extract-induced deoxygenation. Green Chem. 13 (2011), 1990-1996.

[32] Kang SM, Park S, Kim D, Park SY, Ruoff RS, Lee H. Simultaneous reduction and surface functionalization of graphene oxide by mussel-inspired chemistry. Adv. Funct. Mater. 21 (2011), 108-112.

[33] Esfandiar A, Akhavan O, Irajizad A. Melatonin as a powerful bio-antioxidant for reduction of graphene oxide. J. Mater. Chem. 21 (2011), 10907-10914.

[34] Akhavan O, Ghaderi E, Esfandiar A. Wrapping bacteria by graphene nanosheets for isolation from environment, reactivation by sonication, and inactivation by near-infrared irradiation. J. Phys. Chem. B 115 (2011), 6279-6288.

[35] Pham TA, Kim JS, Kim JS, Jeong YT. One-step reduction of graphene oxide with l-glutathione. Colloid. Surf. A. 384 (2011), 543-548.

[36] Liu J, Fu S, Yuan B, Li Y, Deng Z. Toward a universal "adhesive nanosheet" for the assembly of multiple nanoparticles based on a protein-induced reduction/decoration of graphene oxide. J. Am. Chem. Soc. 132 (2010), 7279-7281.

[37] Salas E, Sun Z, Luttge A, Tour J, Lüttge A. Reduction of graphene oxide via bacterial respiration. ACS Nano 4 (2010), 4852-4856.

[38] Akhavan O, Ghaderi E. Escherichia coli bacteria reduce graphene oxide to bactericidal graphene in a self-limiting manner. Carbon 50 (2012), 1853-1860.

[39] Paredes JI, Villar-Rodil S, Solís-Fernández P, Martínez-Alonso A, Tascón JMD. Atomic force and scanning tunneling microscopy imaging of graphene nanosheets derived from graphite oxide. Langmuir 25 (2009), 5957-5968.

[40] Stocker P, Lesgards J-F, Vidal N, Chalier F, Prost M. ESR study of a biological assay on whole blood: antioxidant efficiency of various vitamins. Biochim. Biophys. Acta 1621 (2003), 1-8.

[41] Endo N, Nishiyama K, Otsuka A, Kanouchi H, Taga M, Oka T. Antioxidant activity of vitamin B6 delays homocysteine-induced atherosclerosis in rats. Br. J. Nutr. 95 (2006), 1088-1093.

[42] Toyosaki T, Mineshita T. Antioxidant effect of riboflavin in aqueous solution. Agric.Food Chem. 37 (1989), 286-289.

[43] Papadopoulos K, Triantis T, Dimotikali D, Nikokavouras J. Evaluation of food antioxidant activity by photostorage chemiluminescence. Anal. Chim. Acta 433 (2001), 263-268.

[44] Manikam VR, Cheong KY, Razak KA. Chemical reduction methods for synthesizing Ag and Al nanoparticles and their respective nanoalloys. Mater. Sci. Eng. B 176 (2011), 187-203.

[45] Babizhayev MA. Antioxidant activity of L-carnosine, a natural histidine-containing dipeptide in crystalline lens. Biochim. Biophys. Acta 1004 (1989), 363-371.

[46] Capitani CD, Carvalho ACL, Rivelli DP, Barros SBM, Castro IA. Evaluation of natural and synthetic compounds according to their antioxidant activity using a multivariate approach. Eur. J. Lipid Sci. Technol. 111 (2009), 1090-1099.

[47] Xie J, Lee JY, Wang DIC, Ting YP. Silver nanoplates: from biological to biomimetic synthesis. ACS Nano 1 (2007), 429-439.

[48] Solís-Fernández P, Rozada R, Paredes JI, Villar-Rodil S, Fernández-Merino MJ. Guardia L, Martínez-Alonso A, Tascón JMD. Chemical and microscopic analysis

of graphene prepared by different reduction degrees of graphene oxide. J. Alloys Compd. 536 (2012), S532-S537.

[49] Zhang G, Sun S, Yang D, Dodelet J-P, Sacher E. The surface analytical characterization of carbon fibers functionalized by H_2SO_4/HNO_3 treatment. Carbon 46 (2008), 196-205.

[50] Dimiev AM, Alemany LB, Tour JM. Graphene oxide. Origin of acidity, its instability in water, and a new dynamic structural model. ACS Nano 7 (2012), 576-588.

[51] Solís-Fernández P, Paredes JI, Villar-Rodil S, Martínez-Alonso A, Tascón JMD. Determining the thickness of chemically modified graphenes by scanning probe microscopy. Carbon 48 (2010), 2657-2660.

[52] Greenwood NN, Earnshaw A. Chemistry of the elements. Pergamon Press. Oxford. 1989: 598.

[53] Moon I, Lee J, Ruoff R, Lee H. Reduced graphene oxide by chemical graphitization. Nat. Commun. 1 (2010), 73.

[54] Pei S, Zhao J, Du J, Ren W, Cheng H-M. Direct reduction of graphene oxide films into highly conductive and flexible graphene films by hydrohalic acids. Carbon 48 (2010), 4466-4474.

[55] Liao K-H, Mittal A, Bose S, Leighton C, Mkhoyan KA, Macosko CW. Aqueous only route toward graphene from graphite oxide. ACS Nano 5 (2011), 1253-1258.

[56] Feldheim DL, Colby Jr A. Metal nanoparticles: synthesis, characterization, and applications. Marcel Dekker. New York, 2002:13.

[57] Nair L, Laurencin C. Silver nanoparticles: synthesis and therapeutic applications. Biomed. Nanotechnol. 3 (2007), 301-316.

[58] Nadagouda MN, Varma RS. Green and controlled synthesis of gold and platinum nanomaterials using vitamin B_2: density-assisted self-assembly of nanospheres, wires and rods. Green Chem. 8 (2006), 516-518.

[59] Rosi NL, Mirkin CA. Nanostructures in biodiagnostics. Chem. Rev. 105 (2005), 1547-1562.

[60] Kamat PV. Graphene-based nanoarchitectures. Anchoring semiconductor and metal nanoparticles on a two-dimensional carbon support. J. Phys. Chem. Lett. 1 (2009), 520-527.

[61] Mao CF, Vannice MA. Formaldehyde oxidation over Ag catalysts. J. Catal. 154 (1995), 230-244.

[62] Panáček A, Kvítek L, Prucek R, Kolář M, Večeřová R, Pizúrová N, Sharma VK, Nevěčná T, Zbořil R. Silver colloid nanoparticles: synthesis, characterization, and their antibacterial activity. Phys. Chem. B 110 (2006), 16248-16253.

[63] Hu B, Wang S-B, Wang K, Zhang M, Yu S-H. Microwave-assisted rapid facile "green" synthesis of uniform silver nanoparticles: self-assembly into multilayered films and their optical properties. J. Phys. Chem. C 112 (2008), 11169-11174.

[64] Roy B, Bairi P, Nandi AK. Selective colorimetric sensing of mercury(ii) using turn off-turn on mechanism from riboflavin stabilized silver nanoparticles in aqueous medium. Analyst 136 (2011), 3605-3607.

[65] Jacob JA, Naumov S, Mukherjee T, Kapoor S. Preparation, characterization, surface modification and redox reactions of silver nanoparticles in the presence of tryptophan. Coll. Surf. B. 87 (2011), 498-504.

[66] Liu Z, Xing Z, Zu Y, Tan S, Zhao L, Zhou Z, Sun T. Synthesis and characterization of L-histidine capped silver nanoparticles. Mater. Sci. Eng. C 32 (2012), 811-816.

[67] Evanoff DD, Chumanov G. Synthesis and optical properties of silver nanoparticles and arrays. ChemPhysChem 6 (2005), 1221-1231.

[68] Crist BV. Handbook of monochromatic XPS spectra. Vol. 1. The elements & Native Oxides. California, USA: XPS International LLC. California, USA, 2004, 1-4.

[69] Hervés P, Pérez-Lorenzo M, Liz-Marzán LM, Dzubiella J, Lu Y, Ballauff M. Catalysis by metallic nanoparticles in aqueous solution: model reactions. Chem. Soc. Rev. 41 (2012), 5577-5587.

[70] Lu Y, Mei Y, Ballauff M, Drechsler M. Thermosensitive core-shell particles as carrier systems for metallic nanoparticles. J. Phys. Chem. B 110 (2006), 3930-3937.

[71] Eising R, Signori AM, Fort Sb, Domingos JB. Development of catalytically active silver colloid nanoparticles stabilized by dextran. Langmuir 27 (2011), 11860-11866.

[72] Signori AM, Santos KO, Eising R, Albuquerque BL, Giacomelli FC, Domingos JB. Formation of catalytic silver nanoparticles supported on branched polyethyleneimine derivatives. Langmuir 26 (2010), 17772-17779.

[73] Zhang J-T, Wei G, Keller TF, Gallagher H, Stötzel C, Müller FA, Gottschaldt M, Schubert US, Jandt KD. Responsive hybrid polymeric/metallic nanoparticles for catalytic applications. Macromol. Mater. Eng. 295 (2010), 1049-1057.

[74] Harish S, Sabarinathan R, Joseph J, Phani KLN. Role of pH in the synthesis of 3-aminopropyl trimethoxysilane stabilized colloidal gold/silver and their alloy sols and their application to catalysis. Mater. Chem. Phys. 127 (2011), 203-207.

[75] Murugadoss A, Chattopadhyay A. A 'green' chitosan-silver nanoparticle composite as a heterogeneous as well as micro-heterogeneous catalyst. Nanotechnology 19 (2008), 015603/1-015603/9.

[76] Zhang P, Shao C, Zhang Z, Zhang M, Mu J, Guo Z, Liu Y. In situ assembly of well-dispersed Ag nanoparticles (AgNPs) on electrospun carbon nanofibers (CNFs) for catalytic reduction of 4-nitrophenol. Nanoscale 3 (2011), 3357-3363.

[77] Lu Y, Mei Y, Schrinner M, Ballauff M, Möller MW, Breu J. In Situ formation of Ag nanoparticles in spherical polyacrylic acid brushes by UV irradiation. J. Phys. Chem. C 111 (2007), 7676-7681.

[78] Rashid MH, Mandal TK. Synthesis and catalytic application of nanostructured silver dendrites. J. Phys. Chem. C 111 (2007), 16750-16760.

[79] Xu R, Wang D, Zhang J, Li Y. Shape-dependent catalytic activity of silver nanoparticles for the oxidation of styrene. Chem. Asian J. 1 (2006), 888-893.

Supplementary Material

for

Identifying efficient natural bioreductants for the preparation of graphene and graphene-metal nanoparticle hybrids with enhanced catalytic activity from graphite oxide

M.J. Fernández-Merino, S. Villar-Rodil, J.I. Paredes, P. Solís-Fernández, L. Guardia, R. García, A. Martínez-Alonso, J.M.D. Tascón

Instituto Nacional del Carbón, INCAR-CSIC, Apartado 73, 33080 Oviedo, Spain

1. Additional characterization of reduced graphene oxide

1.1. UV-vis absorption spectroscopy

Fig. S1 shows the UV-vis spectra of the dispersions of unreduced GO and GO reduced with different bioreductants. The spectrum of a dispersion of graphene oxide reduced at 95 ºC with hydrazine (2 mM, 15 min) has been added for comparison. The UV-vis spectrum of GO (orange plot) exhibits two characteristic features: a maximum at 231 nm and a shoulder around 300 nm, corresponding to $\pi \rightarrow \pi^*$ transitions of aromatic C-C bonds (λ_{max}) and to $n \rightarrow \pi^*$ transitions of C=O bonds, respectively [1]. Upon reduction, the recovery of electronic conjugation in the structure causes a red-shift of the $\pi \rightarrow \pi^*$ absorption maximum and a significant increase in absorbance for the whole range of wavelengths larger than 231 nm [2]. Indeed, the absorption maxima of the dispersions reduced with the bioreductants display absorption maxima in the 264-268 nm range (see Table S1). The RGO dispersion obtained with hydrazine (grey plot) possesses an absorption maximum at 268 nm [3]. In fact (and within the experimental error of the spectrometer), 268-270 nm is the most red-shifted value obtained for aqueous dispersions of graphene materials, being the one obtained for, e. g., aqueous dispersions of pristine, unoxidized graphene obtained with the assistance of surfactants [4]. Taking the red-shift of λmax as criterion for the degree of reduction of GO, the weakest reducing agent would be GSH (λ_{max} ~264 nm), the strongest being B_2 and B_2 salt (λ_{max} ~268 nm).
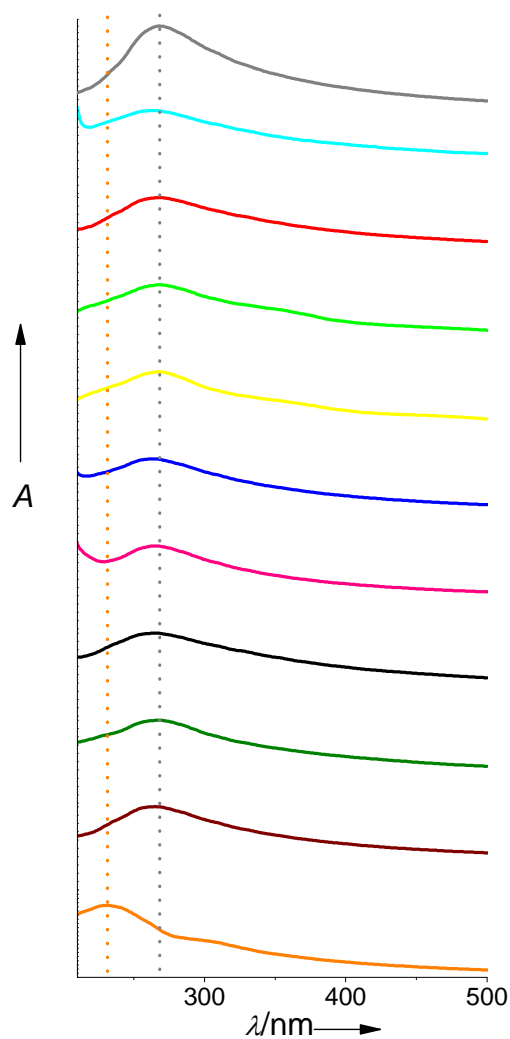
Figure S1. UV-vis absorption spectra of dispersions of unreduced graphene oxide (orange) and graphene oxide reduced with PN (cyan), PM (red), B_2 (fluorescent green), B_2 salt (yellow), Arg (blue), GSH (pink), His (black), Tryp (olive green) and Glu (wine). The spectrum of a dispersion of graphene oxide reduced at 95 ºC with 2 mM hydrazine for 15 min (grey plot) has been added for comparison. To facilitate the analysis of the graph, two dotted lines at λ =231 nm (orange), which is the location of the absorption maximum for the $\pi \rightarrow \pi^*$ transition of C=C bonds of unreduced graphene oxide, and at λ=268 nm (black), which is the most red-shifted position found for such maximum for highly reduced samples, have been included.

1.2. Raman spectroscopy

Raman measurements were made with a Horiba Jobin-Yvon LabRam instrument at a laser excitation wavelength of 532 nm. To avoid damage to the samples, a low incident laser power (~0.5 mW) was used. Raman measurements were accomplished on free-standing paper-like films prepared by vacuum filtration of the aqueous RGO dispersions through alumina membrane filters 47 mm in diameter and 0.2 μm of pore size (Whatman).

Fig. S2. Raman spectra of unreduced GO (orange), and GO reduced with PM (red), Arg (blue), His (black), Tryp (olive green), and hydrazine (grey).

Fig. S2 shows first and second-order Raman spectra of GO, paper-like RGO films obtained from RGO dispersions reduced with some selected bioreductans, and a RGO film obtained with hydrazine, as a reference. All these first-order Raman spectra show the two bands expected for any carbon material (from graphitic to amorphous carbon) [5]. Indeed, the first order spectrum of disordered graphite shows two main features at 1580-1600 cm^{-1} (G band) and ~1350 cm^{-1} (D band), which are assigned to zone center phonons of E_{2g} symmetry and K-point phonons of A_{1g} symmetry,

respectively [5]. Such modes are originated by in-plane bond stretching of pairs of sp^2 carbons (aromatic or not) and to breathing of six-fold aromatic rings, respectively, and also dominate the Raman spectrum of amorphous carbon [5].

While in perfect graphite, the D band does not appear because it is symmetry-forbidden, the band is activated by defects in disordered graphite and thus, the intensity ratio of D to G band can be used as an indicator of the graphitic disorder. The I_D/I_G value for the starting material in this series (GO) is ~1.5 [2], while the corresponding ratio for the RGO films obtained with the bioreductants is 1.7-1.8 (see Table S1), i. e., there is an increased I_D/I_G following reduction, as has been previously reported for other reductions of GO [6-10]. In the case of reduction with hydrazine, it has been previously reported that the I_D/I_G ratio remains approximately constant upon reduction [2] (see Table S1) or increases sligthly [6]. The increase in the I_D/I_G upon reduction would be unexpected if both GO and RGO were purely graphitic non-amorphous materials. However, as heavily functionalized GO must have a certain degree of amorphization (sp^3 character), a non-monotonically decrease in I_D/I_G could be expected [2, 5].

For the sample reduced with hydrazine, two shoulders appear for bands D and G, at ~1200 cm-1 and at ~1620 cm-1 (known as D' band), respectively. These additional features are typical of disordered graphite and thus point to a slightly less amorphous structure for this material than for the rest of RGO samples.

The second-order Raman spectra are shown in the 2300-3300 cm^{-1} range in Fig. S2 and, in more detail, in Fig. S3. Four well-defined features would be expected for common graphite: G* band (~ 2460 cm^{-1}) assigned to a combination mode of optical and acoustic phonons; G´ peak (~ 2695 cm^{-1}), which is the overtone of the D band (for this reason, it is usually referred to as the 2D band); ~2950 cm^{-1} (D+G band, a combination mode of the D and G bands) and ~3190 cm^{-1} (2D´ band, overtone of the D´ band) [11]. However, as can be seen in Fig. S3, the second-order spectra of the RGO paper-like films obtained with different bioreductants are very similar and consist of a broad band over the whole wavenumber range where three maxima can be distinguished. This observation points to a high degree of structural disorder in the RGO samples: (i) the G* band, a relatively weak but well-defined feature in highly ordered graphitic structures, does not appear in any of the samples as it tends to fade away and/or broaden in the presence of significant amounts of disorder; (ii) while the 2D band is the main feature for graphite, the D+G band, which is exclusively induced by

defects and is not present in highly ordered graphite, is the most prominent feature for all these RGO samples; (iii) the 2D´ peak is broader than would be expected for a graphitic sample, most of all for the utterly disordered GO.
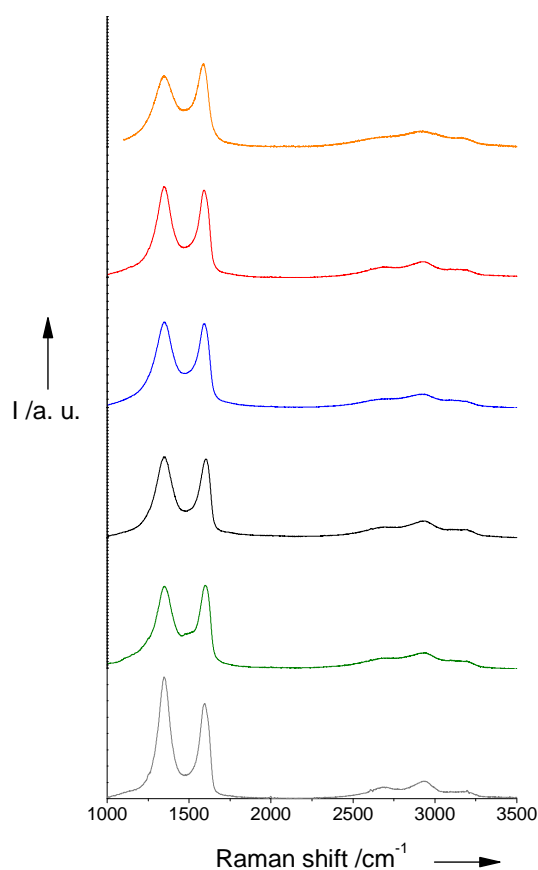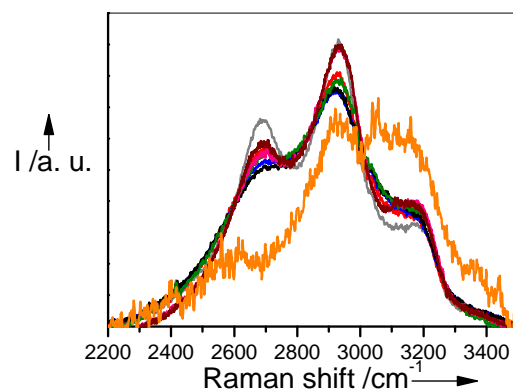

Fig. S3. Second-order Raman spectra of unreduced GO (orange), and GO reduced with PM (red), Arg (blue), His (black), Tryp (olive green), and hydrazine (grey).

The 2D line shape and location allows distinguishing monolayer graphene from few-layer graphene stacked in the Bernal (AB) configuration, and also distinguishing 3D-ordered crystalline graphite from turbostratic graphite [12]. As the RGO paper-like films in this study were produced by vacuum-assisted assembly of the individual, single-layer sheets (see AFM images in Fig. 5 and the accompanying text in the manuscript) from their aqueous dispersion, the sheets are expected to be randomly piled over each other, leading to turbostratic stacking. Indeed, their broad, Lorentzian-shaped 2D band centred at ~2690-2700 cm^{-1} is typical of turbostratic graphite in which the layers are stacked with rotational disorder [11, 13]. The identification of the number of stacked layers by Raman spectroscopy is only well-established for AB Bernal stacking [12], but not for turbostratic stacking. The absence of strong electronic interlayer coupling makes the 2D band of turbostratic graphite similar to that of monolayer graphene in that it is a single Lorentzian. However, while the expected width for the 2D band of monolayer graphene would be ~25 cm^{-1}, it is ~45-60 cm^{-1} for these RGO samples, as expected for turbostratically stacked samples [12]. Furthermore, the expected wavenumber for monolayer graphene would be ~2680 cm^{-1} vs. ~2700 cm^{-1}, for tusbostratic graphite. Finally, the 2D band of monolayer graphene would be expected to be more intense that the G band, while the opposite is expected for graphite.

The broad, weak 2D band of the GO paper-like film prepared in this work also indicates turbostratic stacking.

1.3. X-ray diffraction

X-ray diffraction (XRD) was performed on a Bruker D8 Advance diffractometer using Cu Kα radiation (λ = 0.154 nm) at a step size and time of 0.02° (2θ) and 1 s, respectively. Free-standing paper-like films prepared by vacuum filtration were analysed by XRD.

Fig S4 shows diffractograms of RGO paper obtained with different biomolecules together with those of GO and RGO paper obtained though reduction with hydrazine. XRD provides indirect information on the reduction of the RGO dispersions, as it is expected that, the better the degree of reduction, the more compact the stacking of RGO in paper-like films should be, yielding decreased interlayer spacings. The diffactogram of GO shows a diffraction peak at 2θ~ 11°, which yields an interlayer distance d_{002} of 0.7-0.8 nm consistent with previous reports from the literature [14] (see Table S1 below). The RGO papers yielded low intensity, broad 002 peaks, as previously found for materials obtained with a similar method [8, 14]. Their d_{002} values were in the 0.36-0.38 nm range, still far from 0.34 nm, the expected value for graphite. For the materials obtained with B_2, B_2 salt, Arg and Tryp, there is an additional diffraction peak at 2θ~ 9-12 °, corresponding to interlayer distances in the 0.73-0.96 nm range that is attributed to the presence of some residual amount of bioreductant and/or its oxidized form intercalated between the RGO sheets. A similar result was recently obtained when dextran was used as a reductant of GO [9]. In the case of B_2 and B_2 salt, this result could be anticipated from their characterization with TGA and ATR-FTIR spectroscopy (see main text).

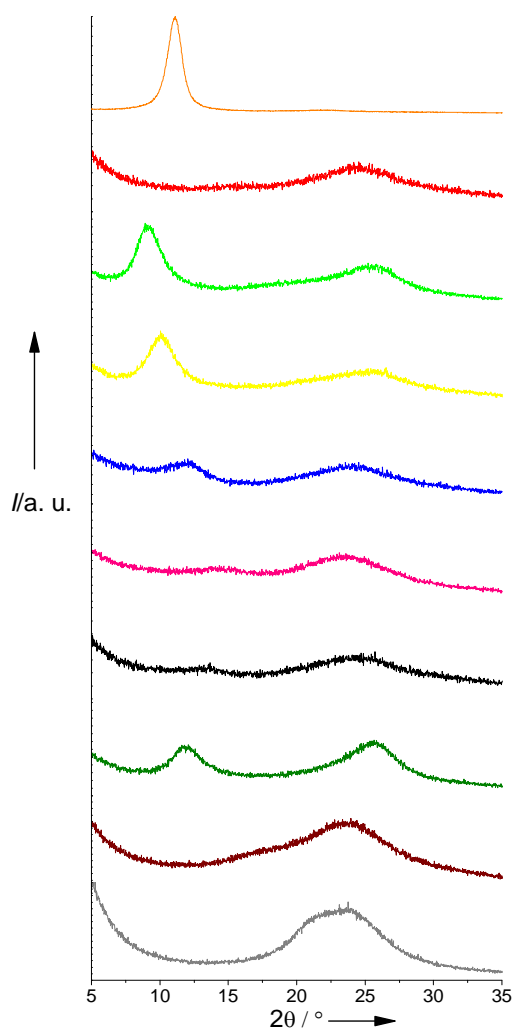**Figure S4.** X-ray diffractograms of paper-like films obtained by vacuum-filtration of dispersions of unreduced graphene oxide (orange) and graphene oxide reduced with PM (red), B_2 (fluorescent green), B_2 salt (yellow), Arg (blue), GSH (pink), His (black), Tryp (olive green) and Glu (wine). The spectrum of a dispersion of graphene oxide reduced at 95 ℃ with 2 mM hydrazine for 15 min (grey plot) has been added for comparison.

2. Comparison with previously reported RGO obtained with green reductants

Table S1. A comparison of RGO obtained with different green reducing agents on the basis of: (i) the position of the UV absorption maximum for the $\pi\rightarrow\pi^*$ transition of C=C bonds (λ_{max}) obtained by UV-vis absorption spectroscopy; (ii) the intensity ratio of D to G bands (I_D/I_G) from Raman results; (iii) the interlayer distance d_{002} obtained from the XRD diffractograms; (iv) electrical conductivity; (v) sheet resistance (R_s). Hydrazine, a non green but commonly used reductant is added for comparison. N/A stands for not available.

Bioreductant	λ_{max} (nm)	I_D/I_G	d_{002} (nm)	Conductivity (S m^{-1})	R_s (Ω/sq)	Reference
None (graphene oxide)	231	1.43	0.798			[2]
None (graphene oxide)					$\sim 10^{10}\text{-}10^{11}$	[15]
Ammonia	257	N/A		3.24×10^{-1}	5.33×10^5	[3]
Pyridoxine (PN)	267	N/A	N/A	2.63×10^2	8.99×10^2	Present work
Pyridoxamine dihydrochloride (PM)	267	1.7	0.361	2.03×10^2	7.57×10^2	Present work
(-)-riboflavin (B$_2$)	268	N/A	0.356	2.16×10^{-1}	1.70×10^6	Present work
riboflavin 5'-monophosphate sodium salt hydrate (B$_2$ salt)	268	N/A	0.361	3.40×10^{-2}	4.50×10^6	Present work
L-arginine (Arg)	266	1.8	0.369	3.92	4.52×10^4	Present work
L-glutathione (GSH)	264	1.8	0.377	1.31×10^2	1.39×10^3	Present work
L-histidine (His)	265	1.8	0.361	3.83×10^1	6.24×10^3	Present work
L-tryptophan (Tryp)	267	1.8	0.351	1.26×10^2	3.39×10^3	Present work
α-D-glucose (Glu)	267	1.7	0.384	5.39×10^2	2.77×10^2	Present work
α-D-glucose (Glu)	261	N/A	N/A	N/A	N/A	[8]
Dextran	267	1.03	0.445	1.1	N/A	[9]
Melatonin	N/A	N/A	N/A	N/A	8.2×10^5	[16]
Tannins	N/A	1.18	N/A	4.244×10^2	N/A	[17]

Bioreductant	λ_{max} (nm)	I_D/I_G	d_{002} (nm)	Conductivity (S m^{-1})	R_s (Ω/sq)	Reference
Green tea polyphenols	N/A	N/A	N/A	N/A	1.1×10^8	[18]
Green tea polyphenols in the presence of iron	N/A	N/A	N/A	N/A	3.9×10^5	[18]
Gallic acid	N/A	N/A	0.34	33.6	N/A	[19]
Vitamin C	268	N/A	N/A	7.70×10^3	2.78×10^1	[3]
Escherichia coli	N/A	N/A	N/A	N/A	3.4×10^9	[15]
Hydrazine	N/A	1.46	N/A	N/A	N/A	[2]
Hydrazine (optimized conditions)	268	N/A	N/A	9.96×10^3	2.42×10^1	[3]

3. Proposed mechanism

The actual reaction mechanism for the reduction of GO with most reductants is still an open question even in the case of those most widely employed to this end (e.g., hydrazine) [20]. As for the newly reported bioreductants, there is a great amount of literature on the oxidation mechanism of these bioreductants in biological media, which could however not apply in comparatively high temperatures (T~95 ° C) and different pH and in absence of specific enzymes. The identification of oxidation products for such bioreductants the by high performance liquid chromatography/mass spectrometry, which will help to establish the actual reaction taken place, is currently being undertaken by us, and the results will be documented elsewhere. However, on the basis of what has been previously reported in the literature for other bioreductants [16, 17, 21], we suggest here possible reaction mechanisms for some of them. In what follows, GO is represented by its most abundant functionalities, i. e., hydroxyl and epoxy groups in its basal plane.

3.1. Pyridoxine (PN) and pyridoxamine (PM)

It is expected that the oxidation of PN and PM will yield an aldehyde (pyridoxal). In the case of PN, the oxidation semi-reaction can be expressed as follows:
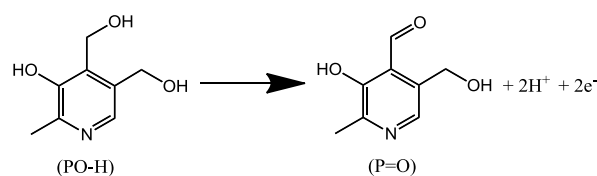
PM also yields pyridoxal, as can be easily detected by UV-vis absorption spectroscopy, (see Fig. S5). As the compounds can be in cationic, neutral, zwitterionic or anionic form depending on the pH, care must be taken with this parameter. According to the literature, at pH=10, the anionic forms of pyridoxine and pyridoxamine both show absorption maxima at 245 and 310 nm while the anionic form of pyridoxal shows maxima at 240 and 302 nm [22]. The spectra of the filtrates of GO dispersions before (cyan plot in Fig. S5) and after reduction with PM (blue plot) correspond respectively to PM and pyridoxal.
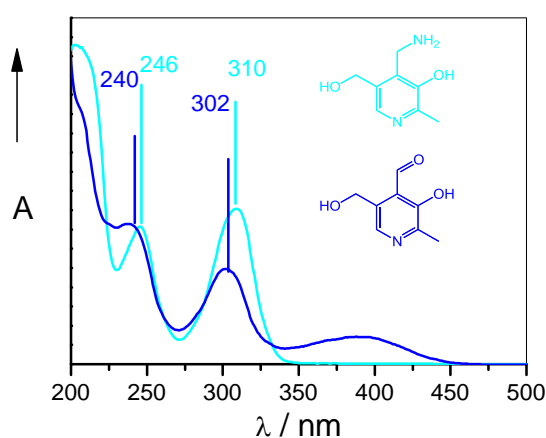
Figure S5. Normalized UV-vis absorption spectra of the filtrate of a 0.1 g mL^{-1} graphene oxide dispersion with 0.25 mM PM, before (cyan) and after (blue) heating at 95 ° C for 8 hours.

We propose a similar mechanism for the reduction of GO to those previously speculated in the case of hydrazine [6], vitamin C [21] and tannins [17], i. e., S_N2 nucleophilic reaction followed by thermal elimination. In the case of PN, the reaction pathway could be as follows for epoxy groups:
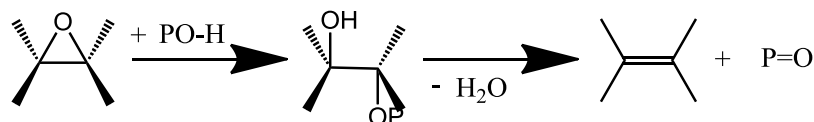
And hydroxyl groups in GO:
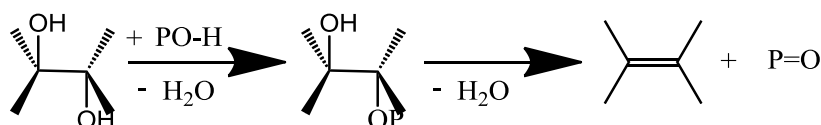
3.2. Arginine
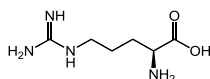
In the case of arginine, the oxidation semirreaction could be:
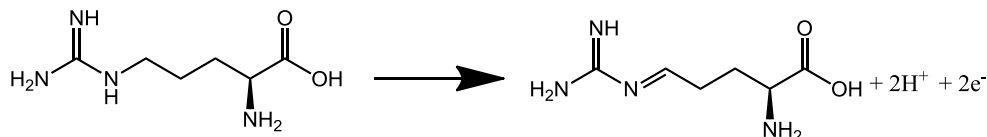
The mechanism for the reduction of epoxy groups could be similar to the one previously proposed for hydrazine [6]:
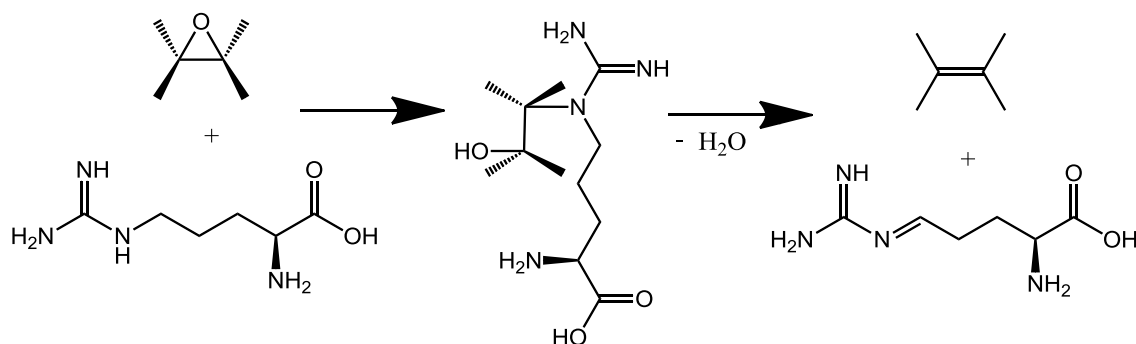
3.3. Glutathione (GSH)
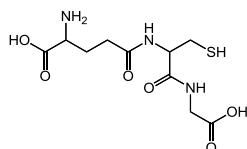
Generally speaking, disulfide bonds are usually formed from the oxidation of the sulfhydril/thiol/SH groups ($S^{2-/}$oxidation state $^{-2}$ to S_2^{2-}/oxidation state $^{-1}$):

$$2\ RSH \rightarrow RSSR + 2H^+ + 2e^-$$

A variety of oxidants promote this reaction including air and H_2O_2. GO contains hydroxyl and epoxy groups in its basal planes which could be reactive enough.

In physiological conditions GSH is oxidised to glutathione disulfide (GSSG):

(G-SH) (G-S-S-G) $+ 2 H^+ + 2e^-$
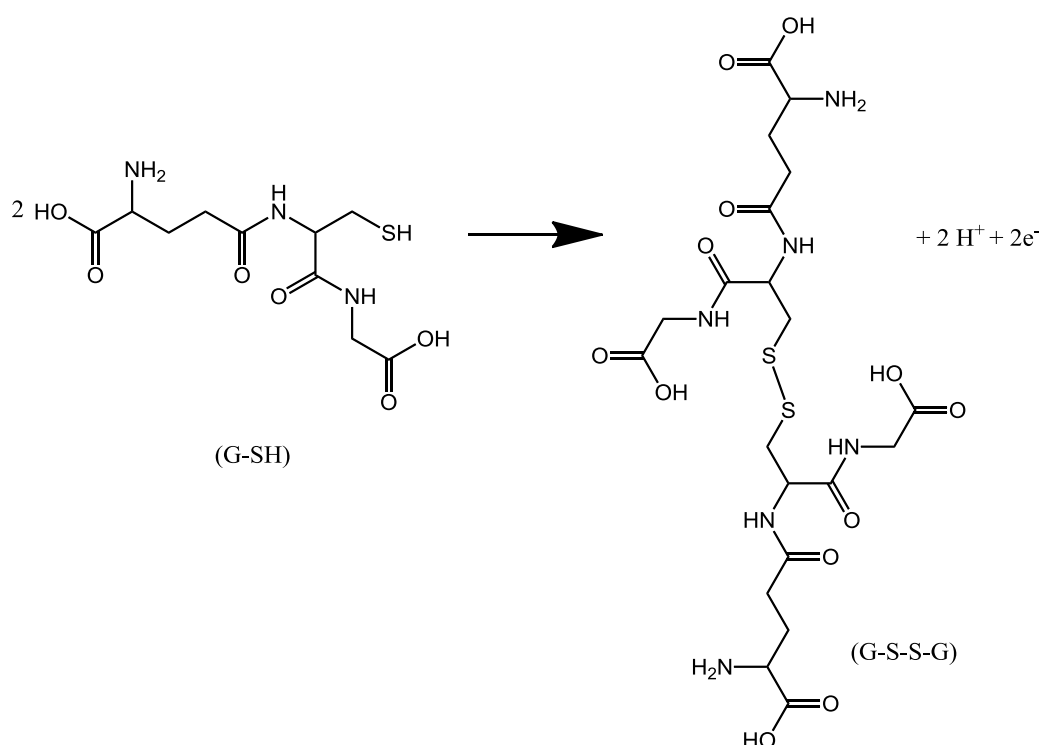
An enzyme is needed in such conditions but it might not be needed at higher temperatures (~95 ° C in our case). Indeed, Pham et al., who first used GSH as reductant for GO, proposed such reaction [23].

The mechanisms for epoxy and hydroxyl reduction could be two-step S_N2 nucleophilic reactions followed by one step of thermal elimination:
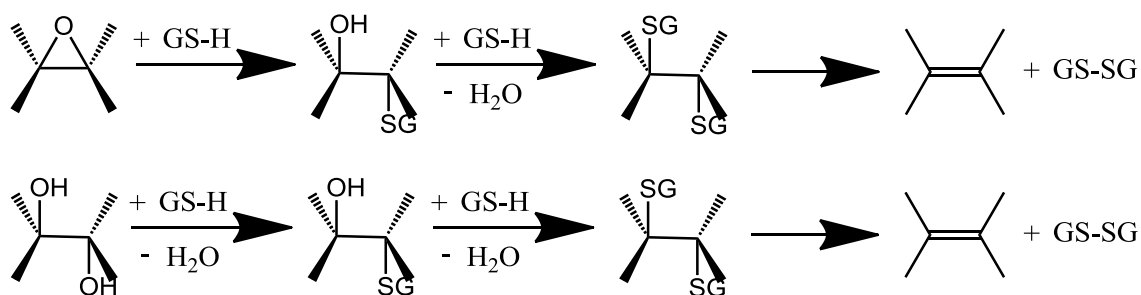
The other (non successful) S-containing aminoacid we have tried (methionine), S is not in thiol form so that this possibility is not available.
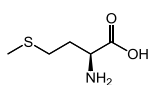
3.4. Histidina
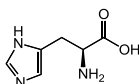
The electrochemical oxidation products of histidine in alkaline medium have been determined to be carbon dioxide, ammonia, formic acid and imidazole [24]. The oxidation reaction can be expressed as follows [25]

$$+ 2OH^- \rightarrow e^- + CO_2 + NH_3 + 2HCOO^- +$$
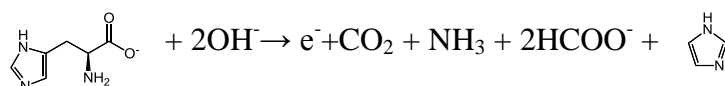
3.5. Tryptophan (Tryp)
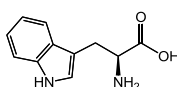
Tryptophan could suffer a similar oxidation process to those suffered by melatonin [26], i. e., either:

$$+ 2H_2O \longrightarrow \qquad + 2H^+ + 2e^-$$

or:

$$2 \qquad \longrightarrow \qquad + 2H^+ + 2e^-$$
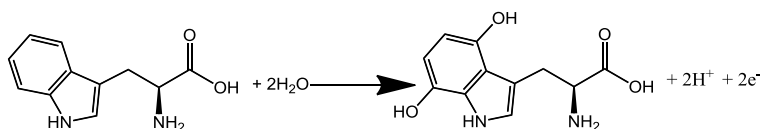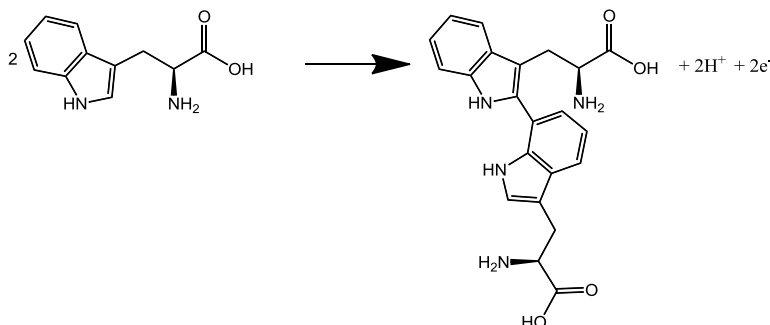
The mechanisms for the reduction of epoxy and hydroxyls in the basal plane would be those involving the aromatic part that this molecule has in common with melatonin and that were previously proposed by Esfandiar et al. [16].

3.6. Glucose

Glucose has been previously reported as reducing agent for GO [8]. The oxydized product is gluconic acid. The oxidation semireaction in basic medium is:
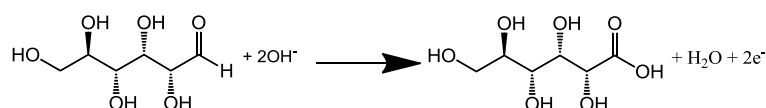
$$+ 2OH^- \longrightarrow \qquad + H_2O + 2e^-$$

4. Comparison of areal rate constants obtained for the reduction of *p*-nitrophenol with NaBH$_4$ using a number of Ag NP-based catalysts.

To allow comparison of the catalytic activities of our RGO-Ag NP hybrids on an equal footing and also to compare them with previously reported values measured for the same reaction using other Ag NP-based catalysts, the apparent rate constants were normalized to the surface area of silver employed per unit volume of dispersion (areal rate constant), and the results are collected in Table S2 along with previously reported values measured for the same reaction using other Ag NP-based catalysts [26-35]. To the best of our knowledge, the present Arg- and PM-derived RGO-Ag NP hybrids exhibit the highest catalytic activities that have ever been documented for Ag NPs in this reaction (areal rate constants ~3-5 times higher than the previous largest values). By contrast, the performance of the His-derived hybrids is comparable (slightly lower) to that of the standard, citrate-capped Ag NPs.

Table S2. Areal rate constants obtained for the reduction of *p*-nitrophenol with NaBH$_4$ using a number of Ag NP-based catalysts.

Catalytic system	Areal rate (L m^{-2} s^{-1})	Reference
RGO-supported Ag NPs prepared with Arg	7.61	Present work
RGO-supported Ag NPs prepared with PM	4.63	Present work
RGO-supported Ag NPs prepared with His	0.56	Present work
Colloidal, dextran T500-stabilized Ag NPs	1.41	[28]
Commercial citrate-caped Ag NPs	0.85	Present work
Ag NP-polyethyleneimine derivative composite	0.57	[29]
Ag NPs embebbed in polymeric microgel	0.12-0.20	[30]
Colloidal, aminosilicate-stabilized Ag NPs	0.08-0.20	[31]
Chitosan-Ag NP composite	0.15	[32]
Ag NPs on polymer-derived carbon nanofibers	0.15	[33]
Ag NPs in polyelectrolyte brush particles	0.08	[34]
Ag NPs in core-shell polymeric microgel	0.05	[27]
Spherical Ag NPs	0.02	[35]

5. Characrterization of reduced graphene oxide-gold nanoparticle hybrids

5.1. UV-vis absorption spectroscopy

After heating a dispersion of 0.1 g mL^{-1} graphene oxide at 95 ºC for 5 hours with 1 mM pyridoxamine, its color changes from brown-yellow to reddish-black in the

presence of 0.15 mM HAuCl₄. The UV-vis absorption spectrum of the resulting dispersion revealed the appearance of a feature at ~520 nm (Fig. S5), which can be ascribed to the well-known surface plasmon resonance band characteristic of metallic gold nanostructures [36].
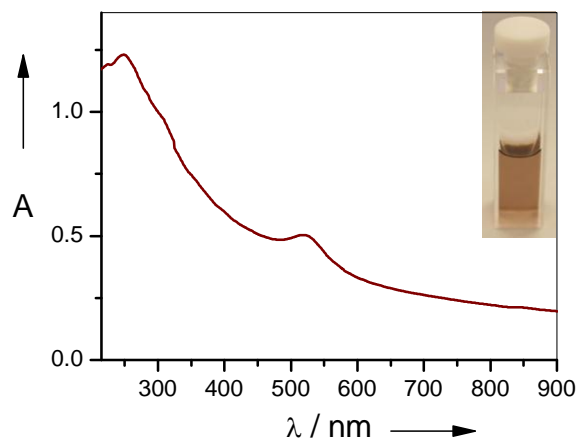
Figure S6. UV-vis absorption spectrum of a 0.1 g mL^{-1} graphene oxide dispersion reduced with 1 mM pyridoxamine in presence of 0.15 mM HAuCl₄. Inset: digital picture of the dispersion.

5.2. *Scanning transmission electron microscopy (STEM)*

Microscopic characterization indicated that gold was present in the form of nanoparticles exclusively associated to the graphene sheets. The particle size was estimated to be ~25 nm.
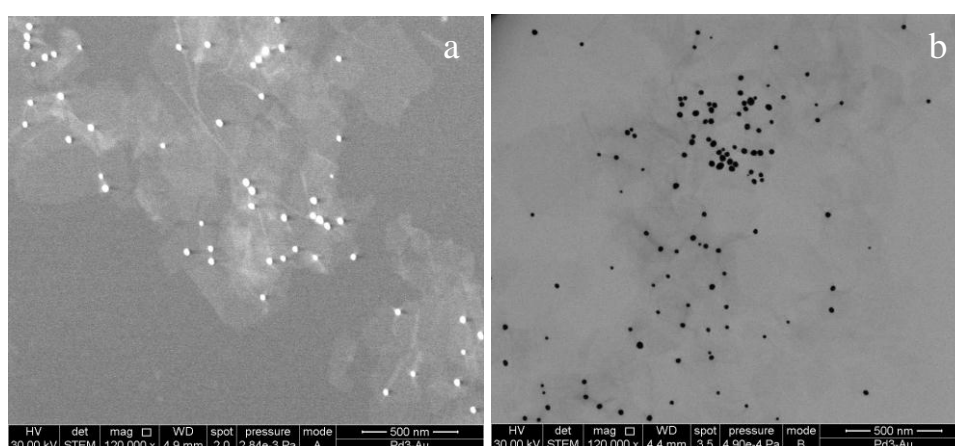
Figure S7. Dark-field (a) and bright-field (b) STEM images of a reduced graphene oxide-gold nanoparticle hybrid prepared with 1 mM pyridoxamine and 0.15 mM HAuCl₄.

References

[1]   Paredes JI, Villar-Rodil S, Martínez-Alonso A, Tascón JMD. Graphene oxide dispersions in organic solvents. Langmuir 24 (2008), 10560-10564.

[2]   Paredes JI, Villar-Rodil S, Solís-Fernández P, Martínez-Alonso A, Tascón JMD. Atomic force and scanning tunneling microscopy imaging of graphene nanosheets derived from graphite oxide. Langmuir 25 (2009), 5957-5968.

[3]   Fernández-Merino MJ, Guardia L, Paredes JI, Villar-Rodil S, Solís-Fernández P, Martínez-Alonso A, Tascón JMD. Vitamin C is an ideal substitute for hydrazine in the reduction of graphene oxide suspensions. J. Phys. Chem. C 114 (2010), 6426-6432.

[4]   Guardia L, Fernández-Merino MJ, Paredes JI, Solís-Fernández P, Villar-Rodil S, Martínez-Alonso A, Tascón JMD. High-throughput production of pristine graphene in an aqueous dispersion assisted by non-ionic surfactants. Carbon 49 (2011), 1653-1662.

[5]   Ferrari AC, Robertson J. Interpretation of Raman spectra of disordered and amorphous carbon. Phys. Rev. B 61 (2000), 14095-14107.

[6]   Stankovich S, Dikin DA, Piner RD, Kohlhaas KA, Kleinhammes A, Jia Y, Wu Y, Nguyen ST, Ruoff RS.. Synthesis of graphene-based nanosheets via chemical reduction of exfoliated graphite oxide. Carbon 45 (2007), 1558-1565.

[7]   Tung VC, Allen MJ, Yang Y, Kaner RB. High-throughput solution processing of large-scale graphene. Nat. Nanotechnol. 4 (2009), 25-29.

[8]   Zhu C, Guo S, Fang Y, Dong S. Reducing sugar: new functional molecules for the green synthesis of graphene nanosheets. ACS Nano 4 (2010), 2429-2437.

[9]   Kim Y-K, Kim M-H, Min D-H. Biocompatible reduced graphene oxide prepared by using dextran as a multifunctional reducing agent. Chem. Commun. 47 (2011), 3195-3197.

[10]   Ai K, Liu Y, Lu L, Cheng X, Huo L. A novel strategy for making soluble reduced graphene oxide sheets cheaply by adopting an endogenous reducing agent. J. Mater. Chem. 21 (2011), 3365-3370.

[11]   Pimenta MA, Dresselhaus G, Dresselhaus MS, Cancado LG, Jorio A, Saito R. Studying disorder in graphite-based systems by Raman spectroscopy. Phys. Chem. Chem. Phys. 9 (2007), 1276-1290.

[12]   Malard LM, Pimenta MA, Dresselhaus G, Dresselhaus MS. Raman spectroscopy in graphene. Phys. Rep. 473 (2009), 51-87.

[13]   Cançado LG, Takai K, Enoki T, Endo M, Kim YA, Mizusaki H, Speziali NL, Jorio A, Pimenta MA. Measuring the degree of stacking order in graphite by Raman spectroscopy. Carbon 46 (2008), 272-275.

[14]   Abouimrane A, Compton OC, Amine K, Nguyen ST. Non-annealed graphene paper as a binder-free anode for lithium-ion batteries. J. Phys. Chem. C 114 (2010), 12800-12804.

[15]   Akhavan O, Ghaderi E. Escherichia coli bacteria reduce graphene oxide to bactericidal graphene in a self-limiting manner. Carbon 50 (2012), 1853-1860.

[16]   Esfandiar A, Akhavan O, Irajizad A. Melatonin as a powerful bio-antioxidant for reduction of graphene oxide. J. Mater. Chem. 21 (2011), 10907-10914.

[17]   Lei Y, Tang Z, Liao R, Guo B. Hydrolysable tannin as environmentally friendly reducer and stabilizer for graphene oxide. Green Chem. 13 (2011), 1655-1658.

[18]   Akhavan O, Kalaee M, Alavi ZS, Alavi ZS, Esfandiar A. Increasing the antioxidant activity of green tea polyphenols in the presence of iron for the reduction of graphene oxide. Carbon 50 (2012), 3015-3025.

[19] Wang J, Shi Z, Fan J, Ge Y, Yin J, Hu G. Self-assembly of graphene into three-dimensional structures promoted by natural phenolic acids. J. Mater. Chem. 22 (2012), 22459-22466.

[20] Pei S, Cheng H-M. The reduction of graphene oxide. Carbon 50 (2012), 3210-3228.

[21] Gao J, Liu F, Liu Y, Ma N, Wang Z, Zhang X. Environment-friendly method to produce graphene that employs vitamin C and amino acid. Chem. Mater. 22 (2010), 2213-2218.

[22] Metzler DE, Snell EE. Spectra and ionization constants of the vitamin B_6 group and related 3-hydroxypyridine derivatives. J. Am. Chem. Soc. 77 (1955), 2431-2437.

[23] Pham TA, Kim JS, Kim JS, Jeong YT. One-step reduction of graphene oxide with l-glutathione. Colloid. Surf. A 384 (2011), 543-548.

[24] Ogura K, Kobayashi M, Nakayama M, Miho Y. In-situ FTIR studies on the electrochemical oxidation of histidine and tyrosine. J. Electroanal. Chem. 463 (1999), 218-223.

[25] Liu Z, Xing Z, Zu Y, Tan S, Zhao L, Zhou Z, Sun T. Synthesis and characterization of L-histidine capped silver nanoparticles. Mater. Sci. Eng. C 32 (2012), 811-816.

[26] Crespi F, Ratti E, Trist DG. Melatonin, a hormone monitorable in vivo by voltammetry? Analyst 119 (1994), 2193-2197.

[27] Lu Y, Mei Y, Ballauff M, Drechsler M. Thermosensitive core-shell particles as carrier systems for metallic nanoparticles. J. Phys. Chem. B 110 (2006), 3930-3937.

[28] Eising R, Signori AM, Fort Sb, Domingos JB. Development of catalytically active silver colloid nanoparticles stabilized by dextran. Langmuir 27 (2011), 11860-11866.

[29] Signori AM, Santos KdO, Eising R, Albuquerque BL, Giacomelli FC, Domingos JB. Formation of catalytic silver nanoparticles supported on branched polyethyleneimine derivatives. Langmuir 26 (2010), 17772-17779.

[30] Zhang J-T, Wei G, Keller TF, Gallagher H, Stötzel C, Müller FA, Gottschaldt M, Schubert US, Jandt KD. Responsive hybrid polymeric/metallic nanoparticles for catalytic applications. Macromol. Mater. Eng. 295 (2010), 1049-1057.

[31] Harish S, Sabarinathan R, Joseph J, Phani KLN. Role of pH in the synthesis of 3-aminopropyl trimethoxysilane stabilized colloidal gold/silver and their alloy sols and their application to catalysis. Mater. Chem. Phys. 127 (2011), 203-207.

[32] Murugadoss A, Chattopadhyay A. A 'green' chitosan-silver nanoparticle composite as a heterogeneous as well as micro-heterogeneous catalyst. Nanotechnology 19 (2008), 015603/1 - 015603/3.

[33] Zhang P, Shao C, Zhang Z, Zhang M, Mu J, Guo Z, Liu Y. In situ assembly of well-dispersed Ag nanoparticles (AgNPs) on electrospun carbon nanofibers (CNFs) for catalytic reduction of 4-nitrophenol. Nanoscale 3 (2011), 3357-3363.

[34] Lu Y, Mei Y, Schrinner M, Ballauff M, Möller MW, Breu J. In situ formation of Ag nanoparticles in spherical polyacrylic acid brushes by UV irradiation. J. Phys. Chem. C 111 (2007), 7676-7681.

[35] Rashid MH, Mandal TK. Synthesis and catalytic application of nanostructured silver dendrites. J. Phys. Chem. C 111 (2007), 16750-16760.

[36] Hu M, Chen J, Li Z-Y, Au L, Hartland GV, Li X, Marquez M, Xia Y. Gold nanostructures: engineering their plasmonic properties for biomedical

applications. Chem. Soc. Rev. 35 (2006), 1084-1094.

4.2. Surfactantes para la estabilización coloidal de dispersiones acuosas de óxido de grafeno reducido y grafeno prístino.

Artículo III

Publicado en la revista Carbon: "Investigating the influence of surfactants on the stabilization of aqueous reduced graphene oxide dispersions and the characteristics of their composite filmes".

Artículo IV

Publicado en la revista Carbon: "High-throughput production of pristine graphene in an aqueous dispersion assisted by non-ionic surfactants".

Entre los diferentes métodos existentes para la obtención de grafeno a gran escala investigados hasta el momento, el basado en el óxido de grafito es uno de los que atrae mayor interés. Sin embargo, es necesario tener en cuenta que las dispersiones acuosas de óxido de grafeno reducido sólo son estables bajo ciertas condiciones, a saber: pH básico, concentración de óxido de grafeno relativamente baja, láminas de pequeñas dimensiones y en ausencia de cantidades significativas de electrolitos. En condiciones diferentes a las anteriores (por ejemplo, pH ácido, alta concentración de óxido de grafeno o láminas de gran tamaño), el uso de agentes estabilizadores se convierte en esencial para que las dispersiones no aglomeren y/o precipiten. En el *Artículo III* se realiza un estudio comparativo de la capacidad de una amplia gama de surfactantes para mantener dispersiones de óxido de grafeno reducido estables en agua bajo diferentes condiciones.

Los surfactantes utilizados fueron: ácido pirenobutírico (PBA), deoxicolato de sodio (DOC), taurodeoxicolato de sodio (TDOC), poli (4-estirensulfonato) de sodio (PSS), dodecilbenceno sulfonato de sodio (SDBS), dodecilsulfato de sodio (SDS), 3-[(3-Cholamidopropil)dimetilamonio]-1-propansulfonato hidratado (CHAPS), n-dodecil β-D-maltosa (DBDM), goma arábiga de acacia, Pluronic® P-123 (P-123), polioxietilen (4) dodecil eter (Brij 30), polioxietilen (100) octadecil eter (Brij 700), polioxietilen octil (9-10) fenileter (Triton X-100), polioxietilen sorbitan monooleato (Tween 80), polioxietilen sorbitan trioleato (Tween 85) y polivinilpirrolidona (PVP).

Es un hecho conocido que si la reducción con hidracina de óxido de grafeno se lleva a cabo en un medio con alta fuerza iónica y en ausencia de surfactantes, el material reducido precipita inmediatamente y de forma irreversible. Por ello, a una dispersión acuosa de óxido de grafeno con una alta concentración de KOH se añadieron diversos surfactantes (aniónicos, iónicos y zwitteriónicos) en distintas concentraciones para determinar su capacidad de evitar la aglomeración de las láminas y mantenerlas coloidalmente estables a largo plazo. Igualmente, se realizaron ensayos en medio acuoso a pH 1 con los surfactantes, a fin de comprobar la eficacia de los mismos. Para los surfactantes más eficaces se llevaron a cabo los ensayos en medio ácido y básico a diferentes concentraciones de óxido de grafeno. Se estudió el efecto del tamaño de las láminas de óxido de grafeno en las dispersiones, para lo cual se prepararon dispersiones con láminas de menos de una micra y con láminas de gran tamaño, de varias micras.

Mediante espectroscopía de absorción UV-vis se comparó la eficacia de los distintos surfactantes para estabilizar coloidalmente las láminas de óxido de grafeno en términos de la cantidad de material que permanecía en el sobrenadante de las dispersiones tras someterlas a un proceso de ultracentrifugación. En casi todos los casos, cuanto mayor era la concentración de surfactante utilizada, mejores resultados se obtenían (mayor concentración de material en el sobrenadante), lo que en principio se atribuyó a una mayor concentración de moléculas de surfactante adsorbidas sobre las láminas de óxido de grafeno reducido, las cuales adquieren así una mayor estabilidad coloidal.

En medio básico, todos los surfactantes aniónicos probados mostraron buena eficacia, con excepción del SDS. Es de esperar que un surfactante aniónico estabilice el óxido de grafeno reducido porque su segmento hidrófobo se adsorbe sobre los dominios hidrófobos del óxido de grafeno reducido, mientras que su parte polar se extiende hacia el agua y proporciona a las láminas cargas negativas, estabilizándolas por repulsión electrostática. En medio ácido las condiciones son más adversas para la estabilización de las dispersiones con surfactantes aniónicos. En este caso, se debe distinguir entre surfactantes basados en aniones permanentes, que pueden seguir siendo capaces de estabilizar las láminas por repulsión electrostática incluso a valores de pHs muy bajo, y surfactantes basados en aniones mucho más dependientes del pH, que a valores de pH suficientemente bajos se protonan y dejan de proporcionar repulsión electrostática.

La capacidad de los surfactantes no iónicos para estabilizar láminas de óxido de grafeno reducido en medio acuoso se debe principalmente a la presencia de largas cadenas polares, frecuentemente constituidas por óxidos de etileno. En principio, se espera que la parte hidrófoba del surfactante interactúe con las láminas de óxido de grafeno reducido, mientras que los átomos de oxígeno de su sección polar forman puentes de hidrógeno con las moléculas de agua del entorno, estabilizando así la dispersión. Sin embargo, teniendo en cuenta que el óxido de grafeno reducido no es exclusivamente hidrófobo (ya que presenta pequeñas regiones fuertemente oxidadas), pueden producirse puentes de hidrogeno entre las láminas y las secciones polares del surfactante. En principio, es de esperar una menor influencia del pH sobre la capacidad estabilizadora de los surfactantes no iónicos. Aunque en líneas generales esto resultó ser cierto, se observaron algunas excepciones.

La combinación de los surfactantes con las láminas de óxido de grafeno reducido permite formar filmes híbridos mediante filtración de las dispersiones, cuyas características fueron investigadas. Las medidas de conductividad eléctrica sugirieron que la presencia de surfactante reduce el grado de contacto eléctrico entre láminas vecinas, disminuyendo así la movilidad de los portadores de carga eléctrica y por tanto los valores de conductividad. La presencia de surfactante intercalado se puso de manifiesto mediante difracción de rayos X y análisis termogravimétrico.

Se llevó a cabo una investigación preliminar del comportamiento electroquímico de los filmes híbridos de óxido de grafeno reducido-surfactante mediante voltametría cíclica, que indicó que la capacidad específica de la mayoría de los filmes es mucho menor que la del filme libre de surfactante, exceptuando los casos de filmes preparados con Tween 80 y PSS, que dieron lugar a capacidades específicas significativamente mejoradas. En el caso del SDS, los valores de la capacidad específica son muy similares a los obtenidos para los filmes libres de surfactante, este efecto puede atribuirse a que este surfactante se encuentra intercalado en menor proporción.

A pesar de que el método basado en el óxido de grafito es uno de los más estudiados para la obtención de grafeno, el tipo de grafeno obtenido posee una gran cantidad de defectos estructurales así como grupos funcionales oxigenados residuales que no han podido ser eliminados. Un método alternativo que permite la obtención de grafeno libre de defectos y óxidos en dispersión coloidal se basa en la exfoliación directa de grafito prístino en agua mediante ultrasonidos. El principal requerimiento de

dicho método es el uso de un agente dispersante que estabilice las láminas altamente hidrófobas de grafeno prístino. En el *Artículo IV* se realiza un estudio sobre la capacidad y eficacia de distintos surfactantes iónicos y no iónicos para conseguir dispersiones estables de grafeno prístino en agua mediante exfoliación de grafito por ultrasonidos.

Los surfactantes utilizados son: PBA, DOC, TDOC, PSS, SDBS, SDS, CHAPS, DBDM, goma arábiga de acacia, P-123, Brij 30, Brij 700, Triton X-100, Tween 80, Tween 85, PVP y bromuro de hexadeciltrimetilamonio (CTAB).

Los ensayos se realizaron partiendo de dispersiones de grafito prístino en agua, las cuales se sometieron a sonicación y se centrifugaron en presencia de distintas concentraciones de los surfactantes. Con el fin de obtener concentraciones finales de grafeno razonables, se optó por utilizar elevadas concentraciones de partida de grafito Mediante espectroscopía de absorción UV-vis se comparó la eficacia de los distintos surfactantes, pudiendo estimarse para cada uno de ellos la concentración de grafeno en la dispersión final. Se obtuvieron concentraciones superiores a 0.10 mg ml^{-1} para distintos surfactantes, e incluso entre 0.5 y 1 mg ml^{-1} en el caso de Tween 80 y P-123. Los resultados indican que los surfactantes no iónicos son más eficaces que los iónicos, es decir, la repulsión estérica parece ser más eficiente que la repulsión electrostática para estabilizar láminas de grafeno prístino en agua. Se estudió asimismo el efecto del tiempo de sonicación en la concentración final de grafeno, obteniéndose una mayor dependencia con dicho parámetro en el caso del P-123. Para las dispersiones más representativas se estudió el grado de exfoliación, la calidad estructural y el tamaño de las láminas obtenidas mediante AFM y TEM, concluyendo que las dispersiones están formadas por láminas monocapa o de unas pocas capas, con un tamaño lateral de unos pocos centenares de nm y una muy alta calidad estructural.

Las dispersiones obtenidas permitieron la preparación de estructuras macroscópicas que pueden ser utilizadas potencialmente en aplicaciones reales. Así, se prepararon filmes e hidrogeles a partir de las dispersiones más representativas. Los filmes fueron estudiados mediante SEM, AFM y STEM, comprobándose su homogeneidad y la estructura libre de defectos de sus láminas. También se realizaron medidas de conductividad eléctrica, constatándose la disminución de la conductividad eléctrica de los filmes con el aumento de su contenido en surfactante.

Investigating the influence of surfactants on the stabilization of aqueous reduced graphene oxide dispersions and the characteristics of their composite films

(Carbon 50 (2012), 3184-3194)

M. J. Fernández-Merino[a], J. I. Paredes[a], S. Villar-Rodil[a], L. Guardia[a], P. Solís-Fernández[a], D. Salinas-Torres[b], D. Cazorla-Amorós[b], E. Morallón[b], A. Martínez-Alonso[a], and J. M. D. Tascón[a]

[a]Instituto Nacional del Carbón, CSIC, Apartado 73, 33080 Oviedo, Spain

[b] Instituto Universitario de Materiales, Universidad de Alicante, Apartado 99, 03080 Alicante, Spain

Abstract

The stabilization of reduced graphene oxide (RGO) sheets in aqueous dispersion using a wide range of surfactants of anionic, non-ionic and zwitterionic type has been investigated and compared under different conditions of pH, surfactant and RGO concentration, or sheet size. The observed differences in the performance of the surfactants were rationalized on the basis of their chemical structure (e.g., alkylic vs. aromatic hydrophobic tail or sulfonic vs. carboxylic polar head), thus providing a reference framework in the selection of appropriate surfactants for the processing of RGO suspensions towards particular purposes. RGO-surfactant composite paper-like films were also prepared through vacuum filtration of the corresponding mixed dispersions and their main characteristics were investigated. The composite paper-like films were also electrochemically characterized. Those prepared with two specific surfactants exhibited a high capacitance in relation to their surfactant-free counterpart.

1. Introduction

Owing to its exceptional physical properties and prompted by its first experimental isolation in 2004, research on both fundamental and application-related aspects of graphene has been gaining significant momentum over the last few years [1-5]. The potential of graphene in a number of technological applications (e.g., electronic devices [6], sensors [7], composite materials [8] or energy generation and storage [9]) has already been demonstrated. However, the actual implementation of this novel two-

dimensional material in practical uses currently faces several challenges, the first of which pertains to its large-scale preparation and processing. Among the different methods towards the mass production of graphene being investigated at present [5], the one based on reduction of exfoliated graphite oxide has drawn considerable attention. Although this type of graphene exhibits a lower structural quality than that of graphenes repared by other methods, it also boasts a number of features that are important from a utilitarian point of view: its production is massively scalable, it is dispersible as individual single-layer sheets in aqueous and organic media, and is particularly suitable towards chemical functionalization [5, 10, 11].

In many cases, the preparation of graphene from graphite oxide is carried out in the aqueous phase, involving exfoliation of the graphite oxide particles via sonication or vigorous stirring to yield a suspension of single-layer sheets (graphene oxide sheets), which are then chemically reduced using, e.g., hydrazine, sodium borohydride or vitamin C [5, 10, 12]. The presence of a large number of hydrophilic oxygen groups makes unreduced graphene oxide sheets to readily form stable suspensions in water, but the same does not hold true for their reduced counterparts, which tend to agglomerate and precipitate, thus loosing their attraction as individual objects and hampering further processing of the material. The main reason for this behavior is the increased hydrophobicity of the sheets that results from removal of most of their oxygen-containing groups during the reduction step.

Even though it has been shown that stable aqueous suspensions of reduced graphene oxide (RGO) sheets can be produced without the need of adding foreign stabilizers, this is only possible under stringent conditions of basic pH, relatively low concentration and small size of the sheets, and absence of significant amounts of any electrolyte [13]. In this case, stability is due to electrostatic repulsion between sheets afforded by their residual oxygen-containing groups, many of which become negatively charged (deprotonated). Under different conditions to those described above (e.g., acidic pH, high concentration of RGO or large sheet size), the use of dispersants becomes essential to keep the suspension stabilized. During the last years, a number of anionic surfactants [14-19] and polymers (including polyelectrolytes and biopolymers) [20-29] have been used towards this end. However, the performance of different dispersants has not generally been compared, and therefore it is currently not known which of them are the most efficient in stabilizing RGO in the aqueous phase and how

their efficiency is affected by some experimental parameters. In the present work, we have investigated and compared the ability of a wide range of dispersants to render stable suspensions of RGO sheets in water under several different conditions. This type of information should assist in selecting appropriate stabilizers for specific purposes in the manipulation and processing of RGO and RGO-based materials. Likewise, materials that combine RGO sheets with surfactants can be useful for a number of potential applications [21, 30, 31]. Hence, we also report here the preparation and characterization of RGO-surfactant composite paper-like films and explore their electrochemical behavior.

2. Experimental

2.1. Preparation and processing of reduced graphene oxide dispersions

Graphite oxide was produced from natural graphite powder (Fluka 50870) by the Hummers method [32]. The oxidized product was purified by rinsing with 10% HCl solution and then thoroughly washing with large amounts of Milli-Q water. From this purified material, two different batches of aqueous graphene oxide suspension were prepared for use in the subsequent experiments. One of them was made by suspending graphite oxide in water, sonicating in an ultrasound bath cleaner (J.P. Selecta Ultrasons system, 40 kHz) for 2 h, centrifuging (Eppendorf 5424 microcentrifuge, 8000g, 5 min) and finally collecting the top ~75% of the supernatant. This procedure afforded a graphene oxide dispersion made up of sheets with typical lateral sizes below 1 µm. For the other batch, the sonication and centrifugation steps were replaced by stirring with a magnetic bar for 10 days and then allowing the resulting suspension to settle down. Compared to sonication, stirring is a mild process that significantly avoids tearing and breaking up the exfoliated material, thus leading to aqueous suspensions with larger sheets (typically 5–10 µm). The concentration of both suspensions was estimated by UV–vis absorption spectroscopy following a previously reported methodology [33].

The sonicated suspension was used as a testbed to study and compare the efficiency of a number of different surfactants of general use towards stabilizing the chemically reduced sheets. Fig. 1 shows the chemical structures, names and abbreviations of the surfactants employed in this work. A given surfactant was added to an as-prepared, 0.1 mg mL^{-1} aqueous graphene oxide dispersion so as to reach a

concentration of either 0.05 or 0.50% wt/vol. The surfactant concentration was not optimized, but was above the critical micelle concentration (cmc) in all cases except for SDS at 0.05% wt/ vol (cmc of SDS ~0.24% wt/vol). Subsequently, KOH, which provides a basic medium (pH ~12) favorable for reduction, and the reducing agent hydrazine monohydrate were added to the solution at a concentration of 100 mM and 2.1 mM, respectively. The resulting mixture was heated at 95 ºC for 1 h, after which the yellow–brown color characteristic of the unreduced graphene oxide dispersion turned completely black, which is indicative of successful deoxygenation of the sheets. To compare the suspending ability of the surfactants in basic medium, the as-reduced dispersionswere centrifuged at 10,000g for 10 min and the absorbance of the supernatant at 450 nm determined by UV–vis absorption spectroscopy, thus providing a relative measure of the amount of RGO that each surfactant can retain in the solution. Such wavelength was chosen to avoid the contribution to absorption from the surfactant molecules themselves, which is pronounced up to 400 nm for many of them but approaches zero in all cases at 450 nm and above. The efficiency of the surfactants was also evaluated under acidic conditions. In this case, before centrifuging and measuring the absorbance at 450 nm, the pH of the as-reduced suspensions was lowered to ~1 by the addition of HCl solution. Those surfactants that provided the best results were additionally tested for their ability to suspend larger concentrations of reduced graphene oxide sheets (sonicated suspensions) as well as sheets of larger size (stirred suspensions).

Mixed dispersions (250 mL) of RGO and several of the investigated surfactants (0.05% wt/vol), prepared by reduction of graphene oxide (0.1 mg mL^{-1}) in basic medium with hydrazine monohydrate (2.1 mM) and ammonia (26 mM), were processed into RGO-surfactant composite paper-like films by vacuum filtration through polycarbonate membrane filters 47mm in diameter and 0.2 lm of pore size (Whatman). The filtered material was allowed to dry under ambient conditions and finally peeled off the membrane filter.

2.2. Characrterization

UV–vis absorption spectra were recorded with a double-beam Heλios a spectrophotometer, from Thermo Spectronic. X-ray photoelectron spectroscopy (XPS) was carried out on a SPECS system working under 10^{-1} Pa with a monochromatic Al K$_\alpha$

Ionic

1-Pyrenebutyric acid
(PBA)

Sodium deoxycholate
(DOC)

Sodium taurodeoxycholate
hydrate (TDOC)

Poly(sodium 4-styrenesulfonate)
(PSS)

Sodium dodecylbenzene
sulfonate (SDBS)

Sodium dodecyl sulphate
(SDS)

Zwitterionic

3-((3-Cholamidopropyl)
dimethylammonium)-1-
propanesulfonate (CHAPS)

Non-ionic

n-Dodecyl β-D-maltoside
(DBDM)

D-galactose 41-53%   L-arabinose 25-27%   L-rhamnose 10-14%   D-glucuronic acid 12-18%

Gum Arabic from acacia tree

x:y:z=20:70:20

Pluronic® P-123
(P-123)

Polyoxyethylene (4) dodecyl
ether (Brij30)

Polyoxyethylene (100) octadecyl
ether (Brij700)

Polyoxyethylene octyl (9-10) phenyl
ether (Triton X-100)

w+x+y+z=20

Polyoxyethylene sorbitan
monooleate (Tween80)

w+x+y+z=20

Polyvinylpyrrolidone
(PVP)

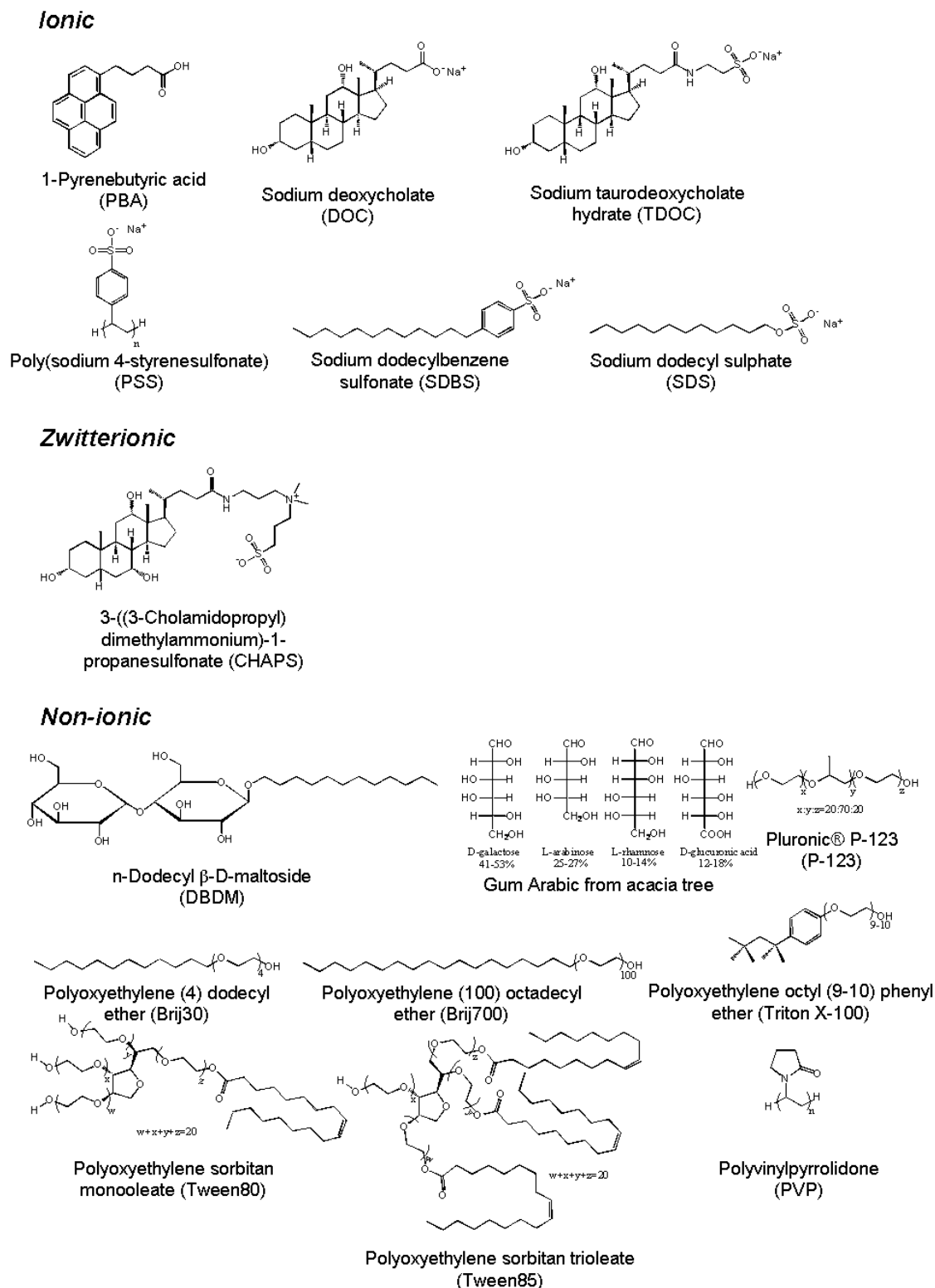Polyoxyethylene sorbitan trioleate
(Tween85)

Figure 1. Chemical structure of the surfactants used in the study together with their names and corresponding acronyms used throughout the text.

X-ray source. Atomic force microscopy (AFM) of RGO sheets from the surfactant-stabilized dispersions was accomplished under ambient conditions (RH ~40%, 22–24 ºC) with a Nanoscope IIIa Multimode apparatus (Veeco Instruments) in the tapping mode of operation and using rectangular Si cantilevers with nominal spring constant of ~40Nm^{-1} and resonance frequency of 250–300 kHz. Samples for AFM imaging were prepared by drop-casting the suspensions onto preheated (~50–60 ºC) highly oriented pyrolytic graphite (HOPG) substrates, which were then thoroughly rinsed with Milli-Q water to sweep the surfactant off the surface and allow better visualization of the RGO sheets. Scanning electron microscopy (SEM) was performed on a Zeiss DSM-942 system operating at 10 kV. The electrical conductivity of the RGO-surfactant composite paper-like films was measured by the van der Pauw method using a home-made setup that consisted of an Agilent 6614C DC power supply and a Fluke 45 digital multimeter. To this end, the paper-like films were cut into 12 x 12 mm^{-2} squares and their thickness evaluated by SEM. Thermogravimetric analysis (TGA) was carried out on Pt crucibles with an SDT Q600 thermobalance under synthetic air flow (100 mL min^{-1}) at a heating rate of 3 ºC min^{-1}. X-ray diffraction (XRD) was accomplished with a Bruker D8 Advance diffractometer using Cu K$_\alpha$ radiation (k = 0.154 nm) at a step size and time of 0.02º (2h) and 1 s, respectively. Electrochemical experiments on the paper-like films were performed in a three-electrode glass cell in 0.5 M H$_2$SO$_4$ solution, with a platinum counter electrode and a reversible hydrogen electrode introduced in the same electrolyte as a reference electrode. The working electrodes were prepared by supporting the paper-like films onto a stainless steel grid. Cyclic voltammograms (CVs) were recorded with a 263A EG&G potentiostat within a potential range from 0 to 1 V at 2 mV s^{-1} scan rate.

3. Results and discussion

When hydrazine reduction of an aqueous graphene oxide suspension is carried out in a medium with high ionic strength (100 mM KOH) in the absence of any surfactants, the reduced material precipitates immediately and irreversibly (see inset to Fig. 2: first and second cuvettes from the left correspond to the suspension before and after reduction, respectively). By contrast, the addition of surfactants to the suspension generally avoids the agglomeration of the RGO sheets and leads to visually homogeneous dispersions whose long-term stability depends on the specific type of surfactant employed, as will be discussed below. For example, the third and fourth

cuvettes from the left in the inset to Fig. 2 show dispersions obtained upon reduction in the presence of 0.05% wt/vol of the anionic surfactant DOC and the non-ionic one Brij 700, respectively. The UV–vis absorption spectra of the DOC- and Brij 700-stabilized RGO suspensions, together with that of their starting, unreduced graphene oxide counterpart are presented in Fig. 2 (green,1 red and orange plots, respectively). These two specific surfactants were chosen because they barely absorb UV light in the wavelength range above 220 nm, so that they do not obscure the spectral features of RGO itself. Upon reduction, we note a red-shift (from ~231 to ~268 nm) of the absorption peak corresponding to $\pi \rightarrow \pi^*$ transitions of C=C chromophore as well as a significant increase of absorbance in the whole wavelength range above 268 nm for both surfactant-stabilized RGO dispersions. This result is consistent with an increased electronic conjugation of the RGO sheets associated to their reduction [13].
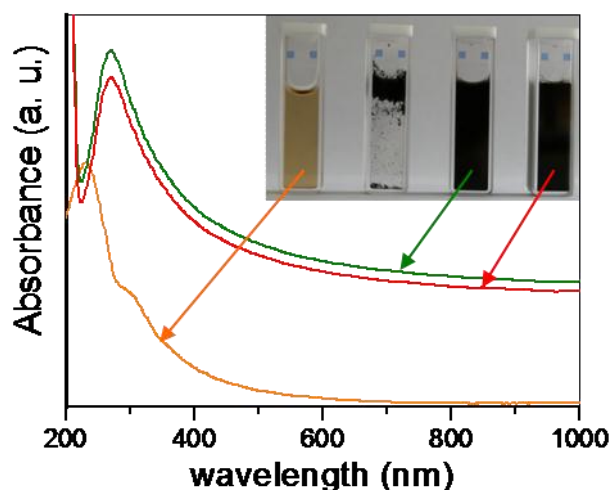

Figure 2. UV–vis absorption spectra for 0.1 mg mL^{-1} unreduced (orange) and reduced graphene oxide dispersions in water stabilized by DOC (green) and Brij 700 (red). Inset: from left to right, digital pictures of aqueous dispersions of graphene oxide, RGO coagulated in a medium with high ionic strength, and the same dispersion stabilized by 0.05% wt/vol of DOC and Brij 700.
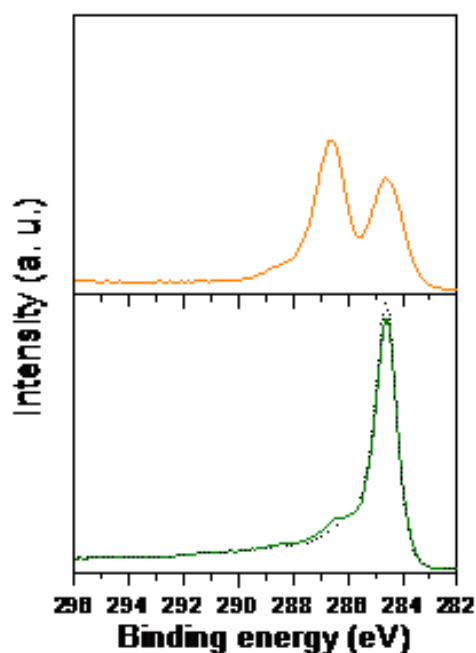
Figure 3. High resolution C1s X-ray photoelectron spectra of graphene oxide (orange plot), RGO obtained from a dispersion stabilized by the surfactant DOC (green plot), and highly reduced graphene oxide taken as a reference sample (black dotted line).

The UV–vis absorption peak position for the sheets reduced in the presence of surfactants (i.e. 268 nm, Fig. 2) was measured to be the same as that reported previously for highly reduced graphene oxide samples [12, 13]. Since the absorption peak position is a good indicator of the extent of reduction of graphene oxide [12], we conclude that the surfactant-stabilized sheets have been efficiently reduced. XPS investigations also confirmed an effective reduction in the presence of surfactant. Fig. 3 shows high resolution C1s spectra for the starting graphene oxide (orange plot), RGO obtained froma DOC-stabilized dispersion (green plot), and a highly reduced graphene oxide taken as a reference sample (black dotted plot), which was obtained through hydrazine reduction without surfactant according to procedures documented before [12]. Preparation of specimens for XPS analysis from the surfactant-stabilized dispersions required special precautions in removing the surfactant, because many of them contain C–O groups and thus their presence prevents a proper assessment of the reduction degree of graphene oxide.To this end, the dispersions were first destabilized by adding ethanol and NaOH until flocculation. The sediment was collected, thoroughly washed with ethanol and centrifuged (20,000g, 5 min) for a number of cycles, and finally

suspended in Milli-Q water and dialyzed for a week using a cellulose membrane. The spectrum of graphene oxide displays three clearly defined bands with the following binding energies and assignments: 284.6 eV, carbon atoms in aromatic, unoxidized sp^2 structures; 286.6 eV, carbons in hydroxyl and epoxy groups, and also possibly in defective structures; and 287.9 eV, carbons doubly bonded to oxygen [34-36]. For the DOC-stabilized RGO sheets, there is a large drop in the intensity of the band associated to singly-bonded oxygen, suggesting a significant deoxygenation of the material. Indeed, such spectrum is identical to that of the highly reduced graphene oxide reference sample (dotted black plot), except for a slightly higher relative intensity at 286.6 eV. Because this difference is remarkably small, we conclude that effective reduction of graphene oxide is not hampered by the presence of DOC. Similar results were obtained for the other surfactants found successful to stabilize the RGO dispersions.

Fig. 4 shows representative AFM images of RGO sheets deposited onto atomically flat HOPG substrates from dispersions stabilized by different selected ionic (DOC and SDBS) and non-ionic (Brij 700 and Tween 80) surfactants, together with superimposed line profiles taken along the marked white lines. The main aim in connection with AFM imaging was to demonstrate that the RGO sheets keep their individual, single-layer nature after hydrazine reduction in the presence of the surfactants and do not agglomerate. To this end, we needed to remove the surfactant molecules from the sheets after their deposition on the HOPG substrate to be able to demonstrate that we had single-layer objects. Surfactant removal was accomplished by thoroughly rinsing the substrate with deionized water. In all cases, the appearance of the observed objects (lateral size (from a few to several hundred nm), shape (irregular polygons) and thickness (~1 nm)) is the same as that of the single-layer, unreduced graphene oxide sheets (images not shown) [33], which indicates that agglomeration of the RGO sheets was effectively prevented by the use of these surfactants. The small particles (yellow/ white dots) that are occasionally seen on the sheets or at their edges can be attributed to some remnants of surfactant.
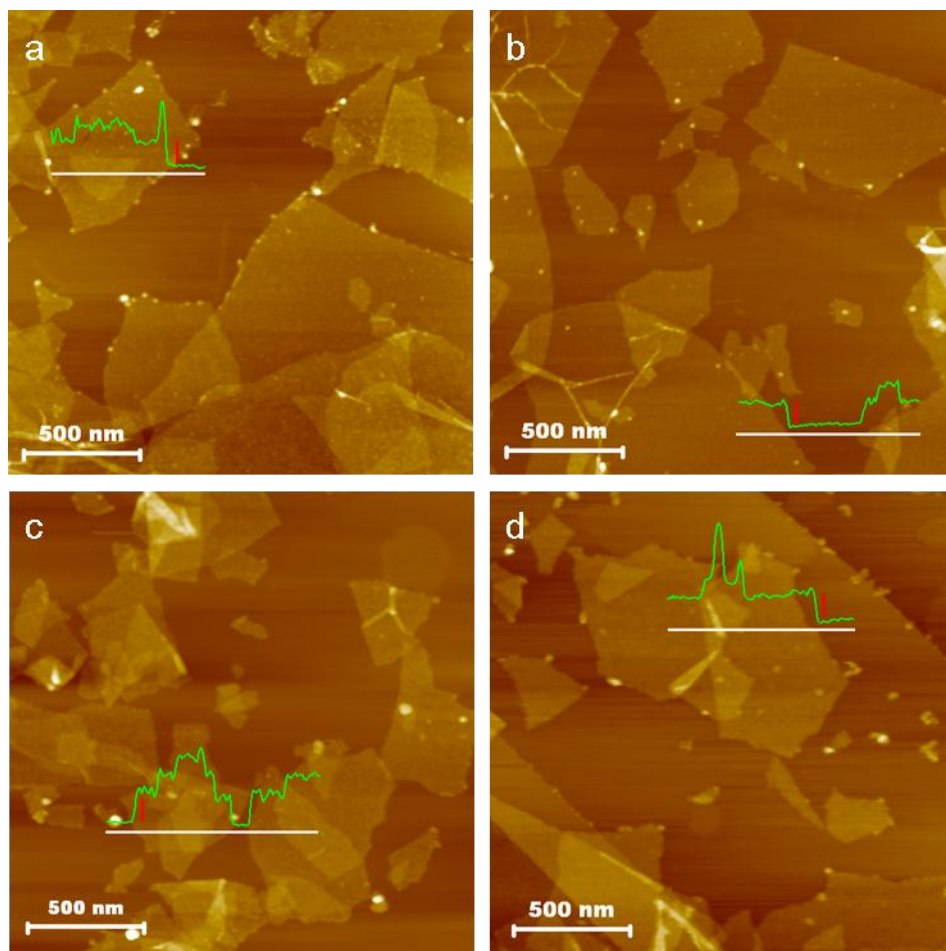
Figure 4. AFM images of RGO sheets deposited onto HOPG substrates from ispersions stabilized by the surfactants Brij 700 (a), DOC (b), SDBS (c) and Tween 80 (d). Representative line profiles taken along the marked white lines are shown superimposed on the images. The red vertical bars correspond to a height of 1 nm in the line profiles.

To compare the efficiency of the surfactants in keeping the RGO sheets suspended in aqueous medium, the just reduced, surfactant-stabilized dispersions were centrifuged (10,000g, 10 min) and the relative amount of RGO remaining in the supernatant determined by UV–vis absorption spectroscopy. Fig. 5 shows the performance of the whole range of surfactants used in this work (Fig. 1) for hydrazine-reduced, 0.1 mg mL^{-1} graphene oxide dispersions under basic (pH ~12, Fig. 5a) and acidic (pH ~1, Fig. 5b) conditions. In both cases, two surfactant concentrations were employed, namely, 0.05% and 0.50% wt/vol. All the surfactants are of anionic or non-ionic character, except the bile salt detergent CHAPS, which is zwitterionic. Cationic surfactantswere not employed because they usually destabilize aqueous suspensions of

graphene oxide or reduced graphene oxide sheets [37]: the positively charged polar head of the surfactant molecule tends to neutralize the negative charges present on the sheets, while its hydrophobic tail decreases further the affinity of the sheets for the aqueous medium, leading to their agglomeration and precipitation. First, we note that the results reported in Fig. 5 generally correlated with the long-term stability observed for the corresponding as-prepared, noncentrifuged dispersions, i.e. those dispersions that remained without precipitating for longer times tended to yield larger amounts of sheets in the supernatant after centrifugation. This indicates that such results reflect the degree of stability afforded by the surfactants to the RGO sheets. Likewise, as could be expected, and with the only exception of the surfactants SDBS and PSS, we see that using a higher surfactant concentration (0.50% wt/vol) leads to better results, i.e. a larger number of sheets remaining in the supernatant after centrifugation. A higher surfactant concentration should in principle lead to a larger amount of surfactant molecules adsorbed on the sheets, which in turn should increase their stability towards the aqueous medium.

Under basic conditions (Fig. 5a), all the tested anionic surfactants exhibited a good performance, except SDS. The lowest concentration used (0.05% wt/vol) is below the cmc for SDS (0.24% wt/vol), so that no dispersion ability can be expected as a result. However, SDS does not work either at the higher concentration (0.50% wt/vol). To explain this qualitative difference between SDS and the other surfactants, as well as the semiquantitative trends between them, some general ideas on the process by which the suspension is stabilized have to be taken into account. Briefly, in an anionic surfactant- stabilized RGO suspension, the hydrophobic tail of the surfactant molecule can be expected to adsorb onto the hydrophobic RGO sheets, while its polar head extends into water and provides the sheets with negative charges that afford electrostatic repulsions between them and avoid their agglomeration. Given the planar, predominantly aromatic structure of RGO, interaction will be more efficient with those surfactants whose hydrophobic tail contains planar or nearly planar polycyclic structures, and/or unsaturated or aromatic moieties where a relatively strong π–π interaction between the RGO sheet and the surfactant molecule is possible. This could be one of the reasons that explain the different performance observed between SDS and SDBS. The hydrophobic tail of the latter surfactant possesses an aromatic ring in
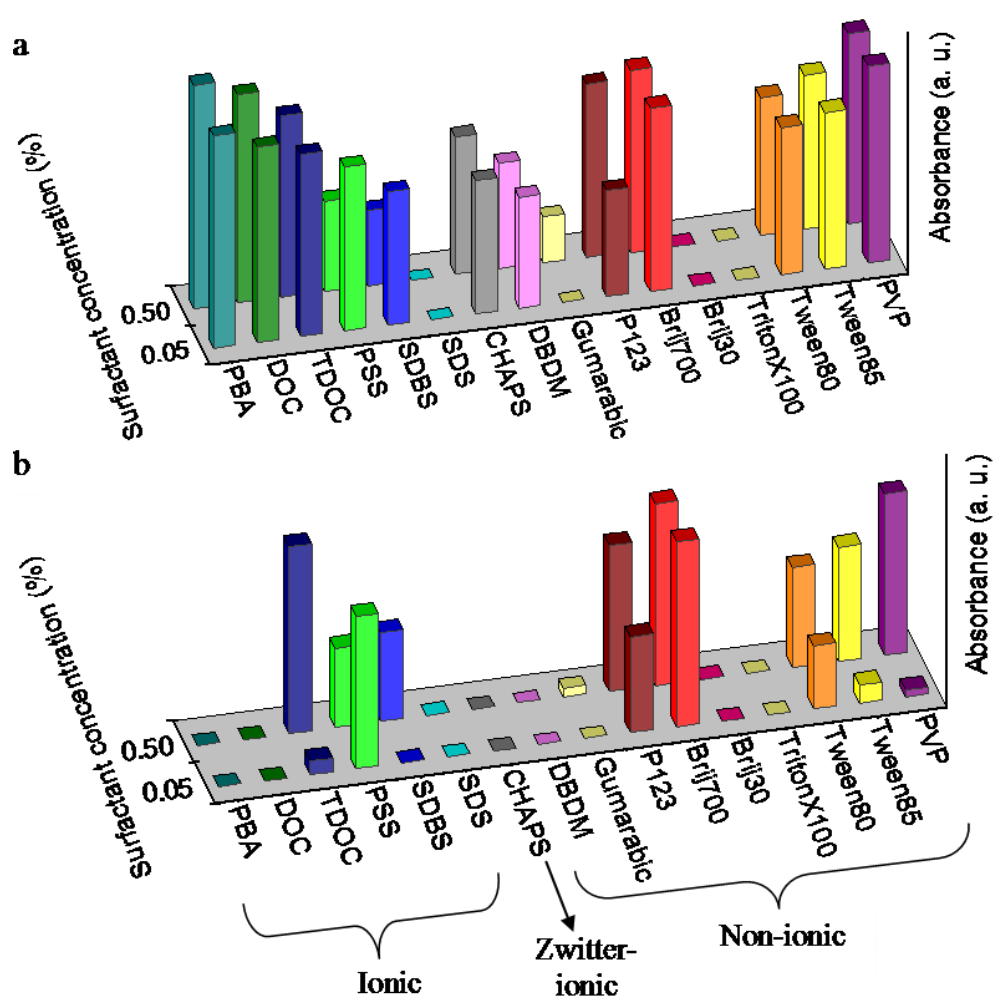
Figure 5. UV–vis absorbance at 450 nm measured on the supernatant of centrifuged (10,000g, 10 min), surfactant-stabilized 0.1 mg mL^{-1} RGO dispersions in basic (a) and acidic (b) medium (pH 12 and 1, respectively). Two surfactant concentrations are shown: 0.05% and 0.50% wt/vol.

addition to the dodecyl chain, which is not present in the case of SDS (see Fig. 1). Nevertheless, interaction of the alkyl chains with the hydrophobic RGO sheets should be neither negligible, and therefore factors other than just the absence of an aromatic ring should be probably responsible for the poor performance of SDS in stabilizing RGO. The fact that the highest concentration of surfactant employed in this work (0.50% wt/vol) was not much higher than the cmc of SDS (0.24% wt/vol) could also possibly contribute to the observed behavior. The polyelectrolyte PSS yields similar results to those of SDBS, with its monomer having the same polar head and a similar aromatic tail to that of the SDBS molecule. PBA, DOC and TDOC exhibit a higher dispersion ability compared to that of SDBS and PSS. The three former surfactants

possess relatively bulky polycyclic hydrophobic moieties that may confer the sheets with further stabilization by way of steric hindrance (in addition to the electrostatic repulsion component) [38]. For the specific case of PBA, the contribution of a strong $\pi-\pi$ interaction arising from its pyrene group, which is not present in DOC and TDOC, is probably the reason of its particularly good performance under basic conditions. The zwitterionic surfactant CHAPS, whose chemical structure is similar to that of TDOC but with an additional segment containing a positively charged quaternary amine (Fig. 1), is somewhat less effective than the latter. This behavior can be possibly put down to the fact that its positive charge can partly neutralize the negative charges in the head of other surfactant molecules or even those residually present in the RGO sheets themselves, thus decreasing the electrostatic repulsion between the sheets and consequently their stability.

In acidic medium (Fig. 5b), the conditions are more adverse for stabilization of the suspension with the anionic surfactants. In this case, a distinction should be made between surfactants based on permanent anions (sulfonate: TDOC, PSS and SDBS) and surfactants based on much more pH-dependent anions (carboxylate: PBA and DOC). The former are still relatively effective under acidic pH of 1, especially at the higher concentration of 0.50% wt/vol, while the latter can no longer stabilize the sheets. Sulfonic acids are known to be much stronger acids than carboxylic ones (pK_a values of $\sim$ - 2 and $\sim$5, respectively) [39], and therefore at pH 1 are still expected to be mainly in deprotonated, negatively charged sulfonate form. By contrast, their carboxylic acid counterparts should be virtually in the completely protonated, electrically neutral carboxyl form. Consequently, high concentrations of sulfonate- based surfactants could still be able to stabilize the RGO sheets at pH 1 on account of electrostatic repulsions afforded by negative charges on the surfactant molecules, whereas the same does not hold true for the carboxylate based iones, as actually observed in the experiments (Fig. 5b). The zwitterionic CHAPS is ineffective in stabilizing the RGO sheets under acidic conditions. As was the case of basic medium, CHAPS displays a worse performance than that of its relative TDOC, but the reason behind its complete inefficiency in acidic medium is currently not understood.

The ability of non-ionic surfactants to stabilize RGO sheets in the aqueous medium should be mainly based on the presence of long and/or branched polar chains. In principle, the hydrophobic tail of the surfactant is expected to interact with the RGO

sheets, while the electron-rich oxygen atoms of its polar section should form hydrogen bonds with the surrounding water molecules, thus stabilizing the suspension. However, taking into account that RGO is not an exclusively hydrophobic object, but instead has been shown to be a nanometer- scale patchwork of essentially defect-free graphene (hydrophobic) areas interspersed with some highly defective, still oxidized (hydrophilic) regions [40-42], hydrogen bonding between oxygen functional groups from the latter regions and the polar sections of the surfactant molecules should not be discarded. This could explain why, having both a dodecyl- type hydrophobic tail, DBDM appears to be reasonably effective in stabilizing the RGO sheets in basic medium whereas SDS does not (Fig. 5a), as both the hydrophobic and hydrophilic parts of DBDM can interact with the different types of domains in the RGO sheets. The surfactants with polar heads consisting of poly(ethylene oxide) (PEO) chains (P-123, Brij 30, Brij 700, Triton X-100, Tween 80 and Tween 85) stabilize RGO dispersions by coiling their PEO sections into a bulky hydrated layer that prevents p–p stacking of the sheets through steric hindrance [43]. The effectiveness of the repulsive barrier afforded by such mechanism can be generally expected to increase with the molecular weight of the PEO chain. In fact, only those surfactants of this type with a small number (610) of ethylene oxide units per molecule (i.e. Brij 30 and Triton X-100) did not succeed in dispersing the RGO sheets. PVP has been shown to have a particularly high affinity towards graphite and carbon nanotube surfaces [44, 45], so it can be anticipated to exhibit a good performance in stabilizing the RGO sheets, as actually noticed from Fig. 5a.

In principle, pH would be expected to have only a minor effect on the behavior of non-ionic surfactants. Indeed, this is the case for Brij 700 and P-123. Nevertheless, some of these surfactants are not stable in strongly acidic medium, as they contain bonds that can be hydrolyzed under such conditions. More specifically, glycosidic linkages in the disaccharides of DBDM and Gum Arabic, as well as ester bonds in Tween 80 and Tween 85, can be broken in acidic medium [39, 46], and the smaller fragments resulting from hydrolysis will have poorer or none ability as surfactants.

The most successful surfactants ascertained from the screening experiments reported in Fig. 5 were then selected for the preparation of more concentrated RGO dispersions. Indeed, concentrations up to ~ 1 mg mL^{-1} could be achieved in basic medium with the ionic PBA and DOC and under both acidic and basic conditions with

the non-ionic Brij 700 and PVP with a surfactant concentration of 0.50% wt/vol. For a surfactant concentration of 1 % wt/vol, values of up to 2.3 mg mL^{-1} with DOC and PVP in basic medium and with Brij 700 in both acidic and basic media were attained. Such dispersions exhibited reasonable long-term stabilities (up to several weeks). Likewise, large individual RGO sheets (typically 5–10 µm in lateral size) obtained from stirred, rather than sonicated, graphite oxide suspensions could be stabilized in aqueous dispersion in the presence of suitable surfactants, such as DOC or DBDM (see Fig. 6 for a representative AFM image), while they invariably precipitated in their absence even at very low sheet concentration (e.g., ~0.005 mg mL^{-1}).
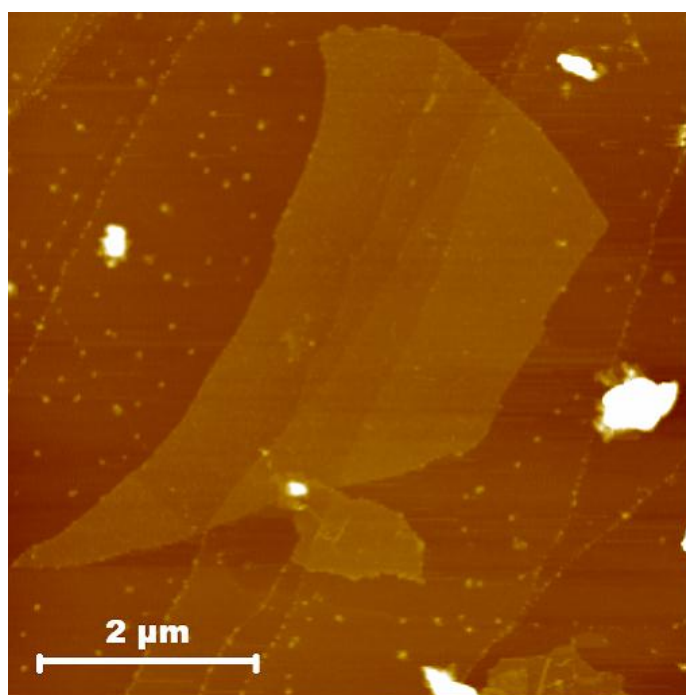
Figure 6. Representative AFM image of a large RGO sheet deposited onto HOPG from a DBDM-stabilized suspension, which in turn was obtained from reduction of stirred graphite oxide dispersion.

Irrespective of their ability to stabilize aqueous RGO suspensions under a range of different conditions, the combination of surfactants with RGO sheets is potentially interesting in itself, because the hybrid material might exhibit attractive characteristics that can be useful for practical applications [30]. We prepared free-standing RGO-surfactant composite paper-like films by vacuum filtration of the corresponding mixed dispersions. Fig. 7 shows representative SEM images of composite films with the

surfactants PBA (a) and PSS (b), which are typically a few tens of micrometers thick and exhibit a layered morphology similar to that typically observed in their surfactant-free counterpart (images not shown). Composite films were prepared with most of the surfactants indicated in Fig. 1 and using the same procedure in all cases: filtration of a volume of 250 mL containing 0.05% wt/vol of surfactant and RGO obtained by hydrazine reduction of 0.1 mg mL^{-1} of graphene oxide. Considering that virtually all the RGO material is retained on the membrane filter (the filtrate did not show evidence of the presence of RGO sheets), the paper-like films prepared with the different surfactants should all comprise the same amount of RGO (~ 12 mg, as determined from the weight of surfactant-free films). On the other hand, a certain amount of surfactant molecules, which will generally depend on the surfactant used, can be expected to pass through the pores (0.2 μm in size) of the membrane filter during filtration, and hence only a fraction of their original mass (125 mg) will be retained in the composite film. Therefore, the mass percentage of RGO in the composite films will be expected to vary with the specific surfactant. This is confirmed by the data reported in Table 1, which were derived from the measured weight of the composite films, showing values that range from 10% (with Brij 700) up to 87% (with SDS), though most of them lie between 29 and 47%. In an attempt to corroborate these results, the composite paper-like films were subjected to TGA under flowing air to discriminate the gasification steps, and therefore the weights, corresponding to surfactant (gasification at 200–300 ºC) and RGO (~550–600 ºC) [42]. In some cases (e.g., with DOC or SDS), the thermogravimetric data were consistent with those shown in Table 1, but for other surfactants (e.g., PSS or Tween 80) the fraction of RGO in the films estimated by TGA was somewhat larger. The discrepancy could be due to potential inaccuracies derived from the specific features of the thermogravimetric plots; for example, the fact that RGO exhibits a steady and non-negligible weight loss from 100 ºC up to the onset of gasification proper at 550 ºC [42]. However, it is also possible that confinement of the surfactant molecules between the RGO sheets hampers their gasification, so that a certain amount of them would be pyrolyzed rather than gasified at 200–300 ºC. The carbon residue resulting from the surfactant would subsequently gasify at a temperature close to that of RGO, which in turn would lead to an overestimation of the fraction of the latter in the composite films.

The electrical conductivity data for the composite films are also given in Table 1.With the exception of the RGO-SDS composite film, which exhibits the lowest amount of surfactant of all the composite films and a high conductivity (4680 S m^{-1}), the values typically range between 0.01 and several S m^{-1}, and are therefore much lower than that measured for the surfactant- free RGO film prepared under the same conditions (~7550 S m^{-1}). The presence of surfactant molecules intercalated with the RGO sheets in the composite films should decrease the extent of electrical contact between neighboring sheets, which in turn would hamper the mobility of the charge carriers across the films and thus result in a decrease of their electrical conductivity compared to their surfactant free counterpart. Evidence of surfactant intercalation in the composite films was obtained by means of XRD. In agreement with previous reports in the literature for air-dried, vacuum filtered RGO paper-like films [47], the XRD pattern of the surfactant-free film (Fig. 8, black plot) shows a peak at ~24º, corresponding to an intersheet spacing of 0.37 nm. As exemplified for the surfactants SDBS and Tween 80 (Fig. 8, blue and orange plots, respectively), the XRD patterns of the composite films were seen to be dominated in almost all cases by two peaks that, depending on the specific surfactant, are located between 5.6º and 7.3º (corresponding to a spacing between 1.59 and 1.21 nm) and between 20.8º and 24.0º (spacing between 0.43 and 0.37 nm), the latter yielding the same or a slightly larger spacing than that obtained for the surfactant free RGO film. Having confirmed that neither of these two peaks is related to the surfactant itself, we interpret that these vacuum-filtered composite films possess a heterogeneous structure, consisting both of regions with no or little surfactant intercalated between the sheets, which give rise to a small intersheet spacing of 0.37–0.43 nm, and of regions with greater amounts of intercalated surfactant, yielding larger intersheet spacing values (1.21–1.59 nm).
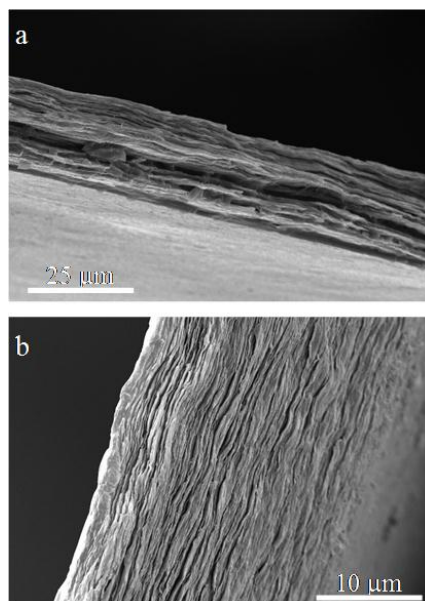
Figure 7. Cross-sectional SEM images of RGO-surfactant composite paper-like films prepared with PBA (a) and PSS (b).

Table 1. Percentage of RGO in the different RGO-surfactant composite paper-like films, together with their electrical conductivity and specific capacitance.

Film	RGO (wt %)	Conductivity $(S\ m^{-1})$	Specific capacitance $(F\ g^{-1})$
RGO	100 (~12 mg)	7548	38
RGO/PBA	36	13.31	1
RGO/DOC	47	0.06	1
RGO/TDOC	36	2.18	3
RGO/PSS	41	10.51	114
RGO/SDBS	29	0.87	7
RGO/SDS	87	4679	46
RGO/CHAPS	36	0.92	2
RGO/DBDM	11	0.01	3
RGO/P-123	38	5.53	12
RGO/Brij 700	10	1.08	6
RGO/Tween 80	13	0.41	95
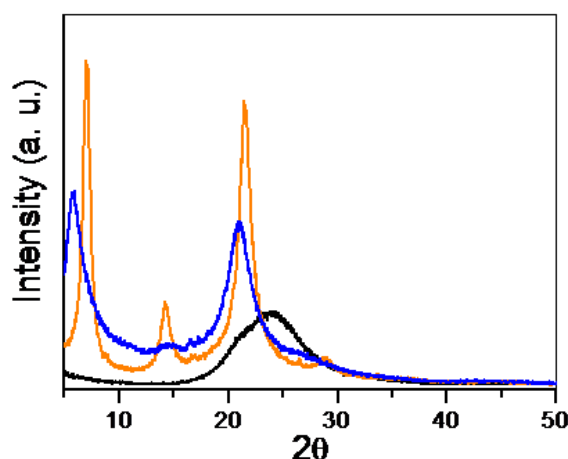
Figure 8. XRD patterns of surfactant-free RGO (black plot), RGO-SDBS composite (blue) and RGO-Tween 80 composite (orange) paper-like films.
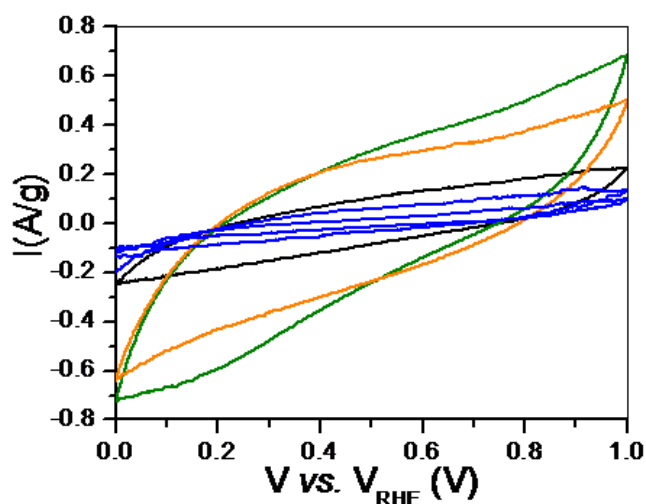
Figure 9. CVs of surfactant-free RGO film (black curve) and of RGO-PSS (green), RGO-Tween 80 (orange) and RGO-SDBS (blue) composite paper-like films.

The preparation of RGO films with increased intersheet spacing by intercalation of surfactant molecules could be of special interest in electrochemical applications where thin films of materials with enough conductivity are required. One example is their use as electrodes for supercapacitors. The performance of carbon materials towards this purpose is known to critically depend on the presence of high and accessible surface areas, which can be provided by sufficiently large interlayer distances (e.g., in the form of porosity) [48, 49]. For this reason, a preliminary investigation of the

electrochemical behavior of the composite films has been carried out. The capacitance of the samples has been obtained by cyclic voltammetry. Fig. 9 shows the CVs of some selected samples: surfactant-free RGO film (black plot) as well as composite films with PSS (green), Tween 80 (orange) and SDBS (blue). The specific capacitance of the films, as derived from the CV data, is given in Table 1. The values were calculated assuming that the surfactant contribution to capacitance is negligible and the RGO sheets are the only active component in the composite films. First, we note that the specific capacitance of the surfactant-free film is relatively small (38 F g^{-1}), which is not surprising considering that the paper-like film displays a compact structure of restacked sheets with interlayer spacing (0.37 nm) close to that of graphite (0.335 nm). We also see from Table 1 that the performance of most of the composite films is much poorer than that of their surfactant-free counterpart, the only exceptions being the films prepared with SDS (46 F g^{-1}), Tween 80 (95 F g^{-1}) and PSS (114 F g^{-1}). The similar capacitance of the surfactant-free and RGO-SDS composite films could be anticipated, because the latter is by far the composite film with the lowest amount of intercalated surfactant. Only PSS and Tween 80 afforded composite films with significantly improved capacitance, the origin of which is not clearly understood at present. Measurements carried out with electrodes made with the surfactants alone showed that neither PSS nor Tween 80 contribute significantly to the reported capacitance values. An increased intersheet distance should certainly favor the formation of the electrochemical double layer (EDL) in the composite films compared with the surfactant-free case. However, this reason alone cannot explain the observed results, because almost all of the composite films exhibited similarly increased intersheet distances (e.g., SDBS, Fig. 8) but most of them yielded poor capacitance values. It is therefore plausible that the surfactant molecules of different type and characteristics present in the interlayer spaces of the films contribute in different ways to the formation (or not) of the EDL on the surface of the RGO sheets, for example, by modulating the wettability of the film or the penetration degree of the electrolyte. Elucidating these questions will require more in-depth investigations in the future.

4. Conclusions

The ability of a wide range of surfactants (anionic, non-ionic and zwitterionic) to stabilize suspensions of RGO sheets in aqueous medium under different conditions has been determined and compared. The general trends observed could be explained in terms of the chemical structure of the surfactants. These results should provide a guide to select the most appropriate stabilizers towards the manipulation and processing of RGO suspensions for specific purposes. RGO-surfactant composite paper-like films could be prepared by vacuum filtration of the corresponding mixed dispersions. The films usually exhibited a heterogeneous structure composed of regions with low and high content of intercalated surfactant. Finally, two specific surfactants (PSS and Tween 80) afforded a significant increase of the capacitance performance of their composite paper-like films in comparison with that of the surfactant-free RGO film.

Acknowledgements

References

[1] Novoselov KS, Geim AK, Morozov SV, Jiang D, Zhang Y, Dubonos SV, Grigorieva IV, Firsov AA. Electric field effect in atomically thin carbon films. Science 306 (2004), 666-669.

[2] Geim AK, Novoselov KS. The rise of graphene. Nat. Mater. 6 (2007), 183-191.

[3] Geim AK. Graphene: status and prospects. Science 324 (2009), 1530-1534.

[4] Allen MJ, Tung VC, Kaner RB. Honeycomb carbon: a review of graphene. Chem. Rev. 110 (2009), 132-145.

[5] Dreyer DR, Ruoff RS, Bielawski CW. From conception to realization: an historial account of graphene and some perspectives for its future. Angew. Chem. Int. Edit. 49 (2010), 9336-9344.

[6] Schwierz F. Graphene transistors. Nat. Nanotech. 5 (2010), 487-496.

[7] Yang W, Ratinac KR, Ringer SP, Thordarson P, Gooding JJ, Braet F. Carbon nanomaterials in biosensors: should you use nanotubes or graphene? Angew. Chem. Int. Edit. 49 (2010), 2114-2138.

[8] Potts JR, Dreyer DR, Bielawski CW, Ruoff RS. Graphene-based polymer nanocomposites. Polymer 52 (2011), 5-25.

[9] Brownson DAC, Kampouris DK, Banks CE. An overview of graphene in energy production and storage applications. J. Power Sources 196 (2011), 4873-4885.

[10] Park S, Ruoff RS. Chemical methods for the production of graphenes. Nat Nanotech. 4 (2009), 217-224.

[11] Eda G, Chhowalla M. Chemically derived graphene oxide: towards large-area thin-film electronics and optoelectronics. Adv. Mater. 22 (2010), 2392-2415.

[12] Fernández-Merino MJ, Guardia L, Paredes JI, Villar-Rodil S, Solís-Fernández P, Martínez-Alonso A, Tascón JMD.Vitamin C is an ideal substitute for hydrazine in the reduction of graphene oxide suspensions. J. Phys. Chem. C 114 (2010), 6426-6432.

[13] Li D, Mueller M, Gilje S, Kaner R, Wallace G, Müller M. Processable aqueous dispersions of graphene nanosheets. Nat. Nanotech. 3 (2008), 101-105.

[14] Xu Y, Bai H, Lu G, Li C, Shi G. Flexible graphene films via the filtration of water-soluble noncovalent functionalized graphene sheets. J. Am. Chem. Soc. 130 (2008), 5856-5857.

[15] Lomeda JR, Doyle CD, Kosynkin DV, Hwang W-F, Tour JM. Diazonium functionalization of surfactant-wrapped chemically converted graphene sheets. J. Am. Chem. Soc. 130 (2008), 16201-16206.

[16] Su Q, Pang S, Alijani V, Li C, Feng X, Müllen K. Composites of graphene with large aromatic molecules. Adv. Mater. 21 (2009), 3191-3195.

[17] Liu H, Gao J, Xue M, Zhu N, Zhang M, Cao T. Processing of graphene for electrochemical application: noncovalently functionalize graphene sheets with water-soluble electroactive methylene green. Langmuir 25 (2009), 12006-12010.

[18] Li F, Bao Y, Chai J, Zhang Q, Han D, Niu L. Synthesis and application of widely soluble graphene sheets. Langmuir 26 (2010), 12314-12320.

[19] Dong X, Su C-Y, Zhang W, Zhao J, Ling Q, Huang W, Chen P, Li L-J. Ultra-large single-layer graphene obtained from solution chemical reduction and its electrical properties. Phys. Chem. Chem. Phys. 12 (2010), 2164-2169.

[20] Stankovich S, Piner RD, Chen X, Wu N, Nguyen ST, Ruoff RS. Stable aqueous dispersions of graphitic nanoplatelets via the reduction of exfoliated graphite oxide in the presence of poly(sodium 4-styrenesulfonate). J. Mater. Chem. 16 (2006), 155-158.

[21] Zu S-Z, Han B-H. Aqueous dispersion of graphene sheets stabilized by pluronic copolymers: formation of supramolecular hydrogel. J. Phys. Chem. C 113 (2009), 13651-13657.

[22] Patil AJ, Vickery JL, Scott TB, Mann S. Aqueous stabilization and self-assembly of graphene sheets into layered bio-nanocomposites using DNA. Adv. Mater. 21 (2009), 3159-3164.

[23] Liu S, Tian J, Wang L, Li H, Zhang Y, Sun X. Stable aqueous dispersion of graphene nanosheets: noncovalent functionalization by a polymeric reducing agent and their subsequent decoration with Ag nanoparticles for enzymeless hydrogen peroxide detection. Macromolecules 43 (2010), 10078-10083.

[24] Yang F, Liu Y, Gao L, Sun J. pH-Sensitive highly dispersed reduced graphene oxide solution using lysozyme via an in situ reduction method. J. Phys. Chem. C 114 (2010), 22085-22091.

[25] Yang Q, Pan X, Huang F, Li K. Fabrication of high-concentration and stable aqueous suspensions of graphene nanosheets by noncovalent functionalization with lignin and cellulose derivatives. J. Phys. Chem. C 114 (2010), 3811-3816.

[26] Gudarzi MM, Sharif F. Characteristics of polymers that stabilize colloids for the production of graphene from graphene oxide. J. Colloid Interf. Sci. 349 (2010), 63-69.

[27] Fang M, Long J, Zhao W, Wang L, Chen G. pH-Responsive chitosan-mediated graphene dispersions. Langmuir 26 (2010), 16771-16774.

[28] Zhou X, Liu Z. A scalable, solution-phase processing route to graphene oxide and graphene ultralarge sheets. Chem. Commun. 46 (2010), 2611-2613.

[29] Jo K, Lee T, Choi HJ, Park JH, Lee DJ, Lee DW, Kim B-S. Stable aqueous dispersion of reduced graphene nanosheets via non-covalent functionalization with conducting polymers and application in transparent electrodes. Langmuir 27 (2011), 2014-2018.

[30] Park S, Mohanty N, Suk J, Nagaraja A, An J, Piner R, Cai W, Dreyer D, Berry V, Ruoff RS. Biocompatible, robust free-standing paper composed of a TWEEN/graphene composite. Adv. Mater. 22 (2010), 1736-1740.

[31] Zhang K, Mao L, Zhang LL, On Chan HS, Zhao XS, Wu J. Surfactant-intercalated, chemically reduced graphene oxide for high performance supercapacitor electrodes. J. Mater. Chem. 21 (2011), 7302-7307.

[32] Hummers WS, Offeman RE. Preparation of graphitic oxide. J. Am. Chem. Soc. 80 (1958), 1339.

[33] Paredes JI, Villar-Rodil S, Solís-Fernández P, Martínez-Alonso A, Tascón JMD. Atomic force and scanning tunneling microscopy imaging of graphene nanosheets derived from graphite oxide. Langmuir 25 (2009), 5957-5968.

[34] Biniak S, Szymański G, Siedlewski J, Świątkowski A. The characterization of activated carbons with oxygen and nitrogen surface groups. Carbon 35 (1997), 1799-1810.

[35] Yang D-Q, Sacher E. Carbon 1s x-ray photoemission line shape analysis of highly oriented pyrolytic graphite: the influence of structural damage on peak asymmetry. Langmuir 22 (2005), 860-862.

[36] Paredes JI, Villar-Rodil S, Martínez-Alonso A, Tascón JMD. Graphene oxide dispersions in organic solvents. Langmuir 24 (2008), 10560-10564.

[37] Liang Y, Wu D, Feng X, Müllen K. Dispersion of graphene sheets in organic solvent supported by ionic interactions. Adv. Mater. 21 (2009), 1679-1683.

[38] Lin S, Shih C-J, Strano MS, Blankschtein D. Molecular insights into the surface morphology, layering structure, and aggregation kinetics of surfactant-stabilized graphene dispersions. J. Am. Chem. Soc. 133 (2011), 12810-12823.

[39] Vollhardt KPC. Oraganic chemistry. 1987.

[40] Gómez-Navarro C, Meyer J, Sundaram R, Chuvilin A, Kurasch S, Burghard M, Kern K, Kaiser U. Atomic structure of reduced graphene oxide. Nano Lett. 10 (2010), 1144-1148.

[41] Erickson K, Erni R, Lee Z, Alem N, Gannett W, Zettl A. Determination of the local chemical structure of graphene oxide and reduced graphene oxide. Adv. Mater. 22 (2010), 4467-4472.

[42] Solís-Fernández P, Paredes JI, Villar-Rodil S, Guardia L, Fernández-Merino MJ, Dobrik G, Biró LP, Martínez-Alonso A, Tascón JMD. Global and local oxidation behavior of reduced graphene oxide. J. Phys. Chem. C 115 (2011), 7956-7966.

[43] Rosen MJ. Surfactants and interfacial phenomena: Wiley. 2004.

[44] Otsuka H, Esumi K. Interaction between poly(N-vinyl-2-pyrrolidone) and anionic hydrocarbon/fluorocarbon surfactant on hydrophobic graphite. J. Colloid Interf. Sci. 170 (1995), 113-119.

[45] O'Connell MJ, Boul P, Ericson LM, Huffman C, Wang Y, Haroz E, Kuper C, Tour J, Ausman KD, Smalley RE. Reversible water-solubilization of single-

walled carbon nanotubes by polymer wrapping. Chem. Phys. Lett. 342 (2001), 265-271.

[46] Nelson DL, Cox MM. Lehninger principles of biochemistry. New York. 2004.

[47] Chen H, Müller MB, Gilmore KJ, Wallace GG, Li D. Mechanically strong, electrically conductive, and biocompatible graphene paper. Adv. Mater. 20 (2008), 3557-3561.

[48] Simon P, Gogotsi Y. Materials for electrochemical capacitors. Nat. Mater. 7 (2008), 845-854.

[49] Zhang LL, Zhou R, Zhao XS. Graphene-based materials as supercapacitor electrodes. J. Mater. Chem. 20 (2010), 5983-5992.

High-throughput production of pristine graphene in an aqueous dispersions assisted by non-ionic surfactants
(Carbon 49 (2011), 1653-1662)

L. Guardia, M. J. Fernández-Merino, J. I. Paredes , P. Solís-Fernández, S. Villar-Rodil,
A. Martínez-Alonso, and J. M. D. Tascón

Instituto Nacional del Carbón, CSIC, Apartado 73, 33080 Oviedo, Spain

Abstract

The preparation of aqueous graphene dispersions by exfoliation of pristine graphite in the presence of a wide range of surfactants is reported. High graphene concentrations, up to about 1 mg mL^{-1}, were obtained with the use of some non-ionic surfactants. The dispersions consisted of single- and few-layer graphene platelets with their basal planes virtually free of even atomic-sized (point) defects. The potential utility of such highly concentrated dispersions toward the low-cost, large-scale manipulation and processing of graphene was demonstrated by processing them into electrically conductive, freestanding paper-like films.

1. Introduction

Graphene has generated in recent years significant attention from the research community as a result of its outstanding physical properties and enormous potential in practical uses, which span the fields of nanoelectronics, composite materials, energy storage or molecular sensors [1-3]. At present, one of the main obstacles to the development of graphene in large-scale applications is the lack of high-throughput, inexpensive methodologies for the production of this material. To overcome such problem, considerable efforts are being devoted to the exploration of different production strategies [4-6], one of the most promising of which is the preparation of colloidally dispersed graphene by liquid-phase processing of graphite or graphite derivatives [4]. This approach readily lends itself to further manipulation and processing of graphene into, e.g., thin films, coatings or composite and hybrid materials, making the colloidal route particularly attractive for many prospective applications.

Graphene dispersions are usually prepared through conversion of graphite to graphite oxide, subsequent exfoliation of the latter in aqueous or organic medium to yield graphene oxide sheets, and finally chemical reduction of the exfoliated dispersion [4, 7-9]. Such procedure boasts the merit of affording single-layer sheets in very large quantities and has proved suitable toward some specific applications [10, 11]. Still, the resulting graphenes bear a substantial amount of structural defects and residual oxygen inherited from the oxidation step [3]. This constitutes a serious drawback, as many of the unique properties of graphene are severely degraded by the presence of disorder. With a view to attaining dispersions of defect-free graphene, some recent research has concentrated on the liquid-phase exfoliation of more pristine forms of graphite, rather than graphite oxide [12-21]. In particular, aqueous dispersions of relatively defect-free graphene stabilized by some ionic surfactants have been demonstrated [14, 15, 18-21]. However, the reported concentrations were typically on the order of 0.01 mg mL^{-1}, which are too low for many practical uses. Likewise, the availability of aqueous dispersions of highquality graphene with surfactants of different types (e.g., non-ionic) could facilitate its use in a wider range of applications. To the best of our knowledge, these issues have not yet been addressed.

Here, we present the preparation of aqueous dispersions of high-quality graphene in a wide range of surfactants. We compare the performance of non-ionic and ionic surfactants toward the ultrasound-assisted dispersion/exfoliation of pristine graphite in water. We find the former to be generally superior to the latter as regards the amount of exfoliated material that can be stably suspended. Concentrations of high-quality, single- and few-layer graphene as high as ~1mg mL^{-1} can be attained with some specific surfactants. The potential utility of these highly concentrated dispersions is demonstrated by processing them into different materials, such as free-standing paper-like films and hydrogels.

2. Experimental

2.1. *Preparation and processing of graphene dispersion.*

The dispersions were prepared through sonication of natural graphite powder (Fluka 50870) at an initial concentration of 100 mg mL^{-1} in an aqueous surfactant solution by means of an ultrasound bath cleaner (JP Selecta Ultrasons system, 40 kHz).

Table 1 lists the surfactants used according to their character (non-ionic vs. ionic) and the acronyms used to refer to some of them throughout the text. Their chemical structure is given in the Supplementary content. The surfactant concentration (0.5 % and 1.0 % wt./vol.) was not optimized, but was above the critical micelle concentration for all of them. Typical sonication times were 2 h, although the effect of somewhat longer sonication was also investigated. As the initial concentration of graphite in the solution was rather high (100 mg mL^{-1}), the vials were removed from the ultrasound bath every 30 min during sonication and stirred for about 1 min to homogenize the graphite particles throughout the liquid. Following sonication, the dispersions were usually centrifuged (Eppendorf 5424 microcentrifuge) at 5000g for 5 min to sediment unexfoliated particles or thick flakes of graphite, and the top ~65% of supernatant, which was the final graphene dispersion, was collected. In comparing the dispersing ability of the different surfactants toward graphene, qualitatively similar results were obtained when different centrifugal forces (e.g., 500g or 10,000g) or centrifuging times (e.g., 30 min) were employed, and also when the centrifugation step was avoided and the sonicated dispersions were just allowed to settle down for several (e.g., 15) days.

Graphene/surfactant composite paper-like films were prepared by vacuum filtration of those dispersions that showed better performance (e.g., P-123, Brij 700 and PSS) through polycarbonate membrane filters 47mm in diameter and 0.05 µm of pore size (Whatman). The filtered material was allowed to dry under ambient conditions and peeled off the membrane filter. Graphene-containing supramolecular hydrogels were prepared from the P-123-stabilized graphene dispersions through formation of inclusion complexes between α-cyclodextrin (α-CD) and the polyethylene oxide (PEO) chains of the P-123 surfactant [22]. To this end, graphene dispersions were prepared by sonicating (2 h) graphite (100 mg mL^{-1}) in 5% wt./vol. surfactant solutions, centrifuging (5000g, 5 min) and collecting the supernatant. α-CD was subsequently added (100 mg mL^{-1}) to the graphene suspensions and allowed to settle down. Under these conditions, gelification was seen to take place in about 1 day, but was faster (several hours) for control samples (i.e., for surfactant solutions without graphene). Hydrogels could also be formed with lower concentrations of P-123 (e.g., 2% or 1% wt./vol.), but in such cases gelification was slower (several days).

Table 1. List of surfactants and their acronyms used throughout the text.

Surfactant name	Acronym
Non ionic	
Pluronic ® P-123	P-123
Tween 80	
Brij 700	
Gum arabic for acacia tree	
Triton X-100	
Tween 85	
Polyvinylpyrrolidone	PVP
n-Dodecyl- β-D-maltoside	DBDM
Ionic	
Poly(sodium 4-styrenesulfonate)	PSS
3-[(3-Cholamidopropyl) dimethyl ammonio]-1-propanesulfonate	CHAPS
Sodium deoxycholate	DOC
Sodium dodecylbenzene-sulfonate	SDBS
1-Pyrenebutyric acid	PBA
Sodium dodecyl sulphate	SDS
Sodium taurodeoxycholate hydrate	TDOC
Hexadecyltrimethylammonium bromide	HTAB

2.2. *Sample characterization*

UV–vis absorption spectra of the surfactant-stabilized aqueous graphene dispersions were recorded using a double beam Heλios a spectrophotometer, from Thermo Spectronic. The spectra were measured in the 200–800 nm wavelength range. The observed spectral features in the mentioned range could be attributed to the exfoliated graphitic material, absorption by surfactant molecules being negligible, except for those dispersions stabilized by surfactants containing aromatic moieties in their structure (e.g., PSS, PBA or SDBS). In such a case, absorption below 400 nm was seen to be dominated by the surfactant molecules rather than the suspended graphene. However, in all cases surfactant absorption approached zero at ~450 nm and above.

Such observation allowed to use the suspension absorbance at, e.g., 660 nm as a measure of the concentration of suspended graphene. The concentration was estimated from the absorbance at 660 nm by using the extinction coefficient of graphene (α = 1390 mL mg^{-1} m^{-1}) previously determined in surfactant/water solutions [15]. The effect of extending the sonication time up to several hours on the final concentration of dispersed graphene was also monitored by measuring the absorbance of the suspensions at 660 nm. For such experiments, 10 g of the starting natural graphite powder was suspended by bath sonication in 100 mL of 0.5% wt./ vol. surfactant solution. Brij 700, HTAB, P-123, PSS, SDBS, TDOC and Tween 80 were chosen for this study. Three millilitres aliquots of suspension were taken every 30 min from the sonicating vial, centrifuged at 5000g for 5 min, and their absorbance measured at 660 nm.

The exfoliated material in the different suspensions was deposited onto SiO$_2$ /Si substrates for investigation by atomic force microscopy (AFM). To this end, the SiO$_2$/Si substrates were first surface-modified with N-(3-(trimethoxysilyl)propyl)-ethylenediamine, and then immersed in the graphene suspension for 15 min, dried under a stream of pure synthetic air, thoroughly rinsed with Milli-Q water and dried again. The paper-like films were also studied by AFM and scanning tunnelling microscopy (STM). Prior to imaging, the films were gently rinsed with water to remove surfactant from their surface and allow better visualization of the assembled graphene platelets. AFM and STM images were obtained under ambient conditions (relative humidity ~40%, temperature ~22–24° C) with a Nanoscope IIIa Multimode apparatus (Veeco Instruments). AFM was performed in the tapping mode of operation, using rectangular Si cantilevers with spring constant of ~ 40N m^{-1} and resonance frequency of ~250–300 kHz. STM imaging was accomplished in the constant current mode (variable height) with mechanically prepared Pt/Ir (80/20) tips and typical tunneling parameters of 1 nA (tunneling current) and 100 mV (bias voltage). Transmission electron microscopy (TEM) observations were performed on a JEOL 2000 EX-II instrument operated at 160 kV. A few drops of surfactant-stabilized graphene dispersion were cast onto a copper grid (200 mesh) covered with a lacey carbon film and allowed to dry in air.

Raman spectra were recorded on a Horiba Jobin–Yvon LabRam instrument at a laser excitation wavelength of 532 nm for the starting natural graphite powder, the exfoliated/ dispersed material in the different aqueous surfactant solutions and the graphene/surfactant composite paper-like films. The spectra of the material dispersed in

the aqueous surfactant solutions were obtained directly from the liquid suspensions. The highly concentrated, aqueous graphene dispersions stabilized by P-123 were investigated by X-ray photoelectron spectroscopy (XPS). To this end, the suspensions were first destabilized and precipitated by adding KCl and heating at 95ºC for about 1 h. This process is known to favor the flocculation of P-123 surfactants [23]. The precipitated material was collected, thoroughly washed with Milli-Q water and centrifuged (20,000g, 30min) for a number of cycles to ensure the largest possible removal of surfactant from the surface of the graphene flakes. The XPS measurements were carried out on a SPECS system working under 10^{-7} Pa with Mg K_α X-ray source (100 W). The electrical conductivity of the graphene/surfactant composite paper-like films was determined following a previously reported procedure with a Fluke 45 digital multimeter [24, 25]. To this end, the films were cut into rectangular strips about 6 x 25 mm^2 large and their thickness was estimated by scanning electron microscopy (SEM; Zeiss DSM 942 instrument). Thermogravimetric analysis (TGA) for the graphene/surfactant composite paper-like films was accomplished by means of an SDT Q600 thermobalance (TA Instruments) under O_2 gas flow (100 mL min^{-1}) at a heating rate of 3 ºC min^{-1}, using Pt crucibles.

3. Results and discussion

Aqueous graphene dispersions were prepared in a variety of non-ionic and ionic surfactants (see Table 1) by dispersion/ exfoliation of pristine graphite by sonication. The initial concentration of graphite in the surfactant solutions (100 mg mL^{-1}) was purposely chosen to be rather large. This is due to the fact that the exfoliation rate of graphite to singleand few-layer graphene was very low. Therefore, to attain reasonably large concentrations in the resulting graphene dispersions, either the sonication time should be extended to very long times for relatively low initial concentrations of graphite or, alternatively, the initial graphite concentration should be high if relatively short sonication times are employed. Given the very low cost of this type of graphite, and to avoid as far as possible the unnecessary introduction of structural damage to the graphene sheets as a result of extended sonication, we adopted the latter protocol. To allow direct comparisons between the dispersing ability of the different surfactants, the preparation procedure was carried out under identical conditions for all the surfactants.

Fig. 1a–f shows vials containing aqueous graphene dispersions stabilized by some representative surfactants. It becomes immediately apparent that there are significant differences in the ability of the surfactants to disperse the exfoliated material. For example, the bile salt detergent TDOC yields a faint, highly transparent dispersion (Fig. 1b), suggesting a poor suspending power toward graphene. By contrast, the non-ionic surfactants Brij 700 and P-123 are able to disperse much larger amounts of exfoliated graphite, as evidenced by their completely black and opaque suspensions (Fig. 1e and f, respectively). Intermediate behaviors are also observed (e.g., Fig. 1c and d for PBA and CHAPS, respectively). The dispersions were observed to be stable for at least several weeks, showing little, if any, signs of precipitated material during such period of time. The electronically conjugated, graphitic nature of the suspended material was revealed by means of UV–vis absorption spectroscopy, as exemplified in Fig. 1g for a dispersion stabilized by P-123. The absorption peak is seen to be located at ~ 269 nm, and can be attributed to $\pi\rightarrow\pi^*$ transitions of aromatic C–C bonds [26]. This result, together with the observation of strong absorbance in the whole wavelength range above 269 nm, is consistent with the dispersions being constituted by graphitic objects [25]. We note that the absorption peak position of the present suspensions is virtually the same as that reported for highly reduced graphene oxide in water, which in turn is significantly red-shifted (~ 40 nm) compared to that of the heavily oxygenated, unreduced graphene oxide dispersions [7].

To provide a more quantitative comparison of the dispersing ability of the surfactants, we measured the absorbance of the suspensions at a specific wavelength (660 nm) and estimated the corresponding concentrations therefrom. To this end, we made use of the reported extinction coefficient for graphene dispersions in surfactant/water solutions (α = 1390 mL mg^{-1} m^{-1}) [15]. The results are plotted in Fig. 1h. The most significant trend is that non-ionic surfactants appear to be more effective in the stabilization of the exfoliated material compared to ionic ones. The concentrations typically achieved with the latter lie in the 0.01– 0.10 mg mL^{-1} range, which are consistent with those previously reported for some of these surfactants (e.g. SDBS) [15], whereas non-ionic surfactants yield in most cases values above 0.10 mg mL^{-1}.

Particularly remarkable is the performance of two surfactants, Tween 80 and P-123, which readily afford concentrations in the range between 0.5 and 1.0 mg mL^{-1} under the preparation conditions described above.
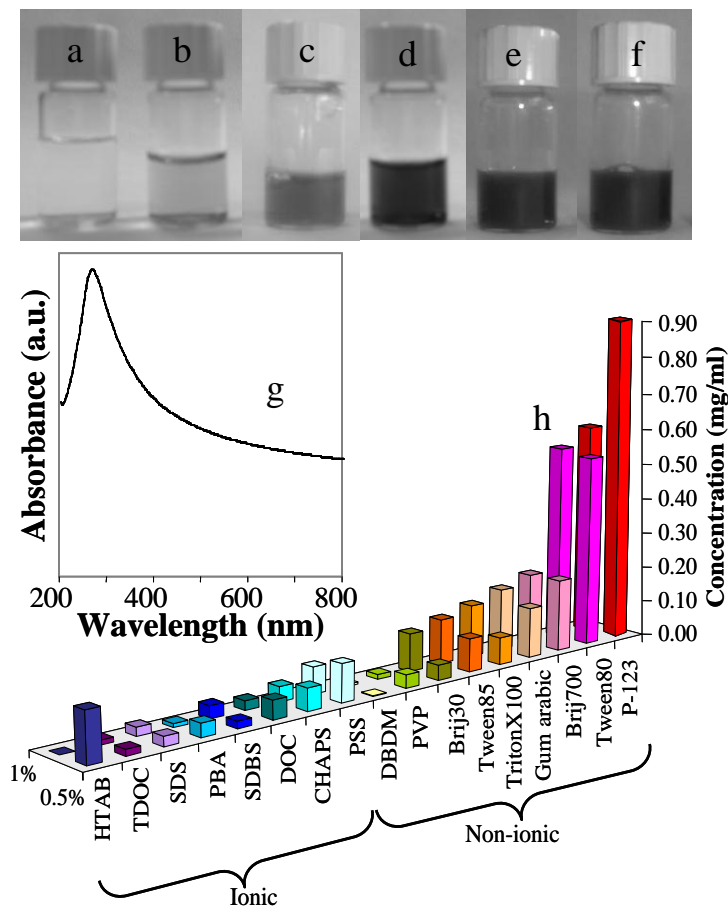
Figure 1. (a-f) Digital pictures of vials containing only water (a) and aqueous graphene dispersions stabilized by 0.5 % wt/vol of TDOC (b), PBA (c), CHAPS (d), Brij 700 (e) and P-123 (f). (g) Typical UV-vis absorption spectrum of P-123-stabilized graphene dispersion. (h) Concentration of graphene in aqueous dispersions achieved by the use of different surfactants, as estimated from UV-vis absorption measurements. Two surfactant concentrations are shown: 0.5 and 1.0 % wt/vol.
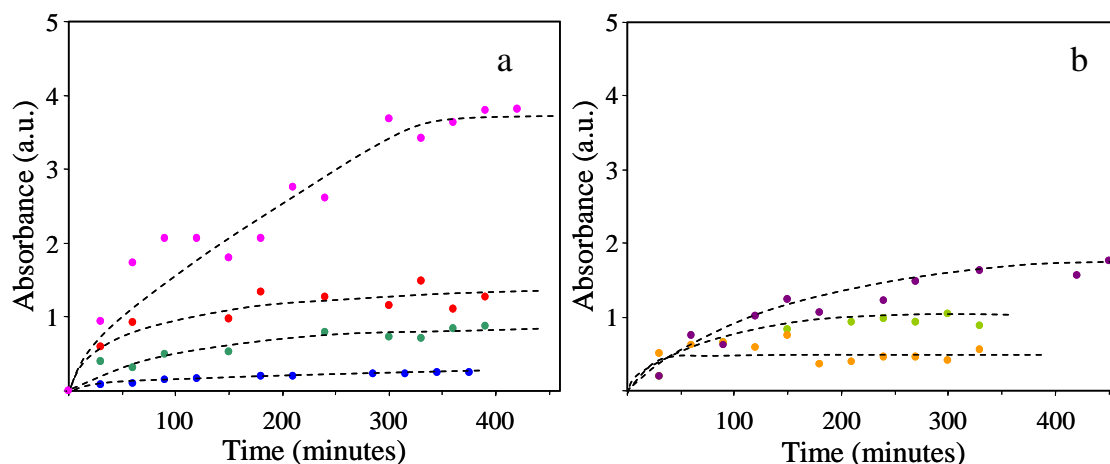
Figure 2. Absorbance at 660 nm measured for graphene dispersions with different surfactants as a function of sonication time. (a) P-123 (pink), HTAB (red), SDBS (green), PSS (blue). (b) Tween 80 (violet), Brij 700 (light green), TDOC (orange). (For interpretation of the references to color in this figure legend, the reader is referred to the web version of this article.)

Fig. 2 illustrates the effect of sonication time (up to several hours) on the final concentration, determined through measurement of optical absorbance at 660 nm, of dispersed graphene using a number of selected surfactants (Brij 700, HTAB, P-123, PSS, SDBS, TDOC and Tween 80). For the non-ionic surfactant P-123, a moderate increase in sonication time, from 2 h routinely used in the present work to 5 h, significantly raised the concentration of stably dispersed graphene, from ~0.9 to ~1.5 mg mL^{-1}. In comparison, the other surfactants yielded much more moderate increases in the amount of suspended material with sonication time. Such result suggests that P-123 is a particularly effective surfactant for the preparation of graphene dispersions.

To assess the suitability of the present dispersions, particularly those with the highest concentrations, as a highthroughput route toward colloidally stabilized graphene, knowledge of some basic features of the suspended material (exfoliation degree, structural quality and lateral size) is required. These characteristics were evaluated using different techniques. Fig. 3 shows some representative results obtained by AFM from dispersions stabilized by P-123 and deposited onto SiO$_2$/Si substrates. The suspended material was seen to be constituted by flakes or sheets with lateral
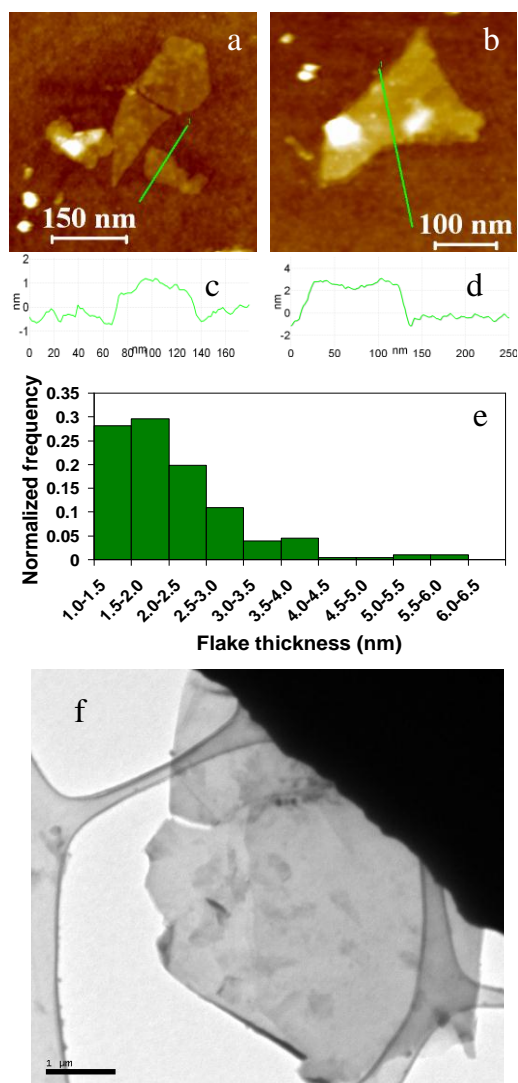
Figure 3. (a and b) Representative AFM images of graphene flakes deposited onto SiO$_2$/Si substrates from dispersions stabilized by the non-ionic surfactant P-123. (c and d) Line profiles taken along the green lines in (a) and (b), respectively, indicating that the sheets in (a) correspond to single-layer graphene and that in (b) to few-layer graphene. (e) Histogram showing the distribution of apparent flake thickness measured on ~200 objects from the AFM images. (f) TEM image of graphene sheets supported onto a large graphitic piece deposited onto a lacey carbon film from a P- 123-stabilized graphene dispersion.

dimensions between 50 and several hundred nm (Fig. 3a and b), which was corroborated also by TEM imaging (Fig. 3f). Line profiles taken from the AFM images

(Fig. 3c and d) revealed the thinnest flakes to have an apparent thickness of ~1.0–1.2 nm (e.g., Fig. 3c), and most others to be between 1.4 and 3.0 nm (e.g., Fig. 3d), as evidenced from the histogram shown in Fig. 3e. In accordance with previous reports on micromechanically cleaved graphene supported onto SiO_2/Si [27], we attribute the 1.0–1.2 nm-thick sheets, which amount to ~10–15% of the measured objects, to single-layer graphene, while the remaining flakes can be mostly ascribed to few-layer graphene (up to 5 layers). Similar results were obtained for dispersions stabilized by the other surfactants. We thus conclude that the produced suspensions, including the highly concentrated ones, are constituted by single- and few-layer graphene flakes.

Fig. 4a–c shows Raman spectra (both first- and second order) of the starting graphite (a), a representative aqueous graphene dispersion (stabilized by the non-ionic surfactant P-123) (b), and for comparison, a highly reduced graphene oxide sample (c). The latter sample was prepared by hydrazine reduction of a graphene oxide suspension in water and subsequent processing into a paper-like film through vacuum filtration [28]. A general comparison of the three spectra suggests that, from a structural point of view, the exfoliated material forming the highly concentrated aqueous suspensions in surfactant is much more similar to the starting graphite than it is to highly reduced graphene oxide. The first-order spectrum of the starting graphite (Fig. 4a) is dominated by the G band (~1584 cm^{-1}), but displays two additional bands, D and D´, located at ~1352 and 1620 cm^{-1}, respectively. The D and D´ bands are both related to the presence of structural disorder in graphite/graphene, and their small intensity in comparison with the G band (e.g., D–G integrated intensity ratio, I_D/I_G, of 0.10) indicates that the starting material possesses a high structural quality (very low defect content). Although the graphene dispersions display more intense D and D´ bands (Fig. 4b), e.g., I_D/I_G ~0.53, such bands are much weaker (and also narrower) than those observed for highly reduced graphene oxide (Fig. 4c), suggesting an improved structural quality in the present surfactant-stabilized dispersions compared to reduced graphene oxide. The observed increase in I_D/I_G ratio can be mainly attributed to an increased fraction of graphene edges in the dispersed material (relatively small flake size, Fig. 3a and b), rather than to the generation of defects within their basal plane. Experimental evidence supporting such assumption will be provided below.

The second order spectrum of the starting graphite is dominated by the 2D band, located at ~2700 cm^{-1} (Fig. 4a), which is seen as a broad and weak feature in the case of
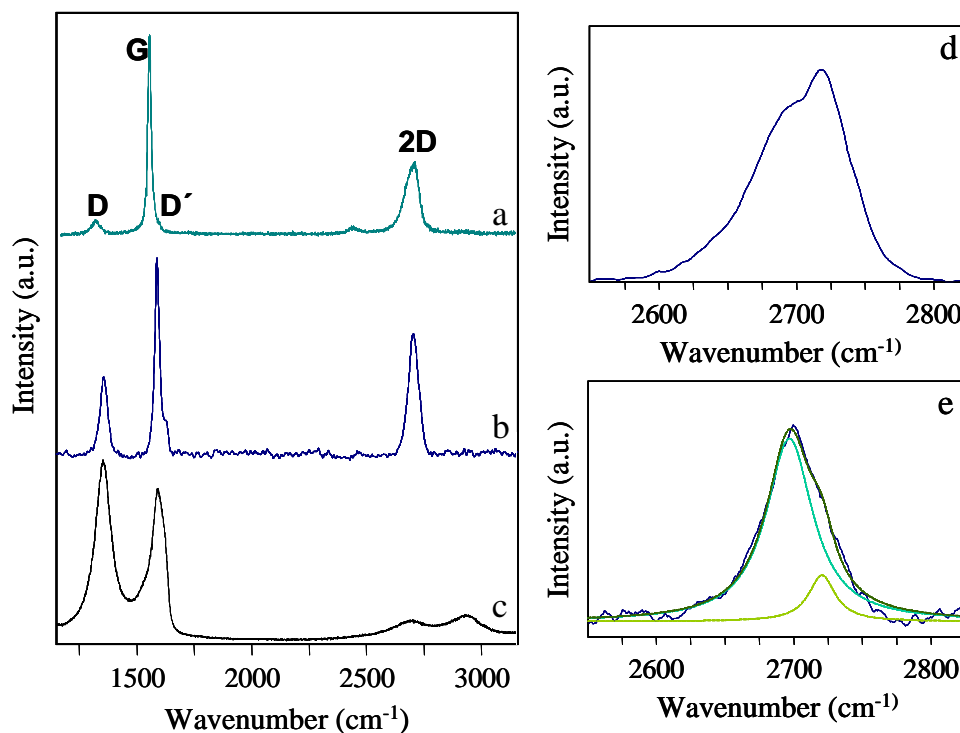
Figure 4. Raman spectra of (a) pristine natural graphite powder, (b) graphene dispersion stabilized by the non-ionic surfactant P-123, and (c) chemically reduced graphene oxide. The P-123-stabilized graphene and chemically reduced graphene oxide samples in (b) and (c), respectively, were prepared starting from the natural graphite powder in (a). (d and e) Detailed 2D Raman bands for the starting natural graphite powder (d) and P-123-stabilized graphene dispersions (e).

reduced graphene oxide (Fig. 4c). A broad and weak 2D band has been related to significant structural disorder in graphitic materials, as opposed to the sharp and strong one exhibited by highly crystalline specimens [29, 30]. We note that the latter character -ristics are displayed by the 2D band of both the starting graphite and the graphene dispersions (Fig. 4a and b). Also, lattice disorder in graphitic materials usually leads to the appearance of an additional band at ~2920 cm^{-1}, which is not present in defect-free graphite [29]. Such band is clearly discernible for reduced graphene oxide, but not for the starting graphite and the graphene dispersions. Likewise, the shape of the 2D band reflects the number of layers in graphene samples, and can be used to distinguish single-layer, few-layer and multi-layer flakes [31, 32]. The shape of the 2D band in our surfactant-stabilized dispersions (Fig. 4e) is clearly different to that of multi-layer, bulk graphite (Fig. 4d), and is consistent with the dispersions being dominated by few-layer

graphene flakes [31, 32]. Such result is in agreement with the AFM data of Fig. 3. Taken together, the previous observations provide strong indication that the aqueous graphene suspensions, including the highly concentrated ones prepared with non-ionic surfactants such as Tween 80 and P-123 possess a good structural quality.
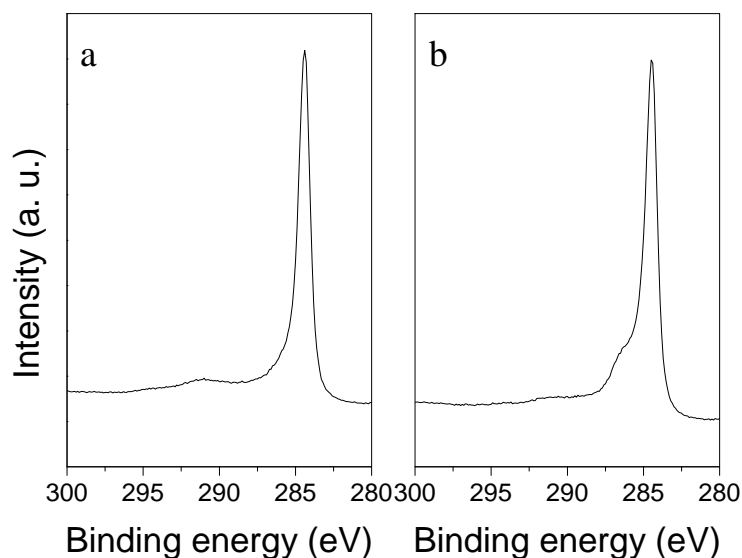
Figure 5. High-resolution C1s X-ray photoelectron spectra for the starting natural graphite powder (a) and for the material recovered from an aqueous graphene dispersion stabilized by P-123 (b).

In addition to (and related with) its high structural quality, the suspended material was seen to be essentially free of oxygen functionalities, as evidenced by XPS. This is also in contrast to the case of reduced graphene oxide, which bears a significant amount of residual functionalities [28]. Fig. 5 shows the high-resolution C1s spectra of the starting graphite (a) and of the material recovered from a P-123-stabilized suspension (b). Both spectra are dominated by the graphitic C=C component located at 284.6 eV. In addition, the surfactant stabilized material displays a small, very narrow and well defined component at ~286 eV, which we attribute to the presence of residual surfactant in the sample (C–O species). In fact, the relative contribution of such component was clearly seen to decrease with the number of washing cycles that the sample was subjected to. By contrast, the residual oxygenated functionalities present in highly reduced graphene oxide give rise to several components in the C1s spectrum that

span the 285–290 eV binding energy range [28]. This is not observed for the surfactant-stabilized samples reported here.

The present work demonstrates a straightforward route toward aqueous graphene dispersions with low defect content and high concentration (up to ~1mg mL^{-1}). Such dispersions are made possible through the use of some specific surfactants (e.g., Tween 80 and P-123). However, a more general conclusion is that non-ionic surfactants tend to perform better than ionic ones as regards their suspending ability for graphene (Fig. 1h). Such result suggests that steric repulsion is more efficient than electrostatic repulsion in the stabilization of graphene sheets in water. Steric stabilization with non-ionic surfactants is provided by their hydrophilic part extending into water. The hydrophilic moieties frequently consist of linear or branched polyethylene oxide (PEO), those with higher molecular weight providing enhanced stabilization. This is clearly seen in our case when comparing the performance of Brij 30 and Brij 700 (Fig. 1h), which essentially differ in the length of their PEO chain.
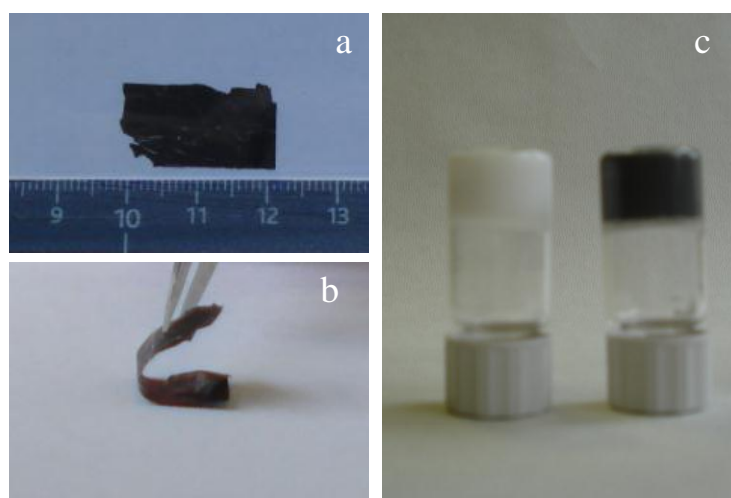
Figure 6. Digital pictures of (a and b) a P-123/graphene composite paper sample and (c) a P-123 hydrogel (left) and a P-123/ graphene composite hydrogel (right) prepared by formation of inclusion complexes between α-CD and the PEO chains of the surfactant. The scale in (a) corresponds to cm.

The ability to suspend graphene in water in significant quantities with a variety of non-ionic surfactants should facilitate the practical use of this novel material in applications that have remained as yet almost unexplored. For instance, many of the reported non-ionic surfactants are widely used in biomedical research [33, 34], which

could provide good opportunities for the integration of high quality graphene with biological systems. In many cases, processing the graphene dispersions into macroscopic materials will be required. We demonstrate this possibility by preparing surfactant/ graphene composite free-standing, paper-like films using some of the most concentrated dispersions (P-123, Brij 700 and PSS; Fig. 6a and b). Likewise, P-123/graphene hydrogels were prepared (Fig. 6c). The paper-like films were produced by vacuum filtration of the dispersions, can be handled without breaking (Fig. 6b) and are stable in water (e.g., they can be soaked in water for 1 month without disintegrating).

As revealed by SEM (Fig. 7a and b), the composite paperlike films displayed a generally smooth and homogeneous appearance, with uniform thickness in the range from a few to several micrometers. A more detailed morphological characterization of the films by AFM (Fig. 7c–f) indicated that the graphene platelets lay parallel to the film surface and were assembled into a close-packed, overlapped arrangement. The platelets were typically between several tens and a few hundred nanometers in lateral size, consistent with the dimensions measured for flakes from the as-prepared dispersions before their processing into films (Fig. 3a and b). Even though the films were gently rinsed with water prior to their study by AFM to remove surfactant from their surface and allow proper visualization of the graphene platelets, some remnants of surfactant were occasionally found (e.g., Fig. 7f). Higher resolution imaging by STM provided direct evidence of the pristine, defect-free nature of the flakes (Fig. 7g and h). It is well-known that the presence of even very small-sized defects (i.e., point defects such as atomic vacancies or interstitial and substitutional impurities) can be readily detected on graphitic structures with this technique [35-38]. Such defects are usually visualized as protrusions with diameters between one and a few nanometers in the high-resolution STM images. However, the basal plane of the graphene flakes appeared completely flat and featureless, and contrast was only observed at the flake edges (Fig. 7g). Furthermore, the atomic-scale triangular pattern characteristic of highly ordered graphitic systems was seen all across the basal surface of the flakes without showing any kind of discontinuity or local alteration (Fig. 7h). We therefore conclude that the graphene flakes in our surfactant-stabilized dispersions are virtually free of in-plane defects. The increase in the I_D/I_G ratio of the dispersed material in relation to that of the starting graphite reported by Raman spectroscopy (Fig. 4) must then be related exclusively to the contribution of graphene edges, whose relative abundance is enlarged

for flakes of relatively small size, such as those obtained here in the aqueous dispersions. We also note that the D, G, D´ and 2D bands in the Raman spectra of graphene flakes obtained directly from the aqueous dispersions (Fig. 4b) and from the vacuum assembled films (spectra not shown) are essentially indistinguishable from each other. This result indicated that the suspended and assembled flakes are structurally identical, as could be expected.
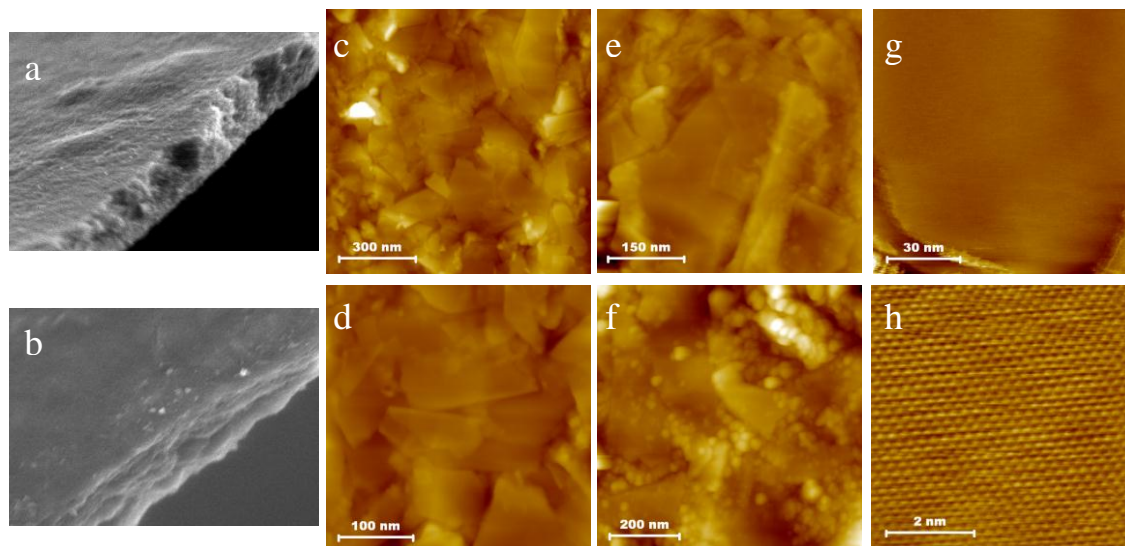
Figure 7. (a,b) SEM images of P-123/graphene (a) and Brij 700/graphene (b) composite paper-like films. (c–f) AFM images of Brij 700/graphene (c,d), PSS/graphene (e) and P-123/graphene (f) composite films. (g,h) High resolution STM images of grapheneflakes in Brij 700/graphene composite films.

TGA under flowing O_2 was used to determine the mass percentage of surfactant in the vacuum-assembled paper-like films. As an example, a thermogravimetric (TG) plot of P-123/ graphene composite film is shown in Fig. 8. These surfactant/ graphene films typically exhibited two well-defined mass losses, which took place at ~250–300ºC and ~550–600 ºC, and can be attributed to gasification of the surfactant molecules and the graphene flakes, respectively. For instance, the mass percentage of surfactant was calculated to be 9, 12 and 43 for PSS/, P-123/ and Brij 700/graphene composite films, respectively. We note that the fraction of surfactant in the films does not correlate with the concentration of graphene that the surfactants are able to sustain in the aqueous dispersions. In principle, we would anticipate higher graphene fractions, and therefore lower fractions of surfactant, for those films prepared from dispersions with surfactants

Figure 8. Thermogravimetric plot (blue) and its derivative (green) of P-123/ graphene composite paper-like film.

that allow larger concentrations of graphene. Thus, according to the results of Fig. 1h, the surfactant fraction in the films should follow the order P-123 < Brij 700 < PSS. The fact that t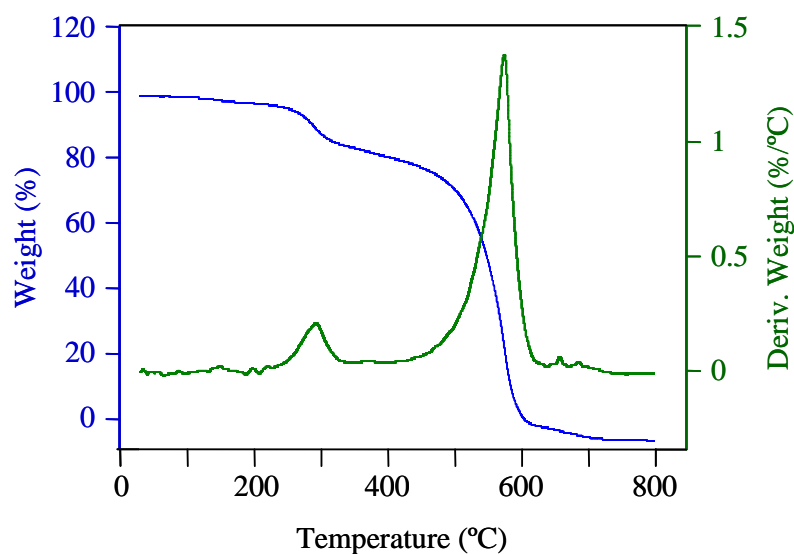his trend was not actually observed is not understood at present. Nevertheless, the measured electrical conductivity of the films (3600, 1160 and 190 Sm 1 for PSS/, P-123/ and Brij 700/graphene films) did in fact parallel their real surfactant fraction. It can be reasonably expected that the electrical contacts between neighboring graphene platelets, and consequently the electrical transport in the films, would be hindered by the presence of surfactant molecules; thus, the larger fraction of surfactant in the films, the lower the resulting conductivity, as it was indeed observed. In any case, the measured conductivity values are comparable to those of similarly prepared graphene films reported by other authors [15, 21].

4. Conclusions

It has been shown that non-ionic surfactants can exfoliate and disperse pristine graphene from graphite in water at significant concentrations, which can be as high as ~1 mg mL^{-1} with some specific surfactants. The resulting dispersions are constituted by single- and few-layer graphene sheets whose basal planes are essentially free of structural defects, even of the smallest size (point defects). These dispersions can be processed into potentially useful macroscopic materials, such as paper-like films with significant values of electrical conductivity. The present results should facilitate the

low-cost, high-throughput production and manipulation of this material toward different applications.

Acknowledgements

References

[1]   Geim AK, Novoselov KS. The rise of graphene. Nat. Mater. 6 (2007), 183-191.

[2]   Rao CNR, Sood AK, Subrahmanyam KS, Govindaraj A. Graphene: the new two-dimensional nanomaterial. Angew. Chem. Int. Edit. 48 (2009), 7752-7777.

[3]   Allen MJ, Tung VC, Kaner RB. Honeycomb carbon: a review of graphene. Chem. Rev. 110 (2009), 132-145.

[4]   Park S, Ruoff RS. Chemical methods for the production of graphenes. Nat. Nanotech. 4 (2009), 217-224.

[5]   Li X, Cai W, An J, Kim S, Nah J, Yang D, Piner R, Velamakanni A, Jung I, Tutuc E, Banerjee S, Colombo L, Ruoff RS. Large-area synthesis of high-quality and uniform graphene films on copper foils. Science 324 (2009), 1312-1314.

[6]   Emtsev KV, Bostwick A, Horn K, Jobst J, Kellogg GL, Ley L, McChesney JL, Ohta T, Reshanov SA, Rohrl J, Rotenberg E, Schmid AK, Waldmann D, Weber HB, Seyller T. Towards wafer-size graphene layers by atmospheric pressure graphitization of silicon carbide. Nat. Mater. 8 (2009), 203-207.

[7]   Li D, Muller MB, Gilje S, Kaner RB, Wallace GG. Processable aqueous dispersions of graphene nanosheets. Nat. Nanotech. 3 (2008), 101-105.

[8]   Park S, An J, Jung I, Piner RD, An SJ, Li X, Velamakanni A, Ruoff RS. Colloidal suspensions of highly reduced graphene oxide in a wide variety of organic solvents. Nano Lett. 9 (2009), 1593-1597.

[9]   Villar-Rodil S, Paredes JI, Martinez-Alonso A, Tascon JMD. Preparation of graphene dispersions and graphene-polymer composites in organic media. J. Mater. Chem. 19 (2009), 3591-3593.

[10]   Agarwal S, Zhou X, Ye F, He Q, Chen GCK, Soo J, Boey F, Zhang H, Chen P. Interfacing live cells with nanocarbon substrates. Langmuir 26 (2010), 2244-2247.

[11]   Dua V, Surwade SP, Ammu S, Agnihotra SR, Jain S, Roberts KE, Park S, Ruoff RS, Manohar SK. All-organic vapor sensor using inkjet-printed reduced graphene oxide. Angew. Chem. Int. Edit. 49 (2010), 2154-2157.

[12]   Osváth Z, Darabont A, Nemes-Incze P, Horváth E, Horváth ZE, Biró LP. Graphene layers from thermal oxidation of exfoliated graphite plates. Carbon 45 (2007), 3022-3026.

[13]   Hernandez Y, Nicolosi V, Lotya M, Blighe FM, Sun Z, De S, McGovern IT,

Holland B, Byrne M, Gun'Ko YK. High-yield production of graphene by liquid-phase exfoliation of graphite. Nat. Nanotech. 3 (2008), 563-568.

[14] Hao R, Qian W, Zhang L, Hou Y. Aqueous dispersions of TCNQ-anion-stabilized graphene sheets. Chem. Commun. 0 (2008), 6576-6578.

[15] Lotya M, Hernandez Y, King PJ, Smith RJ, Nicolosi V, Karlsson LS, Blighe FM, De S, Wang Z, McGovern IT, Duesberg GS, Coleman JN. Liquid phase production of graphene by exfoliation of graphite in surfactant/water solutions. J. Am. Chem. Soc. 131 (2009), 3611-3620.

[16] Bourlinos AB, Georgakilas V, Zboril R, Steriotis TA, Stubos AK. Liquid-phase exfoliation of graphite towards solubilized graphenes. Small 5 (2009), 1841-1845.

[17] Vadukumpully S, Paul J, Valiyaveettil S. Cationic surfactant mediated exfoliation of graphite into graphene flakes. Carbon 47 (2009), 3288-3294.

[18] Englert JM, Röhrl J, Schmidt CD, Graupner R, Hundhausen M, Hauke F, Hirsch A. Soluble graphene: generation of aqueous graphene solutions aided by a perylenebisimide-based bolaamphiphile. Adv. Mater. 21 (2009), 4265-4269.

[19] Green AA, Hersam MC. Solution phase production of graphene with controlled thickness via density differentiation. Nano Lett. 9 (2009), 4031-4036.

[20] Lee JH, Shin DW, Makotchenko VG, Nazarov AS, Fedorov VE, Yoo JH, Yu SM, Choi J-Y, Kim JM, Yoo J-B. The superior dispersion of easily soluble graphite. Small 6 (2010), 58-62.

[21] Zhang M, Parajuli RR, Mastrogiovanni D, Dai B, Lo P, Cheung W, Brukh R, Chiu PL, Zhou T, Liu Z, Garfunkel E, He H. Production of graphene sheets by direct dispersion with aromatic healing agents. Small 6 (2010), 1100-1107.

[22] Wenz G, Han B-H, Müller A. Cyclodextrin rotaxanes and polyrotaxanes. Chem. Rev. 106 (2006), 782-817.

[23] Napper DH, Netschey A. Studies of the steric stabilization of colloidal particles. J. Colloid Interf. Sci. 37 (1971), 528-535.

[24] Choucair M, Thordarson P, Stride JA. Gram-scale production of graphene based on solvothermal synthesis and sonication. Nat Nanotech. 4 (2009), 30-33.

[25] Fernández-Merino MJ, Guardia L, Paredes JI, Villar-Rodil S, Solís-Fernández P, Martínez-Alonso A, Tascón JMD. Vitamin c is an ideal substitute for hydrazine in the reduction of graphene oxide suspensions. J. Phys. Chem. C 114 (2010), 6426-6432.

[26] Skoog DA, Holler FJ, Nieman TA. Principles of instrumental analysis. Philadelphia. 1998.

[27] Novoselov KS, Geim AK, Morozov SV, Jiang D, Zhang Y, Dubonos SV, Grigorieva IV, Firsov AA. Electric field effect in atomically thin carbon films. Science 306 (2004), 666-669.

[28] Paredes JI, Villar-Rodil S, Solís-Fernández P, Martínez-Alonso A, Tascón JMD. Atomic force and scanning tunneling microscopy imaging of graphene nanosheets derived from graphite oxide. Langmuir 25 (2009), 5957-5968.

[29] Chieu TC, Dresselhaus MS, Endo M. Raman studies of benzene-derived graphite fibers. Phys. Rev. B, Condensed matter 26 (1982), 5867-5877.

[30] Paredes JI, Burghard M, Martínez-Alonso A, Tascón JMD. Graphitization of carbon nanofibers: visualizing the structural evolution on the nanometer and atomic scales by scanning tunneling microscopy. Appl Phys A 80 (2005), 675-682.

[31] Ferrari AC, Meyer JC, Scardaci V, Casiraghi C, Lazzeri M, Mauri F, Piscanec S,

Jiang D, Novoselov KS, Roth S, Geim AK. Raman spectrum of graphene and graphene layers. Phys. Rev. Lett. 97 (2006), 187401.

[32] Graf D, Molitor F, Ensslin K, Stampfer C, Jungen A, Hierold C, Wirtz L. Spatially resolved raman spectroscopy of single- and few-layer graphene. Nano Lett. 7 (2007), 238-242.

[33] Kogan A, Garti N. Microemulsions as transdermal drug delivery vehicles. Adv. Colloid Interfac 123-126 (2006), 369-385.

[34] Batrakova EV, Kabanov AV. Pluronic block copolymers: Evolution of drug delivery concept from inert nanocarriers to biological response modifiers. J. Control. Release 130 (2008), 98-106.

[35] Hahn, Kang H. Vacancy and interstitial defects at graphite surfaces: Scanning tunneling microscopic study of the structure, electronic property, and yield for ion-induced defect creation. Phys. Rev. B, Condensed Matter 60 (1999), 6007-6017.

[36] Kibsgaard J, Lauritsen JV, Lægsgaard E, Clausen BS, Topsøe H, Besenbacher F. Cluster−support interactions and morphology of MoS_2 nanoclusters in a graphite-supported hydrotreating model catalyst. J. Am. Chem. Soc. 128 (2006), 13950-13958.

[37] Tapaszto L, Dobrik G, Nemes Incze P, Vertesy G, Lambin P. Tuning the electronic structure of graphene by ion irradiation. Phys. Rev. B. 78 (2008), 233407-233410.

[38] Paredes JI, Solís-Fernández P, Martínez-Alonso A, Tascón JMD. Atomic vacancy engineering of graphitic surfaces: controlling the generation and harnessing the migration of the single vacancy. J. Phys. Chem. C 113 (2009), 10249-10255.

Supporting Information for

High-throughput production of pristine graphene in an aqueous dispersions assisted by non-ionic surfactants

(Carbon 49 (2011), 1653-1662)

L. Guardia, M. J. Fernández-Merino, J. I. Paredes, P. Solís-Fernández, S. Villar-Rodil, A. Martínez-Alonso, and J. M. D. Tascón

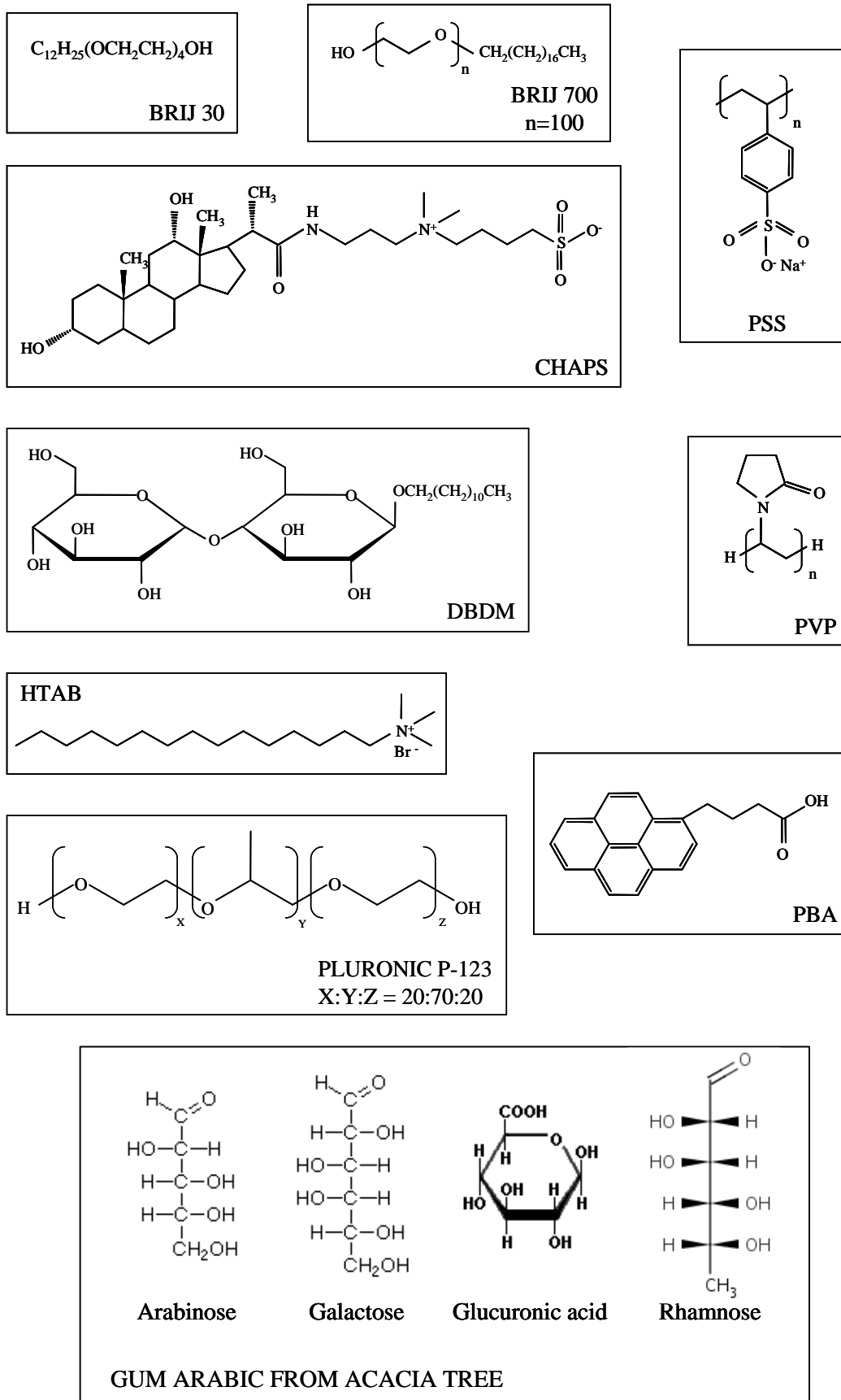Instituto Nacional del Carbón, CSIC, Apartado 73, 33080 Oviedo, Spain

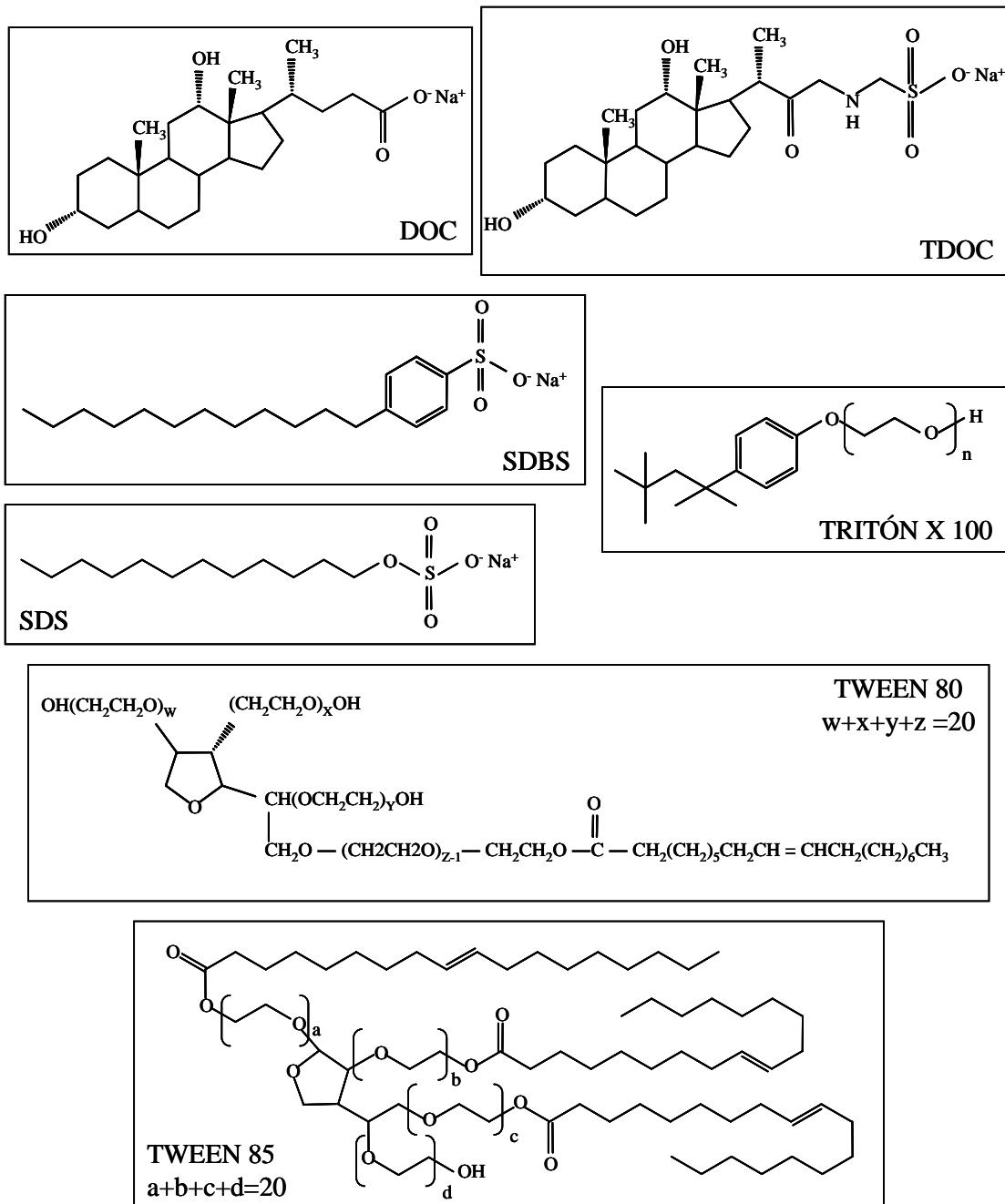**Figure S1.** Chemical structures of the surfactants used

Figure S1. *Continued.*

4.3. Preparación de materiales híbridos basados en grafeno.

Artículo V

Publicado en la revista Microporous and Mesoporous Materials: "Synthesis and characterization of graphene-mesoporous silica nanoparticle hybrids".

Artículo VI

Enviado: "Developing green photochemical approaches towards the synthesis of carbon nanofiber- and graphene-supported silver nanoparticles and their use in the catalytic reduction of 4-nitrophenol".

En el *Artículo V* se exploró la formación de estructuras híbridas formadas por grafeno y sílice, en forma de nanopartículas mesoporosas soportadas sobre las láminas de grafeno, haciendo especial hincapié en la influencia de los parámetros experimentales sobre las características de las estructuras resultantes.

Se utilizó óxido de grafeno como precursor del grafeno, tetraetilortosilicato (TEOS) como precursor de la sílice y un surfactante catiónico (CTAB) como agente director de la estructura. Los materiales obtenidos se sometieron a tratamiento térmico en atmósfera inerte para eliminar el surfactante y reducir el óxido de grafeno. Se estudió el efecto de la concentración de TEOS en las características de los materiales. Se observó que la concentración de surfactante debía ser suficiente para que se formasen micelas que estabilizasen las láminas de óxido de grafeno y sirviesen de plantilla de la sílice mesoporosa, pero no tan alta como para la nucleación homogénea de la sílice fuera de las láminas de óxido de grafeno. Por otro lado, la concentración de TEOS debía ser lo bastante pequeña como para favorecer la nucleación y crecimiento de la sílice específicamente sobre el óxido de grafeno. Fue necesario también regular el pH para que las partículas formadas no fuesen demasiado pequeñas o las dispersiones inestables.

Distintas técnicas experimentales (SEM, TEM, AFM, DRX, etc.) confirmaron que los materiales obtenidos están formados por láminas de óxido de grafeno reducido que soportan nanopartículas de sílice amorfa. En función de la cantidad de TEOS utilizada, se observaron diferencias tanto en la densidad de partícula por lámina como en el tamaño de partícula. El óxido de grafeno era necesario para la formación de las nanopartículas ya que estas se generaban a partir de micelas acopladas

electrostáticamente a las láminas. Un análisis de la textura porosa corroborado mediante TEM indicó que las partículas de sílice poseen mesoporos internos de tamaño definido quedando huecos mesoporosos de diferentes tamaños entre partículas vecinas, especialmente en las muestras con mayor densidad de partículas, que presentan un empaquetamiento compacto.

En el *Artículo VI* se exploraron métodos fotoquímicos en fase líquida para la síntesis de nanopartículas de plata soportadas sobre dos materiales de carbono nanoestructurados: nanofibras de carbono tipo "platelet" y óxido de grafeno. Dichos métodos consisten en la irradiación con luz UV de una dispersión coloidal del material de carbono, en la que está presente un precursor metálico ($AgNO_3$) y un biorreductor. Se hizo hincapié en la elección de disolventes lo más benigna posible desde el punto de vista medioambiental. En el caso del óxido de grafeno, se pudo utilizar agua debido a que las láminas son coloidalmente estables en dicho medio, pero en el caso de las nanofibras se utilizó etanol debido a que éstas no son dispersables en agua, pero sí en un determinado número de disolventes orgánicos, entre los cuales el etanol es el que posee un menor impacto ambiental.

En el caso de las nanofibras, el bioreductor utilizado para reducir los iones Ag^+ a Ag^0 en presencia de luz UV fue la piridoxamina. Las condiciones óptimas de reacción requerían la presencia adicional de amoníaco y surfactante (PVP). El PVP actúa como agente protector de las nanopartículas, limitando su tamaño, mientras que el amoníaco era necesario para controlar la densidad de nanopartículas sobre las nanofibras. En presencia de amoníaco, los iones Ag^+ forman un complejo estable, $(Ag(NH_3)_2)^+$ o reactivo de Tollens, cuya forma reducida también es estable, favoreciendo la generación de un gran número de núcleos con plata que finalmente dan lugar a una alta densidad de nanopartículas relativamente pequeñas sobre las nanofibras.

Para el óxido de grafeno en agua el uso de piridoxamina no permitió la formación de nanopartículas de plata, en cuyo caso se observó que la glucosa si permitía su formación. No fue necesaria la adición de PVP para controlar los tamaños de partículas, aunque se usó amoníaco para estabilizar las dispersiones. Las nanopartículas obtenidas tenían un tamaño similar al de las generadas sobre las nanofibras.

Se propuso un mecanismo para explicar la observación de que la piridoxamina es capaz de reducir los iones Ag^+ a Ag^0 en etanol y no en agua mediante irradiación con luz UV. Se supone que la piridoxamina se fotoexcita por su interacción con luz UV

volviéndose más reactiva. A continuación, la piridoxamina fotoexcitada puede interaccionar con las moléculas del disolvente, ya que se puede producir una transferencia de electrones del etanol hacia la piridoxamina excitada, de manera que ésta puede reducir fácilmente el ión Ag^+. En el caso del agua, la transferencia de electrones puede dar lugar a radicales OH·, que atacan y descomponen la piridoxamina excitada, impidiendo la reducción del ión Ag^+. De este modo, utilizando etanol como disolvente se forman nanopartículas de plata, mientras que en el caso de utilizar agua como disolvente las nanopartículas no se formaron.

Asimismo, se determinó que los híbridos nanopartícula de plata-material carbonoso poseían una gran actividad catalítica en la reducción de 4-nitrofenol a 4-aminofenol con $NaBH_4$, especialmente las obtenidas con óxido de grafeno como soporte.

También se observó que la glucosa en presencia de luz UV no es muy efectiva como agente reductor del óxido de grafeno. Sin embargo, se demostró que el glutatión sí lo es, lo que proporcionó un método novedoso y efectivo de reducción del óxido de grafeno a temperatura ambiente con el uso de un agente natural.

Synthesis and characterization of graphene-mesoporous silica nanoparticle hybrids

(Microporous and Mesoporous Materials 160 (2012), 18-24)

L. Guardia, F. Suárez-García, J. I. Paredes, P. Solıís-Fernández, R. Rozada, M. J. Fernández-Merino, A. Martínez-Alonso, and J. M. D. Tascón

Instituto Nacional del Carbón, CSIC, Apartado 73, 33080 Oviedo, Spain

Abstract

We report the synthesis of graphene–mesoporous silica nanoparticle (MSN) hybrids by selective growth of the latter on graphene oxide sheets using a cationic surfactant-templated method. The MSNs were just a few tens of nanometers in size, exhibited internal mesopores ~3.7–4 nm wide and appeared to be firmly attached to the graphene sheets. The nanoparticles could also be produced with varying densities on the graphene support, from isolated entities up to close-packed monolayers uniformly coating both sides of the sheets, which allowed fine-tuning the porous texture of the materials on the basis of their interparticle porosity. The experimental conditions that afford the generation of these graphene–MSN hybrids are also discussed.

1. Introduction

As a novel two-dimensional material with exceptional electronic, mechanical, thermal and optical properties, graphene has received in recent years enormous attention and dedicated efforts from the research community [1-6]. At present, both fundamental science aspects of graphene [7-9] and its prospective technological application in fields as diverse as electronics and photonics [10, 11], energy generation and storage [12] or biomedicine [13] are being intensively investigated. In this regard, a particularly active area of research concerns the development of graphene-based hybrid materials, which seek to combine the attractive features of the two-dimensional carbon lattice with some additional functionality afforded by a second component, for instance metal or semiconductor nanoparticles, polymers or organic molecules [14-22]. These hybrid structures have already shown promise for use as catalysts, electrodes for supercapacitors and Li-ion batteries, or sensors, to name a few examples.

Mesoporous silica nanoparticles (MSNs) synthesized by softtemplating routes have also been the focus of significant attention during the last decade [23-29]. A number of advantageous characteristics, including their high surface area (both internal and external) or the fact that they are amenable to processing in the form of colloidal suspensions, make MSNs serious candidates in, e.g., biomolecule/ drug immobilization and delivery, host–guest chemistry or thin film technology applications [30-33]. Although their combination with graphene sheets could potentially yield hybrid materials with enhanced functionality, to the best of our knowledge such graphene–MSN hybrids have not yet been reported. Only recently, graphene–mesoporous silica composites have been prepared and documented [34-36], but in these cases the silica component consisted of a smooth uniform coating and not of a collection of discrete, nanometer-sized particles. In the present work, we report the selective synthesis and characterization of smallsized (a few tens of nanometers) MSNs on graphene sheets, and demonstrate that simply modulating some experimental parameters (e.g., the amount of silica precursor used) affords control over the density of nanoparticles on the sheets, from isolated objects to close-packed arrangements. As will be shown below, such control allows fine-tuning the textural properties of the resulting materials.

2. Experimental

Graphene–MSN hybrids were synthesized using graphene oxide sheets and tetraethyl orthosilicate (TEOS) as respective precursors of the two components. Based on previously reported procedures [37], aqueous graphene oxide dispersions were produced by sonicating (2 h in a J.P. Selecta ultrasound bath cleaner) graphite oxide particles obtained via the Hummers method, centrifuging the resulting suspension (10,000g for 10 min in an Eppendorf 5424 microcentrifuge) and finally collecting the upper ~75% of the supernatant. The concentration of graphene oxide in these aqueous dispersions was determined by means of UV–vis absorption spectroscopy [37]. For the synthesis of the hybrids, a number of different experimental conditions, which will be commented upon below, were explored, but a typical optimized process was the following: 200 mg of the cationic surfactant cetyltrimethylammonium bromide (CTAB) were added to an aqueous graphene oxide suspension (10 mL, 0.6 mg mL 1) with the pH of the solution adjusted to 8.5 using NaOH. After bath sonication for 1 h, different amounts of TEOS (25, 50, 100, 150 or 200 μL) were added to the mixture, which was

then stirred at 40 ºC for 20 h. The resulting material was isolated by centrifugation (20,000g,3 min), thoroughly washed with ethanol, dried (60 ºC,12 h) and finally subjected to heat treatment at 350 ºC for 30 min under argon flow (50 mL min^{-1}) with a twofold purpose: removing the organic surfactant and converting the graphene oxide sheets to graphene by way of thermal reduction. The different graphene–MSN samples were denoted as G–MSN(x), where the number between parentheses x refers to the amount of TEOS (in µL) used in the preparation (e.g., G–MSN(25), where 25 stands for 25 µL of TEOS). For comparison purposes, a standard ordered mesoporous silica (MCM-48) was also synthesized. The preparation was carried out in aqueous medium using TEOS and CTAB following a previously reported procedure [38].

Characterization of the materials was carried out by UV–vis absorption spectroscopy, X-ray diffraction (XRD), Raman spectroscopy, atomic force microscopy (AFM), field emission scanning electron microscopy (FE-SEM), transmission electron microscopy (TEM), energy-dispersive X-ray spectroscopy (EDX), thermogravimetric analysis (TGA) and nitrogen physisorption. UV–vis absorption spectra were recorded in a double-beam Heλios a spectrophotometer (Thermo Spectronic). XRD was carried out with a Bruker D8 Advance diffractometer using CuK$_\alpha$ radiation (α = 0.154 nm). Raman spectra were recorded on a Horiba Jobin– Yvon LabRam instrument with a laser excitation wavelength of 532 nm and an incident power of ~0.5 mW. AFM images were obtained with a Nanoscope IIIa Multimode apparatus (Veeco Instruments) working in the tapping mode of operation under ambient conditions and using rectangular silicon cantilevers. FE-SEM and EDX analyses were accomplished in a Quanta FEG 650 instrument, from FEI Company. TEM images were obtained with a JEOL 2000 EX-II microscope under an acceleration voltage of 160 kV. TGA was performed in a SDT Q600 thermobalance (TA Instruments) under synthetic air flow (100 mL min^{-1}) at a heating rate of 3 ºC min^{-1}, using platinum crucibles. Nitrogen adsorption–desorption isotherms at - 196 ºC were recorded in a volumetric apparatus (ASAP 2010, from Micromeritics). Prior to the measurement, the samples were outgassed at 80 ºC overnight.

3. Results and discussion

The results of the optical characterization of the starting aqueous graphene oxide dispersion and a representative graphene– MSN sample (G–MSN(100)) dispersed in

ethanol, are shown in Fig. 1 (a: digital pictures of the suspensions; b: UV–vis absorption spectra). The starting dispersion exhibits the well-known yellow– brown color distinctive of unreduced graphene oxide (Fig. 1a, left cuvette), and is constituted by sheets with a typical lateral size of a few hundred nanometers (~200–500 nm) and an apparent thickness of ~1 nm as determined by AFM (see Fig. 3a below). Such apparent thickness is consistent with the sheets being single-layer objects, i.e., individual graphene oxide sheets [37, 39]. The UV–vis absorption spectrum of the graphene oxide dispersion (Fig. 1b, orange plot) displays a maximum at ~231 nm, attributed to $\pi \rightarrow \pi^*$ transitions from small electronically conjugated domains, together with a shoulder at ~300 nm, which is ascribed to $n \rightarrow \pi^*$ transitions from C=O groups [40, 41]. Although the graphene–MSN samples are produced in dry powder form, they can be dispersed in ethanol through gentle grinding with a mortar and pestle followed by mild sonication, yielding stable black-colored suspensions (Fig. 1a, middle cuvette). This black color is a first indication that the graphene oxide sheets in the hybrid samples have been reduced (deoxygenated). Further, the UV–vis absorption spectra of these samples (e.g., black plot in Fig. 1b for sample G– MSN(100)) display a red-shifted absorption peak (located at ~262 nm) as well as increased absorbance in the whole wavelength range above 262 nm. These two features are known to be characteristic of reduced graphene oxide [37, 40]. In particular, the magnitude of the red-shift in the absorption peak originally located at 231 nm for unreduced graphene oxide is a good indicator of the extent of reduction, and the value measured in the present case (~31 nm) indicates that the graphene oxide sheets in the hybrid samples have been properly reduced [42]. Reduction of the graphene oxide sheets in the hybrid samples was brought about by the heat treatment step at 350 ºC under Ar flow. Previous thermogravimetric analyses of graphene oxide have revealed a sharp mass loss between about 150 and 250 ºC, which is due to desorption of the labile oxygen groups present on this material [42]. Therefore, any heat treatment carried out at temperatures above ~150 ºC will lead to an effective deoxygenation/reduction of graphene oxide. Also, as could be expected, removal of the graphene sheets from the hybrid samples through their gasification in air at high temperature [43] leads to dry white silica powders as well as to transparent or slightly whitish dispersions in ethanol (Fig. 1a, right cuvette), the latter being indicative of some scattering of light by the silica particles (Fig. 1b, dark gray plot).
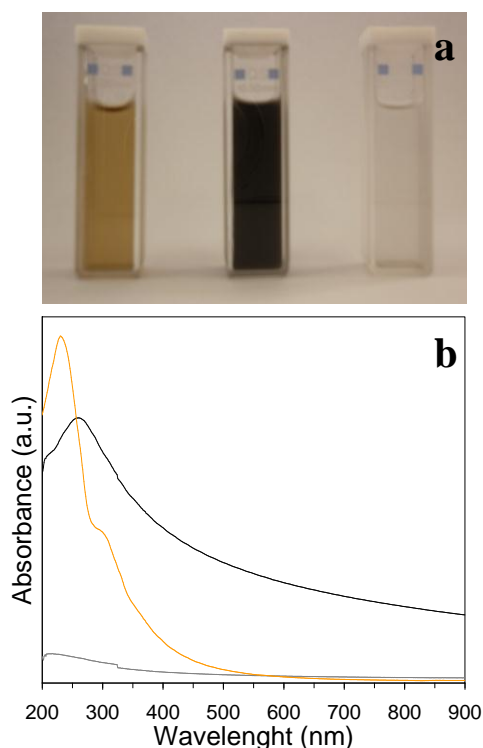
Figure 1. Digital photographs (a) and UV–vis absorption spectra (b) of the starting aqueous graphene oxide dispersion (left cuvette and orange plot), a suspension of sample G–MSN(100) in ethanol (center cuvette and black plot), and an ethanol suspension of sample G–MSN(100) after removal of its graphene component (right cuvette and gray plot). (For interpretation of the references to color in this figure legend, the reader is referred to the web version of this article.)

Structural characterization of the graphene–MSN hybrids was carried out by means of XRD and Raman spectroscopy. Fig. 2 shows low angle (a) and wide angle (b) X-ray diffractograms together with Raman spectra (c) of some representative samples. For comparison purposes, data for the ordered mesoporous silica MCM-48 are also included. Both MCM-48 and the graphene–MSN samples display a broad peak at ~23º (2h) in the wide angle diffractogram (Fig. 2b), indicating that they all comprise amorphous silica. However, peaks at low angle were only observed for MCM-48 (Fig. 2a), which implies that the graphene–MSN hybrids lack an ordered pore structure. The reason for such result will be discussed below. We note that in the absence of graphene oxide sheets in the synthesis solution, and keeping the other synthesis parameters the same, silica structures could be hardly generated. Significant amounts of silica could
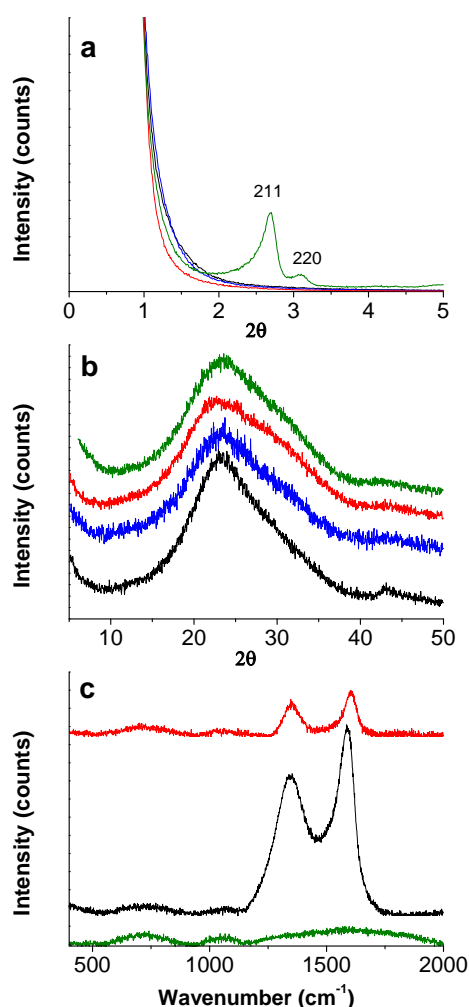
Figure 2. XRD patterns recorded at low (a) and high (b) angle for samples G–MSN(50) (black plot), G–MSN(100) (blue), G–MSN(200) (red) and MCM-48 (green). (c) Raman spectra of G–MSN(50) (black), G–MSN(200) (red) and MCM-48 (green). (For interpretation of the references to color in this figure legend, the reader is referred to the web version of this article.)

only be produced when graphene oxide was present in the synthesis solution, indicating that the latter is required for their formation. The Raman spectra of the hybrids are dominated by two strong bands at about 1350 and 1590 cm^{-1} (Fig. 2c). These two bands can be assigned, respectively, to the D and G peaks characteristic of graphitic materials in general and of reduced graphene oxide in particular [37]. In addition to the D and G bands, the Raman spectra of the hybrids display two weak, very broad features below 1150 cm^{-1}, which are never observed for stand-alone reduced graphene oxide and are attributed to the amorphous structure of the silica nanoparticles in the hybrids. In fact,

the Raman spectrum of MCM-48, also shown in Fig. 2c, exhibited the same two broad features. Taken together, the XRD and Raman spectroscopy results indicate the presence of both graphene and silica components in the investigated samples.

Fig. 3b–i shows several representative AFM images of different graphene–MSN samples deposited onto atomically flat highly oriented pyrolytic graphite (HOPG) substrates, which reveal the nanoparticulate morphology of their silica component. We note that when silica structures were generated from the graphene oxide sheets (as determined by, e.g., XRD), the only change observed in the AFM images was the appearance of nanoparticles clustered around the graphene sheets, in such a way that the higher the amount of silica precursor (TEOS) used, the larger the number of nanoparticles formed on the sheets. Consequently, we infer that these nanoparticles correspond to the formed silica structures. For samples prepared with the lowest amount of TEOS (G– MSN(25), Fig. 3b9, the graphene sheets tend to be decorated with isolated nanoparticles whose typical height lies in the 20–25 nm range (see superimposed line profile in Fig. 3b). The use of intermediate quantities of TEOS, e.g., samples G–MSN(50) (Fig. 3c and d) and G–MSN(100) (Fig. 3e and f), leads to higher densities of nanoparticles on the sheets, which appear to be quite uniform in size. As exemplified in the overlaying line profile of Fig. 3c, the local height of these structures was either ~25 or ~50 nm. We interpret that the former situation arises at sheet locations with just one nanoparticle on either side of the sheet, while the value of about 50 nm would be expected at sites having a ~25 nm high nanoparticle on both sides of the sheet. Thus, if the sheets were coated with a close-packed monolayer of nanoparticles on both sides, the resulting slab-like objects should possess a more or less uniform thickness of approximately 50 nm. Such a case was actually achieved for samples prepared with the highest amount of TEOS (G–MSN(200)), as evidenced in Fig. 3g and h. Fig. 3i presents a more detailed AFM image of the close-packed arrangement of nanoparticles, where the color scale has been adjusted to highlight even minor topographical variations. In addition to the expected trenches and voids between neighboring nanoparticles, the nanoparticles themselves are seen to display a slightly irregular surface, rather than a perfectly smooth one. Significantly, for any amount of TEOS employed, we never observed sheets that were free of nanoparticles and we hardly observed stand-alone nanoparticle (i.e., separated from the sheets), indicating that the latter are only generated in physical association with the graphene sheets (that is to say, covering the sheets).
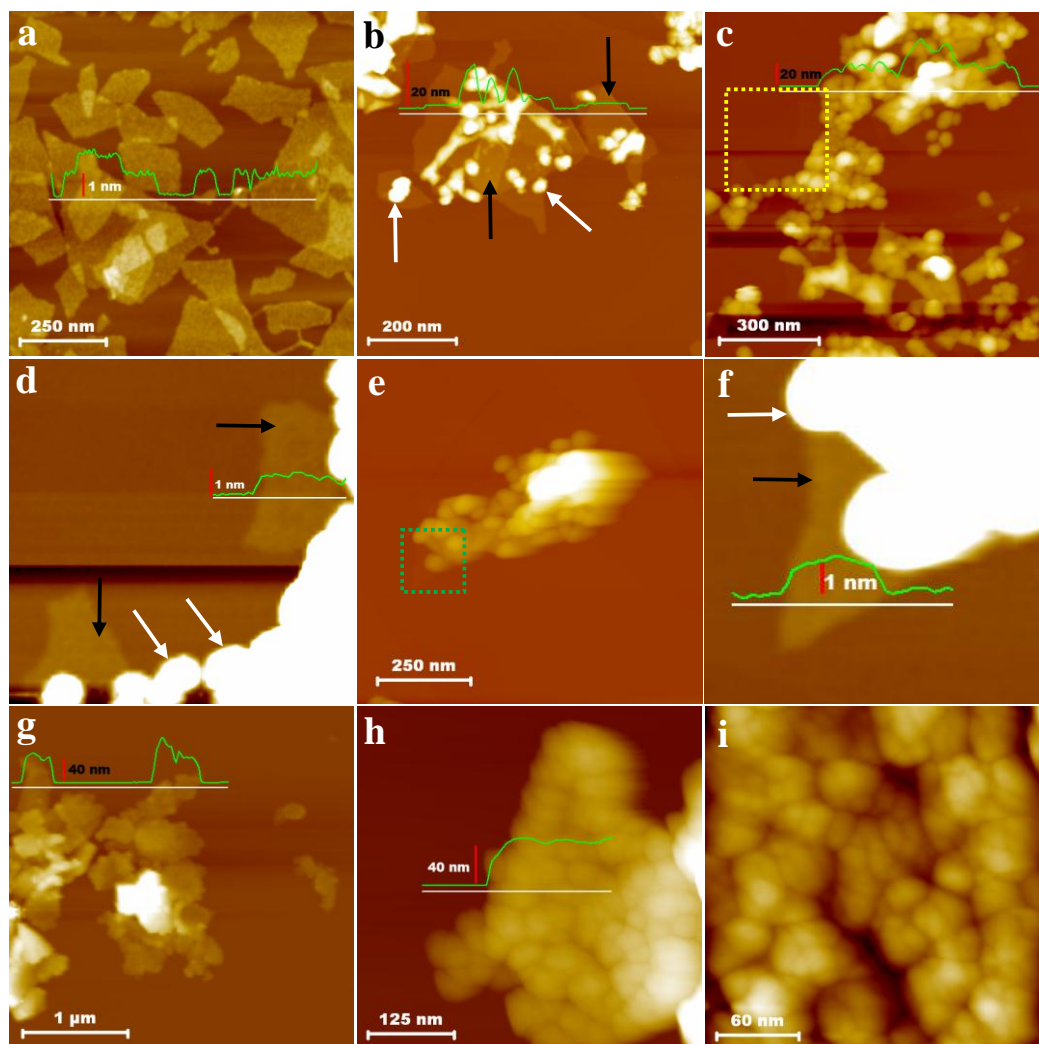
Figure 3. Representative AFM images of the starting graphene oxide (a) and different graphene–MSN samples (b–i) deposited onto atomically flat HOPG substrates. (b) Sample G–MSN(25). (c and d) Sample G–MSN(50), with d corresponding to magnification of the area within the dotted yellow square in c. (e and f) Sample G–MSN(100), with f corresponding to magnification of the area within the dotted green square in e. (g–i) Sample G–MSN(200). In several cases, a line profile (green plot) taken along the marked white line is shown superimposed on the image. The vertical red bar indicates the height scale for the line profile. In some of the images, black (white) arrows indicate the position of representative graphene sheets (silica nanoparticles). (For interpretation of the references to color in this figure legend, the reader is referred to the web version of this article.)

This was most evident in the case of samples with isolated nanoparticles (Fig. 3b). For samples with intermediate nanoparticle densities (Fig. 3c and e), the graphene sheets were frequently seen sticking out from the silica aggregates (e.g., Fig. 3d and f for the areas within the yellow and green dotted squares from Fig. 3c and e, respectively). In the case of samples made up of ~50 nm thick slabs of close-packed nanoparticles (Fig. 3g), the shape and lateral size of the objects were commensu rate with those of the starting graphene oxide sheets (Fig. 3a), and stand-alone 1 nm-thick sheets were never observed. As will be further discussed below, these observations imply a selective nucleation of the silica nanoparticles on the graphene oxide sheets, rather than throughout the whole synthesis solution.

We also stress that the starting material for the synthesis of the hybrids is an aqueous dispersion of exfoliated graphite oxide prepared by sonication and subsequent centrifugation, where it is well established that the graphite oxide particles are fully cleaved into individual, single-layer graphene oxide sheets [39]. In fact, AFM imaging of the present graphene oxide suspensions (Fig. 3a) indicated that these sheets have an apparent thickness of about 1 nm, which is consistent with single-layer graphene oxide [37, 39]. During the preparation of the hybrids (in particular, upon addition of CTAB), we did not observe agglomeration of the sheets. Therefore, every individual single-layer graphene oxide sheet can be expected to be coated with MSNs, so that after the heat-treatment step at 350 ºC, a single-layer graphene–MSN hybrid is obtained. This point can be corroborated in the AFM images of the hybrids prepared from low amounts of TEOS so that the sheets are still clearly made out, e.g., sample G–MSN(25) (Fig. 3b). From Fig. 3b, we see flat objects with an apparent thickness of ~1 nm, which is also consistent with their being single-layer reduced graphene oxide sheets [37, 40]. Furthermore, the original lateral size of the graphene oxide sheets (~200–500 nm, Fig. 3a) is not expected to change as a result of the processing steps that lead to the graphene–MSN hybrids. Indeed, in the samples with the lowest density of MSNs on graphene (G–MSN(25)), for which the entire contour of the individual sheets can still be appreciated (Fig. 3b), sheets sizes are also typically between 200 and 500 nm. For the sample with the highest density of MSNs (G–MSN(200)), the resulting ~50 nm thick slabs of close-packed nanoparticles exhibit the same lateral dimensions as those of the starting graphene oxide sheets. This can be appreciated by comparing the silica slabs of Fig. 3g with the stand-alone sheets of Fig. 3a.
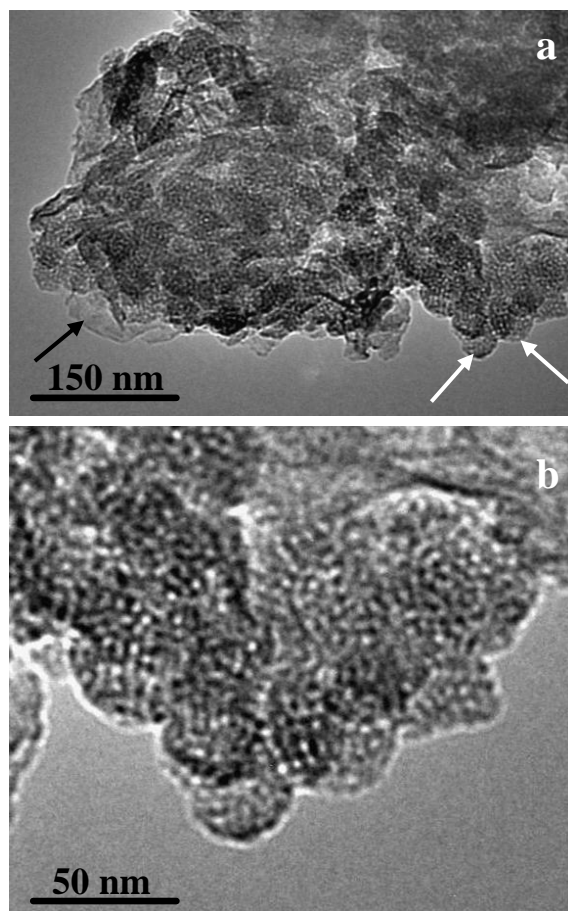
Figure 4. TEM images of sample G–MSN(200). (a) General view showing the nanoparticulate morphology of the sample. (b) Detailed image revealing the internal mesoporous structure of the silica nanoparticles. In (a), black (white) arrows indicate the position of graphene sheets (silica nanoparticles).

Because their growth was templated by the surfactant CTAB, the silica nanoparticles in the graphene–MSN hybrids are expected to possess an internal structure of mesoporous character, which was confirmed by TEM imaging. For example, Fig. 4a shows a general TEM image of sample G–MSN(200). The overall structure seen in this image is consistent with the close-packed arrangement of nanoparticles documented above by AFM for G–MSN(200) (e.g., Fig. 3h). In addition, mesoporous voids in the form of white/light gray dots are clearly observed within individual nanoparticles throughout the sample, which can be appreciated in more detail in Fig. 4b. From these images, the mesopore width was estimated to be ~3.5–4.0 nm.

Further characterization was carried out by FE-SEM and EDX spectroscopy. To this end, a relatively large amount of sample was cast from its ethanol suspension onto an HOPG substrate, forming a spatially inhomogeneous deposit. One example is presented in the FE-SEM image of Fig. 5a for sample G–MSN(50), which shows a thick deposit of material on the left part of the image, while on the right part the HOPG substrate is only sparingly covered with the hybrid. Higher resolution images of the thick deposit corroborate the nanoparticulate morphology of the sample (e.g., Fig. 5b), in agreement with the AFM results. Also in accordance with expectations, the EDX spectra recorded on the thick deposits (Fig. 5c) indicated that the graphene–MSN hybrids consisted exclusively of silicon, oxygen and carbon. Furthermore, EDX mapping of these three elements for the region shown in Fig. 5a confirmed a uniform distribution of silicon and oxygen on the hybrid material (Fig. 5d and e for the silicon and oxygen maps, respectively), whereas carbon was prevalent on areas that were only sparsely covered by the hybrid and therefore dominated by the graphite substrate (Fig. 5f).
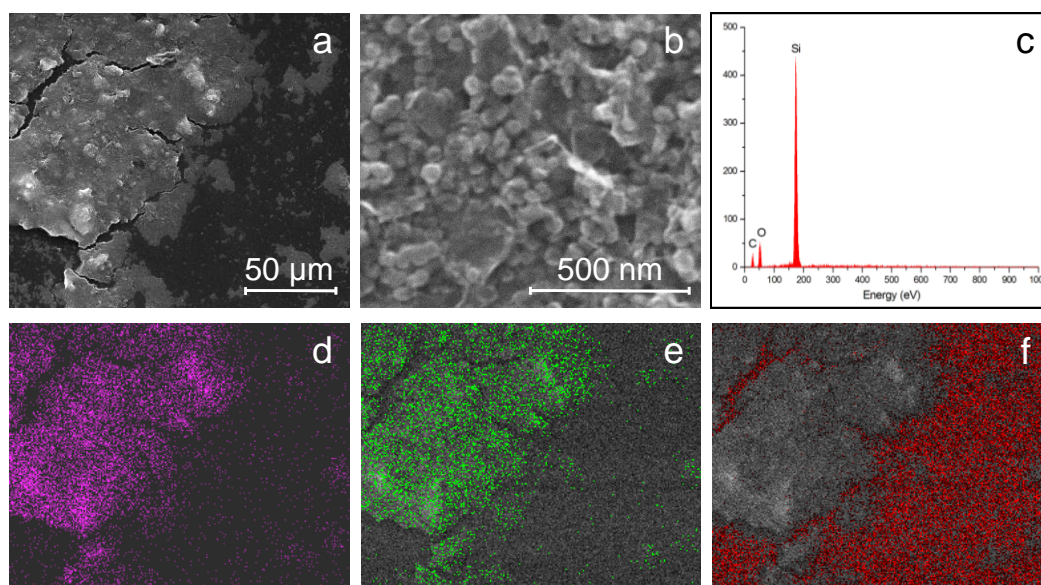

Figure 5. (a, b) FE-SEM images of sample G–MSN(50) cast on HOPG: (a) general image comprising a thick deposit (left) and an area sparingly covered with the sample (right). (b) Detailed image showing the MSNs. (c) EDX spectrum of the thick deposit seen in a. (d–f) Elemental EDX mapping images of silicon (d), oxygen (e) and carbon (f) for the area shown in a.

The amount of graphene in the hybrids was assessed by means of TGA under flowing air atmosphere. Fig. 6 presents the thermogravimetric plots for several graphene–MSN samples, which are all characterized by a mass loss step in the ~350–600 ℃ region. Such a mass loss can be attributed to gasification of the reduced graphene oxide component [43] and therefore allows the weight percentage of graphene sheets in the hybrids to be estimated as 38, 19, 15 and 5 for samples G–MSN(50), G–MSN(100), G–MSN(150) and G–MSN(200), respectively. Thus, the contribution of graphene to the total weight of the hybrids decreases when the amount of TEOS used in the synthesis is raised, consistent with the AFM observation of increasing densities of silica nanoparticles on the graphene sheets (Fig. 3). In addition, no mass loss was detected by TGA for any of the graphene–MSN hybrids in the temperature range between ~150 and 250 ℃, providing further indication that the graphene oxide sheets in the hybrids had been effectively reduced (deoxygenated). As mentioned previously, TGA of unreduced graphene oxide under Ar flow reveals a sharp mass loss at 150–250℃ due to desorption of the labile oxygen functionalities. It has been well established that reduction of graphene oxide, whether it is carried out by chemical, thermal or other means, removes these labile groups [5], so that well-reduced samples do not exhibit such mass loss anymore in their thermograms [42].
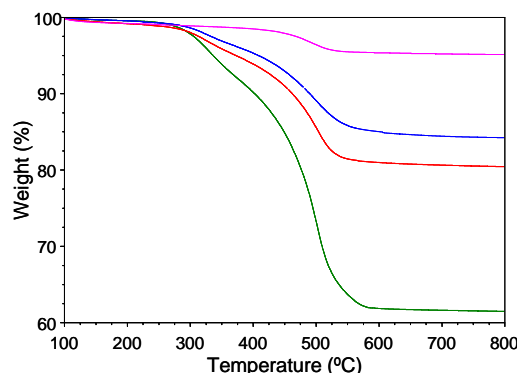
Figure 6. Thermogravimetric plots recorded under flowing air atmosphere for samples G–MSN(50) (green), G–MSN(100) (red), G–MSN(150) (blue) and G–MSN(200) (pink). (For interpretation of the references to color in this figure legend, the reader is referred to the web version of this article.)

From the results presented above, we can expect the porous texture of the graphene–MSN hybrids to be determined not only by the internal mesoporous structure of the silica nanoparticles (intraparticle porosity) but also by the presence of voids

between adjacent nanoparticles (interparticle porosity), especially for samples with a high density of close-packed nanoparticles on the graphene sheets (e.g., G–MSN(200), Fig. 3i). Fig. 7 shows nitrogen adsorption/desorption isotherms (a) and corresponding pore size distributions (PSDs) derived by the BJH method (b) for some representative samples: G–MSN(50), G–MSN(100) and G–MSN(200). In all cases, type IV isotherms indicative of mesoposous materials were recorded. The BET surface area and different pore volumes of these samples are given in Table 1. The surface area of the graphene–MSN sample with the highest content of silica (G–MSN(200), 866 m^2 g^{-1}) is comparable to those of other MSNs reported in the literature [25, 27, 28, 30, 31]. The PSDs were dominated by a sharp peak centered at 3.7–4.0 nm. Such a well-defined pore size agrees with that observed within individual silica nanoparticles by TEM (Fig. 4), and is therefore ascribed to intraparticle porosity. The remaining features in the PSDs are dependent on the specific sample and can be attributed to interparticle porosity. For samples G–MSN(50) and G–MSN(100), there is a non-negligible amount of porosity with a broad size distribution from 5 up to ~15–20 nm. These samples comprise relatively high densities of silica nanoparticles on the graphene sheets in a loose rather than compact disposition (Figs. 3c and e and 5b), which should lead to voids with a wide variety of sizes between neighboring nanoparticles, as actually noticed in their PSD. By contrast, sample G–MSN(200) consists of a close-packed arrangement of nanoparticles on the sheets (Fig. 3h), and consequently the interparticle voids should be comparatively small and possess well-defined sizes (narrower size distribution). This is reflected in the corresponding PSD, which exhibits two relatively narrow peaks centered at 2.5 and 6.1 nm that were not present in the former samples. Hence, the porous texture of the hybrids can be modulated to some degree by simply changing the density of nanoparticles on the graphene sheets.
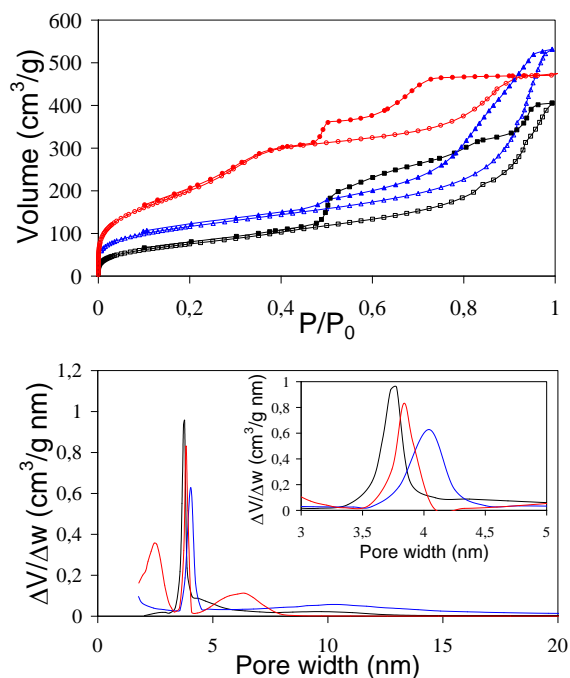
Figure 7. Nitrogen adsorption–desorption isotherms (a) and PSDs (b) for samples G–MSN(50) (black plots), G–MSN(100) (blue plots) and G–MSN(200) (red plots). In a the adsorption (desorption) branch of the isotherms is depicted with open (full) symbols. The inset in b shows the PSDs in the 3–5 nm range in more detail. (For interpretation of the references to color in this figure legend, the reader is referred to the web version of this article.)

Table 3. BET surface area (SBET), total pore volume (VT), micropore volume determined by the Dubinin–Radushkevich equation (VDR) and mesopore volume determined by the DFT method (Vm) obtained from the nitrogen adsorption/desorption isotherms of Fig. 7a. Surface areas are given in m2 g 1 and pore volumes in cm^3 g^{-1}.

Graphene-MSN sample	S_{BET}	V_T	V_{DR}	V_m
G-MSN (50)	278	0.5846	0.0882	0.4964
G-MSN (100)	408	0.7954	0.1660	0.6293
G-MSN (200)	866	0.7277	0.2293	0.4984

Finally, we briefly discuss the experimental conditions that allow the generation of the silica nanoparticles selectively on graphene oxide as observed here. Graphene oxide sheets under neutral or basic conditions are known to be negatively charged as a result of deprotonation of some of their oxygen-containing groups (e.g., carboxyls), and these negative charges are ultimately responsible for the colloidal stability of the stand-

alone sheets in water [40]. When a cationic surfactant such as CTAB is added to an aqueous suspension of negatively charged graphene oxide sheets, two possible scenarios would in principle be possible: (i) at low surfactant concentration, the positively charged headgroup of the surfactant molecules is expected to strongly adsorb onto the graphene oxide sheets by way of electrostatic attraction, thus neutralizing the negative charges on the sheets and compromising their colloidal stability. At the same time, the alkyl chain of the adsorbed surfactant molecule should increase the hydrophobicity of the graphene oxide sheets, thus inducing their agglomeration and precipitation [44]. We have indeed observed such behaviour for CTAB concentrations of just a few mg per mL or below. This situation is not desirable because it would inevitably lead to the generation of inhomogeneous graphene–MSN materials. (ii) At sufficiently high surfactant concentrations, the surfactant molecules that bind electrostatically to graphene oxide can be expected to initiate the formation of micellar aggregates (admicelles) firmly attached to the sheets. These admicelles would serve two purposes, that is to say, they would colloidally stabilize the graphene oxide sheets on the basis of their net positive charge and template the formation of mesoporous silica structures on the sheets. As a matter of fact, high surfactant concentrations did not lead to precipitation of the graphene oxide dispersion in our experiments, which is advantageous for the preparation of homogeneous graphene–silica hybrids. On the other hand, the synthesis of mesoporous silica particles with nanometer-sized dimensions has been shown to entail the use of low surfactant concentrations [26, 45]. By choosing a CTAB concentration of 20 mg mL^{-1}, we found that a compromise between these two opposite requirements could be made. Likewise, we used very small amounts of TEOS to favor the nucleation and polymerization of the silicate species selectively on the graphene oxide sheets rather than homogeneously in the bulk of the synthesis solution [35]. Indeed, control experiments indicated that silica nanoparticles could be hardly generated in the absence of graphene oxide sheets for all the amounts of TEOS employed in this work, implying that the sheets play a pivotal role in their formation under the experimental conditions used here. Furthermore, stand-alone nanoparticles (i.e., detached from the sheets) were rarely observed by AFM or FE-SEM even after ultrasound treatment of the hybrids, which also suggests that there is a strong linkage between the sheets and the MSNs. It is likely that covalent bridges between the two components can form as a result of condensation reactions between the growing silicate

species and the hydroxyl groups that are known to be abundant in graphene oxide [46]. We also note that the admicelles assembled on graphene oxide can be expected to be spherical rather than cylindrical (lying flat on the sheets). The latter conformation would have led to mesoporous channels running parallel to the sheets, which were not observed by TEM (Fig. 4). Although hemicylindrical admicelles are known to form on the atomically flat, oxide- and defect-free surface of pristine graphite, in terms of atomic-scale roughness, polarity and inhomogeneity the surface of graphene oxide is more similar to that of, e.g., amorphous silica, where spherical admicelles have been reported [47]. The surface irregularity of graphene oxide also suggests that the CTAB admicelles cannot be expected to arrange in an orderly fashion on the sheets, and so an ordered pore structure can neither be expected, as actually observed by XRD (Fig. 2a).

The generation of the graphene–MSN hybrids was also seen to be strongly dependent on the pH of the synthesis solution. Under acidic pH (e.g., ~4–5), no silica structures could be produced on the graphene oxide sheets. This result can be possibly put down to the fact that under such conditions some of the negative charges present on graphene oxide are neutralized by protons [40], so that the build-up of CTAB admicelles (and consequently the generation of the MSNs) on the sheets becomes less favorable. By contrast, strong binding of CTAB admicelles to the highly negatively charged graphene oxide under basic conditions should facilitate the formation of the MSNs on the sheets, as evidenced from the results presented above at pH 8.5. For higher pH values, silica nanoparticles could also be produced on the graphene oxide sheets, but their size tended to be smaller. For example, at a pH of 10.4, the sizes were typically below 10–15 nm. We interpret that under more alkaline conditions, hydrolysis of TEOS proceeds much slower than its condensation, which could limit nanoparticle growth [48]. Finally, in an effort to modulate the mesostructure of the MSNs, the preparation of the hybrids was attempted with the addition of ethanol to the aqueous synthesis solution [49]. However, this usually led to immediate agglomeration of the graphene oxide sheets. It was observed that aqueous solutions of either graphene oxide or CTAB alone were stable in the presence of ethanol, and only the mixed graphene oxide-CTAB solutions became destabilized upon addition of the alcohol. The origin of such behavior is not understood at present, but it is probably related to an ethanol-induced change in the conformation of the admicelles. Elucidating this point and finding

effective approaches to control the mesostructure of the silica nanoparticles generated on the graphene oxide sheets is suggested as a direction of future work.

4. Conclusions

Graphene–mesoporous silica nanoparticle hybrids have been successfully prepared by means of a cationic surfactant-templated approach. The nanoparticles could be selectively grown on graphene oxide sheets under controlled conditions of basic pH, low surfactant concentration and small amount of silica precursor used. Hybrids comprising a range of nanoparticle densities, from isolated nanoparticles up to close-packed monolayers coating both sides of the graphene sheets, could be generated by simply fine-tuning the amount of silica precursor employed in the synthesis. These graphene-based hybrids could be potentially useful in several prospective applications, including drug delivery, molecular sensing or thin film technology (e.g., low dielectric constant materials).

References

[1]   Geim AK, Novoselov KS. The rise of graphene. Nat. Mater. 6 (2007), 183-191.

[2]   Geim AK. Graphene: status and prospects. Science 324 (2009), 1530-1534.

[3]   Allen MJ, Tung VC, Kaner RB. Honeycomb carbon: a review of graphene. Chem. Rev. 110 (2009), 132-145.

[4]   Dreyer DR, Ruoff RS, Bielawski CW. From conception to realization: an historial account of graphene and some perspectives for its future. Angew. Chem. Int. Edit. 49 (2010), 9336-9344.

[5]   Singh V, Joung D, Zhai L, Das S, Khondaker SI, Seal S. Graphene based materials: Past, present and future. Prog. Mater. Sci. 56 (2011), 1178-1271.

[6]   Huang X, Qi X, Boey F, Zhang H. Graphene-based composites. Chem. Soc. Rev. 41 (2012), 666-686.

[7]   Garaj S, Hubbard W, Reina A, Kong J, Branton D, Golovchenko JA. Graphene as a subnanometre trans-electrode membrane. Nature 467 (2010), 190-193.

[8]   Chen J-H, Li L, Cullen WG, Williams ED, Fuhrer MS. Tunable Kondo effect in graphene with defects. Nat Phys 7 (2011), 535-538.

[9]   Rutter GM, Jung S, Klimov NN, Newell DB, Zhitenev NB, Stroscio JA. Microscopic polarization in bilayer graphene. Nat. Phys 7 (2011), 649-655.

[10]   Schwierz F. Graphene transistors. Nat. Nanotech. 5 (2010), 487-496.

[11]   Bonaccorso F, Sun Z, Hasan T, Ferrari AC. Graphene photonics and optoelectronics. Nat. photonics 4 (2010), 611-622.

[12]   Brownson DAC, Kampouris DK, Banks CE. An overview of graphene in energy production and storage applications. J. Power Sources 196 (2011), 4873-4885.

[13]   Feng L, Liu Z. Graphene in biomedicine: opportunities and challenges. Nanomedicine-UK 6 (2011), 317-324.

[14]   Bai H, Li C, Shi G. Functional composite materials based on chemically converted graphene. Adv. Mater. 23 (2011), 1089-1115.

[15]   Huang X, Yin Z, Wu S, Qi X, He Q, Zhang Q, Yan Q, Boey F, Zhang H. Graphene-based materials: synthesis, characterization, properties, and applications. Small 7 (2011), 1876-1902.

[16]   Wu D, Zhang F, Liu P, Feng X. Two-dimensional nanocomposites based on chemically modified graphene. Chem. – Eur. J. 17 (2011), 10804-10812.

[17]   Huang X, Zhou X, Wu S, Wei Y, Qi X, Zhang J, Boey F, Zhang H. Reduced graphene oxide-templated photochemical synthesis and in situ assembly of Au nanodots to orderly patterned Au nanodot chains. Small 6 (2010), 513-516.

[18]   Qi X, Pu K-Y, Zhou X, Li H, Liu B, Boey F, Huang W, Zhang H. Conjugated-polyelectrolyte-functionalized reduced graphene oxide with excellent solubility and stability in polar solvents. Small 6 (2010), 663-669.

[19]   Qi X, Pu K-Y, Li H, Zhou X, Wu S, Fan Q-L, Liu B, Boey F, Huang W, Zhang H. Amphiphilic graphene composites. Angew. Chem. Int. Edit. 49 (2010), 9426-9429.

[20]   Huang X, Li H, Li S, Wu S, Boey F, Ma J, Zhang H. Synthesis of gold square-like plates from ultrathin gold square sheets: the evolution of structure phase and shape. Angew. Chem. Int. Edit. 50 (2011), 12245-12248.

[21]   Cao X, He Q, Shi W, Li B, Zeng Z, Shi Y, Yan Q, Zhang H. Graphene oxide as a carbon source for controlled growth of carbon nanowires. Small 7 (2011), 1199-1202.

[22]   Huang X, Li S, Huang Y, Wu S, Zhou X, Gan C, Boey F, Mirkin C, Zhang H. Synthesis of hexagonal close-packed gold nanostructures. Nat. Commun. 2 (2011), 292.

[23]   Fowler CE, Khushalani D, Lebeau B, Mann S. Nanoscale materials with mesostructured interiors. Adv. Mater. 13 (2001), 649-652.

[24]   Mori H, Uota M, Fujikawa D, Yoshimura T, Kuwahara T, Sakai G, Kijima T. Synthesis of micro-mesoporous bimodal silica nanoparticles using lyotropic mixed surfactant liquid-crystal templates. Micropor. Mesopor. Mat. 91 (2006), 172-180.

[25]   Möller K, Kobler J, Bein T. Colloidal suspensions of nanometer-sized mesoporous silica. Adv. Funct. Mat. 17 (2007), 605-612.

[26]   Trewyn BG, Slowing II, Giri S, Chen H-T, Lin VSY. Synthesis and functionalization of a mesoporous silica nanoparticle based on the sol–gel process and applications in controlled release. Accounts Chem. Res. 40 (2007), 846-853.

[27]   Nandiyanto ABD, Kim S-G, Iskandar F, Okuyama K. Synthesis of spherical mesoporous silica nanoparticles with nanometer-size controllable pores and outer

diameters. Micropor. Mesopor. Mat. 120 (2009), 447-453.

[28] Chiang Y-D, Lian H-Y, Leo S-Y, Wang S-G, Yamauchi Y, Wu KCW. Controlling particle size and structural properties of mesoporous silica nanoparticles using the Taguchi method. J. Phys. Chem. C 115 (2011), 13158-13165.

[29] Zhang X, Tsapatsis M. Mesoporous silica nanoparticles from a clear sol and their transformation to lamellar silicalite-1 particles and films. Micropor. Mesopor. Mat. 138 (2011), 239-242.

[30] Kobler J, Bein T. Porous thin films of functionalized mesoporous silica nanoparticles. ACS Nano 2 (2008), 2324-2330.

[31] Hoshikawa Y, Yabe H, Nomura A, Yamaki T, Shimojima A, Okubo T. Mesoporous silica nanoparticles with remarkable stability and dispersibility for antireflective coatings. Chem. Mater. 22 (2009), 12-14.

[32] Vivero-Escoto JL, Slowing II, Trewyn BG, Lin VSY. Mesoporous silica nanoparticles for intracellular controlled drug delivery. Small 6 (2010), 1952-1967.

[33] Popat A, Hartono SB, Stahr F, Liu J, Qiao SZ, Qing Lu G. Mesoporous silica nanoparticles for bioadsorption, enzyme immobilisation, and delivery carriers. Nanoscale 3 (2011), 2801-2818.

[34] Yang S, Feng X, Wang L, Tang K, Maier J, Müllen K. Graphene-based nanosheets with a sandwich structure. Angew. Chem. Int. Edit. 49 (2010), 4795-4799.

[35] Wang Z-M, Wang W, Coombs N, Soheilnia N, Ozin GA. Graphene oxide−periodic mesoporous silica sandwich nanocomposites with vertically oriented channels. ACS Nano 4 (2010), 7437-7450.

[36] Kim Y-T, Han JH, Hong BH, Kwon Y-U. Electrochemical synthesis of CdSe quantum-dot arrays on a graphene basal plane using mesoporous silica thin-film templates. Adv. Mater. 22 (2010), 515-518.

[37] Paredes JI, Villar-Rodil S, Solís-Fernández P, Martínez-Alonso A, Tascón JMD. Atomic force and scanning tunneling microscopy imaging of graphene nanosheets derived from graphite oxide. Langmuir 25 (2009), 5957-5968.

[38] Xu J, Luan Z, He H, Zhou W, Kevan L. A Reliable synthesis of cubic mesoporous MCM-48 molecular sieve. Chem. Mater. 10 (1998), 3690-3698.

[39] Stankovich S, Dikin DA, Dommett GHB, Kohlhaas KM, Zimney EJ, Stach EA, Piner RD, Nguyen ST, Ruoff RS. Graphene-based composite materials. Nature 442 (2006), 282-286.

[40] Li D, Mueller M, Gilje S, Kaner R, Wallace G, Müller M. Processable aqueous dispersions of graphene nanosheets. Nat. Nanotech. 3 (2008), 101-105.

[41] Paredes JI, Villar-Rodil S, Martínez-Alonso A, Tascón JMD. Graphene oxide dispersions in organic solvents. Langmuir 24 (2008), 10560-10564.

[42] Fernández-Merino MJ, Guardia L, Paredes JI, Villar-Rodil S, Solís-Fernández P, Martínez-Alonso A, Tascón JMD. Vitamin C is an ideal substitute for hydrazine in the reduction of graphene oxide suspensions. J. Phys. Chem. C 114 (2010), 6426-6432.

[43] Solís-Fernández P, Paredes JI, Villar-Rodil S, Guardia L, Fernández-Merino MJ, Dobrik G, Biró LP, Martínez-Alonso A, Tascón JMD. Global and local oxidation behavior of reduced graphene oxide. J. Phys. Chem. C 115 (2011), 7956-7966.

[44] Fernández-Merino MJ, Paredes JI, Villar Rodil S, Guardia L, Solis Fernandez P, Salinas-Torres D, Cazorla-Amorós D, Morallón E, Martíínez-Alonso A, Tascón

JMD. Investigating the influence of surfactants on the stabilization of aqueous reduced graphene oxide dispersions and the characteristics of their composite films. Carbon 50 (2012), 3184-3194.

[45] Hollamby MJ, Borisova D, Brown P, Eastoe J, Grillo I, Shchukin D. Growth of mesoporous silica nanoparticles monitored by time-resolved small-angle neutron scattering. Langmuir 28 (2011), 4425-4433.

[46] Cai W, Piner R, Stadermann F, Park S, Shaibat M, Ishii Y, Yang D, Velamakanni A, An S, Stoller M, An J, Chen D, Ruoff RS. Synthesis and solid-state NMR structural characterization of 13C-labeled graphite oxide. Science 321 (2008), 1815-1817.

[47] Manne S, Gaub HE. Molecular organization of surfactants at solid-liquid interfaces. Science 270 (1995), 1480-1482.

[48] Wright JD, Sommerdijk NAJM. Advanced Chemistry Texts. 2001.

[49] Lin HP, Cheng YR, Liu SB, Mou CY. The effect of alkan-1-ols addition on the structural ordering and morphology of mesoporous silicate MCM-41. J. Mater. Chem. 9 (1999), 1197-1201.

Developing green photochemical approaches towards the synthesis of carbon nanofiber- and graphene-supported silver nanoparticles and their use in the catalytic reduction of 4-nitrophenol
(Enviado para publicación)

M. J. Fernández-Merino, L. Guardia, J. I. Paredes, S. Villar-Rodil, Martínez-Alonso, and J. M. D. Tascón

Instituto Nacional del Carbón, CSIC, Apartado 73, 33080 Oviedo, Spain

Abstract

A green, photochemical approach for the liquid-phase synthesis of carbon nanomaterial-supported silver nanoparticles is proposed. The method is based on irradiating a colloidal dispersion containing the carbon nanomaterial, a metal precursor and an environmentally friendly reducing agent (bioreductant) with UV light at room temperature. Two representative carbon materials have been used, namely, platelet-type graphite nanofibers and graphene oxide. The experimental conditions and possible mechanisms that afford the photochemical growth of the nanoparticles on each carbon support are also investigated and discussed. In addition, the resulting carbon-silver nanoparticle hybrids are demonstrated to be notably effective catalysts for the reduction of 4-nitrophenol to 4-aminophenol with NaBH4. Particularly, the graphene oxide-based samples were seen to exhibit exceptional catalytic activity towards such reaction. Finally, it is also shown that with a proper choice of bioreductant the present UV approach can afford highly reduced graphene oxide samples comparable to those attained with well-known, efficient chemical reductants (e. g., hydrazine at ~100 ºC), thus constituting an attractive room temperature alternative to such reduction methods.

1. Introduction

Due to their unique and tunable properties (optical, electronic, catalytic, etc.), noble metal nanoparticles (NPs) have been for the past two decades, and continue to be at present, the subject of widespread interest from the scientific community, offering opportunities for basic research on the size- and shape-dependent properties of matter as well as for their use in a range of technologically relevant applications that cover such diverse fields as optics, electronics, sensing, catalysis or biomedicine [1-4]. Among

noble metals, silver is particularly attractive with a view to many of these prospective uses owing to, e.g., its very high electrical conductivity, antibacterial activity and relatively low cost. From a catalysis perspective, silver nanoparticles (Ag NPs) are relevant to a number of important processes in the chemical industry, such as the selective oxidation of alkanes and alkenes [2], the hydrogenation of dyes [5] or the reduction of 4-nitrophenol (4-NP) to 4-aminophenol (4-AP) as an intermediate step in the synthesis of pharmaceutical compounds (e.g., paracetamol) [6, 7]. For their use in catalysis, the NPs are usually immobilized onto suitable substrates, such as silica, alumina, zeolites and different types of carbon materials, in order to (i) prevent their agglomeration and hence the reduction of their catalytic activity, and (ii) in some cases to enhance their efficiency through a proper interaction with the substrate [2].

The synthesis of Ag NPs (whether supported or unsupported), and of noble metal NPs in general, is frequently carried out by means of wet chemical approaches, mainly because these methods are simple, versatile and scalable [8]. Although originally such methods tended to make extensive use of hazardous reagents and/or solvents, increasing environmental awareness has driven in recent years a move towards the search of more sustainable preparation procedures. In particular, significant progress has been achieved on the green synthesis of unsupported Ag NPs using non- or low-toxic solvents, reductants and capping agents, and to a lesser extent more efficient heating Systems [9-11]. However, similar approaches aiming specifically at the preparation of substrate-supported Ag NPs have been comparatively much less explored. In fact, in the case of carbon substrates only a limited number of reports, published very recently, have addressed the development of environmentally friendly production methods [12-17], and given the utility of these metal-carbon support systems in such relevant fields as, e.g., catalysis [18], further advances along this direction are clearly required.

Here, we report further developments of green methods for the liquid-phase synthesis of carbon-supported Ag NPs. Two different carbon materials relevant as catalyst supports have been chosen as substrates for this study: (i) platelet-type graphite nanofibers (PGNFs), a kind of carbon material with a surface made up exclusively of graphitic edge planes [19] that has been postulated as a suitable support for metal catalysts [18, 20], and (ii) graphene derived from graphite oxide (reduced graphene oxide (RGO)), which is being very actively investigated at present as a support of metal

and other nanostructures towards a number of applications [21-23]. The method proposed here is of photochemical nature, making use of ultraviolet (UV) light to trigger the required reactions at room temperature, and as will be shown below, can be adapted to the specific characteristics of the carbon material and the solvent medium where the synthesis is carried out. In the case of graphene, this method also affords the simultaneous reduction of the precursor graphene oxide (GO) to a limited extent. Furthermore, the prepared PGNF- and RGO-Ag NP hybrids are shown to exhibit a remarkable catalytic activity in the reduction of 4-NP with $NaBH_4$, thus illustrating their application potential.

On the other hand, using glutathione as reducing agent in the absence of the silver salt, GO is reduced to a large extent, similar to that attained heating at 95 ℃ with the most efficient chemical reductants known till present, i. e., vitamin C and the widely used but toxic hydrazine. Such method can therefore be put forward as a convenient and particularly efficient way to reduce GO dispersions at room temperature in a relatively short time.

2. Experimental section

The PGNF- and RGO-Ag NP hybrids were prepared by a photochemical approach in the liquid phase. The PGNFs were acquired from Sigma-Aldrich and used as received. RGO was obtained by photochemically induced reduction of GO sheets. Preparation of the RGO-Ag NP hybrids was carried out in water, starting from stable aqueous dispersions of GO sheets; these dispersions were produced by exfoliation of graphite oxide as described previously [24]. PGNFs are not colloidally stable in water, but have been very recently shown to form stable dispersions in a range of organic solvents including ethanol [19], which, for reasons that will be specified below, was chosen here as the reaction medium to synthesize the PGNF-Ag NP hybrids.

The preparation of the hybrids was based on the irradiation with UV light at room temperature of a water/ethanol solution containing GO/PGNFs, $AgNO_3$ as a metal precursor, glucose/pyridoxamine as an environmentally friendly reducing agent, ammonia, and in some cases polyvinylpyrrolidone (PVP) as a NP capping agent. The effect of different experimental parameters on the resulting hybrids was investigated and will be discussed below. The optimal concentrations for the preparation of the PGNF-Ag NP hybrid in ethanolic solution were 40 μM $AgNO_3$, 48 μM pyridoxamine,

0.002 wt/vol PVP, and 0.136 mg mL^{-1} PGNF. In the case of the RGO-Ag NP hybrid in aqueous solution, 0.5 mM AgNO3, 2 mM glucose, and 0.1 mg mL^{-1} GO. For the reduction of an aqueous dispersion of GO with glutathione in absence of silver salt, 2.5 mM glutathione and 0.1 mg mL^{-1} GO. The pH was adjusted to 10 with ammonia. 10 mL of the resulting solutions were then irradiated with a UV spot lamp (BlueWave 50 unit, from Dymax) for a given time while bubbling them with an argon flow (45 mL min^{-1}). The UV light was emitted from the tip of a lightguide 5 mm in diameter that was positioned ~15 mm above the surface of the solution, delivering an intensity of 1.0-1.2 W cm^{-2} as measured with a hand-held sensor (model UVM-CP, from UV-Consulting Peschl). The lamp emitted in the 280-450 nm wavelength range with a distribution of output intensities of about 15, 40 and 45 % for the 280-320, 320-390 and 390-450 nm wavelength ranges, respectively.

The catalytic activity of the graphene- and nanofiber-supported Ag NPs was evaluated by investigating the reduction reaction of 4-NP to 4-AP with NaBH$_4$ at room temperature. The reduction experiments were typically carried out by first diluting the aqueous/ethanolic suspension of RGO-Ag NP/PGNF-Ag NP hybrid, so as to obtain a concentration of Ag NPs in the resulting solution of ~4-5×10^{10} mL^{-1}. Then, 25 µl of a mixture of 5×10^{-3} M 4-NP and 3 M NaBH$_4$ in water were added to 2.08 mL of the hybrid solution. The subsequent reduction of 4-NP was followed by means of UV-vis absorption spectroscopy. More specifically, since 4-NP in the presence of NaBH$_4$ exhibits a strong absorption peak at ~400 nm that is not present for 4-AP, the evolution (decrease) of absorbance at 400 nm with time can be taken as a measure of the conversion rate of 4-NP to 4-AP.

Characterization of the samples was carried out by UV-vis absorption spectroscopy, field-emission scanning electron microscopy (FE-SEM), energy-dispersive X-ray (EDX) spectroscopy, atomic force microscopy (AFM), transmission electron microscopy (TEM) and X-ray photoelectron spectroscopy (XPS). UV-vis absorption spectra were recorded with a double-beam Heλios α spectrophotometer, from Thermo Spectronic. FE-SEM images and EDX spectra were taken on a Quanta FEG 650 apparatus (FEI Company) on specimens prepared by drop-casting a small volume of the aqueous or ethanolic dispersion of the hybrid onto a pre-heated (~50-60 ℃) highly oriented pyrolytic graphite (HOPG) substrate and allowing it to dry under ambient conditions. A similar procedure was followed for preparing specimens for

AFM, which was carried out under ambient conditions with a Nanoscope IIIa Multimode (Veeco) apparatus in the tapping mode of operation, using silicon cantilevers. TEM imaging was accomplished either with a JEOL 2011 microscope equipped with a LaB6 gun and operating at 200 kV or with a JEOL 2000 EX-II instrument operated at 160 kV. To this end, the suspension of the hybrid in water or ethanol was drop-cast onto a copper grid (200 mesh) covered with either a lacey or a continuous amorphous carbon film and allowed to dry. XPS measurements were carried out on a SPECS system, working at a pressure of 10^{-7} Pa with a monochromatic Al K$_\alpha$ X-ray source (1486.3 eV, 100 W). Specimens for XPS were prepared by casting the aqueous or ethanolic dispersion of the hybrids dropwise onto a metallic sample holder preheated at ~50-60 ºC until a dark film was seen to uniformly cover the sample holder.

3. Results and discussion

To ensure a homogeneous deposition of Ag NPs on the carbon support by a liquid-phase preparation procedure, the carbon material should ideally form a stable colloidal suspension consisting of individual entities (i.e., individual graphite nanofibers or graphene sheets) in the solvent medium. Furthermore, striving for the development of a synthetic approach based on the principles of green chemistry, several issues were taken into account in the implementation of our method, including the preferential use of non-toxic and environmentally benign solvents, reductants and capping agents, as well as the deployment of efficient energy sources to trigger the synthesis reaction (as opposed to the use of, e.g., conventional heating) [9, 11, 25, 26]. Concerning the solvent medium, water is obviously the most environmentally friendly of all solvents, and should thus be the natural choice for the preparation of the hybrids. However, PGNFs are not colloidally stable in water, forming agglomerates than hinder the uniform decoration of the individual nanofibers with Ag NPs. In this case, ethanol was selected as an alternative solvent medium because it displays relatively low toxicity and environmental impact [27] and was very recently shown to afford stable dispersions of individual PGNFs in significant concentrations (Fig. 1a-c) [19]. Moreover, being a versatile, low boiling point solvent, the use of ethanol can facilitate the subsequent processing of the prepared PGNF-Ag NP hybrids. On the other hand, it is known that both GO and RGO can form stable aqueous dispersions consisting of individual, single-layer sheets (Fig, 1d-f) [28]. Therefore, the RGO-Ag NP hybrids were prepared in

water. UV light was chosen as the energy source to promote the desired reaction, i.e. reduction of Ag^+ ions to yield metallic silver, and in the case of GO, also its conversion to RGO. In contrast to conventional or even microwave-assisted heating, with UV light the energy input to the process can in principle be directly targeted to the reacting molecules/species, thus avoiding heating up the bulk of the solution and allowing for the reaction to be carried out at ambient temperature and pressure [25]. This is a particularly attractive feature when using low boiling point solvents and applies in the present case, since neither ethanol not water absorb UV photons from the near and middle ranges, i.e., those covering the wavelength spectrum emitted by the UV lamp used here (280-450 nm).
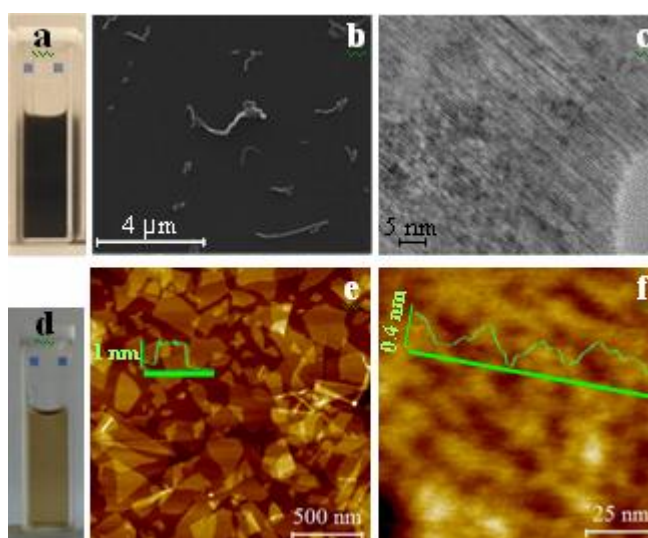

Figure 1. (a) Digital photograph of a PGNF dispersion in ethanol. (b) FE-SEM image of the PGNF dispersion drop-cast onto HOPG. (c) HRTEM image of a PGNF, where its platelet morphology is clearly seen. (d) Digital photograph of an aqueous GO dispersion. (e, f) AFM images of (e) the GO dispersion drop-cast onto HOPG, and (f) an individual sheet on the same atomically flat substrate. In each case a height profile taken along the green line is shown superimposed on the image. (e) The lateral size of the sheets is in the submicron range, while their apparent thickness (measured as their height relative to the substrate) is ~1 nm, which is consistent with the sheets being single-layer objects. (f) Given that the sheets are deposited on an atomically flat substrate, the observed extremely small roughness (< 0.4 nm) must be an intrinsic feature of their structure.

Focusing first on the PGNFs in ethanol, we found that pyridoxamine could trigger the reduction of the Ag+ ions to yield metallic silver in the presence of UV light. Pyridoxamine is one of the naturally occurring forms of vitamin B_6, which plays an essential role in the metabolic function of living organisms [29], and as such it is a completely innocuous, environmentally friendly biomolecule. In the biochemical context, vitamin B_6 has also been reported to possess antioxidant activity [30, 31], and therefore it is plausible that it can act as a reducing agent in a number of other, non-biological chemical reactions. However, to the best of our knowledge, its use and role in the photochemical synthesis of metal NPs has not been documented. FE-SEM revealed that UV irradiation of a PGNF dispersion in ethanol containing 40 μM $AgNO_3$ as a metal precursor and 48 μM pyridoxamine (both soluble in ethanol) for 15 min led to the decoration of the nanofibers with NPs ~30-80 nm in size (Fig. 2a). Control experiments indicated that NPs did not form when the solution was not irradiated with the UV lamp. In the absence of pyridoxamine, however, a very small but finite number of NPs were generated. We note that at sufficiently high temperatures ethanol itself has been shown to act as a reducing agent of Ag^+ ions to afford silver NPs [32]. In the present case, ethanol was not directly heated by the UV lamp, but there was indication that the PGNFs were indeed warmed up, since the temperature of their dispersions in ethanol (without AgNO3, pyridoxamine or any other reagents) rose by several degrees upon UV irradiation (from ~20 to 30 ºC). PGNFs are known to strongly absorb photons from the wavelength range emitted by the UV lamp used here (280-450 nm) [19]. The subsequent relaxation of the photoexcited electrons can lead to a local heating of the nanofibers and, by thermal energy transfer, of the ethanol molecules around them, which in turn could trigger reduction of the Ag^+ ions to some extent. Nevertheless, this process was highly inefficient in producing significant numbers of NPs and most of the PGNFs did not become decorated with any. Only the use of pyridoxamine afforded nanoparticles in considerable quantities.

In an attempt to control the size and increase the density of the generated NPs, the amount of $AgNO_3$ and pyridoxamine in the medium as well as the UV irradiation time were changed. A general trend towards larger NP sizes with increasing amounts of $AgNO_3$ and pyridoxamine as well as irradiation time was observed, whereas NPs did not form when using lower concentrations of reagents. On the other hand, the use of PVP as a capping agent afforded NPs of smaller dimensions, mostly between 10 and 20
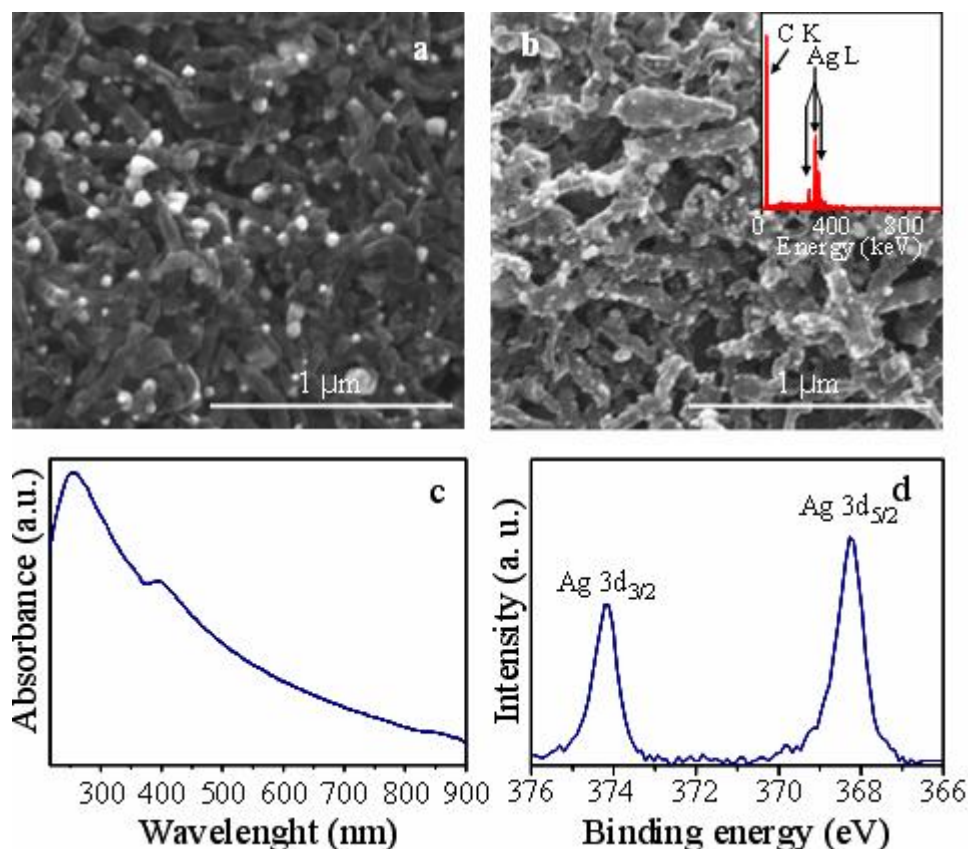
Figure 2. (a,b) FE-SEM images of silver nanoparticles grown onto PGNFs using AgNO3 and pyridoxamine in the absence (a) and presence (b) of PVP and ammonia. EDX spectrum is given as an inset to (b). (c,d) UV-vis absorption spectrum in ethanol and Ag 3d XPS of the sample shown in (b).

nm. Furthermore, it was found that the process could be optimized, particularly in terms of attaining high NP densities, with a combination of PVP and ammonia in the ethanolic solution. Using the amounts of these reagents as specified in the Experimental section led to PGNFs decorated with large numbers of relatively small NPs (Fig. 2b). As could be expected, EDX spectroscopy indicated that carbon and silver were the dominant elements in the PGNF-NP hybrids (Fig. 2b, inset). The metallic character of the Ag NPs was deduced from the observation of a feature at about 410 nm in the UV-vis absorption spectrum of the hybrids (Fig. 2c), which can be attributed to the surface plasmon resonance (SPR) band typical of metallic silver nanostructures [33, 34]. Furthermore, XPS measurements revealed two well-defined and symmetrical peaks centered at 368.2 and 374.2 eV (Fig. 2d), which can be ascribed to photoelectrons ejected from the $3d_{5/2}$ and $3d_{3/2}$ levels, respectively, of Ag(0) [35]. No components associated to oxidized

silver were observed in the XPS spectra, so it can be concluded that the PGNF-Ag NP hybrids only contain metallic silver. TEM imaging disclosed a highly uniform decoration of Ag NPs onto the PGNFs (Fig. 3a). Detailed TEM images (e.g., Fig. 3b) were also employed to estimate NP sizes: a size distribution histogram obtained from the measurement of ~1000 NPs is given as an inset to Fig. 3b, yielding an average size of 16±5 nm.
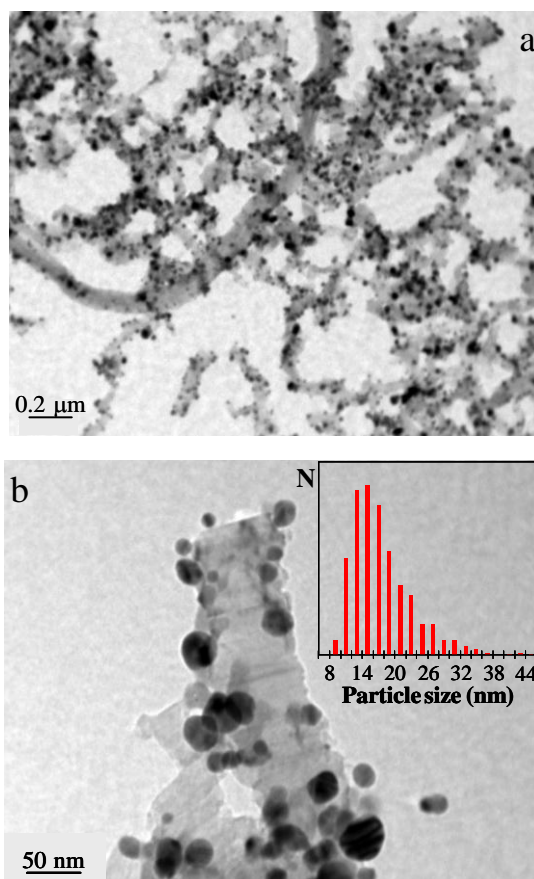
Figure 3. (a, b) TEM images at different magnifications of silver nanoparticles grown onto PGNFs using AgNO3 and pyridoxamine in the presence of PVP and ammonia. A histogram of nanoparticle size distribution is given as an inset to (b).

We stress that the use of pyridoxamine was critical for the successful generation of Ag NPs onto the PGNFs in ethanol. Due to the presence of C=C bonds from its aromatic ring, pyridoxamine strongly absorbs photons from the near and middle ranges of the UV spectrum. Thus, it can be hypothesized that UV-induced photo-excitation of this molecule can trigger the reduction of Ag^+ ions to metallic Ag NPs. However, pyridoxamine was not the only reagent that allowed the generation of Ag NPs by this

method: experiments carried out with pyrogallol, which is a reducing agent with strong absorbance in the near to middle UV range, indicated that NPs could also be produced, albeit of a somewhat larger size. On the other hand, when an UV light-transparent reductant was employed instead (for instance, $NaBH_4$), NPs were hardly generated, similar to what has been described above for the control experiments in the absence of pyridoxamine. The role of ammonia in the reported synthesis also deserves some comment: Ag^+ ions possess a strong affinity towards ammonia molecules, forming the stable ionic complex $(Ag(NH_3)_2)^+$ (Tollens reagent) [9]. In aqueous medium, this complex has been shown to be a convenient precursor of silver nanostructures via reduction with either aldehydes or, more frequently, saccharides [9, 36, 37]. In the present case, it can be argued that the $(Ag(NH_3)_2)^+$ complex is formed following addition of ammonia to the ethanolic solution of $AgNO_3$. Reduction of the complex would be subsequently triggered by photo-excited pyridoxamine, yielding small silver nuclei that would be stabilized by the ammonia ligands. Such stabilization would favor the formation of larger numbers of silver nuclei, which in turn would lead to the generation of a high density of NPs of smaller size (compared to the case where ammonia is not used) upon further growth of the nuclei, as was actually observed. We also note that when the synthesis was carried out in the presence of PGNFs, virtually all the generated Ag NPs were anchored on the nanofiber surface and no stand-alone NPs were noticed. This result can be put down to a strong interaction between metal clusters and the surface oxygen-containing groups present at edges and other defect sites of graphitic structures, including these nanofibers [18, 19, 38, 39]. Thus, an estimate of the Ag NP concentration in the PGNF dispersion can be made based on the number density of NPs per nanofiber unit length, as gauged from the TEM images. For a ~0.14 mg mL^{-1} PGNF suspension in ethanol, with an average nanofiber width of about 100 nm, the number density of Ag NPs on the PGNFs was determined to be ~69 μm^{-1}, yielding a NP concentration of ~5×10^{11} mL^{-1}.

We now turn our attention to the preparation of RGO-Ag NP hybrids. Unlike the case of the PGNFs in ethanol, UV irradiation of an aqueous dispersion of GO sheets in the presence of the appropriate reagents including pyridoxamine failed to yield Ag NPs in any significant amounts. Because GO possesses plenty of oxygen-containing functional groups and other structural defects where metal nuclei can anchor and subsequently grow [40-42], we believe that such result is not due to the use of this

carbon substrate but rather to the solvent medium, which apparently plays a critical role in the performance of pyridoxamine to trigger the reduction of Ag^+ ions. This question will be further discussed below. After testing several alternative biomolecules, glucose was found to be a good substitute for pyridoxamine to grow Ag NPs on the GO sheets in aqueous medium. RGO-Ag NP hybrids prepared at moderate temperatures by simultaneous reduction of GO and silver ions with glucose in presence of PVP to guarantee the colloidal stability of GO have been very recently reported [43]. However, in our case, the optimized procedure did not require the addition of PVP either to guarantee GO colloidal stability (as in the RGO-Ag NP hybrids previously reported in the literature [43]) or to control the NP size (as in the PGNF-Ag NP hybrids described above).
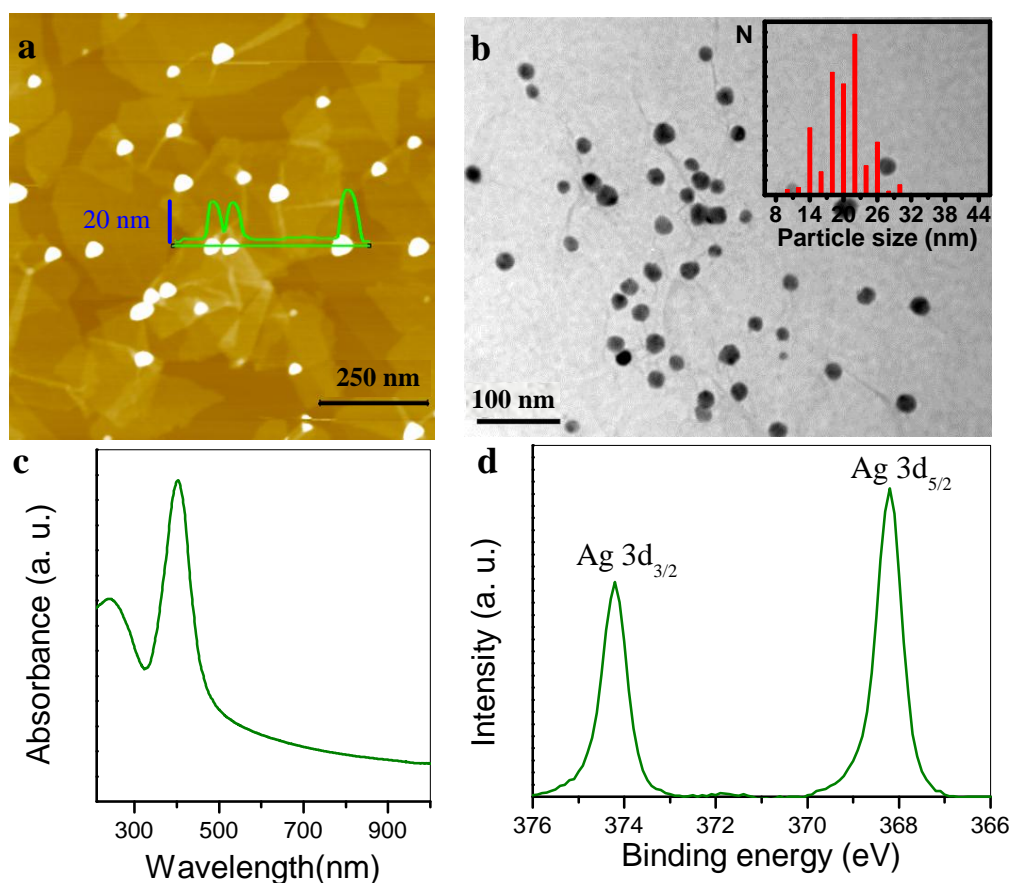

Figure 4. (a) AFM and (b) TEM images of GO-Ag NP hybrids. A histogram of nanoparticle size distribution is given as an inset to (b). (c) UV-vis absorption and (d) Ag 3d XPS spectrum of the sample shown in (a,b).

Only AgNO₃, glucose and ammonia in the amounts described in the Experimental section were added to the aqueous GO dispersion, which was then irradiated for 15 min. The results of a general characterization of these optimized hybrids are presented in Fig. 4. AFM imaging (Fig. 4a) revealed that the individual, single-layer GO sheets, identified as two-dimensional, ~1 nm thick objects in the images (see line profile in Fig. 4a), became uniformly decorated with a large number of bright dots. Such dots were about 20 nm high and were not present on the starting GO sheets (Fig. 1b), indicating that they correspond to the generated Ag NPs. From the AFM images, the density of Ag NPs grown on the GO sheets was estimated to be ~32 μm^{-2}. Using this value, and for a starting GO dispersion with a concentration of 0.1 mg mL^{-1}, we estimate the Ag NP concentration in the aqueous dispersion of the hybrid to be $\sim 3 \times 10^{12}$ mL^{-1}, which is significantly higher than that obtained for their PGNF-based counterpart. In addition to solvent (water vs. ethanol) and reagent (glucose vs. pyridoxamine) effects, this result could be due to the fact that GO possesses a much higher specific surface area than that of PGNFs, and consequently much more abundant surface sites for the anchoring of NPs per unit mass of the carbon support.

The morphology and size of the NPs in the GO-based hybrids was investigated in more detail by TEM (Fig. 4b). Either polygonal or approximately rounded NPs were seen to decorate the GO sheets. Their size distribution (inset to Fig. 4b) ranges from 14 to 26 nm, yielding average size of 19±4 nm. This NP size distribution is narrower and more symmetrical than that found for PGNF-Ag NPs (inset to Fig. 3b). Such difference in the NP size range could have its origin in the different degree of homogeneity in the nanometer scale features of the two carbon supports. The surface of PGNF is relatively heterogeneous in the nanometer scale (see Fig. 1c and Fig. 3b), showing protrusions sized a few nanometers, which produces an heterogeneous environment for the growth of Ag NPs. On the other hand, graphene oxide has uniform, very small roughness on such scale (Fig. 1f), providing a more homogeneous environment for the growth of the Ag NPs.

Fig. 4c and d shows UV-vis absorption and high resolution Ag 3d X-ray photoelectron spectra, respectively, of the GO-based hybrid. Again, the observation of a band centered at 402 nm in the UV-vis spectrum (SPR band) and of two peaks at 368.3 and 373.2 eV in the XPS spectrum provides clear indication of the metallic character of the Ag NPs grown on the GO sheets. We also note that the SPR band of the GO-based

hybrid (Fig. 4c) is much more intense than that of its PGNF counterpart (Fig. 2c) if these bands are compared with the corresponding peak located in the 255-270 nm region. The latter is generally ascribed to $\pi \rightarrow \pi^*$ transitions in C=C structures of graphitic carbon materials [19, 28], and therefore in the present case can be associated to the PGNF and GO/RGO components of the hybrids. Such result is thus consistent with the larger amount of Ag NPs that are generated per unit mass of carbon support when using GO compared with the PGNFs, as discussed above.

In addition to affording significant quantities of Ag NPs on the GO sheets, the method proposed here employing UV light and glucose was found to reduce GO itself. In fact, glucose has been previously reported to reduce GO although through heat treatment at 95 ºC [44]. Indeed, from Fig. 4c, there is a certain red-shift of the band associated to GO ($\pi \rightarrow \pi^*$ transition band) in the UV-vis absorption spectrum of the hybrid material from its initial value of 231 nm. It is well known that reduction of GO induces a red-shift of this band from a value of ~231 nm for the unreduced material up to 268-270 nm for highly reduced samples, and the magnitude of the red-shift is a good indicator of the extent of reduction achieved [28, 45]. To investigate in more detail the efficiency of the present approach towards reducing GO, aqueous solutions containing GO sheets (0.1 mg mL^{-1}), glucose (2 mM), and ammonia (to adjust the pH to a value of 10) were irradiated with the UV lamp following the same procedure employed for the preparation of the hybrids (with the exception that AgNO$_3$ was not included in the solution). The position of the absorption band associated to GO was then monitored as a function of irradiation time and the result is plotted in Fig. 5a (green squares). It can be noticed that the band position becomes increasingly red-shifted with irradiation time, which implies progressive reduction of the GO sheets, until a plateau value (262 nm) is reached after 60 min. This value is only slightly higher than the one obtained by just irradiating GO, in the absence of glucose [46] and still far from that attained by means of chemical reduction at 95 ºC using such powerful reducing agents as hydrazine or vitamin C (268-270 nm) [28, 45], which means that GO can be reduced only to a limited extent by UV irradiation in presence of glucose. In principle, this may come from an intrinsic limitation of the photochemical method itself or of the particular reductant used. To investigate this issue, glutathione, another previously reported bioreductant [47] which does not absorb UV light (see below for the relevance of this point) was assayed. The position of the UV absorption band associated to GO vs.

irradiation time for such experiment is gathered in Fig. 5a, blue squares. UV irradiation of a dispersion of GO in the presence of glutathione (2.5 mM, 5 hours) led to a red-shift similar to that obtained for hydrazine and vitamin C heating at 95 ºC (to 268-270 nm).
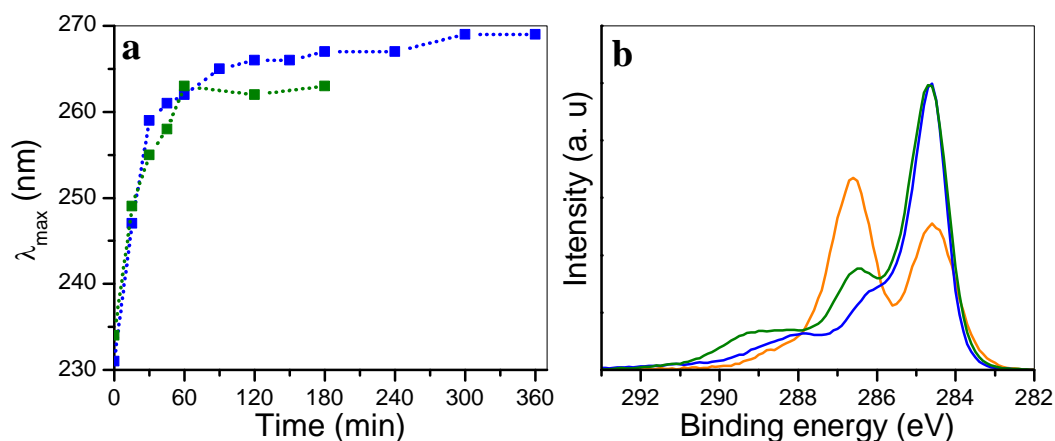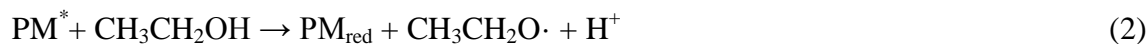

Figure 5. (a) Wavelength of the absorption maxima for the π→π* transition of unsaturated carbon bonds of graphene oxide irradiated with UV light for different periods of time in the presence of glucose (green squares), and of glutathione (blue squares). (b) C1s core level XPS spectra of the starting graphene oxide (orange plot), and that irradiated with UV light treated in the presence of glucose (green plot), and of glutathione (blue plot).

The photochemical reduction method is thus highly efficient, provided that the proper choice of bioreductant is made. Further confirmation of the successful reduction of GO by glutathione was obtained by means of XPS. Analysis of survey spectra (not shown) indicated that deoxygenation had taken place, as the O/C atomic ratio decreased from 0.43 for the starting GO to 0.11 for the sample irradiated with UV light in presence of glutathione. The corresponding high resolution C 1s core level spectra (Fig. 5b) also provided evidence of the actual reduction of GO: unreduced GO exhibits a strong component at ~286.5 eV in its C 1s spectrum (orange plot), implying that a large fraction of its carbon atoms are in an oxidized state (more specifically, carbon atoms singly bonded to oxygen as in, e.g., hydroxyl and epoxy groups) [45]; by contrast, treatment with UV light and glutathione (blue plot) led to a marked decrease of this component and the C 1s spectrum became dominated by a peak at 284.6 eV, which is characteristic of carbon atoms in a graphitic, unoxidized environment (C=C species) [45]. Reduction with glucose (Fig. 5b, green plot), being less effective, yields a similar

C1s spectrum, but with a higher relative abundance of oxygen-containing groups. When glutathione was previously reported as a reducing agent of GO [47], reduction was accomplished by heating the aqueous GO dispersion at 50 ºC for several hours. Likewise, UV light alone has been very recently shown to induce deoxygenation of GO in aqueous medium [46]. However, in these two treatments reduction is less efficient than that attained with their combination, in terms of the extent of reduction achieved (as determined by the red-shift of the GO UV absorption band) and/or the time required to its completion. For instance, the absorption band red-shifted just to 264 nm both using only UV light (5. 5. h) and, in a control experiment with optimized gluthatione concentration and treatment time (1 mM, 3 h), heating at 95 ºC, whereas the combination of UV light and glutathione used here further red-shifted the absorption band to 268-270 nm in 5 h. Such result underlines the advantage of using this combined approach as a highly efficient method to reduce GO at room temperature.

We now discuss the possible mechanisms that allow the reduction of Ag^+ ions to metallic Ag NPs using UV light and pyridoxamine in ethanol but not in water, and why glucose can be a good substitute for pyridoxamine in the latter medium. As already mentioned, the use of pyridoxamine was critical for the successful generation of Ag NPs onto the PGNFs in ethanolic dispersion. Pyridoxamine strongly absorbs photons from the wavelength range emitted by the UV lamp used here (280-450 nm). This process should lead to a phoexcited molecule (PM*), which should thus become much more chemically reactive than its ground state counterpart. A variety of processes can take place afterwards, some of which are complex and not fully understood. However, we hypothesize that at least one of the processes that takes place involves the charge-transfer between pyridoxamine and the solvent molecules. Solvent-specific charge-transfer between a photoexcited aromatic molecule and solvent molecule has been previously reported in the literature [48]. If such a type of interaction occurs, the subsequent fate of the photoexcited molecule, and hence its ability to reduce Ag^+ ions or not, would be dictated by reactions involving the solvent molecules. The fact that Ag NPs could be produced in ethanol but not in aqueous medium is consistent with this idea. Moreover, ethanol is known to be an efficient hole scavenger [49], so its reaction with photoexcited pyridoxamine would be expected to yield a reduced pyridoxamine molecule and an ethoxy radical. The latter could also react with photoexcited pyridoxamine to give acetaldehyde and reduced pyridoxamine (PM_{red}). Finally, the

reduced form of pyridoxamine would readily convert Ag^+ ions to metallic Ag NPs. The set of reactions that lead to the generation of Ag NPs using pyridoxamine (PM) and UV light in ethanol would be summarized as follows:

$$PM \rightarrow PM^* \tag{1}$$
$$PM^* + CH_3CH_2OH \rightarrow PM_{red} + CH_3CH_2O\cdot + H^+ \tag{2}$$
$$PM^* + CH_3CH_2O\cdot \rightarrow PM_{red} + CH_3CHO + H^+ \tag{3}$$
$$PM_{red} + Ag^+ \rightarrow PM_{ox} + Ag^0 \tag{4}$$

On the other hand, hole scavenging of photoexcited pyridoxamine by water molecules can be expected to generate hydroxyl radicals,

$$PM^* + H_2O \rightarrow PM_{red} + OH\cdot + H^+ \tag{5}$$

which possess a strongly oxidizing capability and are well-known to easily degrade many organic compounds, giving carbon dioxide and water molecules as end products [50]. Consequently, we surmise that in aqueous medium both pyridoxamine and its reduced counterpart will be readily decomposed in the presence of UV light and thus will not be able to reduce Ag^+ ions to metallic Ag NPs. Evidence in support of this hypothesis was provided by control experiments in which UV-vis absorption spectra of pyridoxamine solutions in either water or ethanol were recorded before and after irradiation with the UV lamp (Fig. 6). In aqueous medium, fresh pyridoxamine solutions exhibit three absorption bands at 220, 254 and 328 nm (Fig. 6a, blue plot), which can be ascribed to electronic transitions involving the aromatic ring of the molecule modulated by its pendant auxochromic groups [51]. Following UV irradiation of the solution for 15 min, the three characteristic bands of pyridoxamine disappeared and only a weak and featureless background absorbance was observed instead (Fig. 6a, black plot). This result implies that aromatic molecules are not present in the irradiated solution and is therefore strong indication that pyridoxamine has been decomposed. On the other hand, the distinctive bands of pyridoxamine solutions in ethanol, located at 204, 291 and 335 nm (Fig. 6b, red plot), were preserved to a certain extent after UV irradiation for 15 min (Fig. 6b, black plot). Hence, we conclude that pyridoxamine endures the irradiation process in ethanol at least for a period of 15 min without total degradation and is thus able to participate in the reactions that yield Ag NPs (equations (1)-(4)), whereas

decomposition of the molecule in aqueous medium and the presence of highly oxidizing hydroxyl radicals prevents the reduction of Ag^+ ions and the generation of Ag NPs.
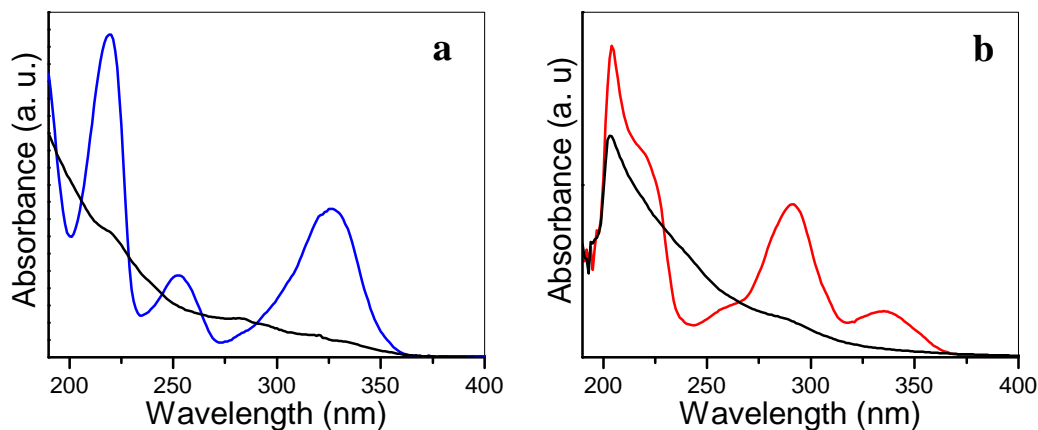

Figure 6. UV-vis absorption of aqueous (a) and ethanolic (b) pyridoxamine solutions before (colored line) and after (black line) UV irradiation for 15 min.

In principle, the use of other molecules that can be photoexcited with UV light should also afford the growth of Ag NPs in ethanol through similar processes to those described by equations (1)-(4). The successful substitution of pyrogallol for pyridoxamime, as described above, constitutes an example of this possibility. In the same line of reasoning, UV light-absorbing molecules should be generally inappropriate for the synthesis of Ag NPs in aqueous medium. In this case, glucose was found to be a good substitute for pyridoxamine to induce the growth of Ag NPs on GO and also to afford a certain degree of reduction of GO itself. Because glucose is transparent to UV light, the mechanisms that allow these processes to take place must be completely different to those occurring with pyridoxamine in ethanol. We believe that the GO sheets play a central role in these processes. Evidence in this regard was obtained from the observation that Ag NPs did not form when GO was excluded from the synthesis solution. By contrast, according to equations (1)-(4), the growth of Ag NPs in ethanol using pyridoxamine should not require the presence of a carbon substrate, and indeed we were able to produce Ag NPs in this medium in the absence of the PGNFs. As is well known, GO also exhibits strong absorbance in the 280-450 nm wavelength [46]. However, unlike the case of pyridoxamine, reaction with water molecules and the subsequent generation of highly reactive hydroxyl radicals are not thought to be dominant processes involving photoexcited GO. If this was the case, we would expect

further oxidation and possibly disintegration of the GO sheets by the hydroxyl radicals [52], but rather the opposite trend (i.e., deoxygenation) has been observed in UV-irradiated GO [46]. Instead, it is very likely that photoexcited GO undergoes relaxation by transferring energy to its lattice in the form of atomic vibrations, implying that the sheets will be locally heated [46]. The single-layer nature of the GO sheets, which means that all of their atoms are surface atoms, would then facilitate the transfer of a significant fraction of the generated thermal energy to the aqueous medium immediately surrounding the sheets. Thus, in the presence of a suitable reducing agent such as glucose, reduction of GO and of Ag^+ ions should become kinetically favored by the locally high temperatures, leading to the decoration of the sheets with metallic Ag NPs.
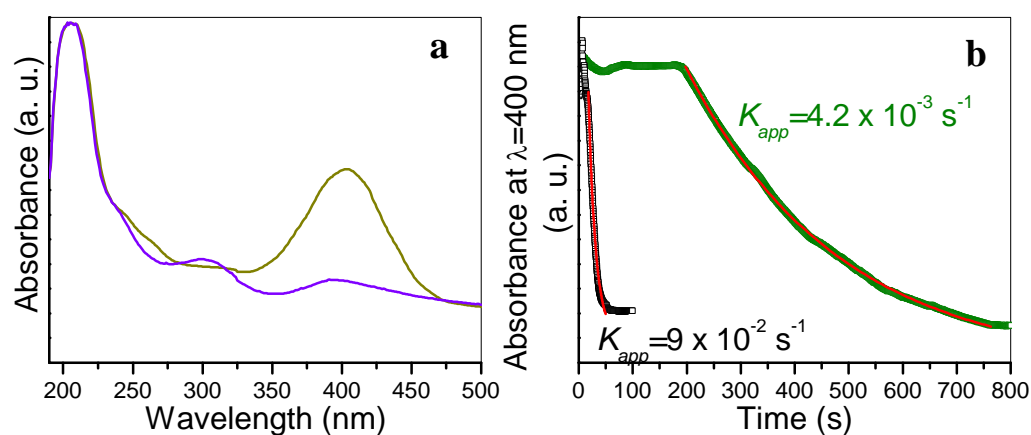

Figure 7. (a) UV-vis absorption spectra for the reduction of 4-NP to 4-AP with $NaBH_4$ at room temperature in the presence of PGNF-supported silver nanoparticles just before (dark yellow plot) and after (violet plot) reduction. (b) Plot of the time evolution of the intensity of the peak at 400 nm of 4-nitrophenolate ion in presence of the PGNF-Ag NP (green squares) or RGO-Ag NP (black squares) hybrids. The experimental kinetic profiles could be well fitted to exponential decay functions, which are shown as overlaid orange and red lines, respectively. Experimental conditions: (4-NP) = 0.06 mM; $(NaBH_4)$ = 35.6 mM; (Ag NP) ~1-1.5 µg mL^{-1}.

Finally, to demonstrate the suitability of these PGNF- and RGO-supported Ag NPs as effective catalysts, we investigated their performance in the reduction of 4-NP to 4-AP with $NaBH_4$ in aqueous medium as a model reaction. Although such a reaction is known to be thermodynamically favorable, it possesses a high kinetic barrier and thus

typically requires the use of a noble metal catalyst to proceed at a significant rate at room temperature [6, 53, 54]. The reaction progress can be readily followed with UV-vis absorption spectroscopy. In basic medium (generated upon addition of $NaBH_4$), 4-NP is in deprotonated form (4-nitrophenolate ion), which exhibits a strong absorption peak at ~400 nm (Fig. 7a, dark yellow plot) that is not present in the case of 4-AP, the latter displaying a relatively weak band at about 295 nm (Fig. 7a, violet plot) [6]. Therefore, monitoring the drop in intensity of the absorption peak at 400 nm as a function of reaction time provides a measure of the rate of conversion of 4-NP to 4-AP achieved with the catalyst, as exemplified in Fig. 7b for the PGNF-Ag NP (green squares) and RGO-Ag NP (black squares) hybrids. In the experiments, the concentration of $NaBH_4$ used was much higher than that of 4-NP (35.6 vs. 0.06 mM) to ensure that such parameter was essentially kept constant throughout the reaction. In addition, the evolution of the absorbance at 400 nm with time during the reaction could be well fit to an exponential decay (Fig. 7b, solid lines), with residuals in the ± 0.03 over the analyzed profiles. Therefore, the reduction reaction can be regarded to obey a pseudo-first-order kinetic behavior with respect to 4-NP, so that

$$\frac{d(4\text{-NP})}{dt} = -k_{app}(4\text{-NP}) \qquad (6)$$

where (4-NP) is the concentration of 4-NP and k_{app} is the observed rate constant. Using the PGNF- and RGO-supported Ag NPs as a catalyst, the rate constant was measured to be $k_{app} = (4.2 \pm 0.9) \times 10^{-3}$ s^{-1} and $(9 \pm 2) \times 10^{-2}$ s^{-1}, respectively. We stress that no conversion of 4-NP to 4-AP was observed to occur either in the absence of the hybrids or when only the nanofibers or the graphene sheets (without NPs) were present in the reaction solution, confirming the catalytic role played by the NPs. We also note that essentially full conversion of 4-NP to 4-AP was achieved in the experiments, because the band at 400 nm virtually came to disappear. The very same weak absorption band noticed after reaction completion at about 396 nm (Fig. 7a, violet plot) was already observed in the reaction solution in the absence of any added 4-NP, and can be ascribed to the SPR band of the Ag NPs. This band is known to blue-shift (in the present case, from 410 to 396 nm) as a result of the injection of electrons from the nucleophilic BH4$^-$ anion onto

the Ag NP surface [6]. Likewise, the background absorbance observed both before and after reaction completion in Fig. 7a can be attributed to the carbon material.

Table 4. Comparison of areal rate constants obtained for the reduction of p-nitrophenol with NaBH4 using a number of Ag NP-based catalysts.

Catalytic system	Areal rate (L m^{-2} s^{-1})	Rate normalized to Ag NP concentration (L g^{-1} s^{-1})	Reference
PGNF-supported Ag NP hybrids	0.1	3.8	Present work
RGO-supported Ag NPs hybrids	2	50	Present work
Ag NP-linear polyethylene imine colloidal systems	1.7		54
Colloidal, dextran T500-stabilized Ag NPs	1.4		55
Ag NP-polyethyleneimine derivative composite	0.57		56
Ag NPs embebbed in polymeric microgel	0.12-0.20		57
Colloidal, aminosilicate-stabilized Ag NPs	0.08-0.20		58
Chitosan-Ag NP composite	0.15		59
Ag NPs on polymer-derived carbon nanofibers	0.15	3.3	60
Ag NPs in polyelectrolyte brush particles	0.08		61
Ag NPs in core-shell polymeric microgel	0.05		62
Ag NPs stabilized by cationic polynorbornenes		1.4	63
Spherical (and dendritic) Ag NPs	0.02 (*)	1.4-4.0	64
Ag nanodendrites	0.02	0.01	65
Ag NPs embedded in porous carbon spheres		0.01	66

(*) The areal rates could only be estimated for the spherical Ag NPs with the available data.

To compare the catalytic performance of the carbon-supported Ag NPs with that of other catalysts reported in the literature, the observed rate constant was normalized to either the surface area or the mass of silver employed per unit volume, yielding estimated values of 0.1 L s^{-1} m^{-2} and 3.8 L s^{-1} g^{-1} for the PGNF-Ag NP system and 2 L s^{-1} m^{-2} and L 50 s^{-1} g^{-1} for the RGO-Ag NP system, respectively. Table 1 gathers normalized rate constants obtained in recent years with efficient catalysts based on Ag

NPs [55-67]. As can be seen, the materials prepared here exhibit an outstanding catalytic activity, even better than the most remarkable values reported until present. This feature combined with their long-term colloidal stability (several months at least) make them stand out as excellent catalysts for this reaction.

4. Conclusions

A green photochemical approach based on the use of intense UV light and appropriate environmentally friendly biomolecules has been shown to be efficient towards the room-temperature, liquid-phase synthesis of silver nanoparticles supported onto two different carbon nanomaterials, namely, platelet-type graphite nanofibers and graphene oxide. The resulting nanostructured hybrids exhibited long-term colloidal stability in water or ethanol, which can be advantageous with a view to their further manipulation and use in practical applications. Thus, it was demonstrated that the hybrids possess a high catalytic activity in the reduction of 4-nitrophenol to 4-aminophenol with $NaBH_4$. In particular, the catalytic activity of the graphene oxide-based hybrids was found to be one of the highest that have ever been reported with silver nanoparticle based catalysts for such a reaction. Finally, a synergistic effect was found between UV light and glutathione (a well-known natural antioxidant) towards the reduction of graphene oxide sheets, affording a degree of deoxygenation in a room-temperature process that is only matched by the use of the most efficient chemical reductants of graphene oxide (e.g., hydrazine) at higher (80-100 ºC) temperatures.

References

[1] Jain PK, Huang X, El-Sayed IH, El-Sayed MA. Noble metals on the nanoscale: optical and photothermal properties and some applications in imaging, sensing, biology, and medicine. Accounts Chem. Res. 41 (2008), 1578-1586.

[2] Campelo JM, Luna D, Luque R, Marinas JM, Romero AA. Sustainable preparation of supported metal nanoparticles and their applications in catalysis. ChemSusChem 2 (2009), 18-45.

[3] Sau TK, Rogach AL. Nonspherical noble metal nanoparticles: colloid-chemical

synthesis and morphology control. Adv. Mater. 22 (2010), 1781-1804.

[4] Sau TK, Rogach AL, Jäckel F, Klar TA, Feldmann J. Properties and applications of colloidal nonspherical noble metal nanoparticles. Adv. Mater. 22 (2010), 1805-1825.

[5] Jiang Z-J, Liu C-Y, Sun L-W. Catalytic Properties of silver nanoparticles supported on silica spheres. J. Phys. Chem. B 109 (2005), 1730-1735.

[6] Pradhan N, Pal A, Pal T. Silver nanoparticle catalyzed reduction of aromatic nitro compounds. Colloid. Surface. A 19 (2002), 247-257.

[7] Saha S, Pal A, Kundu S, Basu S, Pal T. Photochemical green synthesis of calcium-alginate-stabilized Ag and Au nanoparticles and their catalytic application to 4-nitrophenol reduction. Langmuir 26 (2009), 2885-2893.

[8] Burda C, Chen X, Narayanan R, El-Sayed MA. Chemistry and properties of nanocrystals of different shapes. Chem. Rev. 105 (2005), 1025-1102.

[9] Sharma VK, Yngard RA, Lin Y. Silver nanoparticles: Green synthesis and their antimicrobial activities. Colloid Interface Sci. 145 (2009), 83-96.

[10] Iravani S. Green synthesis of metal nanoparticles using plants. Green Chem. 13 (2011), 2638-2650.

[11] Nadagouda MN, Speth TF, Varma RS. Microwave-assisted green synthesis of silver nanostructures. Acc. Chem. Res. 44 (2011), 469-478.

[12] Kurva S, Kathi J, Rhee K-Y, Park S. A complete green protocol: wrapping of multiwall carbon nanotubes with silver nanoparticles. J. Nanosci. Nanotech. 11 (2011), 4463-4465.

[13] Fan J, Shi Z, Ge Y, Wang J, Wang Y, Yin J. Gum arabic assisted exfoliation and fabrication of Ag-graphene-based hybrids. J. Mater. Chem. 22 (2012), 13764-13772.

[14] Chen L, Xie H, Yu W. Multi-walled carbon nanotube/silver nanoparticles used for thermal transportation. J Mater Sci 47 (2012), 5590-5595.

[15] Zhang Y, Liu S, Wang L, Qin X, Tian J, Lu W, et al. One-pot green synthesis of Ag nanoparticles-graphene nanocomposites and their applications in SERS, H_2O_2, and glucose sensing. RSC Advances 2 (2012), 538-545.

[16] Wang X, Huang P, Feng L, He M, Guo S, Shen G, et al. Green controllable synthesis of silver nanomaterials on graphene oxide sheets via spontaneous reduction. RSC Advances 2 (2012), 3816-3822.

[17] Yuan W, Gu Y, Li L. Green synthesis of graphene/Ag nanocomposites. Appl. Surf. Sci. 261 (2012), 753-758.

[18] Serp P, Figueiredo JL. Carbon materials for catalysis. Hoboken: John Wiley & Sons. 2009.

[19] Guardia L, Paredes JI, Villar-Rodil S, Rouszaud J-N, Martínez-Alonso A, Tascón JMD. Discovery of effective solvents for platelet-type graphite nanofibers. Carbon 53 (2013), 222-230.

[20] Hsieh C-K, Tsai M-C, Yen M-Y, Su C-Y, Chen K-F, Ma C-CM, Chen F-R, Tsai C-H. Direct synthesis of platelet graphitic-nanofibres as a highly porous counter-electrode in dye-sensitized solar cells. Phys. Chem. Chem. Phys. 14 (2012), 4058-4061.

[21] Huang X, Qi X, Boey F, Zhang H. Graphene-based composites. Chem. Soc. Rev. 41 (2012), 666-686.

[22] Bai S, Shen X. Graphene-inorganic nanocomposites. RSC Advances 2 (2012), 64-98.

[23] Machado BF, Serp P. Graphene-based materials for catalysis. Catal. Sci. Tech. 2

(2012), 54-75.

[24] Paredes JI, Villar-Rodil S, Solís-Fernández P, Martínez-Alonso A, Tascón JMD. Atomic force and scanning tunneling microscopy imaging of graphene nanosheets derived from graphite oxide. Langmuir 25 (2009), 5957-5968.

[25] Lancaster M. Green chemistry: An introductory text. Cambridge: Royal Society of Chemistry. 2002.

[26] Hu B, Wang S-B, Wang K, Zhang M, Yu S-H. Microwave-assisted rapid facile "green" synthesis of uniform silver nanoparticles: self-assembly into multilayered films and their optical properties. J. Phys. Chem. C 112 (2008), 11169-11174.

[27] Capello C, Fischer U, Hungerbuhler K. What is a green solvent? A comprehensive framework for the environmental assessment of solvents. Green Chem. 9 (2007), 927-934.

[28] Li D, Mueller M, Gilje S, Kaner R, Wallace G, Müller M. Processable aqueous dispersions of graphene nanosheets. Nat. Nanotechnol. 3 (2008), 101-105.

[29] Zempleni J, Rucker RB, McCormick DB, Suttie JW. Handbook of vitamins. Boca Raton: CRC Press. 2007.

[30] Stocker P, Lesgards J-F, Vidal N, Chalier F, Prost M. ESR study of a biological assay on whole blood: antioxidant efficiency of various vitamins. Biochim. Biophys. Acta 1621 (2003), 1-8.

[31] Endo N, Nishiyama K, Otsuka A, Kanouchi H, Taga M, Oka T. Antioxidant activity of vitamin B6 delays homocysteine-induced atherosclerosis in rats. Brit. J. Nutr. 95 (2006), 1088-1093.

[32] Pal A, Shah S, Devi S. Microwave-assisted synthesis of silver nanoparticles using ethanol as a reducing agent. Mater. Chem. Phys. 114 (2009), 530-532.

[33] Sun Y, Xia Y. Gold and silver nanoparticles: A class of chromophores with colors tunable in the range from 400 to 750 nm. Analyst 128 (2003), 686-691.

[34] Evanoff DD, Chumanov G. Synthesis and optical properties of silver nanoparticles and arrays. ChemPhysChem 6 (2005), 1221-1231.

[35] Crist BV. Handbook of Monochromatic XPS Spectra. Vol. 1. The elements & Native Oxides. California, USA: XPS International LLC. 2004.

[36] Kvitek L, Prucek R, Panacek A, Novotny R, Hrbac J, Zboril R. The influence of complexing agent concentration on particle size in the process of SERS active silver colloid synthesis. J. Mater. Chem. 15 (2005), 1099-1105.

[37] Dondi R, Su W, Griffith GA, Clark G, Burley GA. Highly size- and shape-controlled synthesis of silver nanoparticles via a templated tollens reaction. Small 8 (2012), 770-776.

[38] Lopez-Salido I, Lim DC, Kim YD. Ag nanoparticles on highly ordered pyrolytic graphite (HOPG) surfaces studied using STM and XPS. Surf. Sci. 588 (2005), 6-18.

[39] Felten A, Bittencourt C, Colomer JF, Van Tendeloo G, Pireaux JJ. Nucleation of metal clusters on plasma treated multi wall carbon nanotubes. Carbon 45 (2007), 110-116.

[40] Fampiou I, Ramasubramaniam A. Binding of Pt nanoclusters to point defects in graphene: adsorption, morphology, and electronic structure. J. Phys. Chem. C 116 (2012), 6543-6555.

[41] Groves MN, Malardier-Jugroot C, Jugroot M. Improving platinum catalyst durability with a doped graphene support. J. Phys. Chem. C 116 (2012), 10548-10556.

[42] Yang M, Zhou M, Zhang A, Zhang C. Graphene oxide: an ideal support for gold

nanocatalysts. J. Phys. Chem. C 116 (2012), 22336-22340.

[43] Tang X-Z, Li X, Cao Z, Yang J, Wang H, Pu X, Yu Z-Z. Synthesis of graphene decorated with silver nanoparticles by simultaneous reduction of graphene oxide and silver ions with glucose. Carbon 59 (2013), 93-99.

[44] Zhu C, Guo S, Fang Y, Dong S. Reducing sugar: new functional molecules for the green synthesis of graphene nanosheets. ACS Nano 4 (2010), 2429-2437.

[45] Fernández-Merino MJ, Guardia L, Paredes JI, Villar-Rodil S, Solís-Fernández P, Martínez-Alonso A, Tascón JMD. Vitamin C is an ideal substitute for hydrazine in the reduction of graphene oxide suspensions. J. Phys. Chem. C 114 (2010), 6426-6432.

[46] Guardia L, Villar-Rodil S, Paredes JI, Rozada R, Martínez-Alonso A, Tascón JMD. UV light exposure of aqueous graphene oxide suspensions to promote their direct reduction, formation of graphene–metal nanoparticle hybrids and dye degradation. Carbon 50 (2012), 1014-1024.

[47] Pham TA, Kim JS, Kim JS, Jeong YT. One-step reduction of graphene oxide with l-glutathione. Colloid. Surf. A. 384 (2011), 543-548.

[48] Choi J, Choi W, Mhin BJ. Solvent-specific photolytic behavior of octachlorodibenzo-p-dioxin. Environ. Sci. Technol. 38 (2004), 2082-2088.

[49] Hegyi J, Horváth O. Photocatalytic reduction of mercury(II) and simultaneous oxidative degradation of surfactants in titanium dioxide suspensions. In: Zrínyi M, Hórvölgyi ZD, eds. From Colloids to Nanotechnology: Springer Berlin Heidelberg 2004 p. 10-16.

[50] Ray MB, Chen JP, Wang LK, Pehkonen SO. Advanced physicochemical treatment processes: Handbook of Environmental Engineering: Springer. 2006.

[51] Matsushima Y, Martell AE. Pyridoxal Analogs. IX. Electron absorption spectra and molecular species in methanol solution. J. Am. Chem. Soc. 89 (1967), 1322-1330.

[52] Solís-Fernández P, Paredes JI, Villar-Rodil S, Guardia L, Fernández-Merino MJ, Dobrik G, Biró LP, Martínez-Alonso A, Tascón JMD. Global and local oxidation behavior of reduced graphene oxide. J. Phys. Chem. C 115 (2011), 7956-7966.

[53] Ge J, Zhang Q, Zhang T, Yin Y. Core–satellite nanocomposite catalysts protected by a porous silica shell: controllable reactivity, high stability, and magnetic recyclability. Angew. Chem. Int. Edit. 47 (2008), 8924-8928.

[54] Jin Z, Xiao M, Bao Z, Wang P, Wang J. A general approach to mesoporous metal oxide microspheres loaded with noble metal nanoparticles. Angew. Chem. Int. Edit. 51 (2012), 6406-6410.

[55] Santos KdO, Elias WC, Signori AM, Giacomelli FC, Yang H, Domingos JB. Synthesis and catalytic properties of silver nanoparticle–linear polyethylene imine colloidal systems. J. Phys. Chem. C 116 (2012), 4594-4604.

[56] Eising R, Signori AM, Fort Sb, Domingos JB. Development of catalytically active silver colloid nanoparticles stabilized by dextran. Langmuir 27 (2011), 11860-11866.

[57] Signori AM, Santos KdO, Eising R, Albuquerque BL, Giacomelli FC, Domingos JB. Formation of catalytic silver nanoparticles supported on branched polyethyleneimine derivatives. Langmuir 26 (2010), 17772-17779.

[58] Zhang J-T, Wei G, Keller TF, Gallagher H, Stötzel C, Müller FA, Gottschaldt M, Schubert US, Jandt KD. Responsive hybrid polymeric/metallic nanoparticles for catalytic spplications. Macromol. Mater. Eng. 295 (2010), 1049-1057.

[59] Harish S, Sabarinathan R, Joseph J, Phani KLN. Role of pH in the synthesis of 3-

aminopropyl trimethoxysilane stabilized colloidal gold/silver and their alloy sols and their application to catalysis. Mater. Chem. Phys. 127 (2011), 203-207.

[60] Murugadoss A, Chattopadhyay A. A 'green' chitosan-silver nanoparticle composite as a heterogeneous as well as micro-heterogeneous catalyst. Nanotechnology 19 (2008), 015603.

[61] Zhang P, Shao C, Zhang Z, Zhang M, Mu J, Guo Z, Liu Y. In situ assembly of well-dispersed Ag nanoparticles (AgNPs) on electrospun carbon nanofibers (CNFs) for catalytic reduction of 4-nitrophenol. Nanoscale 3 (2011), 3357-3363.

[62] Lu Y, Mei Y, Schrinner M, Ballauff M, Möller MW, Breu J. In situ formation of Ag nanoparticles in spherical polyacrylic acid brushes by UV irradiation. J. Phys. Chem. C 111 (2007), 7676-7681.

[63] Lu Y, Mei Y, Ballauff M, Drechsler M. Thermosensitive core-shell particles as carrier systems for metallic nanoparticles. J. Phys. Chem. B 110 (2006), 3930-3937.

[64] Baruah B, Gabriel GJ, Akbashev MJ, Booher ME. Facile synthesis of silver nanoparticles stabilized by cationic polynorbornenes and their catalytic activity in 4-nitrophenol reduction. Langmuir 29 (2013), 4225-4234.

[65] Rashid MH, Mandal TK. Synthesis and catalytic application of nanostructured silver dendrites. J. Phys. Chem. C 111 (2007), 16750-16760.

[66] Zhang W, Tan F, Wang W, Qiu X, Qiao X, Chen J. Facile, template-free synthesis of silver nanodendrites with high catalytic activity for the reduction of p-nitrophenol. J. Hazard. Mater. 217-218 (2012), 36-42.

[67] Tang S, Vongehr S, Meng X. Controllable incorporation of Ag and Ag-Au nanoparticles in carbon spheres for tunable optical and catalytic properties. J. Mater. Chem. 20 (2010), 5436-5445.
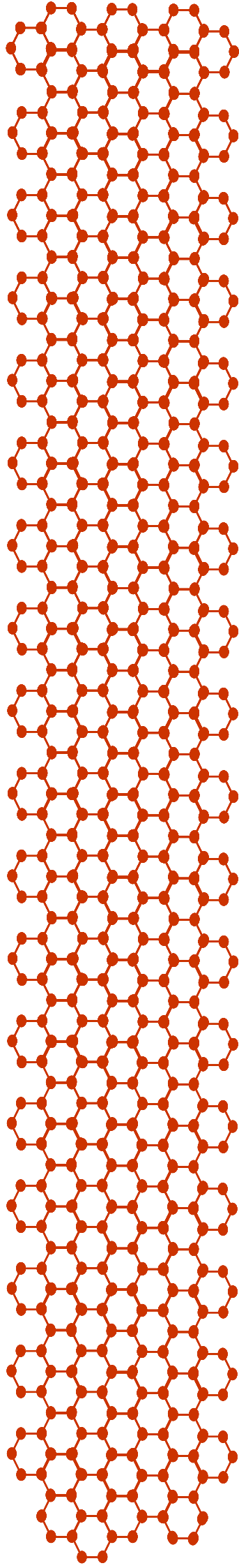
5. CONCLUSIONES

Los resultados expuestos en la presente Memoria permiten extraer las siguientes conclusiones generales:

- Es posible reemplazar la hidracina como agente reductor del óxido de grafeno por sustitutos eficaces, seguros y medioambientalmente sostenibles. Se han identificado 9 nuevos agentes reductores para dicho propósito, en concreto vitaminas y aminoácidos naturales, todos ellos clasificados como biomoléculas benignas.

- La combinación de irradiación con luz ultravioleta y glutatión permite una reducción eficaz de dispersiones acuosas de óxido de grafeno a temperatura ambiente.

- Es posible estabilizar dispersiones acuosas de óxido de grafeno reducido bajo condiciones fisicoquímicas desfavorables, tales como pH ácido, alta concentración de óxido de grafeno o grandes dimensiones laterales de las láminas. Esto se ha conseguido mediante la introducción de surfactantes adecuados en el medio coloidal. La presencia de surfactantes concretos mejora muy significativamente la capacidad específica de filmes de óxido de grafeno reducido.

- La obtención de dispersiones acuosas estables de grafeno estructuralmente perfecto por exfoliación de grafito prístino mediante ultrasonidos a concentraciones significativas es realizable por medio de la introducción de un surfactante en el medio, siendo los surfactantes no iónicos más eficaces que los iónicos.

- El uso de agentes reductores naturales, combinado o no con radiación ultravioleta, permite preparar distintos materiales híbridos formados por láminas de óxido de grafeno reducido y nanopartículas metálicas. Varios de los híbridos obtenidos que contienen nanopartículas de plata presentan una actividad catalítica muy elevada en la reducción de 4-nitrofenol a 4-aminofenol.

- Es posible preparar nanopartículas de sílice mesoporosa soportadas sobre óxido de grafeno con densidades controladas mediante una selección cuidadosa de las condiciones de síntesis de la sílice.
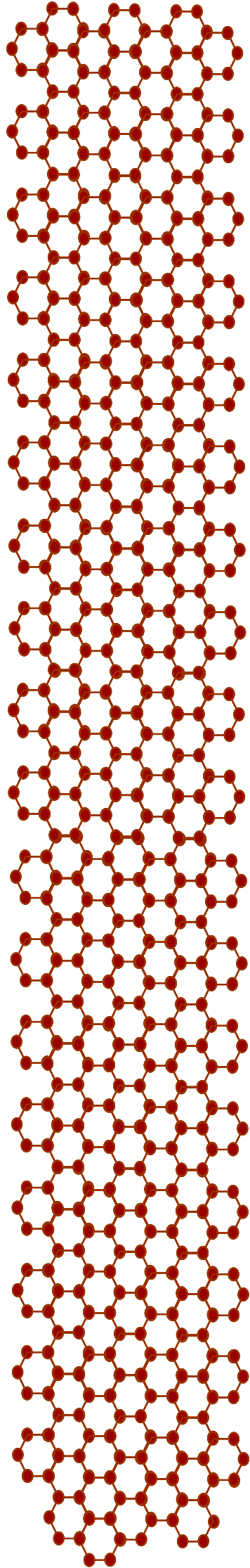
6. ANEXO

Durante la realización de la tesis doctoral se generaron una serie de publicaciones no incluidas en esta memoria, aunque de temática íntimamente relacionada.

- Paredes JI, Villar-Rodil S, Solís-Fernández P, Fernández-Merino MJ, Guardia L, Martínez-Alonso A, Tascón JMD. Preparation, characterization and fundamental studies on graphenes by liquid-phase processing of graphite. J. Alloy. Compd. 536 (2012), S450-S455.

- Paredes JI, Villar-Rodil S, Fernández-Merino MJ, Guardia L, Martínez-Alonso A, Tascón JMD. Environmentally friendly approaches toward the mass production of processable graphene from graphite oxide. J. Mater. Chem. 21 (2011), 298-306.

Aportaciones a congresos:

- Paredes JI, Villar-Rodil S, Solís-Fernández P, Guardia L, Fernández- Merino MJ, Martínez-Alonso A, Tascón JMD. STM imaging of graphene nanosheets derive of graphite oxide. International Forum on Carbon Nanoscience, St John´s College (University of Cambridge), 13 de Noviembre de 2009.

- Fernández-Merino MJ, Guardia L, Paredes JI, Villar-Rodil S, Solís-Fernández P, Martíínez-Alonso A, Tascón JMD. Preparación de grafenos por reducción química de óxido de grafeno: Efecto de distintos reductores. X Reunión del Grupo Español del Carbón, Gerona (España), 9 – 12 Mayo de 2010.

- Solís-Fernández P, Paredes JI, Villar-Rodil S, Guardia L, Fernández- Merino, Dobrik G, Biró LP, Martínez-Alonso A, Tascón JMD. Oxidación local y global de láminas de grafeno químicamente modificadas. X Reunión del Grupo Español del Carbón, Gerona (España), 9 – 12 Mayo de 2010.

- Fernández-Merino MJ, Paredes JI, Villar-Rodil S, Guardia L, Solís-Fernández P, Salinas-Torres D, Cazorla-Amorós D, Murallón E, Martínez-Alonso A, Tascón JMD. Surfactant-stabilized aqueous dispersions of reduced graphene oxide. The annual world conference on Carbon, Krakow (Poland), 17-22 Julio de 2012.

- Solís-Fernández P, Rozada R, Paredes JI, Villar-Rodil S, Fernández-Merino MJ, Guardia L, Martínez-Alonso A, Tascón JMD. Chemical and microscopic analysis of graphene prepared by different reduction degrees of graphene oxide. 18th

International symposium on metastable, amorphous and nanostructured materials (Ismanam), Gijón (Spain), 26 Junio- 1 Julio de 2011.

- Paredes JI, Villar-Rodil S, Solís-Fernández P, Fernández-Merino MJ, Guardia L, Martínez-Alonso A, Tascón JMD. Preparation, characterization and fundamental studies on graphenes by liquid-phase processing of graphite. 18th International symposium on metastable, amorphous and nanostructured materials (Ismanam), Gijón (Spain), 26 Junio- 1 Julio de 2011.

- Fernández-Merino MJ, Paredes JI, Villar-Rodil S, Guardia L, Solís-Fernández p, Salinas-Torres D, Cazorla-Amorós D, Morallón E, Martínez-Alonso A, Tascón JMD. Influencia de surfactantes en la estabilización de dispersiones acuosas de óxido de grafeno reducido y en las características de sus películas. XII Congreso nacional de materiales. XII Congreso iberoamericano de materiales, Universidad de Alicante (España), 30, 31 de Mayo y 1 Junio de 2012.

- Guardia L, Fernández-Merino MJ, Paredes JI, Solís-Fernández P, Villar-Rodil S, Martínez-Alonso A, Tascón JMD. Beneficial effect of ionic surfactants for the high-throughput production of aqueous dispersions of pristine graphene. Imaginenano, Bilbao (Spain), 11-14 Abril de 2011.

- Fernández-Merino MJ, Guardia L, Paredes JI, Villar-Rodil S, Solís-Fernández P, Martínez-Alonso A, Tascón JMD. Vitamin C as an innocuous and safe substitute for hydrazine in the reduction of graphene oxide suspensions. Imaginenano, Bilbao (Spain), 11-14 Abril de 2011.

- Paredes JI, Fernández-Merino MJ, Villar-Rodil S, Solís-Fernández P, Guardia L, García R, Martínez-Alonso A, Tascón JMD. Preparation of graphene and graphene-metal nanoparticle hybrids with enhanced catalytic activity by reduction of graphite oxide with efficient natural bioreductants. Imaginenano, Bilbao (Spain), 23-26 Abril de 2013.